

## Aeroacoustic Study of a 26%-Scale Semispan Model of a Boeing 777 Wing in the NASA Ames 40- by 80-Foot Wind Tunnel

*W. Clifton Horne, Nathan J. Burnside, Paul T. Soderman, Stephen M. Jaeger, Bryan R. Reinero, Kevin D. James, and Thomas K. Arledge*



## The NASA STI Program Office . . . in Profile

Since its founding, NASA has been dedicated to the advancement of aeronautics and space science. The NASA Scientific and Technical Information (STI) Program Office plays a key part in helping NASA maintain this important role.

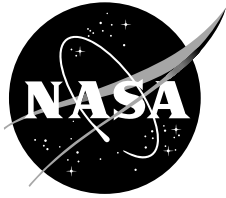
The NASA STI Program Office is operated by Langley Research Center, the Lead Center for NASA's scientific and technical information. The NASA STI Program Office provides access to the NASA STI Database, the largest collection of aeronautical and space science STI in the world. The Program Office is also NASA's institutional mechanism for disseminating the results of its research and development activities. These results are published by NASA in the NASA STI Report Series, which includes the following report types:

- **TECHNICAL PUBLICATION.** Reports of completed research or a major significant phase of research that present the results of NASA programs and include extensive data or theoretical analysis. Includes compilations of significant scientific and technical data and information deemed to be of continuing reference value. NASA's counterpart of peer-reviewed formal professional papers but has less stringent limitations on manuscript length and extent of graphic presentations.
- **TECHNICAL MEMORANDUM.** Scientific and technical findings that are preliminary or of specialized interest, e.g., quick release reports, working papers, and bibliographies that contain minimal annotation. Does not contain extensive analysis.
- **CONTRACTOR REPORT.** Scientific and technical findings by NASA-sponsored contractors and grantees.
- **CONFERENCE PUBLICATION.** Collected papers from scientific and technical conferences, symposia, seminars, or other meetings sponsored or cosponsored by NASA.
- **SPECIAL PUBLICATION.** Scientific, technical, or historical information from NASA programs, projects, and missions, often concerned with subjects having substantial public interest.
- **TECHNICAL TRANSLATION.** English-language translations of foreign scientific and technical material pertinent to NASA's mission.

Specialized services that complement the STI Program Office's diverse offerings include creating custom thesauri, building customized databases, organizing and publishing research results . . . even providing videos.

For more information about the NASA STI Program Office, see the following:

- Access the NASA STI Program Home Page at <http://www.sti.nasa.gov>
- E-mail your question via the Internet to [help@sti.nasa.gov](mailto:help@sti.nasa.gov)
- Fax your question to the NASA Access Help Desk at (301) 621-0134
- Telephone the NASA Access Help Desk at (301) 621-0390
- Write to:  
NASA Access Help Desk  
NASA Center for AeroSpace Information  
7121 Standard Drive  
Hanover, MD 21076-1320



## **Aeroacoustic Study of a 26%-Scale Semispan Model of a Boeing 777 Wing in the NASA Ames 40- by 80-Foot Wind Tunnel**

*W. Clifton Horne*

*Ames Research Center, Moffett Field, California*

*Nathan J. Burnside*

*AerospaceComputing Inc., Ames Research Center, Moffett Field, California*

*Paul T. Soderman*

*Ames Research Center, Moffett Field, California*

*Stephen M. Jaeger*

*Colin Gordan and Associates, San Bruno, California*

*Bryan R. Reinero*

*AerospaceComputing Inc., Ames Research Center, Moffett Field, California*

*Kevin D. James and Thomas K. Arledge*

*Ames Research Center, Moffett Field, California*

National Aeronautics and  
Space Administration

Ames Research Center  
Moffett Field, California 94035-1000

## **Acknowledgments**

This research was funded by the NASA Advanced Subsonic Technology Noise Reduction Program/Quiet Aircraft Technology Programs by William L. Willshire. A large number of individuals from many organizations contributed significantly to the success of this investigation, a partial list follows:

NASA Ames Research Center: Dale Satran, Bruce Storms, Jim Kennon, and James Bell. NASA Langley Research Center: Bart Singer, Mehdi Khorrami, and Craig Streett. Boeing: Rob Stoker and Jim Underbrink.

Available from:

NASA Center for AeroSpace Information  
7121 Standard Drive  
Hanover, MD 21076-1320  
(301) 621-0390

National Technical Information Service  
5285 Port Royal Road  
Springfield, VA 22161  
(703) 487-4650

## TABLE OF CONTENTS

NOMENCLATURE .....	v
1 BACKGROUND .....	2
1.1 Introduction .....	2
1.2 Related Documents .....	2
2 EXPERIMENTAL SETUP .....	4
2.1 Test Facility .....	4
2.2 Model and Support .....	4
2.3 Acoustic Instrumentation .....	5
Traversing Array .....	6
Fixed Array .....	7
Reduction of Microphone Self-Noise .....	8
Array Data Acquisition and Processing .....	8
2.4 Background Noise .....	9
3 BASELINE ACOUSTICAL CHARACTERISTICS .....	11
3.1 Cruise Configuration .....	11
Mach Variation at $\alpha = 4^\circ$ .....	11
Angle-of-Attack Variation at Mach 0.21 .....	11
3.2 Landing Configuration .....	12
Mach Sweep at $\alpha = 6^\circ$ and Traverse T150d .....	12
Angle-of-Attack Sweep, Mach 0.18 High-Fidelity Gear – C3a .....	13
Angle-of-Attack Sweep, Mach 0.21, No Gear – C3 .....	13
Array Traverse, Mach 0.21, $\alpha = 6^\circ$ , Hi-Fi Gear – C3a .....	14
Array Traverse, Mach 0.21, $\alpha = 6^\circ$ , No Gear – C35 .....	14
3.3 Approach Configuration .....	15
Mach Sweep, $\alpha = 6^\circ$ , T150d .....	16
Angle-of-Attack Sweep, $M = 0.21$ .....	16
Array Traverse, $M = 0.21$ , $\alpha = 6^\circ$ .....	16
4 LANDING GEAR SOURCE .....	17
4.1 Landing Gear Configurations and Measurements .....	17
5 FLAP-EDGE SOURCE .....	21
5.1 Flap-Edge Aerodynamic and Acoustic-Baseline Configurations .....	21
5.2 Porous-Surface Flap-Edge Treatment .....	22
5.3 Serrated Trailing Edge .....	23
5.4 Flap Side-Edge Microtabs .....	23
5.5 Flap-Edge Fence .....	24
6 SLAT-GAP AND BRACKET SOURCE .....	25
6.1 Slat Cove Measurements .....	25
6.2 Cove Filler .....	25
6.3 Serrated-Slat Trailing Edge .....	26
6.4 Slat With Thin Trailing Edge .....	26
6.5 Scotchbrite Porous-Sleeve Treatment of Slat Brackets .....	26
7 SLAT-TIP SOURCE .....	28
7.1 Overview of Slat-Tip Noise .....	28

7.2	Dependence of Noise of Untreated Slat Tips on Velocity and Angle of Attack .....	29
7.3	Effect of Outboard-Slat Cove Filler on Slat-Tip Noise .....	29
7.4	Effect of Slat-Tip Fences.....	29
8	CONCLUDING REMARKS .....	31
8.1	Test Model and Instrumentation .....	31
8.2	Baseline Cruise, Landing, and Approach Configurations.....	31
8.3	Effectiveness of Component Source Reduction Methods.....	32
	Landing Gear Source .....	32
	Flap-Edge Source.....	33
	Slat Gap/Bracket Source .....	33
	Slat-Edge Source.....	34
	APPENDIX A: RUN SUMMARY .....	161
	APPENDIX B: CONFIGURATION SUMMARY .....	181
	APPENDIX C: MODEL AND ARRAY GEOMETRY.....	183
	C.1 Model Locations Relative to the Acoustic Arrays.....	183
	C.2 High-Lift System Characteristics.....	187
	APPENDIX D .....	195
	D.1 Integration Method.....	195
	D.2 Scaling the Acoustic Spectra .....	196
	D.3 Array Cavity Simulations.....	197
	APPENDIX E: ARRAY MICROPHONE LOCATIONS .....	205
	APPENDIX F: LIST AND DESCRIPTION OF DATA FILES.....	207

## NOMENCLATURE

AOA or $\alpha$	model angle of attack as measured at wing mean aerodynamic chord, deg
Cove	slat cove region
d	small-scale distance from noise source to array center, ft
D	full-scale distance from noise source to array center, ft
f	frequency, Hz
FS	full scale
hi-fi	high-fidelity landing gear configuration
i	frequency band index
IFIE	inboard flap inboard edge
IFOE	outboard edge of the two element inboard flap
ISIE	inboard slat inboard edge
LE	leading edge
LGTC	landing gear truck center
L <sub>p</sub>	sound level, dB relative to 20 $\mu$ Pa
M	free-stream Mach number
MS	model scale
OFIE	outboard flap inboard edge
OFOE	outboard flap outboard edge
OSIE	outboard slat inboard edge
OSOE	outboard slat outboard edge
R	run number or distance from noise source to array center, ft
R <sub>c</sub>	distance from apparent (convected) noise source to array center, ft
$\hat{R}$	average cross-spectral matrix used in beamforming
SF	scale factor = 0.26
TE	trailing edge
T0	array traverse station 0 in. downstream of model reference center
T100u	array traverse station 100 in. upstream of model reference center
T150d	array traverse station 150 in. downstream of model reference center
T250d	array traverse station 250 in. downstream of model reference center
X <sub>A</sub>	array coordinate relative to array center, positive upstream, in.
X <sub>M</sub>	model coordinate relative to model reference center, positive upstream, in.
X <sub>W</sub>	wind tunnel coordinate relative to turntable center, positive downstream, in.
Y <sub>A</sub>	array coordinate relative to array center, positive toward ceiling, in.
Y <sub>M</sub>	model coordinate relative to model reference center, positive toward ceiling, in.
Y <sub>W</sub>	wind tunnel coordinate relative to turntable center, positive toward right wall, in.
Z <sub>A</sub>	array coordinate relative to array center, positive toward right wall, in.
Z <sub>M</sub>	model coordinate relative to model reference center, positive toward right wall, in.
Z <sub>W</sub>	wind tunnel coordinate relative to turntable, positive toward ceiling, in.

- dB change in noise level relative to baseline configuration, dB
- measured angle between noise source and array center in streamwise plane containing noise source and array center, deg (0° is upstream direction)
- c acoustic emission angle between apparent (convected) noise source and array center in streamwise plane containing noise source and array center, deg (0° is upstream direction)
- measured angle between noise source and array center in plane of test section cross section, deg (0° is downward)

# **Aeroacoustic Study of a 26%-Scale Semispan Model of a Boeing 777 Wing in the NASA Ames 40- by 80-Foot Wind Tunnel**

W. Clifton Horne, Nathan J. Burnside,<sup>\*</sup> Paul T. Soderman, Stephen M. Jaeger,<sup>†</sup> Bryan R. Reinero,<sup>\*</sup> Kevin D. James, and Thomas K. Arledge

Ames Research Center

## **SUMMARY**

An acoustic and aerodynamic study was made of a 26%-scale unpowered Boeing 777 aircraft semispan model in the NASA Ames 40- by 80-Foot Wind Tunnel for the purpose of identifying and attenuating airframe noise sources. Simulated approach and landing configurations were evaluated at Mach numbers between 0.12 and 0.24. Cruise configurations were evaluated at Mach numbers between 0.24 and 0.33. The research team used two Ames phased-microphone arrays—a large fixed array and a small traversing array—mounted under the wing to locate and compare various noise sources in the wing high-lift system and landing gear. Numerous model modifications and noise alleviation devices were evaluated. Simultaneous with acoustic measurements, aerodynamic forces were recorded to document aircraft conditions and any performance changes caused by the geometric modifications. Numerous airframe noise sources were identified that might be important factors in the approach and landing noise of the full-scale aircraft. Several noise-control devices were applied to each noise source. The devices were chosen to manipulate and control, if possible, the flow around the various tips and through the various gaps of the high-lift system so as to minimize the noise generation. Fences, fairings, tip extensions, cove fillers, vortex generators, hole coverings, and boundary-layer trips were tested. In many cases, the noise-control devices eliminated noise from some sources at specific frequencies. When scaled to full-scale third-octave bands, typical noise reductions ranged from 1 to 10 dB without significant aerodynamic performance loss.

---

<sup>\*</sup> AerospaceComputing Inc., Ames Research Center, Moffett Field, Mountain View, CA

<sup>†</sup> Colin Gordan and Associates, San Bruno, CA

# 1 BACKGROUND

## 1.1 Introduction

The purpose of this study was to investigate the airframe noise of a large-scale model transport wing and landing gear and to evaluate the performance of numerous noise-control devices mounted on the model. This work was the culmination of many small-scale studies of airframe noise sources and control devices developed under the Advanced Subsonic Transport (AST) program and the Quiet Aircraft Technology (QAT) program directed by NASA Langley Research Center. In this program, small-scale studies were used to evaluate flow physics and new technologies for aircraft components or for supporting computational studies of aeroacoustics. Large-scale studies were designed to validate small-scale results with good geometric fidelity and high Reynolds number flows that are closer to full scale. Thus, validation of small-scale airframe noise studies was a general objective of this study. In addition some new technologies were also tested.

The Subsonic Transport Aeroacoustic Research (STAR) model used in this study was a 26%-scale semispan duplicate of a production Boeing 777 aircraft fabricated at NASA Ames based on design data provided by Boeing. The model was equipped with a detailed high-lift system, main landing gear, and half-fuselage without empennage or nose gear. The only significant departure from the actual aircraft was the lack of jet engines; flow-through nacelles on the wing were employed instead. The semispan model was mounted close to the wind-tunnel floor, which acted as a reflection plane to simulate the aerodynamic loading on a three-dimensional aircraft model. Adequate space was available to the side of the test section for acoustic surveys of the flyover noise. Two phased-microphone arrays were mounted under the wing for this purpose—one a large fixed array and the other a small traversing array. The array design and performance will be discussed along with the data analysis method.

Interest in identifying and reducing aircraft airframe noise has grown in recent years because of lower engine noise in the fleet, particularly on approach. Motivation is also generated by the trend toward lower airport noise limits. Wind tunnel and flight studies have shown that the important noise sources include landing gear, flap and slat edges, flap and slat gaps, and, to a lesser extent, trailing-edge noise. These noise sources and others were examined in this study and are discussed below, following descriptions of the test facility, the experimental setup, and the baseline acoustical characteristics in the cruise, landing, and approach configurations. Far-field acoustic results are summarized here; a report of the aerodynamic effects will be published separately.

Adjunct information is provided in the appendixes: the run summary (appendix A); configuration summary (appendix B); model and array geometry (appendix C); the integrated source spectra method (appendix D); the array microphone locations (appendix E); and a list and description of the data files (appendix F).

## 1.2 Related Documents

The aerodynamic results of this test are presented in the NASA report: Aerodynamics of a 26%-Scale Semispan Model of the Boeing 777 in the NASA Ames 40- by 80- Foot Wind Tunnel, by Storms, James, and Arledge (in press). Model configurations were influenced by previous tests of

Boeing 777 models and components. Previous Boeing 777 aeroacoustic tests included a 6.3% semispan 777 reported by Stoker and Sen (2001), and a 26% 777 landing gear reported by Jaeger et al. (2003).

The noise treatments evaluated during this test were developed in previous experimental and theoretical studies reported by Ross et al. (1995), Storms et al. (1996, 1998, 2000), Hayes et al. (1997, 1999), Revell et al. (1997), Brooks et al. (2000), Dobzynski et al. (2000), Khorrami et al. (2002), Agarwal and Morris (2002), Casper and Farassat (2002), Choudhari, et al. (2002), Mendoza et al. (2002), and others.

Phased-microphone arrays were used in this study to locate noise sources and to estimate source levels. The development and application of phased-microphone arrays in aeroacoustic testing has been reported by Mosher (1996), Brooks and Humphreys (1999), Horne and James (1999), Jaeger et al. (2000), van der Wal and Sijtsma (2001), Burnside et al. (2002), Dougherty (2002), Soderman et al. (2002), Underbrink (2002), and others.

An extensive literature base on airframe noise theory and experiments prior to the application of phased-microphone arrays was reviewed by Crighton (1991).

## 2 EXPERIMENTAL SETUP

### 2.1 Test Facility

The NASA Ames 40- by 80-Foot Wind Tunnel (40x80) is part of the National Full-Scale Aerodynamics Complex. It is a closed-circuit wind tunnel driven by six 40-ft-diameter, 22,500-hp fans. The test section walls are semi-circular with a flat floor and ceiling. The test section is nominally 40 ft high, 80 ft wide, and 80 ft long. An 8:1 contraction leading into the test section helps to alleviate flow nonuniformity and turbulence. Figure 1 shows the 40 x 80 facility. Maximum test-section velocity is 300 knots ( $M = 0.45$ ).

The inner surface of the test section is covered with an acoustic lining to minimize sound reflection and reverberation. The surface of this acoustic lining is composed of 4- by 4-ft panels; each consisting of a perforated metal sheet with a fine-mesh metal screen bonded to its surface. The panel construction is a compromise between minimizing boundary-layer growth, maximizing acoustic transparency, and adhering to structural requirements. Beneath each panel is a 42-in.-deep cavity filled with fiberglass wedges. Figure 2 shows the acoustic lining assembly. The sound passes through the upper panel and is, to a large extent, absorbed by the fiberglass wedges. The acoustic lining succeeds in absorbing 94% to 97% of the acoustic energy in the low- to mid-frequency range (100 Hz–2,500 Hz) and 78% to 97% in the high-frequency range (4 kHz–20 kHz). This makes the wind tunnel well suited for acoustic testing of randomly generated noise sources such as jet noise or airframe noise. Acoustic quality is also enhanced by use of the two phased-microphone arrays. Further detail of the acoustic lining performance can be found in AIAA conference papers by Soderman et al. (1999, 2000) and in two NASA publications by Soderman et al. (2002).

In order to validate the acoustic results of the Subsonic Transport Aeroacoustic Research (STAR) test, the model aerodynamics had to match those of the production aircraft as closely as possible. In the wind tunnel, forces and moments are measured through a six-component scale system. Typically, a model is mounted on struts attached to the floating frame beneath the tunnel floor. This frame is connected to four lift posts, two side links and a drag link, which in turn are connected to load cells by means of mechanical linkages. Direct measurement of the forces through the main links gives the model forces. Mechanically adding or differencing these linkages gives the model moments. The STAR model was mounted on the floating frame by a semispan turntable. This semispan turntable allowed for model angle-of-attack changes independent of the tunnel turntable. The angle-of-attack range was  $-5^\circ$  to  $25^\circ$ . For the semispan STAR model, the lift loads were measured by the tunnel's side force gauges. The capacity in the model lift direction was  $\pm 32,000$  lb and drag capacity was  $\pm 16,000$  lb. Both of these scales have an accuracy of  $\pm 10$  lb.

### 2.2 Model and Support

The STAR model was a highly accurate 26%-scale semispan replica of a Boeing 777 aircraft. The components of this high-fidelity model were fabricated to a tolerance of 0.03 in. and to within 0.25 in. for overall positioning between any two parts, quite accurate for a 26% model. The model had a steel frame with aluminum and composite cover panels. Many of the wing components were aluminum, and some composites were used for the acoustic treatments. The fuselage had a flexible rubber skirt around its base to minimize airflow underneath the model, while still allowing clearance

between the solid structure of the model and the test-section floor. A fouling circuit was integrated into the skirt at key locations to warn of any skirt compression between model and floor. Because the focus of this test was on the wing, the model had no empennage. Although the engine nacelle was designed to support a jet engine, it was used in a flow-through nacelle for this test. The basic frame of the landing gear was covered with stereolithographic pieces to model the actual shape of the struts with collars, brackets, etc. Other linkages, brake lines, and cables were also modeled. Including all of these detailed parts was important because of their potential to affect model aerodynamics or act as noise sources. Information about the isolated landing gear test can be found in Jaeger et al. (2002).

The wing included all of the aerodynamic control surfaces of the production aircraft's high-lift system including the inboard main flap, inboard aft flap, flaperon, outboard flap, aileron, and all the leading-edge slats. These surfaces could be moved manually to achieve specific flight configurations: takeoff, cruise, approach, and landing. Figure 3 shows the STAR model with the high-lift system deployed. Several acoustic treatments to be described were applied to the wing to attenuate noise sources. Figure C.3 and table C.7 (in App. C) give details of the model geometry and dimensions.

Model instrumentation was another step toward validating the aerodynamic performance, as well as the acoustic performance. The model surface was instrumented with approximately 2,200 static pressure ports. Forty-eight unsteady pressure transducers were installed in key locations throughout the model. These would serve to validate the physical flow phenomenon of a possible noise source; for example, matching vortex shedding frequency to measured acoustic frequency.

## 2.3 Acoustic Instrumentation

To evaluate airframe noise sources and to validate noise treatments it is necessary to accurately measure the source level, location, and directivity. Because of the size of the STAR model, this was accomplished with two phased-microphone arrays. A large fixed array was used for source location at low frequencies, and a smaller traversing array was used to measure source levels and directivity, and to locate sources at high frequency (Burnside et al. 2002). Although two arrays were used in tandem to acquire data during the STAR test, data were never acquired from both arrays simultaneously. Instead, the arrays were selected with a computer-controlled switching network. Figure 4 shows the overall test-section layout for the test. Both arrays utilized Kevlar-covered, recessed microphones to reduce microphone self-noise. The Kevlar covering on both arrays is shown in Figure 5. The ability to traverse the array within the wind tunnel was a great productivity asset. To the knowledge of the authors, this was the first time an array has been traversed in a closed-section wind tunnel.

To optimize both array patterns, a *MATLAB*<sup>®</sup>-based, simulated annealing code was used to reduce beam width and side lobes (Jaeger et al. 2000). Simulated annealing is a Monte Carlo method that optimizes the microphone locations in a manner analogous to metal annealing. When a metal is heated and then cooled slowly, atoms move from local energy minima positions into absolute minima positions (Reid, 1993). Simulated annealing applied to array design causes microphones to move from their original positions in a random direction during an iterative process. At each step, array response is calculated and compared to the response of the previous iteration. If the new pattern is an improvement, it becomes the current pattern and the next iteration begins. At each step in the iterative process, microphones are moved less than in the previous step. The rate at which

microphone movement decreases is a user-defined function and is analogous to the cooling of the molten metal.

### Traversing Array

The traversing array was housed in an aerodynamic fairing mounted atop a dual-rail streamwise linear traverse, as shown in figure 5(a). The 40-in.-square array plate was embedded in a 3-in.-thick fairing with an 80-in. chord. The fairing had an elliptical nose and tail. The traverse system is described by Soderman and Allen (2002). Although the traversing array had a range of about 70 ft, it was only moved from 100 in. upstream and to 350 in. downstream of the model pivot. Appendix C describes the traversing array placement and summarizes pertinent information such as geometric and emission angles for each potential noise source.

The traversing array contained 70 0.25-in. GRAS model TMS140BF microphones and TMS126AC preamplifiers. Long cables that ran the length of the traverse connected the microphones to 35 TMS112AA power supplies in the balance house below the test section. To maximize dynamic range and minimize electrical noise, the GRAS amplifiers provided a 20-dB gain.

**Pattern design and calibration (Burnside et al., 2002).** To design the traversing array, simulated annealing was applied to a 70-element symmetric seed pattern that yielded the pattern shown in figure 6. A code for simulating beam patterns (Underbrink 1995) indicated that the resulting array pattern would have a spatial resolution of  $6.5 \lambda$ , where  $\lambda$  is the acoustic wavelength. In other words, on a noise map at a given frequency, a point source would be represented as a spot with a diameter 6.5 times its wavelength.

The highest side-lobe levels at a number of frequencies was simulated with a point source located 226 in. (18 ft 10 in.) from the array center (Underbrink 1995). At 1 kHz, the highest side-lobe levels were 17.5 dB below the main beam. Side-lobe levels increased with frequency, but at 25 kHz the highest side lobes were still 5.4 dB below the main beam. Figure 7 shows a simulated array response at 5.1 kHz for a point source located 226 in. from the array. The worst case side lobe is 12.9 dB below the main beam.

To verify that the arrays were accurately measuring sound pressure levels, a loudspeaker noise map was integrated using a monopole integration scheme described in appendix D (see also Soderman et al. 2002). Because the test section of the 40 x 80 wind tunnel is nearly anechoic, this was an effective form of array calibration. A rectangular integration region was created around the loudspeaker, as shown in figure 8. Energy within the boxes at each frequency was then integrated to form narrowband spectra and 1/3-octave levels. No Kevlar cavity corrections were made to the integrated speaker data. Traversing array integrated levels compared very well with individual microphone measurements made with no wind. Figure 9 compares the integrated speaker results and the average spectra of all array microphones. The average spectrum represents the response of a single microphone. Because the microphones were flush mounted in a plate, the correction for 6-dB pressure doubling was included in the average spectra. The curves agreed very well up to about 15 kHz, where a difference of about 0.5 dB was found. This trend is consistent with previous work done by Brooks and Humphreys (1999), who showed that response error increased as a function of frequency for a given array. Data above 20 kHz were ignored because the noise source had a low-pass filter corner frequency of 20 kHz.

## Fixed Array

The fixed array was mounted in a large fairing with a thickness of 1 ft and a cord of 11 ft. Figure 10 shows the aerodynamic leading edge and the large support structure. The trailing edge was left blunt to minimize fabrication costs. The array was large enough to place the microphone power supplies inside the fairing. The fixed array placement and convected source angles are discussed in appendix C.

Microphones in the fixed array consisted of a mix of GRAS and B&K 0.25-in. microphones and preamplifiers. B&K type 2822 power supplies powered 30 microphone channels, and the remaining 40 channels used TMS112AA power supplies. All of the power supplies were located in the fixed-array fairing to minimize electrical noise. BNC cables carried the data to the balance house where the 30 B&K channels were amplified by 20 dB using model 6624-k-lp1 programmable Precision Filters (the GRAS power supplies had built-in gains of 20 dB).

**Pattern design and calibration (Burnside et al., 2002).** Previous tests have demonstrated that recessing the microphones of an in-flow array behind a porous screen improves the signal-to-noise ratio, particularly at low frequencies. To recess the fixed-array microphones behind Kevlar, the array pattern had to be grouped into smaller subgroups because a continuous sheet of Kevlar could not be found that would cover the entire array. The subgroups of microphones made the array more difficult to design using simulated annealing. The fixed-array pattern was composed of a small group of 10 center microphones, surrounded by five larger groups of 12 microphones each as shown in figure 11. The outer groups were all identical except each was rotated 72° relative to its placement around the diameter of the fixed array. During the simulated annealing, microphones in the center and one outside grouping were moved to optimize array performance. However, at each step in the annealing process the entire array was evaluated for array characteristics such as beam width and side lobe levels.

A simulated beam pattern for the fixed array is shown in figure 12. Simulations showed that the fixed array had a spatial resolution of 3.4  $\square$ , almost a factor of 2 better than the traversing array. Over the frequency range of interest for the fixed array (200–10,000 Hz), side-lobe levels were comparable to the traversing array. The low and high edges of the operational frequency envelope for each array were similar with respect to side-lobe energy. At 200 Hz, worst-case side lobes were 17.3 dB down, while the traversing array had levels of 17.4 down at 1.0 kHz. Similarly, the fixed-array side-lobe levels increased to 4.8 dB down at 10 kHz, while the traversing array had side lobes 5.4 dB down at 25 kHz. For the fixed array, side lobes above 10 kHz quickly increased, and at 15 kHz side lobe levels exceeded the main beam. Hence, the frequency ranges for the traversing and fixed array were 1–25 kHz and 200–10,000 Hz, respectively.

Consistent with results from Brooks and Humphreys (1999), integrated speaker noise as measured by the large array did not compare as well with a single microphone approximation as the traversing array because of the larger pattern. In the frequency range of interest for this array, below 10 kHz, errors were typically less than 0.5 dB, as shown in figure 13. Above 11 kHz, errors were modest, typically about 1 dB. Above 10 kHz, it was suspected that source coherence was not constant across the face of the array with the wind tunnel running.

## Reduction of Microphone Self-Noise

Microphone array processing has improved dramatically in the past 10 years, but a problem that still plagues researchers is microphone self-noise. In-flow arrays are subject to a turbulent boundary layer over the sensors that increases microphone incoherent background noise. Two methods have been successfully used at Ames to reduce incoherent microphone self-noise. One approach is to alter the diagonal of the cross-spectral matrix  $\hat{R}$  before beam forming. Off-diagonal terms of the cross-spectral matrix contain the cross-spectra between microphones. Diagonal terms of the cross-spectral matrix represent the auto-spectra of a single microphone and contain both coherent signals and incoherent noise (Mosher 1996). By modifying the diagonal values with an average calculated from off-diagonal terms, incoherent background noise is reduced. Further discussion of classic frequency-domain beam forming applied to aeroacoustics can be found in Mosher (1996) and Dougherty (2002).

The second approach, developed at Ames, utilizes a physical means to reduce background noise. Jaeger et al. (2000) performed an extensive study to reduce this noise with a variety of schemes that recessed the microphones below the boundary layer. Recessing the microphones behind a low-mass, low-impedance material isolates them from the turbulent boundary layer. Both arrays were recessed behind a stretched Kevlar sheet to reduce low frequency self-noise. Figure 14 shows a sketch of the microphone mounting scheme. Although Kevlar greatly increases the dynamic range of an array, the data had to be corrected for a Kevlar cavity resonance. A detailed discussion of the Kevlar resonance and the corrections applied can be found in appendix D.

## Array Data Acquisition and Processing

Array microphone signals were switched so that one data acquisition computer with 72 A/D channels could be used for both arrays. A switch box was located in the balance house so the signals from the selected array were conducted to the control room via facility wiring. Signal switching was performed with three HP 1442 VXI cards controlled from a PC located in the control room. An IEEE 1394 Firewire connection between the switch box and the control PC was extended using an NEC device that converted the Firewire signal to a fiber optic signal that could be carried over a long distance. Then a second device converted the fiber optic signal back to Firewire. A schematic of the STAR wiring-layout is shown in figure 15. Dashed lines form boundaries indicating where the equipment was located.

In addition to far-field acoustic data, Endevco unsteady pressure sensors were embedded in the model. The PC that controlled the switch box also acquired the Endevco signals with custom-made *MATLAB* software. To digitize the Endevco data, six-HP 1433 A/D cards were placed in the VXI switch-box-rack. Results of the unsteady pressure measurements, however, will not be discussed in this report.\*

Once array data were acquired, they were processed using in-house MAPPS (Microphone Array Phased Processing System) software on a dual-processor SGI Octane workstation. The MAPPS software corrected the data for microphone and equipment response using a frequency-based neural

---

\* The Endevco data are stored in *MATLAB* binary files that require *MATLAB* and the *Data Acquisition Toolbox 2.0* to read.

network prior to beam forming. The MAPPS software used classic, frequency-domain, spherical beam forming to provide array images. For more information about the MAPPS software refer to the *MAPPS Version 4.0 Manual* (Watts et al. 1999).

The scan plane (planar or nonplanar) is a predetermined set of scan points within the acoustic field that the array processing interrogates to detect sources. Three different scan planes were used during STAR data processing:<sup>\*</sup> (1) inboard wing, (2) outboard wing, and (3) landing-gear scan planes. The size of the model made it necessary to create outboard- and inboard-coplanar scan planes. During MAPPS processing, a process identifier is attached to each data file that was used to identify from which array the data were acquired and what scan plane was used for processing. The result of three scan planes and two arrays was six array process numbers, listed in table 1. Coplanar processes 28, 29, 38, and 39 were used to evaluate wing sources. Figure 16 shows the plane that cuts through the wing. Landing gear sources were evaluated with processes 08 and 18, which resided in a plane that was closer to the landing gear, as shown in figure 17.

Table 1. Array process identifier.

Process	Array	Location
08	Fixed	Inboard gear
18	Traversing	Inboard gear
28	Traversing	Inboard wing
29	Traversing	Outboard wing
38	Fixed	Inboard wing
39	Fixed	Outboard wing

To evaluate noise treatments, array source location maps were integrated using a fixed-box method to evaluate the spectra of a given location. Integrations of the entire aircraft were not made at this stage of processing.<sup>\*</sup> Figures 18 and 19 show the seven integration regions used to evaluate STAR data. Boxes were defined for each source region. Integrations were only performed for the traversing array because its source amplitude accuracy was better than the fixed array, as shown in figures 9 and 13. Refer to appendix D for more source integration information.

One-third-octave full-scale and array source-location plots are presented to evaluate noise sources and noise reduction devices. Plot legends include important information such as run, point, array process, and configuration numbers. Plot legends are formatted in the following syntax: run.point.array process.

## 2.4 Background Noise

Even recessed microphones are susceptible to scrubbing noise from flow over the Kevlar cover, wind-tunnel drive noise, test-section boundary-layer noise, etc. However, array processing should provide a good signal-to-noise ratio even in a noisy environment. Previous studies showed that the phased traversing array was capable of measuring a noise source in the Ames 7- by 10-Foot Wind Tunnel that was almost 14 dB below the average sound levels recorded by the individual array microphones (Jaeger et al. 2000).

---

<sup>\*</sup> By evaluating emission angle of each source, these data could be used to project to the far field.

To verify that the acoustic data had adequate signal-to-noise ratio, we examined the background noise measured by the phased arrays. For individual microphones, the background noise is simply that measured at the appropriate Mach number with the model removed from the test section. However, for phased arrays, the analysis is not quite so simple, because the background noise levels depend on array beam forming, which is a function of frequency and scan plane geometry. And because we show only integrated acoustic spectra, the background noise depends on the integration algorithm and integration area. Therefore, to evaluate the signal-to-noise ratio, we plotted integrated sound levels at the various source integration regions both with the model removed from the test section and with the model in cruise configuration, a very quiet geometry as will be discussed. The integration method sums all the sound levels recorded by the array at each scan point as explained in appendix D. This exaggerates the background noise somewhat, because during an integration with a strong noise source in the region, the algorithm eliminates all scan points with sound levels more than 8 dB below the peak level so as to minimize contamination from side lobes. Nonetheless, comparing an integrated noise source with an integration of background noise should be a reasonable way to evaluate signal-to-noise ratio.

Figure 20 shows integrated landing gear noise in the same region (see fig. 19 for box geometry) with the model in cruise configuration ( $\Delta = 0^\circ$ ) and with the model removed. The data were acquired with the traversing array stationed 150 in. downstream of the model pivot,  $\Delta = 6^\circ$  (landing gear data), and  $M = 0.21$ . Clearly, the landing gear noise was at least 10 dB louder than the background or cruise noise except in the high frequencies where the background noise appeared to intrude at 2.5 kHz and above. Despite this intrusion, we were able to measure differences between high-fidelity and simple landing gear at the high frequencies, as will be discussed in section 4. It should be noted that the peak in the 1.6-kHz band was attributed to side-lobe leakage from the outboard slat inboard edge (OSIE) noise source.

Figures 21–24 show similar results for the slat cove, outboard slat outboard edge (OSOE), OSIE, and outboard flap outboard edge (OFOE) integration regions, respectively. Again, the signal-to-noise ratio was very good for all frequencies except for the highest two or three third-octave bands.

### 3 BASELINE ACOUSTICAL CHARACTERISTICS

Two categories of baseline configurations were used during the STAR test: acoustic and aerodynamic baselines. The only difference between the two categories of configurations was a bulb seal on the outboard edge of the outboard flap tip. The bulb seal, sometimes referred to as fairing No. 8 or the Boeing fairing, was on the model for the aero-baseline configurations. This bulb seal proved to be an effective noise treatment for the flap edge as will be discussed in section 5. However, a few flap-edge treatments were not designed to be used with fairing No. 8, so an acoustic baseline without the fairing was used. In this section noise sources are evaluated that would be found on a production aircraft; therefore, only aero-baseline configurations with the bulb seal will be discussed here.

#### 3.1 Cruise Configuration

The cruise configuration was very quiet compared to the wind-tunnel background noise, as was shown in section 2.4 of this report. Most of the source-location plots for cruise were cluttered with side lobes because the airframe noise was below the noise floor of the two arrays. Source-location maps will be presented illustrating the few sources that were visible in the cruise configuration. Because most cruise noise sources were below the background noise, integrated spectra will not be shown.

All cruise data presented were acquired with the model in baseline-cruise configuration C1.\* In this configuration, the slats and flap were stowed, and the landing gear was removed.

##### Mach Variation at $\alpha = 4^\circ$

The only visible source at a  $4^\circ$  angle of attack was located on the bottom rear side of the flow-through nacelle. Figure 25 shows source location images from the large array for this source at Mach 0.21 and 0.26. The peak levels at the two Mach numbers differed by less than a decibel, and the peak frequency of the source increased with velocity as expected.

##### Angle-of-Attack Variation at Mach 0.21

As discussed above, the only visible cruise noise source at angles of attack of  $4^\circ$  and below occurred on the lower portion of the nacelle, as shown in figure 25. Source location images showed that at higher angles of attack, the nacelle created more broadband noise at the rear of the nacelle, as shown in figure 26.

The only other visible noise source was at the wing tip. The wing-tip source was broadband for angles of attack greater than  $8^\circ$  and was about 3 dB louder than the nacelle noise. The wing-tip noise was visible at  $8^\circ$  angle of attack, as shown in figure 27.

---

\* Appendix B contains configuration information.

### 3.2 Landing Configuration

Baseline-landing data were acquired with the model in three configurations, although two configuration numbers, C35 and C37, were used for same model configuration. Slat deflection angles were 20.7° for the inboard slat and 31.6° for the outboard slat in the landing configurations. Flap settings were 42°, 63°, 30°, and 37.5° relative to the main wing for the inboard-main, inboard-aft, flaperon, and outboard-main flaps, respectively. Fairing No. 8 (bulb seal) was in place during all four baseline-landing configurations. The configuration variations included the landing gear and slat trailing-edge serrations. Configuration C3a included the high-fidelity landing gear on the model. C3 was identical to C3a except the landing gear was removed. The two duplicate configurations, C35 and C37, were similar but not identical to C3; C35 / C37 configurations had slat trailing-edge serrations on slat sections 2, 3, and 4 (counting in from the tip). For all configurations with the high-lift system deployed, the half-fairing on the inboard edge of the inboard flap shown in figure 28 was filled with foam and taped. Figure 29 shows a closer view of the filled fairing.

#### Mach Sweep at $\Delta = 6^\circ$ and Traverse T150d

To evaluate noise associated with the landing gear in configuration C3a, array process 18 was used. For more information about the scan planes used in data processing refer to section 2.3.3. Source location images showed little variation of landing-gear sources with changing velocity. Landing-gear sources dominate the noise below 1,000 and 1,300 Hz for Mach 0.18 and 0.21, respectively. As frequency increased, noise from the slats became louder than the landing gear. The frequencies at which slat and landing-gear sources were comparable in amplitude are shown in figures 30 and 31. In the mid-range frequencies, landing-gear noise was detectable at levels approximately 4 dB below slat noise sources as shown in figure 32.

Scaling data for velocity was done in several steps involving a frequency and amplitude shift. First, model-scale narrowband frequencies were velocity scaled to full-scale frequencies according to the following:

$$f_{FS,M2}(i) = f_{MS,M1}(i) \frac{M_2}{M_1} SF \quad (1)$$

where SF is the scale factor. Sound pressure levels were then scaled to full-scale levels without distance scaling:

$$[L_{p_{FS,M2}}(i)]_D = [L_{p_{MS,M1}}(i)]_d \quad (2)$$

where d is the model-scale distance, and D is the large-scale distance equal to d/SF. Amplitudes at each frequency were then adjusted to account for the increase in velocity:

$$L_{p_{FS,M2}}(i) = L_{p_{FS,M1,D}}(i) + 10 \log \frac{M_2}{M_1} \quad (3)$$

Finally the full-scale velocity scaled data were integrated into 1/3-octave bands using standard filter shapes. Scaled data below 250 Hz were questionable because of the large frequency width of 150 Hz in the narrowband data. Unless specified, all text discussion will refer to the full-scale frequency.

A complete Mach sweep was performed for configuration C37, the baseline-landing detent with no landing gear and serrated slats. Figure 33 shows the upper and lower scan-planes for configuration 37 at Mach 0.22. At 1,053 Hz, many sources were present in the slat region and on the inboard and outboard flap-edges. Strong sources were present on the inboard slat-edge and in the slat gap, as shown in figure 34. High-frequency sources included flap edges as shown in figure 35.

Figure 36 shows the variation in Mach number for configurations C3a and C37, which were baseline-landing cases with and without high-fidelity landing gear. Figure 19 shows the landing gear integration region. Full-scale integrated data scales with velocity to the 5th power for the landing-gear region are also shown. Scaled data fall within 0.5 dB for most bands, as shown in figure 36.

Numerous sources were identified in source-location plots, but unlike the spectral plots little effect of velocity variation could be seen. Some tonal sources such as the OSIE shifted with velocity. Figure 37 shows the OSIE peak-frequency shift from Mach 0.18 to 0.22.

Figure 38 shows the effects of increasing velocity on a number of source-integration regions at an angle of attack of 6°. Figure 18 shows the integration regions used for each source. The OFOE, OSOE, OSIE, and cove integration plots contain data scaled from Mach 0.18 to 0.238 with the 5th power. As with the landing gear, scaled-data frequencies below 250 Hz are not shown.

### **Angle-of-Attack Sweep, Mach 0.18 High-Fidelity Gear – C3a**

An angle-of-attack sweep was performed at Mach 0.18 with the high-fidelity landing configuration C3a. Low-frequency landing-gear noise was visible at all angles of attack; an example is shown in figure 39 for 507 Hz full-scale. Landing-gear noise was the dominant source at low frequencies. Figure 40 shows the effect of increasing angle of attack on the integrated spectra. Levels were almost identical for the three angles of attack shown.

### **Angle-of-Attack Sweep, Mach 0.21, No Gear – C3**

It appeared as though slat-bracket and slat-gap noise occurred at number of frequencies across the entire slat section. Figure 41 shows what appears to be both gap noise and bracket noise at the same frequency. Slat-gap noise was found between the 3rd and 4th slat brackets counting in from the tip. Noise from a bracket was also found on the 5th bracket. Figure 42 shows a source-location map for a frequency when slat-bracket noise was found on the 3rd, 4th, and 5th brackets and gap noise was present between the 5th and 6th brackets.

Storms et al. (1998) found that slat-gap noise decreased, and slat side-edge noise increased with increasing angle of attack. Consistent with these results are the integration plots shown in figures 43(a)–43(d). Figure 43(b) shows that as angle of attack was increased from 4° to 8° the mid- and high-frequency noise of the slat cove decreased by as much as 10 dB in some 1/3-octave bands. Levels increased by as much as 5 dB on the OSIE, as shown in figure 43(c).

### **Array Traverse, Mach 0.21, $\alpha = 6^\circ$ , Hi-Fi Gear – C3a**

Landing-gear sources were evaluated with configuration C3a for an array traverse at Mach 0.21 and an angle of attack of  $6^\circ$ . The traversing array made it possible to acquire data at multiple emission angles. Figure 44 shows the baseline landing configuration, C3a, from four different angles. At each traverse position, similar sources were present, but their appearances are very different because of the widened focus of the array main beam and directionally dependent noise radiation. The closest traverse position to a  $90^\circ$  emission angle for landing gear sources was the T0 position as shown in figure 44(b). Unlike the other three traverse positions, the sources appear relatively round and are easier to locate on the model. A noise source was located on the front axle in the T100u position and on both the front and rear axles at the T0 position (tires are represented as a dotted outline in the geometry model). From the T150 and T250 positions the only visible gear source was on the rear axle. Although the sources look very different in the source-location plots, the integrated spectra from each position were similar, as shown in figure 45. All four curves follow the same general shape. Integrated data shown are not normalized to the same distances.

Landing-gear noise source levels were very repeatable throughout the test. Comparing baseline data acquired in the beginning of the test to baseline data acquired midway through the test, showed good repeatability. Between the repeatability points, the model was changed to approach and then back to landing configuration. Figure 46 shows that the repeat points lie on the original curves.

### **Array Traverse, Mach 0.21, $\alpha = 6^\circ$ , No Gear – C35**

To evaluate noise sources not associated with the landing gear, an array traverse at Mach 0.21 and an angle of attack of  $6^\circ$  was performed for configuration C35. Configuration C35 differs from C3 in that slat sections 2, 3, and 4 (counting in from the tip) were serrated. For a detailed description of the slat trailing-edge serrations refer to section 6.2. Figures 47–50 show configuration C35 array images that will be referred to in the following sections.

**Inboard process 28.** For the inboard source-location plots, five consistent high-lift system sources were identified: (1) the inboard edge of the inboard flap, (2) the outboard edge of the inboard flap, (3) the outboard-flap inboard-edge, (4) the inboard-slat inboard-edge, and (5) the outboard-slat inboard-edge. The outboard-slat cove was also a noise source, but it will be discussed in relation to the outboard source-location maps. Figures 28 and 51 show the inboard and outboard flaps in landing configuration.

From the source-location maps it was difficult to determine if the source near the inboard-flap outboard-edge was located on the inboard flap or the high-speed flaperon. When viewed from traverse positions T100u and T0, the source appeared to be located on the inboard flap as shown in figures 47(a), 47(b), 50(a), and 50(b). However, traverse positions T150d and T250d made the source appear to be on the flaperon as shown in figures 47(c), 47(d), 50(c), and 50(d). Because the T0 traverse position was closest to the  $90^\circ$  emission angle for the inboard flap, images from this position should be the most accurate for source location. So it is likely that the source was located on the inboard-flap edge and not on the flaperon. Figure 52 shows the upper surface of the flaperon and the inboard flap.

The inboard-flap inboard-edge (IFIE) had a source that was visible at all traverse positions and over a broad range of frequencies. Care was taken to seal the most inboard half-fairing and also the gap between the fuselage and the flap so as to simulate the aircraft as closely as possible. There was however, a noise source on the edge of the flap or on the fairing as shown in figures 47–50.

The outboard-flap inboard-edge of (OFIE) had a noise source that was visible at traverse positions T150d and T250d. Figures 49, 50(c), and 50(d) show the small source on the edge of the flap near the trailing edge. The inboard edges of the flap and flaperon are shown in figures 52 and 53. This source was not visible from traverse positions upstream of T150d.

Another source visible from only two traverse positions was the inboard-slat inboard-edge (ISIE.) Figures 47 and 50 show that the inboard-slat source was only visible at traverse positions T100u and T0. The ISIE was not a very strong source and was visible over a limited frequency range.

The outboard-slat inboard-edge (OSIE) produced noise at all traverse positions except T100u. This source was broadband, but at some frequencies was as much as 8 dB above other sources. Figures 47 and 49 show this noise source just above the engine nacelle. Of the high-lift sources present in the inboard scan-plane, this is the only one that was integrated, because noise treatment devices were not fabricated for the other noise sources. Figure 54(c) shows integration results from the traverse. The integrated spectra were similar to the results found from the source-location maps.

**Outboard process 29.** As previously discussed, slat-gap noise and slat-bracket noise combined to create slat-cove noise. Figure 55 shows this noise at 1,872 Hz over the full traverse range. The noise map from the T100u position appears to be skewed away from the slat cove area. This problem may be attributed to a slight Mach-number convection problem that was exacerbated by the extreme emission angle of the upstream traverse position. Figure 54(b) shows the cove-integration results for the four traverse positions. The T100u spectra deviated from the other three traverse positions by as much as 6 dB at high frequency.

The outboard-slat outboard-edge (OSOE) source was not visible at very many frequencies. It was a relatively weak source, and the integrated spectra in figure 54(d) show how quickly the spectra fall off. Unlike the inboard edge that showed a large increase in the third-octave bands surrounding 2 kHz, there were no spectral features for the outboard edge. The integrated spectra all follow the same trends and differ from each other by about 3 dB.

The outboard-flap outboard-edge (OFOE) noise source was the last source present in the outboard scan region. For most frequencies, the OFOE was quiet in the aero baseline. The differences between aero and acoustic baselines are discussed in section 5. Figure 55 does show some noise in the T0 and T250d traverse images. The noise source was present in the T150d case, but was more than 8 dB below the slat-cove source and was therefore not visible with the selected contour range. Integrated spectra showed little variation with traverse position, as shown in figure 54(a).

### 3.3 Approach Configuration

Configuration C14 was the aero-baseline approach configuration. Slat deflections were  $20.7^\circ$  and  $31.6^\circ$  for the inboard and outboard slats, respectively. Flap angles were  $33.1^\circ$ ,  $44.3^\circ$ ,  $31.0^\circ$ , and  $30.3^\circ$  for the inboard-main, inboard-aft, flaperon, and outboard-main flaps, respectively. The aileron

was not deflected and fairing No. 8 (bulb seal) was in place for the baseline data. The landing gear was not installed for the approach configuration.

### **Mach Sweep, $\Delta = 6^\circ$ , T150d**

A Mach sweep was performed for configuration C14 at an angle of attack of  $6^\circ$  and at traverse position T150d. Approach noise sources were very similar to those found in the landing configuration outside the landing gear region except for the outboard-flap outboard-edge (OFOE). The OFOE was a much stronger source in the approach baseline. Above 2-kHz full scale there was a relatively strong broadband source on the flap edge, as shown at 3,471 Hz in figure 56. Little effect of Mach variation could be detected in the source location plots.

Figure 57 shows the 1/3-octave integrated results for Mach 0.21 and 0.18. Also plotted is a curve showing velocity scaling to the 5th power. The tonal feature at 1.6 kHz of the OSIE scaled very well, as shown in figure 57(i). Scaled data from results for the three other high-lift regions were marginal.

### **Angle-of-Attack Sweep, $M = 0.21$**

The source-location plots did not show much variation with angle of attack for the baseline approach configuration. Figure 58 shows a typical outboard scan-plane with both slat-bracket and gap-noise sources at 3,042 Hz. The outboard-flap outboard-edge was visible at most frequencies above 2 kHz, as shown in figure 58.

More information about angle-of-attack effects on the baseline approach configuration was found in the 1/3-octave integrations. Figure 59 shows the results from the baseline integrations for angles of attack of  $4^\circ$ ,  $6^\circ$ , and  $8^\circ$ . Figures 59(c) and 59(d) show that as angle of attack increased, slat-edge noise also increased. Also consistent with landing configuration, slat-cove noise decreased with increased angle of attack. Flap-edge noise remained almost constant between  $4^\circ$  and  $8^\circ$ .

### **Array Traverse, $M = 0.21$ , $\Delta = 6^\circ$**

Figure 60 shows a series of source location images for a baseline approach traverse at 3,666 Hz. It appears from the source location maps that the OFOE and slat-cove sources have some directivity. The T100u upstream traverse position shows side-lobe clutter at this frequency, because the noise sources are very quiet. In figure 60(b), the T0 position, slat-cove sources and a very weak source on the flap edge were visible. As the traversing array was moved downstream, the cove sources got weaker and the flap-edge source got stronger. At the most extreme downstream position of T250d the flap edge becomes the dominant visible source, as shown in figure 60(d).

Integrated levels, however, showed that there was little spectral variation in the slat-cove and flap-edge traverses. Figure 61 shows that other than the 100-in. upstream traverse position, which had an array response filled with side lobes, the slat-cove and flap-edge integrations were not directional. The outboard slat inboard edge was however a more directional source, as shown in figure 61(c).

## 4 LANDING GEAR SOURCE

### 4.1 Landing Gear Configurations and Measurements

The landing gear on modern aircraft such as the Boeing 777 are designed primarily for supporting landing loads and for ease of maintenance, rather than for low drag or low noise. They typically consist of a complex arrangement of cylinders, braces, brackets, cable harnesses, etc., positioned at a wide range of incidence angles to the oncoming flow. At low frequencies, the landing gear can be the loudest noise source on approach, and reductions in this source are needed to achieve noise-reduction targets for commercial aircraft.

Previous investigations of landing gear noise have been conducted using a model gear installed on a semispan 6.3%-scale Boeing 777 model (Stoker and Sen 2001) and an isolated 26% 777 gear (Jaeger et al. 2002 and Jaeger et al., in press). In both investigations, high-fidelity and simplified-geometry representations of the gear were studied with acoustic source-location arrays. The simple-geometry model was representative of the detail typical in wind tunnel models. The results of these studies are consistent with other studies that show that small geometric details such as cable harnesses, brackets, fixtures, and fasteners contribute significantly to the noise field. Since these details are very small on typical wind tunnel model scales of 5%–12%, Reynolds number effects may also introduce discrepancies between model- and full-scale noise sources. Hence, a high-fidelity landing-gear model was tested on the STAR 26% 777 model wing to investigate these questions.

Three gear configurations were studied in this investigation: a high-fidelity gear model with doors (figs. 62 and 63), and a simple-geometry model with and without the main door (fig. 64). The tire tread on the 777 consists of four grooves around the perimeter of the maple tire model as shown in figure 63. On this model, these grooves were approximately 0.1 in. x 0.1 in. with a square cross section and sharp corners at the surface. Previous studies of the isolated 26% gear in the Ames 7- by 10-Foot Wind Tunnel (7x10) (Jaeger et al. 2002) showed that a sharp-edge model-scale tire tread can generate an intense tone that is not present on full-scale aircraft tires with rounded tread shapes. For this reason, the tire treads were taped over for all measurements, except for a specific test sequence to study tire-tread noise, which will be presented at the end of this section. Some simple fairings were installed on the 26%-scale gear model in the previous isolated gear test in the 7x10; time constraints precluded investigation of the fairings or other noise reduction treatments during the current 40x80 wind tunnel test. For all configurations in this investigation, the gear was fully extended with the six-wheel truck at 13° incidence (front wheel closest to the wing).

Because of the extended depth of the gear model, array measurements from two scan planes were analyzed to determine the sensitivity of source intensity to scan plane location. Scan region 18 was parallel to the wing and intersected the lower tire surfaces (fig. 17). Scan region 28 contained the wing and inboard flaps (fig. 16). Source location maps for these two scans are presented in figures 65 and 66, respectively, for a model-scale frequency of 4.5 kHz. The landing gear noise distributions are similar for the most part with similar peak levels. The integration regions for the two scan regions are similar in each region, shown as a quadrilateral shape. Note that the landing gear integration region overlaps the inboard flap so that noise from this source is included in the landing gear integrated level.

Figure 67 compares the integrated levels for the two scan regions for the high-fidelity gear, simple gear with door, and no-gear configurations. Data from process 18 are shown with solid lines and process 28 with symbols. The levels from scan region 28 (lower wheel surface) are comparable or slightly lower than scan region 18 (wing plane). Scan region 18 was selected for integrated level comparisons for the remainder of this section.

Figure 67 shows that the simple gear with door configurations are louder than the no-gear configuration by about 6–7 dB at 1,000 Hz full scale, less at lower and higher frequencies. The high-fidelity gear adds about 8–9 dB to the no-gear level at 1,000 Hz full scale. A tone-like feature at about 1.7 kHz is present in the no-gear spectra, and is also visible in both the simple and high-fidelity gear spectra. Source-location maps showed that this noise source was located on the untreated aft flap. The difference in noise level between the high-fidelity and the simple-geometry gear is comparable to observations from the isolated gear test (Jaeger et al., 2002).

Figure 68 shows the effect of varying angle of attack on integrated levels of noise from the high-fidelity gear. Few effects are observed except near 1,600 Hz full-scale. This may be primarily due to variations in the inboard-flap source. Increasing the angle of attack increases the lift on the wing and the strength of the vorticity bound to the wing. Consequently, increasing the angle of attack should reduce the local flow velocity in the vicinity of the gear, but these effects on noise level appear to be small. This suggests that most of the high-fidelity gear noise sources are located far from the wing, perhaps near the upper or lower surfaces of the gear truck. Sound levels from 250 Hz to 1.25 kHz are independent of angle of attack and are 72 dB in the 1 kHz band.

There is more variation of simple geometry gear noise with angle of attack, as shown in figure 69. However the simple association of higher noise level with lower angles of attack is not evident. At  $\alpha = 4^\circ$  and  $8^\circ$ , band levels from 1.25 kHz to 2.5 kHz are 3–5 dB lower and show more variation than in the high-fidelity gear configuration, suggesting that a portion of high-fidelity gear noise in this frequency range is louder than the flap noise. At 2 kHz, the simple geometry gear is slightly louder than the high-fidelity gear. The 1-kHz band level is about 69 dB, 3 dB lower than the high-fidelity configuration.

Figure 70 shows the effect of variations in angle of attack on the noise from the gear region with the gear removed and the gear cavity sealed. This region includes the inboard flap, as stated previously. For this configuration the 1-kHz band levels are about 68–69 dB.\*

Figure 71 is a source location plot of the landing gear region with gear removed at a model scale frequency of 5,250 Hz (FS frequency = 1,365 Hz). The outboard slat, inboard edge source dominates the source field at this frequency.

Figure 72 shows the variation with traverse position of 1/3-octave-spectral levels of the gear region noise with the high-fidelity gear installed. Although the variation in band levels due to traverse

---

\* The 1.4-kHz peak for the gear-removed configuration is more pronounced than either of the gear-on configurations. This peak may be associated with flap noise that is reduced with the presence of the gear as shown in figure 71.

position is moderate, the distance from the landing gear (truck center) to the array is changing along the traverse as shown in table 2.

Table 2. Geometrical and emission angles and distances, landing gear truck center to traversing array center,  $\alpha = 0^\circ$ ,  $M = 0.22$ .

Traverse position, in.	Geometrical angle	Geometrical distance, in.	Emission angle	Convected distance, in.
-100 upstream	56°	230	45°	268
0	81°	192	69°	204
150 downstream	122°	225	112°	205
250 downstream	139°	291	131°	253

Angles are referenced to the model pivot, with 180° representing a vector parallel with the tunnel airflow; see appendix C for further details regarding the test geometry. An omnidirectional source would appear 2.5 dB louder at the smallest convected distance (0 in. downstream) relative to the largest convected distance (100 in. upstream), disregarding any directional amplification effects. The band levels for the 100-in. upstream position are as high or higher than the other traverse locations, suggesting that the noise is louder in the upstream direction, which is consistent with upstream amplification of noise sources (Soderman and Allen, 2002).

Figure 73 shows the traverse-position variation in 1/3-octave-spectral levels of the gear region with the simple geometry gear model installed. This configuration also included the large gear door, simple braces and lock links. As with the high-fidelity configuration, levels at the upstream traverse location (100 in. upstream) are generally as loud or louder than at the other locations. Levels from 2–3 kHz at the T150d downstream location (near flyover) are 2–3 dB lower than the other locations.

Figure 74 presents 1/3-octave spectra from the landing gear region with the gear removed. The principal noise source in this region is the inboard flap. The narrowband feature at 1.6 kHz is evident at traverse positions 0 and 150 in. downstream, but absent at the other locations.

The gear door is inclined to the flow so it will help deploy the gear in the event of hydraulic power loss. Potential noise sources associated with the gear door include the door tip vortex and attachment brackets. The door may also provide some shielding of noise from strut hardware in the outboard sideline directions. Figure 75 compares 1/3-octave spectra from the simple gear with and without the gear doors at the four traverse locations. The flight conditions are  $M = 0.21$  and  $\alpha = 6^\circ$ . No consistent effect of the door to either increase or decrease noise level is noted.

Figure 76 compares band levels from the landing gear region with the simple-geometry gear (no doors) installed for the three cases: (1) taped tire treads, (2) one front tire untaped with sharp-tread groove edge, and (3) same tire untaped with rounded tread groove edge. The tire tread noise was primarily high-frequency noise as shown in the unmodified tire spectra. The modified tread had no effect on the 3,150 band but reduced the tread noise by 13 dB in the 4,000 Hz band.

A traverse study of the sharp-edge tire groove is shown in figure 77. The tread effect is most apparent at the 100-in. upstream position above 2 kHz, and also at the T0 position above 3 kHz. The strong directionality, small physical size, and sensitivity of tread-noise level to surface detail are consistent with an unstable flow adjacent to the tire surface.

## 5 FLAP-EDGE SOURCE

### 5.1 Flap-Edge Aerodynamic and Acoustic-Baseline Configurations

Turbofan-powered transports generally have one- or two-slotted Fowler flap systems with one or more elements per flap. Some aircraft, such as the DC-10/MD11 employ a vane-flap system where a small turning-vane element between the main element and the flap is used to keep the flow attached on the flap upper surface for large flap deflections. Older aircraft tend to use multi-element flaps with many exposed edges, which can dominate the airframe noise. Newer aircraft have fewer elements and exposed edges, and the flap-edge noise sources are often lower than the slat or gear noise sources.

The Boeing 777 uses a single-element outboard flap and a multi-element inboard flap (see figure C.4 in App. C). The outboard-edge of the outboard-flap was selected for most of the noise reduction treatments because this edge tends to be noisier than the other edges. However, because the microtab treatment was not invasive and required no model modifications, it was also placed on the outboard-edge of the aft flap. Typical source location plots of the outer-wing region (scan plane integration process 29) and inboard region (process 28) are shown in figure 78, with the OFOE and the IFOE integration regions depicted with solid line boundaries.

In this section, the effectiveness of a number of flap-edge noise reduction treatments will be presented. As previously discussed, on the actual aircraft a bulb-seal fairing is attached to the flap lower surface as shown in figure 79. In the test configuration list, this configuration is referred to as the aerodynamic baseline. This fairing was removed to provide a flap-edge configuration similar to those tested and analyzed in previous aeroacoustic studies (Storms et al. 1999). In the test configuration list, this configuration is referred to as the acoustic baseline. Additional noise treatments included porous flap-edge treatment, serrated trailing edge, flap lower-surface microtabs, and flap-edge fence. The acoustic performance of the various treatments, including the bulb-seal fairing, will be compared to the acoustic-baseline configuration in the following sections.

Third-octave spectra will be presented from the traversing array at positions T100u, T0, T150d, and T250d inches upstream (u) and downstream (d) relative to the model pivot. The physical and convected distances and angles from the flap-edge source to the array for these positions are given in table 3 below.

Table 3. Geometrical and emission angles and distances, outboard flap outboard edge to traversing array center,  $\square = 0^\circ$ ,  $M = 0.22$ .

Traverse, in.	Geometrical angle	Geometrical distance, in.	Emission angle	Convected distance, in.
-100 (upstream)	53°	343	43°	402
0	69°	293	57°	324
+150	99°	277	87°	274
+250	118°	309	107°	285

Over this range of traverse, the side range angle (unconvected) to the source varied from  $22^\circ$  to  $27^\circ$ . The geometry is described in detail in appendix C.

Figures 80(a)–80(d) show 1/3-octave spectra from the flap-edge region with and without the bulb-seal fairing for the landing configuration (flap  $30^\circ$ , slat  $20^\circ$ , no gear).\* For traverse positions of T100u, and T0, the fairing had little effect below 700 Hz full scale, but provided up to 2–8 dB reduction from 700 to 4000 Hz. For traverse positions of T150d and T250d, the fairing added some noise (< 2 dB) below 700 Hz, but reduced higher frequency noise.

Figures 81(a)–81(d) show similar 1/3-octave-spectral comparisons for the approach configuration (flap  $20^\circ$ , slat  $20^\circ$ , no gear.) The bulb-seal fairing had little effect below 700 Hz for all traverse positions, but provided some reduction, up to 6 dB at 1 kHz, over the range 700–1,600 Hz, and a smaller reduction from 1,600 to 4 kHz.

## 5.2 Porous-Surface Flap-Edge Treatment

Previous tests have shown that a porous-surface treatment at the flap edge reduces the level of broadband noise originating from that region (Storms et al. 1999). The noise reduction may result from mean flow outward through the porous edge that displaces the tip vortex away from the edge, and also by presenting a lower impedance to pressure fluctuations on the flap-edge surface regions where noise is generated.

Based on these earlier tests, a porous end-cap was fitted to the outboard edge of the outboard flap. The hollow porous shell extended 2 in. inboard from the flap side-edge and from the trailing edge to within a short distance of the leading edge, as seen in figure 82. Although not visible in the photo, the porous treatment was also incorporated in the side edge and in the upper surface. Two devices with nominal flow resistances of 500 mks rayls and 750 mks rayls were tested. Two porous flap-tip treatments were fabricated by bonding stainless steel mesh to 16-gauge perforated steel sheet (62% open) sleeves that were manufactured from 16 gauge to conform to the original shape of the flap edge. The porous treatment of the side edge and upper and lower surfaces extended from the trailing edge to approximately 20% chord aft of the leading edge. The first treatment used 80x700 mesh screen (Purolator 1761534) with a nominal flow resistance of 390 mks rayls at 1 m/sec. When bonded to the perforated sheet, the finished part flow resistance was 500 mks rayls (also at 1 m/sec). The second treatment used 165x1400 mesh screen (Purolator 1761533) with a nominal flow resistance of 480 mks rayls and a finished part resistance of 750 mks rayls at 1 m/sec. Two 0.25-in. holes were also drilled in the leading edge of the 500 mks rayl treatment to study the effects of augmenting the mean flow rate out of the porous edge with ram air pressurization of the porous cavity.

Comparisons between the 500 mks rayls porous flap edge and untreated flap edge are shown in figures 83(a)–83(d) for the landing configuration (flap  $30^\circ$ , slat  $20^\circ$ , no gear) for  $M = 0.21$ ,  $\Delta = 6^\circ$ . In this case, the untreated edge is the acoustic-baseline flap configuration with the Boeing bulb-seal fairing removed. A broadband noise reduction is observed at the traverse position T100u. At

---

\* The slat TE was serrated for the bulb-seal fairing configuration, but not for the baseline configuration; however, this difference is not expected to significantly affect these results.

traverse positions T0, T150d and T250d, the porous edge is 1–4 dB louder than the untreated flap edge at 1.25 kHz, but is 3–7 dB quieter at other frequencies.

Similar comparisons between the 500 mks rayls porous flap edge and untreated flap edge for the approach configuration (flap 20°, slat 20°, no gear) for  $M = 0.21$ ,  $\Delta = 6^\circ$  are shown in figures 84(a)–84(d). For frequencies below 800 Hz and most traverse locations, the noise reduction from the porous treatment is less than when the flap is at 30°; however, the reduction level at the T0 traverse position was much greater for the 20° flap detent.

Three configurations of the porous treatment (500 mks rayl sealed and open LE ports, 750 mks rayl sealed LE) are compared with the untreated flap edge in figure 85 for the case  $M = 0.21$ ,  $\Delta = 6^\circ$ , traverse position = 150 in. downstream. The porous configurations exhibit similar reductions, except at 1,250 Hz where the 750 mks rayl treatment is more effective. Leading-edge ports had negligible effects.

### 5.3 Serrated Trailing Edge

Based on previous experimental and numerical studies, the complex flowfield associated with the flap edge can be associated with a variety of noise source mechanisms (Storms et al. 1999, and Khorrami et al. 2002). Some of these noise source mechanisms are associated with different instabilities of the flap-edge vortex, which originates from the flap lower-surface as a separated shear layer and then rolls up to form a streamwise vortex over the upper flap surface near the flap side edge. In some configurations, noise is generated by an unsteady interaction of the rolled-up vortex as it departs the upper flap surface at the trailing edge. When present, this noise source has been disrupted by positioning a serrated metal plate at the flap-edge trailing edge, as shown in figure 86 (Brooks et al. 2000). This noise reduction method was evaluated as part of the current study. The serrations in this study consisted of three blades approximately 0.75 in. long by 0.5 in. wide.

As seen in figure 87, the serrated TE reduced noise within the 1.6 kHz band, but did not affect the noise level at other frequencies. The flap-edge noise source was not dominant in this configuration, or in previous configurations.

### 5.4 Flap Side-Edge Microtabs

As mentioned in the previous section, the instabilities of the side-edge shear layer and vortex have been associated with noise sources in earlier studies. Disrupting the shear layer at the separation edge was found to reduce noise radiated from that location (Brooks et al. 2000). This was achieved by attaching microtabs to the lower flap surface near the edge as shown in figure 88. Figure 89 shows a sketch of the microtab geometry. Since the flow on the flap surface has a strong spanwise component toward the side-edge, the microtabs introduce spanwise vortex filaments that interfere with the instabilities in the vortex sheet as it rolls up to form the flap-edge vortex.

The OFOE microtabs reduced noise at 1.6 kHz, as shown in figure 90 for the approach configuration. This is the same frequency at which noise was reduced by the serrated trailing edge, as noted in the previous section. Microtab 1 (50°) was 1–2 dB more effective in reducing noise over microtab 2 (70°) from 2 to 3 kHz. The reduction effect was comparable in level and frequency range for the landing configuration.

The  $70^\circ$  microtabs were more effective in reducing noise from the outboard edge of the inboard flap, aft segment, as shown in figure 91 for the approach configuration. A broad reduction of 3–4 dB was observed over the full frequency range of 125 to 4,000 Hz, except for a 1-dB reduction at 500 Hz and about an 8-dB reduction at 1,600 Hz. The unmodified aft flap-edge source was about 2–3 dB lower (without correcting for propagation distance effects) than observed for the outboard flap outboard edge source (OFOE) described previously. The microtab related noise reduction on the aft flap edge was less prominent in the landing configuration, as shown in figure 92, with negligible broadband reduction, but 2–4 dB reduction for the 1.6- and 2-kHz bands, similar to the microtab effect on the outboard flap outboard edge source during landing and approach.

## 5.5 Flap-Edge Fence

Previous experimental studies on unswept, untapered part-span flaps have shown that a fence attached to the flap side edge, which extends approximately one flap thickness below the lower surface is effective in reducing broadband flap-edge noise by 3–4 dB (Storms et al. 1999; Soderman et al. 2002). The device has also been shown to be comparably effective on a 4.7%-scale DC-10 and on a Lancair 4 general aviation aircraft (Hayes et al. 1999; Ross et al. 1995). The flap-edge fence evaluated in the current study is shown in figure 93.

Figures 94(a)–94(d) show comparisons of noise from the flap-edge region with and without the fence installed on the landing configuration (flap  $30^\circ$ , slat  $20^\circ$ , no gear) for  $M = 0.21$ ,  $\alpha = 6^\circ$  for the four traverse locations. Below 400 Hz, the noise reductions by the fence are 1 dB or less for each traverse position. Above this frequency, the fence is more effective with reductions of as much as 4–6 dB. These results are consistent with previous studies. No attempt was made to optimize the fence size or shape during the present study.

## 6 SLAT-GAP AND BRACKET SOURCE

### 6.1 Slat Cove Measurements

Slotted leading-edge slats are fully deployed on the Boeing 777 and on most large transport aircraft during landing and approach. On the 777, a small Krueger (unslotted) slat is located between the engine pylon and the inboard slat. Slat noise-reduction treatments developed in previous studies were applied only to the outboard slat during this study. These treatments included a cove filler, serrated-slat trailing edge, slat thin trailing edge, and bracket treatments.

The integration region for the slat cove is shown in figure 95 as a solid line polygon. The slat brackets are depicted as short solid lines within this region. Note that the noise sources are centered on some of the visible brackets, and also appear in the gap regions between brackets. The slat-cove integration region covers only about 55% of the span of outboard slat in order to exclude the slat tips, which will be considered as separate source regions in the next section. The physical and convected positions of the traversing array are given in table 4 below:

Table 4. Physical and emission angle and distance from outboard slat center to traversing array center,  $\alpha = 0^\circ$ ,  $M = 0.22$ .

Traverse position, in.	Geometrical angle	Geometrical distance, in.	Emission angle	Convected distance, in.
-100 upstream	64°	368	53°	361
0	83°	289	71°	293
150 downstream	111°	307	100°	292
250 downstream	126°	353	116°	318

A photograph of the outboard slat with cove filler installed is shown in figure 96. The outboard slat consisted of six aluminum segments, with two brackets per segment. Figure 97 shows three cuts through the slat with the cove filler installed (slat dimensions are tabulated in table C.7).

Before considering the effectiveness of various slat treatments, including the cove filler, some features of the untreated slat are presented and discussed. Spectra of the untreated slat at  $\alpha = 6^\circ$ ,  $M = 0.18$  and  $0.22$  measured at the T150d traverse position are shown in figure 98. The 4–5-dB base level increase is consistent with a velocity power of 5 to 5.5. There is also a spectral peak between 1 and 2 kHz, which increased 10–12 dB above adjacent frequencies. The peak frequency of this feature increased with Mach number. Another interesting trend is the decrease in the level of the spectral peak as the angle of attack increases from  $4^\circ$  to  $6^\circ$ , as seen in figure 99. The presence of the spectral peaks and their reduction with angle of attack and increased slat loading was noted in previous smaller-scale tests of swept and unswept wings (Storms et al. 1999).

### 6.2 Cove Filler

The slotted-slat configuration used in this test is typical of other similar transports. This slat configuration had a large separation region in the cove that originated at the cusp of the slat and persisted until the flow reattached upstream of the slat trailing edge. The profile of the cove filler was designed using CFD to maintain attached flow throughout the cove region.

Figures 100(a)–100(d) compare spectra from the slat cove with and without the cove filler. The data were measured at the four principal traverse locations with the model in the landing configuration. In general, the filler reduced the noise 2–4 dB below 1 kHz, with greater reduction levels in the downstream direction. The spectral peak at 1.6 kHz was reduced 2–3 dB by the filler as measured at the two upstream traverse locations, but was unchanged or increased at the two downstream traverse locations. Additional reduction is observed over the 2–3-kHz range for the two downstream locations. These reductions are comparable to those observed on smaller configurations including unswept models.

### 6.3 Serrated-Slat Trailing Edge

Figure 101 is a photograph showing the slat trailing-edge modification on the outboard slat elements 2, 3, and 4 (numbered 1–6 from outboard edge inward). This region is contained within the slat-cove integration region outlined in figure 95. The serrations consisted of 0.25-in.-deep notches with an included angle of 60° and 1-in. centers, as shown in figure 102. In previous tests of an unswept wing, serrations were found effective in reducing intense tones at a 20° slat setting, a lightly loaded slat condition (Storms et al. 1999). Figure 101 also shows two slat brackets covered with a 0.25-in.-thick layer of Scotchbrite porous pad used in an effort to discriminate between noise sources associated with either the slat gap or the slat brackets. This topic will be discussed in detail in a later section.

Figures 103(a)–103(d) present spectral comparisons between the unserrated slat and the serrated slat with and without Scotchbrite bracket treatment for the landing configuration, as measured at the four principal traverse locations. The spectral peak at 1.6 kHz, attributed to the slat trailing edge, was reduced by 3–5 dB at each of the traverse locations. The Scotchbrite bracket treatment resulted in little change at the 1.6-kHz band (except for a 2 dB increase at the 0 in. traverse location), but did result in a broadband reduction of 1–2 dB from 600 to 1,250 Hz. Overall, the serrated edges were moderately effective.

### 6.4 Slat With Thin Trailing Edge

Numerical simulations of the slat trailing-edge region have suggested that periodic vortex shedding from the slat trailing edge could generate intense tones with frequencies that scale with the trailing-edge thickness (Khorrami et al., 2002). To investigate this effect, the slat trailing edges were milled to sharp edges prior to the test. The taper began 1-in. from the trailing edge and continued until the thickness was the thinnest that could be achieved with conventional machining techniques. Plastic wedges were machined and glued in place to return the trailing-edge thickness to the scale of previous tests. Figures 104(a)–104(d) (traverse position 100 in. upstream, 0, 150, and 250 in. downstream, respectively) compare spectra from the thin and standard trailing-edge-thickness configurations. The thin trailing edge resulted in a reduction of 1–2 dB from 1–3 kHz.

### 6.5 Scotchbrite Porous-Sleeve Treatment of Slat Brackets

Figure 105 shows the three inboard segments of the outboard slat with Scotchbrite porous sleeves attached to each bracket (two brackets per segment). The Scotchbrite pad was wrapped around each bracket and attached with two zip ties. The seam of the Scotchbrite was roughly aligned with the flow (outboard) in the cove region. In the approach configuration, the noise reduction associated

with porous-sleeve bracket treatment was about twice as much as for the landing configuration (fig. 103), as seen in figures 106(a)–106(d) for the four traverse locations. The spectral peak at 1.6 kHz was also reduced in frequency and amplitude with the porous-sleeve treatment.

The flow in the cove region of the slat trailing edge was very complex, and had a significant spanwise component. Hence, the bracket's wake affected the gap flow both by (1) generating wakes that were directed spanwise through the gap, and (2) by providing periodic obstacles to spanwise flow in the slat cove. The porous-sleeve treatment may be effective by displacing high-velocity flow from the sharp edges of the slat brackets or by thickening the wake and reducing velocity through the gap or by other mechanisms.

## 7 SLAT-TIP SOURCE

### 7.1 Overview of Slat-Tip Noise

Noise originating from the slat tips can be as loud or louder than noise from the slat gap. In previous tests of unswept wings by Storms et al. (1999), the slat-gap noise noise was loudest with light slat loading (large deflection) and decreased with increasing slat loading (small deflection). Slat-tip noise was observed to increase with increasing slat loading, similar to observations of flap-edge noise. Slat-tip fences were found to reduce this source in previous tests (Storms et al. 1999, Soderman et al. 2002). The cove filler described in the previous section also modified the flow at the tip and was expected to affect the tip-noise source as well.

The integration regions for the outboard-slat outboard- and inboard-tips (OSOE, OSIE) are shown in figures 107 and 108, respectively. Note that these regions include 1–2 slat brackets in order to fully enclose the tip source pattern at low frequencies.

The outboard-slat outboard-tip is positioned against the end of the slat cove, similar to simple slat configurations studied previously (except for the short wing segment between the slat tip and the wing tip). The outboard-slat inboard-tip region is more complex, as shown in figure 109, and includes a gap of approximately 1 in. between the slat tip and the nacelle pylon. This gap may act as a large source seen in many of the landing configurations. Physical and emission angles and distances from the slat tips to the center of the traversing array are listed in tables 5 and 6 below. A more detailed description of this geometry is provided in appendix C.

Table 5. Geometrical and emission angles and distances from outboard slat outboard edge (OSOE) to traversing array center.

Traverse position, in.	Geometric angle	Geometric distance, in.	Emission angle	Convected distance, in.
100 upstream	55°	383	45°	446
0	70°	336	58°	371
150 downstream	96°	317	84°	317
250 downstream	113°	342	101°	321

Table 6. Geometrical and emission angles and distances from outboard slat inboard edge (OSIE) to traversing array center.

Traverse position, in.	Geometric angle	Geometric distance, in.	Emission angle	Convected distance, in.
100 upstream	72°	252	60°	277
0	96°	241	84°	242
150 downstream	126°	296	116°	267
250 downstream	139°	364	130°	315

## 7.2 Dependence of Noise of Untreated Slat Tips on Velocity and Angle of Attack

Both the inboard- and outboard-tip regions of the outboard slat generated noise that increased with Mach number, as shown in figures 110(a) and 110(b). The spectral noise level from the outboard tip decreased mostly monotonically with frequency. A spectral peak 10–15 dB over the base level and centered at 1.25 kHz dominates the inboard tip spectrum. The frequency of this peak increases with Mach number. This peak was most likely caused by geometry of the inboard slat edge and the engine nacelle.

Angle of attack also affects the noise from the slat tips. Below 1 kHz, the noise from the outboard slat tip steadily decreased with angle of attack, as shown in figure 111(a). Elevated levels at 1.25 kHz for the 6° and 8° condition relative to the 4° condition may be caused by side lobes from the outboard-slat inboard-edge source. Above 2 kHz, noise from the outboard tip region is insensitive to angle of attack. At the inboard tip of the outboard slat, noise below 1 kHz increased slightly with angle of attack, as shown in figure 111(b). The spectral peak in this region is much more pronounced than at the outboard edge, projecting 10–15 dB over the level of adjacent frequency bands. The noise above 1 kHz increased as  $\alpha$  increased from 4° to 6°. The 8° noise is comparable to the 6° noise level, with an upward shift in the frequency of the spectral peak at 1.25 kHz.

## 7.3 Effect of Outboard-Slat Cove Filler on Slat-Tip Noise

The cove filler altered the shape of the outboard-slat cove from inboard to outboard tip. In the previous section, it was noted that the cove filler resulted in a consistent reduction in noise level over most frequencies. The cove filler also reduced outboard-slat tip noise from 1 to 4 dB over most frequencies and traverse locations, as shown in figures 112(a)–112(d) for the landing configuration,  $\alpha = 6^\circ$ ,  $M = 0.21$ . The reduction was more pronounced at frequencies below 1 kHz.

Similar reductions are noted below 1 kHz in the noise from the inboard-tip region under the same test conditions, as shown in figures 113(a)–113(d). The frequency of the spectral peak near 1.25 kHz is lowered with the cove filler at all traverse locations. At traverse location T0, the level of the narrowband feature is diminished about 4 dB with the cove filler; at the other locations, the level increases from 2–3 dB with the cove filler. It is possible that that slat cove-filler reduces slat-tip noise by displacing slat-tip vortical flows away from the slat side-edge and upper surface, as discussed in the following section.

## 7.4 Effect of Slat-Tip Fences

As noted previously, slat-tip fences were effective in reducing slat-tip noise in unswept, untapered model configurations (Storms et al. 1999) and tapered, swept models (Soderman et al. 2002). A photograph and sketch of a slat-tip fence applied to the outboard edge of the outboard slat is shown in figure 114 (see table C.7 for slat dimensions). A similar device was applied to the inboard edge of the same slat while the outboard device was installed as shown in figure 115. The motivation for these devices came from the successful operation of flap-edge fences. Flow studies of flap-fence devices show that a streamwise vortex bound to the lower edge of the flap-edge fence is impeded from migrating to the upper surface of the flap-edge, which causes a reduction in broadband noise (Storms et al. 1999).

Only a small reduction (1 dB or less) in outboard slat-tip noise resulted when the slat-tip fence was applied to the landing configuration model at 4° and 6°, as shown in figures 116(a) and 116(b). More substantial reductions were observed from 1.25 kHz to 3 kHz (1–5 dB) at  $\Delta = 8^\circ$ , consistent with observations of slat-tip noise becoming more significant at higher slat loading conditions.

The slat-tip fence was less effective in reducing the noise at the inboard tip of the outboard slat for the landing configuration at Mach number 0.21, traverse position at 150 in. downstream, as shown in figures 117(a)–117(c) for  $\Delta = 4^\circ$ , 6°, and 8°, respectively. As a worst case, the spectral peak at 1.6 kHz actually increased about 6 dB with the slat-tip fence at  $\Delta = 6^\circ$ . As described previously, the flow field in the vicinity of the inboard slat is influenced by the proximity of the engine nacelle pylon and the gap between the pylon and the inboard slat edge. The details of this flow and its effects on the noise source are unknown at the present time.

The moderate level of noise reduction achieved at the OSOE with the slat-tip fence varied with traverse position, as shown in figures 118(a)–118(d). The largest level of reduction (1–3 dB) is found at the two forward locations (100 in. upstream and 0 in.), as shown in figures 118(a) and 118(b). Noise reduction at the two downstream locations (150 and 250 in. downstream) was either minimal or limited to a narrow range of frequencies.

Noise reduction was nonexistent over most of the frequency range for the case of the outboard-slat inboard-tip (OSIE) fence for all traverse positions for the landing configuration,  $\Delta = 6^\circ$ ,  $M = 0.21$ , as shown in figures 119(a)–119(d). The spectral peak at 1.6 kHz increased from 3 to 7 dB with application of the fence, depending on traverse location.

The effect of the fence on noise from the outboard-tip of the outboard-edge (OSOE) for the approach configuration was similar to or slightly more pronounced than the reduction observed for the landing configuration, as shown in figure 120. A 1–2 dB increase was observed for the single 1.6-kHz band for the 150-in. downstream position (fig. 120(c)); at other frequencies and traverse locations, the noise was either reduced or unchanged.

## 8 CONCLUDING REMARKS

### 8.1 Test Model and Instrumentation

The STAR 26% 777 aeroacoustic test was unique in both the large-scale of the test article and the advanced phased-microphone array systems used to acquire the data. The large model facilitated a high degree of geometric fidelity for comparison with both flight measurements and results from smaller scale tests. The landing gear and high-lift systems were readily adjusted to predetermined flight configurations.

The two array systems performed well in the low-background noise environment of the acoustically treated test section of the 40- by 80-Foot Wind Tunnel. The available dynamic range permitted accurate measurement of noise from both baseline and noise-reduction configurations. The traversing array provided moderate directivity resolution over an emission angle range of 60° to 120° for most sources and was used for both source location and integrated estimates of component source levels. The large fixed array provided higher resolution source location information at low frequencies. Array self-noise, possibly associated with turbulent flow scrubbing of the Kevlar array covers, limited the frequency response of the arrays to about 16-kHz model scale (4-kHz full scale). Low-frequency response was limited by beamwidth to 100 Hz.

Although some directional information was obtained during the test and could hypothetically be used to project noise reduction effects on EPNL, additional procedures for this purpose need to be developed that are beyond the scope of this report.

Force, moment, and pressure measurements will be discussed in a separate report (Storms et al., 2003).

### 8.2 Baseline Cruise, Landing, and Approach Configurations

A number of sources present in the baseline cruise, landing, and approach configurations were identified and characterized for their dependence on velocity and emission angles. Table 7 provides a brief summary of the noise sources that were evaluated in the landing configuration using noise treatment devices. Direct comparison of noise sources may be misleading because source integrations are dependent on the integration area.

Table 7. Characteristics of the noise sources evaluated in this study, T150D,  $M = 0.21$ , landing configuration.

Source	Classification
Landing gear	Low-frequency broadband
OFOE	Mid-frequency tonal
OSIE	Mid- to high-frequency tonal
OSOE	Broadband
Cove	Broadband with some large tonal features from slat edge

Consistent with previous studies, slat-cove noise decreased and flap-edge noise increased with angle of attack.

Other sources not evaluated in this study were the inboard and outboard edges of the inboard flap. Source location images showed a broadband source on the IFIE with the landing gear removed. Only noise treatment was applied to the IFOE, and this source region was not fully evaluated. The cruise configuration showed only a few sources that were visible to the microphone arrays.

### 8.3 Effectiveness of Component Source Reduction Methods

Noise treatments help to improve the understanding of various noise mechanisms and the effects of airframe geometry on source levels. Ultimately, the decision to incorporate a particular noise treatment into the fleet will be based on a trade-off between a certification metric such as EPNL and cost. The most effective approach to obtaining quieter aircraft will be to design an airplane in which the noise sources do not exist. This preemptive approach to noise reduction requires the designer to understand the fundamental principles of airframe noise and to utilize effective model testing procedures. However, to retrofit existing aircraft, it may be useful to incorporate one or more of the noise reduction approaches described in this report.

The effects of the noise treatments were expectedly complex. Each treatment's effectiveness was a function of source location, source type (narrow or broad), Mach number, angle of attack, configuration (landing or approach), frequency band, and traverse angle. It is useful however, to summarize briefly the effectiveness of the various treatments by tabulating typical noise reduction levels under similar conditions. Arbitrary frequency bands were selected to group together relatively constant reduction effects.

#### Landing Gear Source

Three configurations of the main landing gear were studied with the model in the landing high-lift configuration: high-fidelity gear, simple-geometry gear, and gear removed. The noise of these configurations in the flyover direction exhibited similar trends with the results from a previous test of the isolated landing gear model in the 7- by 10-Foot Wind Tunnel. A summary of landing gear results is shown below in table 8.

Table 8. Summary of typical landing gear noise level increase relative to no-gear, cavity closed landing configuration,  $M = 0.21$ ,  $\alpha = 6^\circ$ , traverse = 150D.

Full-scale frequency band:	125–250 Hz	250–1,250 Hz	1.5–4 kHz
Simple gear, no door	1 to 2 dB	2 to 3 dB	1 to 3 dB
Hi-Fi gear with door	2 to 4 dB	4 to 5 dB	1 to 4 dB

These increases are somewhat lower relative to the gear-removed case than observed in the isolated landing gear study in the 7- by 10-Foot Wind Tunnel test, probably due to the higher noise of the wing in landing configuration of the STAR test that was not present in the isolated gear test. A tone-like feature at 1.5–2 kHz was also observed during the large wind tunnel test. This feature is attributed to noise from the inboard flap system components that were located within the gear integration boundary. Landing gear noise-reduction methods (such as fairings) were not evaluated in this study due to time limitations.

### Flap-Edge Source

Numerous methods for reducing the noise from the flap-edge region were extensively studied in previous small-scale and idealized configurations. Methods that effectively reduced noise with little or no aerodynamic penalty include porous-surface treatment, trailing-edge serrations, lower edge microtabs, and fences. Table 9 summarizes the OFOE noise-reduction results. For this summary the response of the 1.6-kHz band is also listed since some reduction methods (TE serrations, microtabs) were most effective at this source frequency.

Table 9. Summary of typical noise source reduction levels for the flap-edge (OFOE),  $M = 0.21$ ,  $\alpha = 6^\circ$ , traverse = 150D; level reduction relative to acoustic baseline (no treatment) (negative reduction is a noise increase).

Full-scale frequency band	125–600 Hz	600–1,600 Hz	1.6 kHz	1.6–4 kHz
Porous edge (approach)	3 to 4 dB	–3 to 4 dB	2 dB	3 to 6 dB
Porous edge (landing)	0 to 2 dB	2 to 5 dB	2 dB	2 to 3 dB
Lower fence (approach)	0 dB	1 to 4 dB	4 dB	3 to 4 dB
Lower fence (landing)	0 dB	0 to 5 dB	5 dB	3 to 5 dB
Bulb-seal fairing (approach)	0 dB	1 to 5 dB	5 dB	3 to 5 dB
Bulb-seal fairing (landing)	0 dB	0 to 3 dB	0 dB	0 to 2 dB
Serrated TE (approach)	0 dB	0 dB	3 dB	0 dB
Microtabs (approach)	0 dB	0 dB	4 dB	0 dB
Microtabs (landing)	0 dB	0 dB	4 dB	

The first three devices, porous edge, lower-edge fence, and bulb-seal fairing, most likely displace the flap-edge vortex away from its original (untreated flap) location, resulting in reductions over a broad frequency range. The bulb-seal fairing was not a candidate noise treatment, but rather an existing part on the 777 flight configuration. The last two devices (serrated TE, microtabs) were designed to interfere with flap-edge vortex instability mechanisms, and would have a significant reduction effect only if the instability was present in the flow. As discussed in section 5, the microtabs appeared to reduce noise 3–4 dB over a broad frequency range at the outboard edge of the inboard flap aft (IFOE) segment.

### Slat Gap/Bracket Source

The slat noise appeared to be a combination of gap and bracket sources resulting from flow interactions. Treating both brackets and gap structure had the best reduction results, as shown in table 10.

Table 10. Outboard slat cove/bracket treatments: level reduction relative to baseline (no treatment).  $M = 0.21$ ,  $\Delta = 6^\circ$ , traverse = 150D (negative reduction is a noise increase).

Full-scale frequency band	125–600 Hz	600–1,000 Hz	1–2 kHz	2–4 kHz
Cove filler (landing)	3 to 4 dB	2 to 3 dB	-4 to 0 dB	2 to 5 dB
Serrated TE with bracket sleeve (landing)	0 dB	1 to 2 dB	2 to 3 dB	2 to 3 dB
Thin slat TE (landing)	0 to 0.5 dB	0 to 1 dB	1 to 2 dB	2 dB
Thin slat TE (approach)	0 to 1 dB	1 to 4 dB	0 to 4 dB	1 to 3 dB

The cove filler was effective in reducing noise by 3–4 dB except for the spectral peak at 1.6 kHz. The serrated trailing edge reduced the 1.6-kHz level, but had little effect below 1 kHz. This suggests that the 1.6-kHz spectral peak was associated with the slat gap rather than the slat brackets. The thin trailing edge had less impact on noise generation than noted in previous smaller-scale experiments. Treatment of slat brackets with porous sleeves reduced broadband noise and reduced the frequency and amplitude of the narrowband peak at 1.6 kHz for the approach configuration; this effect was less pronounced for the landing configuration.

### Slat-Edge Source

The outboard-tip of the outboard-slat (OSOE) generated noise that decreased nearly monotonically with frequency, as shown in table 11. The inboard edge of the outboard slat (OSIE) was particularly loud, probably due to a 1-in. gap between the slat edge and the engine pylon.

Table 11. Outboard slat tip source: level reduction relative to baseline (no treatment).  $M = 0.21$ ,  $\Delta = 6^\circ$ , traverse = 150D (negative reduction is a noise increase).

Full-scale frequency band	125–600 Hz	600–1,000 Hz	1–2 kHz	2–4 kHz
Cove filler OB (landing)	3 to 4 dB	-2 to 3 dB	-2 to 2 dB	0 to 4 dB
Cove filler IB (landing)	2 to 4 dB	-4 to 2 dB	-5 to 5 dB	2 to 6 dB
Tip fence OB (landing)	0 to 0.5 dB	0.5 to 2 dB	0 to 2 dB	0 to 1 dB
Tip fence IB (landing)	0 to 0.5 dB	0 dB	1 to 7 dB	0 to 2 dB

The cove filler reduced noise at both tips over most of the spectrum and across the range of traverse positions. The 1.6 kHz noise from the inboard slat tip (OSIE) was not reduced, but shifted to a lower frequency.

The slat-tip fence was moderately effective for outboard-tip noise, but ineffective in reducing noise at the inboard tip. The 1.6-kHz noise from this region increased with application of the tip fence. The reduced effectiveness of the fence in this region may be associated with the presence of an unsealed slot between the inboard tip and the nacelle pylon.

## REFERENCES

Agarwal, Anurag and Morris, Phillip J.: Investigation of the Physical Mechanisms of Tonal Sound Generation by Slats. AIAA Paper 2002-2575, 8th AIAA/CEAS Aeroacoustics Conference, Breckenridge, CO, June 2002.

Allen, C. S. and Soderman, P. T.: Scaling and Extrapolating Small-Scale In-Flow Wind Tunnel Jet Noise to Full-Scale Flyover Jet Noise. AIAA Paper 97-1602-CP, 3rd AIAA/CEAS Aeroacoustics Conference, Atlanta, GA, May 1997.

Boyd: Navier-Stokes Computations of a Wing-Flap Model With Blowing Normal to the Flap Surface. NASA CDTM-10039, August, 2002.

Brooks, T. F.; Marcolini, M. A.; and Pope, D. S.: A Directional Array Approach for the Measurement of Rotor Noise Source Distributions with Controlled Spatial Resolution. *J. of Sound & Vibration*, vol. 112, Jan. 1987, pp. 192-197.

Brooks, T. F. and Humphreys, W. M.: Effect of Directional Array Size on the Measurement of Airframe Noise Components. AIAA Paper 99-1958, 5th AIAA/CEAS Aeroacoustics Conference, Bellevue, WA, May 1999.

Brooks, T. F. and Humphreys, W. M.: Flap Edge Aeroacoustic Measurements and Predictions. AIAA Paper 2000-1975, 6th AIAA/CEAS Aeroacoustics Conference, Lahaina, HI, June 2000.

Burnside, N. J.; Horne, W. C.; Jaeger, S. M.; Soderman, P. T.; and Reinero, B. R.: Array Design and Performance for a Large Scale Airframe Noise Study. AIAA Paper 2002-2576, 8th AIAA/CEAS Aeroacoustics Conference, Breckenridge, CO, June 2002.

Casper, J. and Farassat, F.: Trailing-Edge Noise Prediction Based on a New Acoustic Formulation. AIAA Paper 2002-2477, 8th AIAA/CEAS Aeroacoustics Conference, Breckenridge, CO, June 2002.

Choudhari, M.; Khorrami, M.; Lockard, D.; Atkins, H.; and Lilley, G.: Slat-Cove Noise Modeling: A Posteriori Analysis of Unsteady RANS Simulations. AIAA Paper 2002-2468, 8th AIAA/CEAS Aeroacoustics Conference, Breckenridge, CO, June 2002.

Crighton, D. G.: Airframe Noise in Aeroacoustics of Flight Vehicles: Theory and Practice, Vol. II. Harvey H. Hubbard, ed., NASA RP-1258, 1991, pp. 391-447.

Davy, R. and Remy, H.: Airframe Noise Characteristics of a 1/11 Scale Airbus Model A. AIAA Paper 98-2335, 4th AIAA/CEAS Aeroacoustics Conference, Toulouse, France, June 1998.

Dobrzynski, W. and Buchholz, H.: Full-Scale Noise Testing on Airbus Landing Gears in the German Dutch Wind Tunnel. AIAA Paper 97-1597-CP, 3rd AIAA/CEAS Aeroacoustics Conference, Atlanta, GA, May 1997.

Dobrzynski, W.; Nagakura, K.; Gelhar, B.; and Buschbaum, A.: Airframe Noise Studies on Wings with Deployed High-Lift Devices. AIAA Paper 98-2337, 4th AIAA/CEAS Aeroacoustics Conference, Toulouse, France, June 1998.

Dobrzynski, W.; Chow, L. C.; Guion, P.; and Shiells, D.: A European Study on Landing Gear Airframe Noise Sources. AIAA Paper 2000-1971, 6th AIAA/CEAS Aeroacoustics Conference, Lahaina, HI, June 2000.

Dougherty, R. P.: Beamforming in Acoustic Testing in Aeroacoustic Measurements, Mueller, T. J., ed., Springer Verlag/New York, 2002.

Dougherty, R. P.; Scharpf, D. F.; and Underbrink, J. R.: Boeing/NASA Ames Flap-Edge Noise Test: Phased Array Development. NASA CDCR 21-000, Feb. 1995.

Dougherty, R. P. and Stoker, R. W.: Sidelobe Suppression for Phased Array Aeroacoustic Measurements. AIAA Paper 98-2242, 4th AIAA/CEAS Aeroacoustics Conference, Toulouse, France, June 1998.

Fahy, F.: Foundations of Engineering Acoustics, Sec. 8.7.1. Academic Press, London, 2001.

Fink, M. R. and Schlinker, R. H.: Airframe Noise Components Interaction Studies. AIAA Paper 79-0668, 5th AIAA Aeroacoustics Conference, Seattle, WA, Mar. 1979.

Guo, Y. P.; Yamamoto, K. J.; and Stoker, R. W.: A Component Based Empirical Model for Airframe Noise Prediction. AIAA Paper 2002-2574, 8th AIAA/CEAS Aeroacoustics Conference, Breckenridge, CO, June 2002.

Hayes, J. A.; Horne, W. C.; Soderman, P. T.; and Bent, P. H.: Airframe Noise Characteristics of a 4.7% DC-10 Model. AIAA Paper 97-1594, 3rd AIAA/CEAS Aeroacoustics Conference, Atlanta, GA, May 1997.

Hayes, J. A.; Horne, W. C.; Jaeger, S. M.; and Soderman, P. T.: Measurement of Reynolds Number Effect on Airframe Noise in the 12-Foot Pressure Wind Tunnel. AIAA Paper 99-1959, 5th AIAA/CEAS Aeroacoustics Conference, Seattle, WA, May 1999.

Hedges, L. S.; Travin, A. K.; and Spalart, P. R.: Detached-Eddy Simulations Over a Simplified Landing Gear. J. of Fluids Eng., vol. 124, June 2002.

Herkes, W. H. and Stoker, R. W.: Wind Tunnel Measurements of the Airframe Noise of a High-speed Civil Transport. AIAA Paper 98-0472, 36th Aerospace Sciences Meeting & Exhibit, Reno, NV, Jan. 1998.

Horne, C.; Hamid, H.; and Cooper, D.: Design and Calibration of an In-flow, Multiple Reflector Microphone Array. AIAA Paper 97-0492, 35th Aerospace Sciences Meeting & Exhibit, Reno, NV, Jan. 1997.

Horne, W. C. and James, K. D.: Concepts for Reducing Self-Noise of In-flow Acoustic Sensors and Arrays. AIAA Paper 99-1815, 5th AIAA/CEAS Aeroacoustics Conference, Seattle, WA, May 1999.

Horne, W. C.; James, K.; and Storms, Bruce: Flow Survey of the Wake of a Commercial Transport Main Landing Gear. AIAA Paper 2002-2407, 8th AIAA/CEAS Aeroacoustics Conference, Breckenridge, CO, June 2002.

Humphreys, W. M., Jr.; Brooks, T. F.; Hunter, W. H.; and Meadows, K. R.: Design and Use of Microphone Directional Arrays for Aeroacoustic Measurements. AIAA Paper 98-0471, 36th Aerospace Sciences Meeting & Exhibit, Reno, NV, Jan. 1998.

Hutcheson, Florence V. and Brooks, Thomas F.: Measurement of Trailing Edge Noise Using Directional Microphone Array and Coherent Output Power Methods. AIAA Paper 2002-2472, 8th AIAA/CEAS Aeroacoustics Conference, Breckenridge, CO, June 2002.

Jaeger, S. M.; Horne, W. C.; and Allen, C. S.: Effect of Surface Treatment on Array Microphone Self-Noise. AIAA Paper 2000-1937, 6th AIAA/CEAS Aeroacoustics Conference, Lahaina, HI, June 2000.

Jaeger, S. M.; Burnside, N. J.; Soderman, P. T.; Horne, W. C.; and James, K. D.: Microphone Array Assessment of an Isolated, 26%-Scale High-Fidelity Landing Gear, AIAA Paper 2002-2410, 8th AIAA/CEAS Aeroacoustics Conference, Breckenridge, CO, June 2002.

Jaeger, S. M.; Burnside, N. J.; Soderman, P. T.; Horne, W. C.; and James, K. D.: Aeroacoustic Study of an Isolated, High-fidelity, 26%-Scale Landing Gear Model, NASA/TP-2004-212815, (in press).

Kendall, J. M. and Ahtye, W. F.: Noise Generation by a Lifting Wing/Flap Combination at Reynolds Numbers to  $2.8 \times 10^6$ . AIAA Paper 80-0035, Jan. 1980.

Khorrami, M. R.; Berkman, M. E.; Li, F.; and Singer, B. A.: Computational Simulations of Three-Dimensional High-Lift Wing. AIAA Paper 2002-2804, 20th AIAA Applied Aerodynamics Conference, St. Louis, MO, June 2002. (A)

Khorrami, Mehdi R.; Li, Fei; and Choudhari, Meelan: Novel Approach for Reducing Rotor-Tip-Clearance-Induced Noise in Turbofan Engines. AIAA Journal, 40 (8), Aug. 2002 (B), pp. 1518-1528.

Khorrami, M. R.; Lockard, D.; and Li, F.: Computational Aeroacoustic Analysis of a Landing Gear. Presented at the 6th CEAS Workshop on From CFD to CAA, Athens, Greece (C), Nov. 7-8, 2002.

Khorrami, Mehdi R.; Singer, Bart A.; and Berkman, Mert E.: Time-Accurate Simulations and Acoustic Analysis of Slat Free Shear Layer. AIAA Journal, 40 (7), July, 2002 (D), pp. 1284-1291.

Khorrami, Mehdi R.; Singer, Bart A.; and Lockard, D.: Time-Accurate Simulations and Acoustic Analysis of Slat Free-Shear-Layer: Part II. AIAA Paper 2002-2579, 8th AIAA/CEAS Aeroacoustics Conference, Breckenridge, CO, June 2002. (E)

Koop, L.; Ehrenfried, K.; Dillmann, A.; and Michel, U.: Reduction of Flap Side Edge Noise by Active Flow Control. AIAA Paper 2002-2469, 8th AIAA/CEAS Aeroacoustics Conference, Breckenridge, CO, June 2002.

Li, Fei; Khorrami, M. R.; and Malik, M. R.: Unsteady Simulation of a Landing-Gear Flow Field. AIAA Paper 2002-2411, 8th AIAA/CEAS Aeroacoustics Conference, Breckenridge, CO, June 2002.

Lockard, David P.: A Comparison of Ffowcs Williams-Hawkins Solvers for Airframe Noise Applications. AIAA Paper 2002-2580, 8th AIAA/CEAS Aeroacoustics Conference, Breckenridge, CO, June 2002.

Meadows, K. R.; Brooks, T. F.; Humphreys, W. M.; Hunter, W. H.; and Gerhold, C. H.: Aeroacoustic Measurements of a Wing-Flap Configuration. AIAA Paper 97-1595, Atlanta, GA, May 1997.

Mendoza, J. M.; Brooks, T. F.; and Humphreys, W. M., Jr.: Aeroacoustic Measurements of a High-Lift Wing/Slat Model. AIAA Paper 2002-2604, 8th AIAA/CEAS Aeroacoustics Conference, Breckenridge, CO, June 2002.

Michel, U.; Bariskow, B.; Haverich, B.; and Schuttpelz, M.: Investigation of Airframe and Jet Noise in High-Speed Flight with a Microphone Array. AIAA Paper 97-1596-CP, 3rd AIAA/CEAS Aeroacoustics Conference, Atlanta, GA, May 1997.

Mosher, M.: Phased Arrays for Aeroacoustic Testing: Theoretical Development. AIAA Paper 96-1713, 2nd Aeroacoustics Conference, State College, PA, May 1996.

Piet, J. F. and Elias, G.: Airframe Noise Source Localization Using a Microphone Array. AIAA Paper 97-1643-CP, 3rd AIAA/CEAS Aeroacoustics Conference, Atlanta, GA, May 1997.

Reid, M. B.: Design of Optimized Arrays Using Simulated Annealing, Internal NASA Ames Research Center Document, 1993.

Revell, J. D.; Kuntz, H. L.; Balena, F. J.; Horne, W. C.; Storms, B. L.; and Dougherty, R. P.: Trailing-Edge Flap Noise Reduction by Porous Acoustic Treatment. AIAA Paper 97-1646, 3rd AIAA/CEAS Aeroacoustics Conference, Atlanta, GA, May 1997.

Ross, J. C.; Storms, B. L.; and Kumagai, H. Aircraft Flyover Noise Reduction Using Lower Surface Flap-Tip Fences. NASA CDTM-21004, Sept. 1995.

Ross, J. C. and Storms, B. L.: Tip Fence for Reduction of Lift-Generated Airframe Noise, U.S. Patent 5,738,298, 1998.

Soderman, P. T.: Sources and Levels of Background Noise in the NASA Ames 40- by 80-Foot Wind Tunnel – A Status Report. NASA TM 100077, May 1988.

Soderman, P. T.: Aeroacoustic Research Techniques—Jets to Autos, FEDSM99-7240. 3rd ASME/JSME Joint Fluids Engineering Conference, San Francisco, CA, July 1999.

Soderman, P. T.; and Allen, C. S.: Microphone Measurements In and Out of Airstream in Aeroacoustic Measurements, Mueller, T. J., ed., Springer Verlag/New York, 2002.

Soderman, P. T.; Jaeger, S. M.; Hayes, J. A.; and Allen, C. S.: Acoustic Performance of the 40- by 80-Foot Wind Tunnel Test Section Deep Acoustic Lining. AIAA Paper 2000-1939, 6th AIAA/CEAS Aeroacoustics Conference, Lahaina, HI, June, 2000.

Soderman, P. T.; Jaeger, S. M.; Hays, J. A.; and Allen, C. S.: Acoustic Quality of the 40- by 80-Foot Wind Tunnel Test Section After Installation of a Deep Acoustic Lining. NASA/TP-2002-211851, Nov. 2002.

Soderman, P. T.; Kafyeke, F.; Burnside, N. J.; Chandrasekharan, R.; Jaeger, S. M.; and Boudreau, J.: Airframe Noise Study of a CRJ-700 Aircraft Model in the NASA Ames 7- by 10-Foot Wind Tunnel No. 1. AIAA Paper 2002-2406, 8th AIAA/CEAS Aeroacoustics Conference, Breckenridge, CO, June 2002.

Soderman, P. T. and Noble, S. C.: Directional Microphone Array for Acoustic Studies of Wind Tunnel Models. J. of Aircraft, vol. 12, no. 3, Mar. 1975, pp. 168-173.

Soderman, P. T.; Schmitz, F. H.; Allen, C. S.; Jaeger, S. M.; Sacco, J. N.; and Hayes, J. A.: Design of a Deep Acoustic Lining for the 40- by 80-Foot Wind Tunnel Test Section. AIAA Paper 1999-1938, 5th AIAA/CEAS Aeroacoustics Conference, Seattle, WA, May 1999.

Soderman, P. T.; Schmitz, F. H.; Allen, C. S.; Jaeger, S. M.; Sacco, J. N.; Mosher, M.; and Hayes, ~~■■■■■~~: Design of a Deep Acoustic Lining for the 40- by 80- Foot Wind Tunnel Test Section. NASA/TP-2002-211850, Nov. 2002.

Stoker, R. W. and Sen, R.: An Experimental Investigation of Airframe Noise Using a Model-Scale Boeing 777. AIAA Paper 2001-0987, 39th Aerospace Science Meeting & Exhibit, Reno, NV, Jan 2001.

Stoker, R. W.; Underbrink, J. R.; and Neubert, G. R.: Investigations of Airframe Noise in Pressurized Wind Tunnels. AIAA Paper 2001-2107, 7th AIAA/CEAS Aeroacoustics Conference, Maastricht, Netherlands, May 2001.

Storms, B. L.; Mathias, D. L.; and Ross, J. C.: Aerodynamic Effects of Flap-Tip Treatments on an Unswept Wing. AIAA Paper 96-2372, 14th AIAA Applied Aerodynamics Conference, New Orleans, LA, June 1996.

Storms, B. L.; Ross, J. C.; Hayes, J. A.; and Moriarty, P. J.: Aeroacoustic Measurements of Slat Noise on a Three-Dimensional High-Lift System. AIAA Paper 99-1957, 5th AIAA/CEAS Aeroacoustics Conference, Seattle, WA, May 1999.

Storms, B. L.; Ross, J. C.; Horne, W. C.; Hayes, J. A.; Dougherty, R. P.; Underbrink, J. R.; Scharpf, D. F.; and Moriarty, P. J.: An Aeroacoustic Study of an Unswept Wing with a Three-Dimensional High-Lift System. NASA/TM-1998-112222, Feb. 1998.

Storms, B. L.; Jaeger, S. M.; Hayes, J. A.; and Soderman, P. T.: Aeroacoustic Study of Flap-tip Noise Reduction Using Continuous Moldline Technology. AIAA Paper 2000-1976, 6<sup>th</sup> AIAA/CEAS Aeroacoustics Conference, Lahaina, HI, June 2000.

Storms, B. L.; James, K. D.; and Arledge, T. K.: Aerodynamics of a 26%-Scale Semi-Span Model of the Boeing 777 in the NASA Ames 40- by 80-Foot Wind Tunnel. NASA Technical Publication, 2003 (in press).

Underbrink, J. R.: Practical Considerations in Focused Array Design for Passive Broad-band Source Mapping Applications, Thesis for Master of Engineering in Acoustics, Pennsylvania State University, May 1995.

Underbrink, J. R.: Aeroacoustic Phased Array Testing in Low Speed Wind Tunnels in Aeroacoustic Measurements, Mueller, T. J., ed., Springer Verlag/New York, 2002.

Underbrink, J. R.; and Dougherty, R. P.: Array Design for Non-intrusive Measurement of Noise Sources. NOISE-CON 96, Sept.-Oct. 1996.

van der Wal, H. M. M. and Sijtsma, P.: Flap Noise Measurements in a Closed Wind Tunnel with a Phased Array. AIAA Paper 2001-2170, 7th AIAA/CEAS Aeroacoustics Conference, Maastricht, Netherlands, May 2001.

Watts, M. E.; Mosher, M.; and Barnes, M. J.: The Microphone Array Phased Processing System (MAPPS). AIAA Paper 96-1714, 2nd AIAA/CEAS Aeroacoustics Conference, State College, PA, May 1996.

Watts, M. E.; Mosher, M.; Barnes, M.; and Bardina, J.: Microphone Array Phased Processing System (MAPPS) Version 4.0 Manual. NASA/TM-1999-208755, March 1999.



Figure 1. NASA Ames 40- by 80-Foot Wind Tunnel.

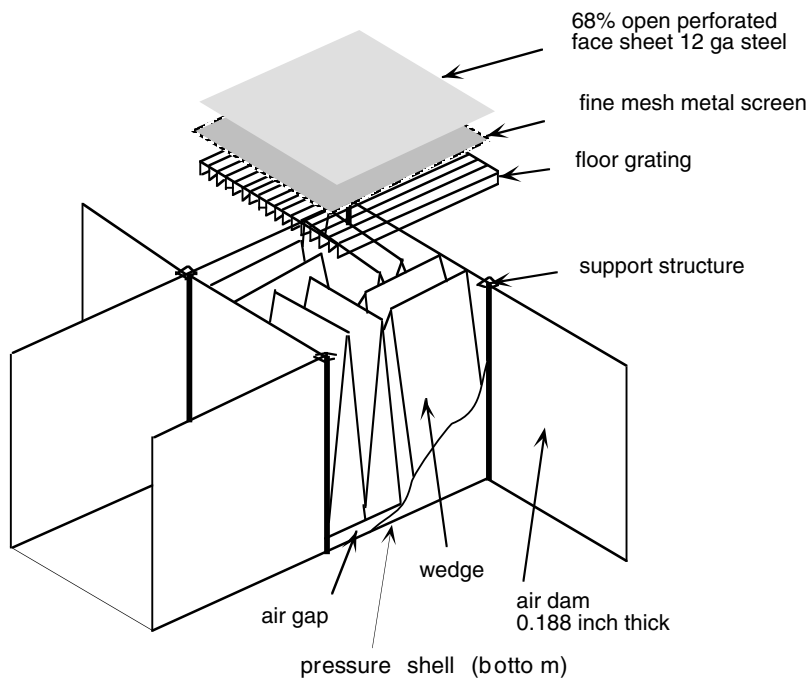


Figure 2. Acoustic lining assembly.

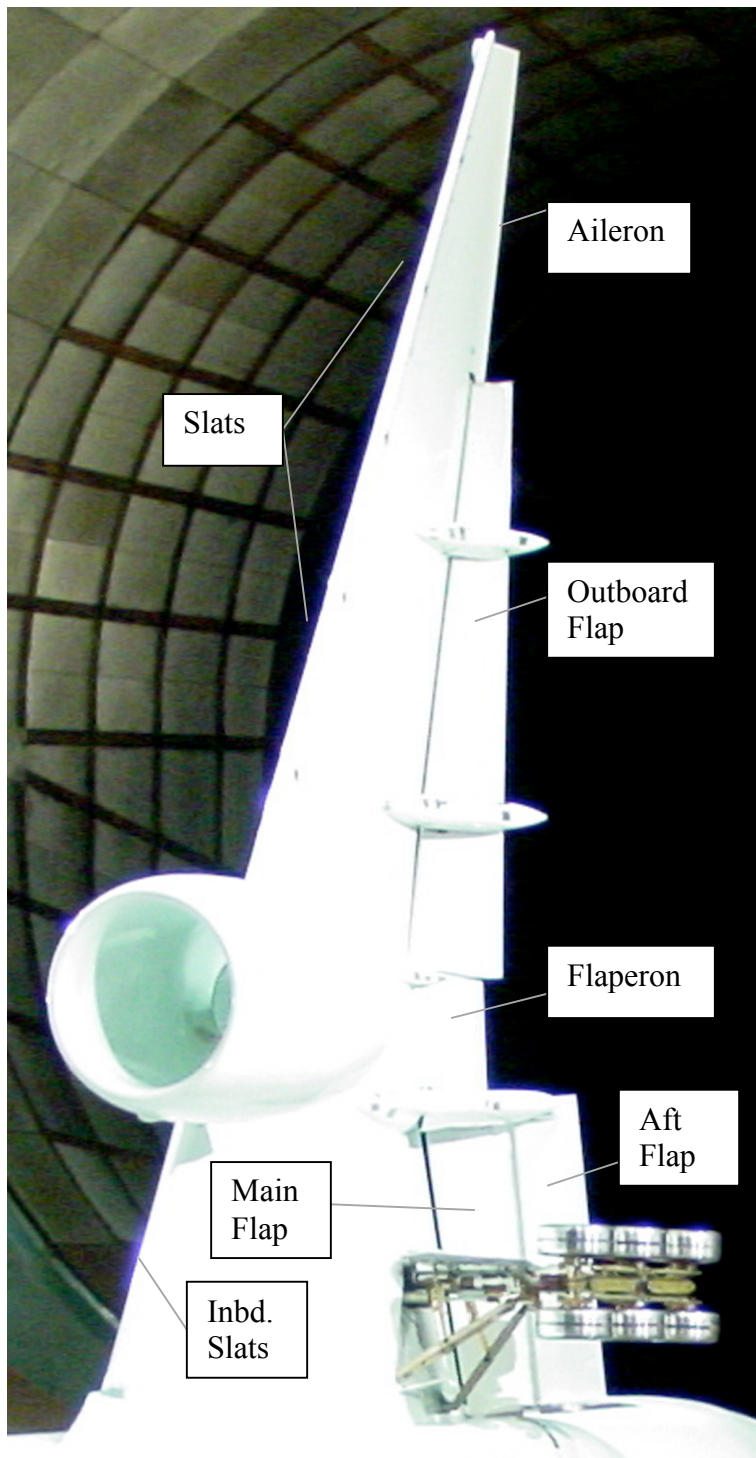


Figure 3. STAR high-lift and control surfaces.

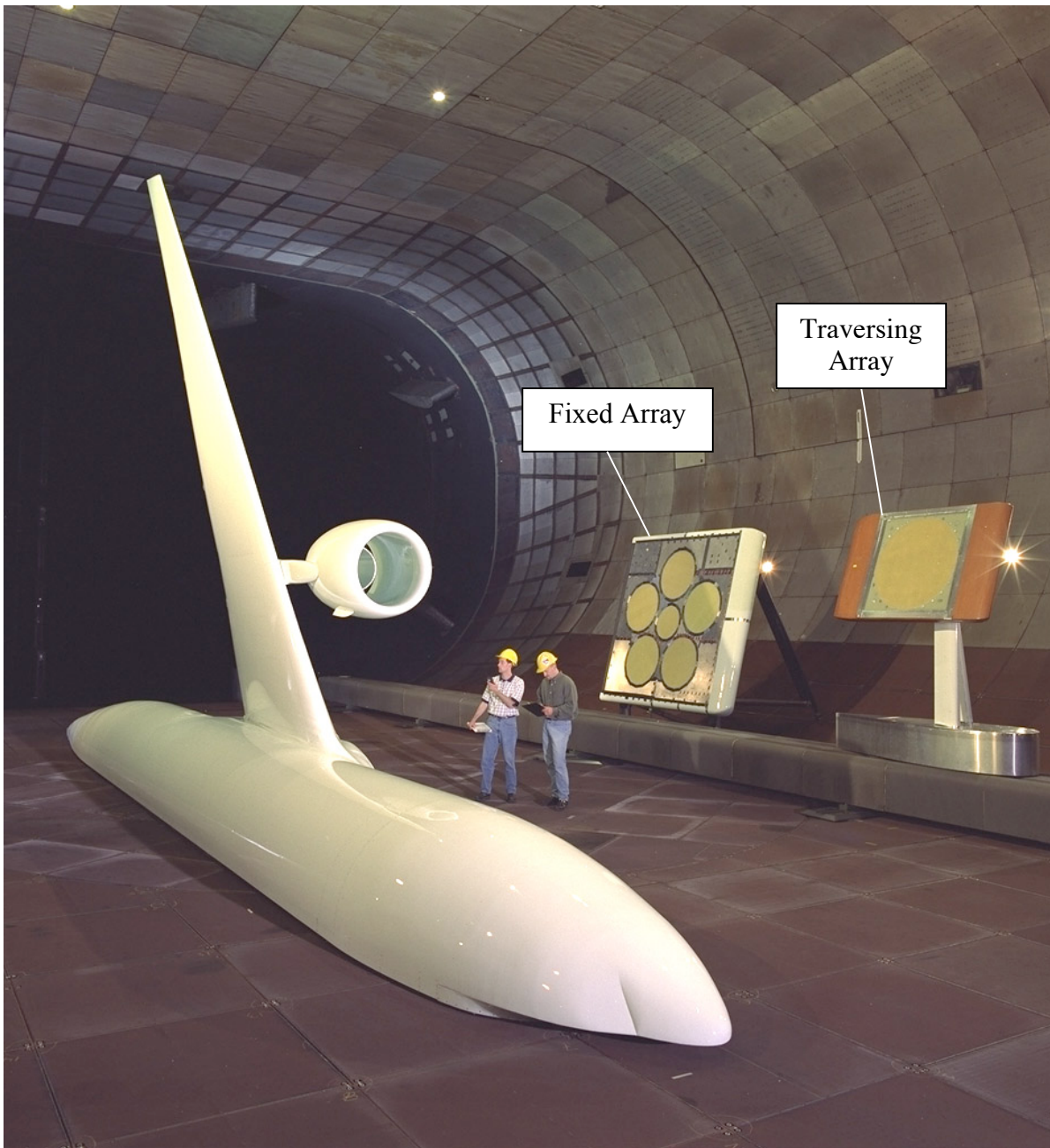
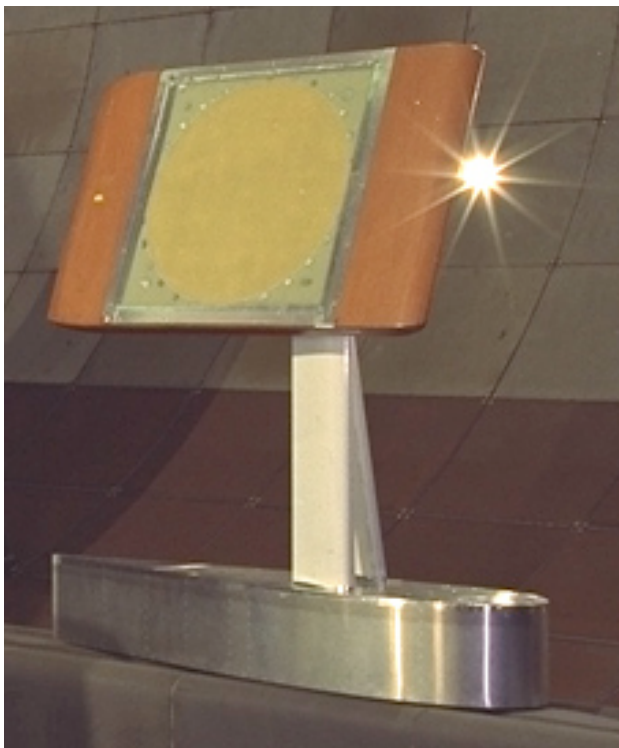
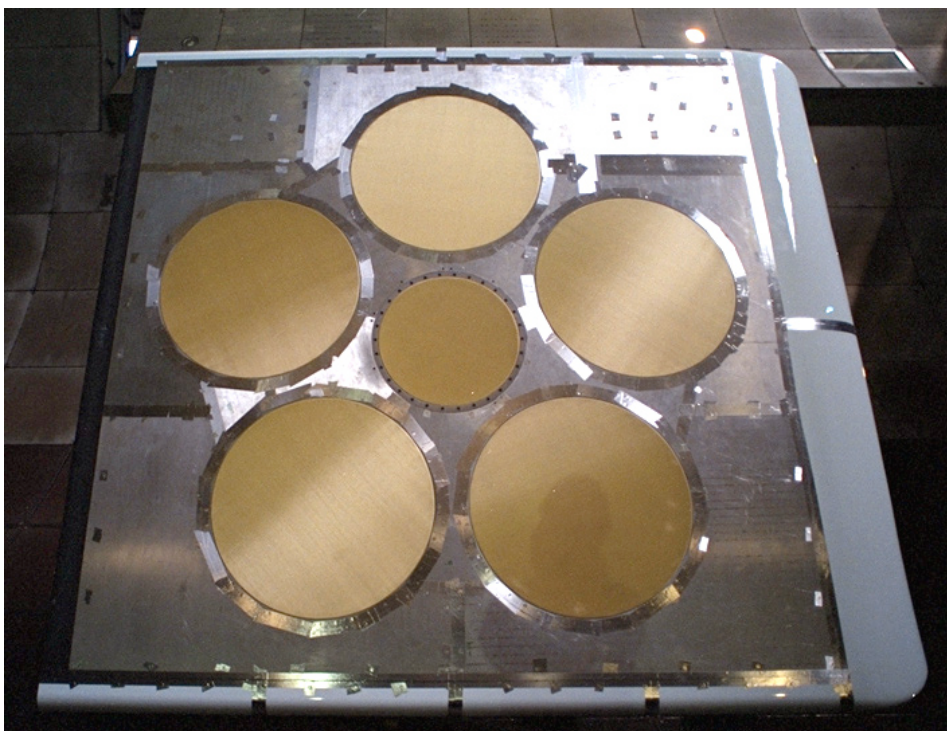


Figure 4. STAR test layout.



(a) Traversing array.



(b) Fixed array.

Figure 5. STAR acoustic arrays.

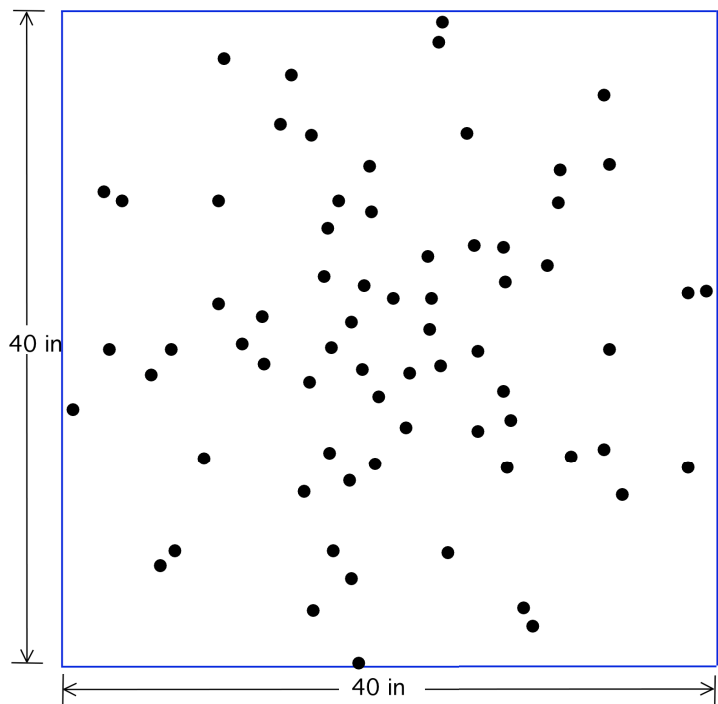


Figure 6. Traversing array pattern designed using simulated annealing.

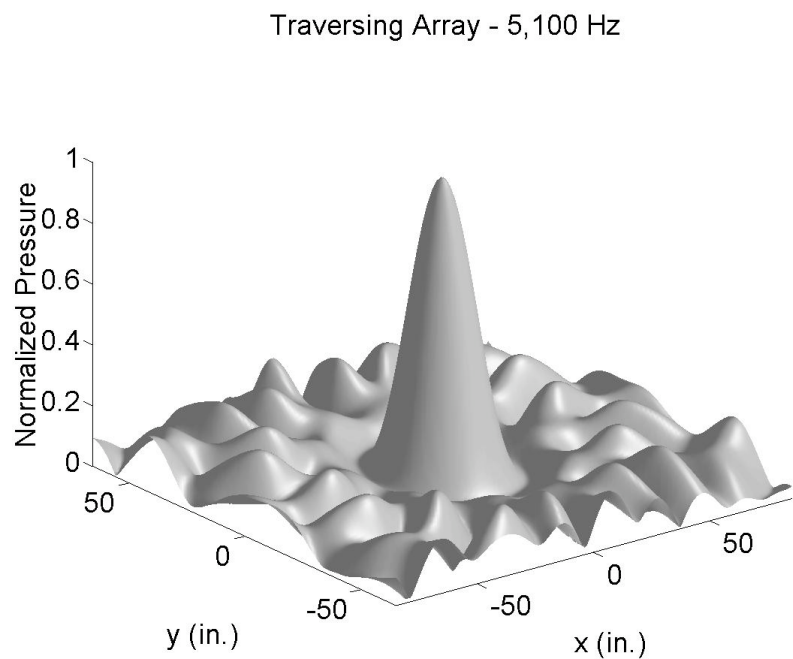


Figure 7. Traversing array simulated beam pattern for a source 226 in. from array center.

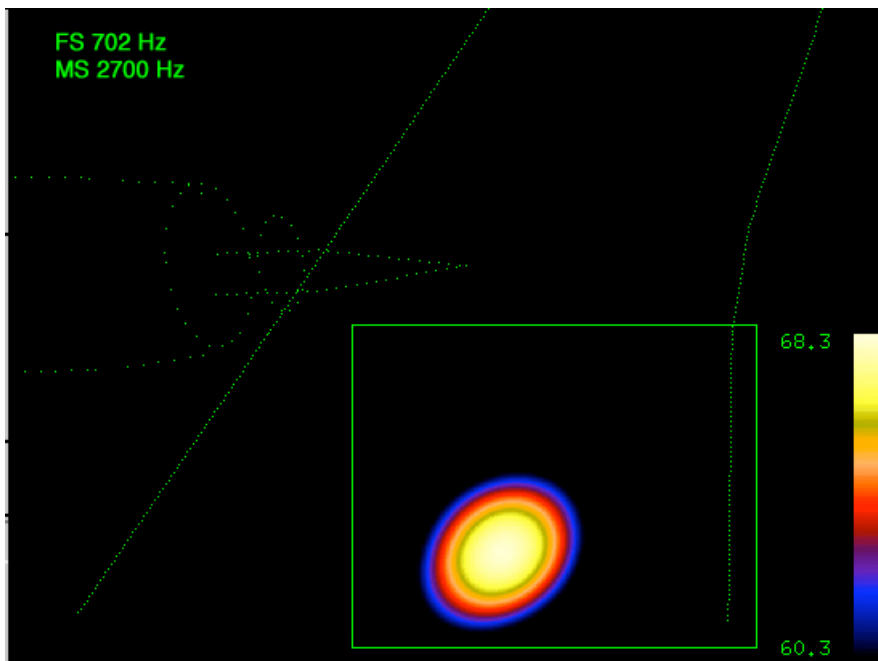


Figure 8. Speaker source integration region.

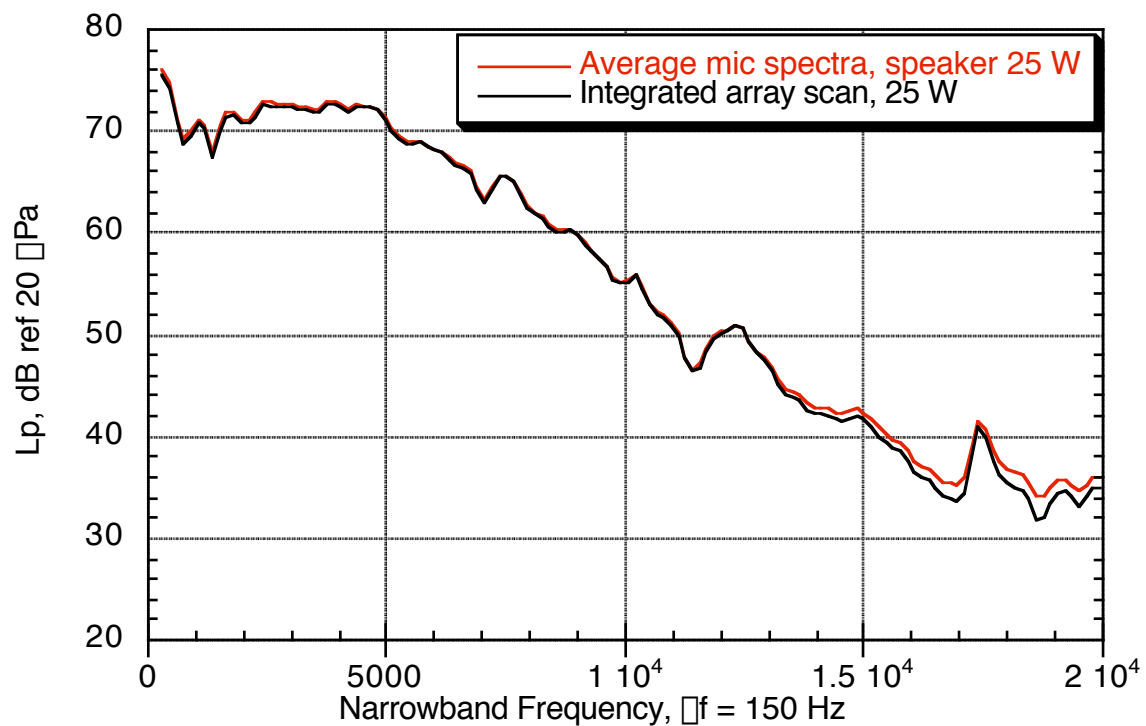


Figure 9. Traversing array amplitude comparison (no wind).

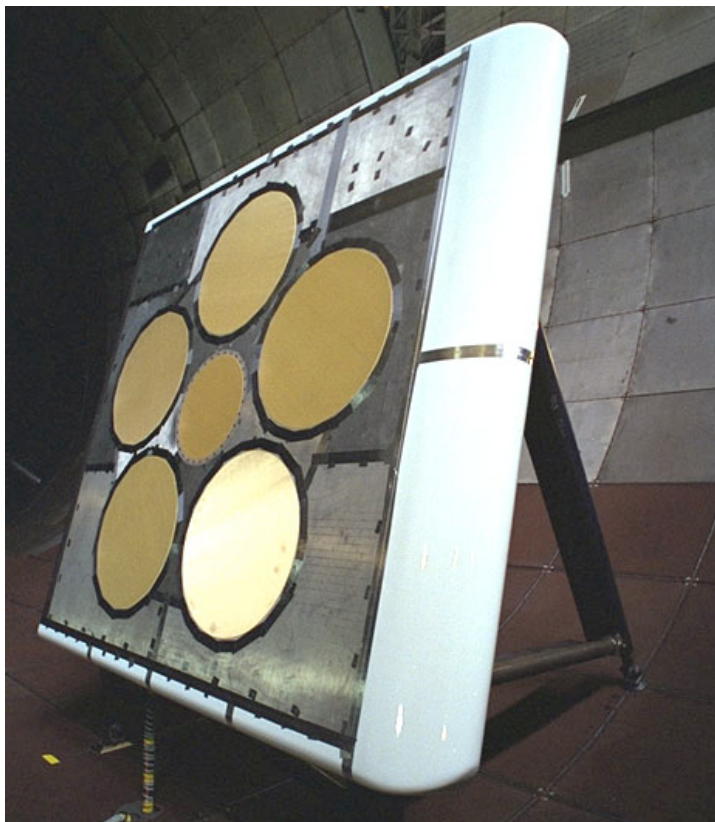


Figure 10. Large array leading-edge fairing.

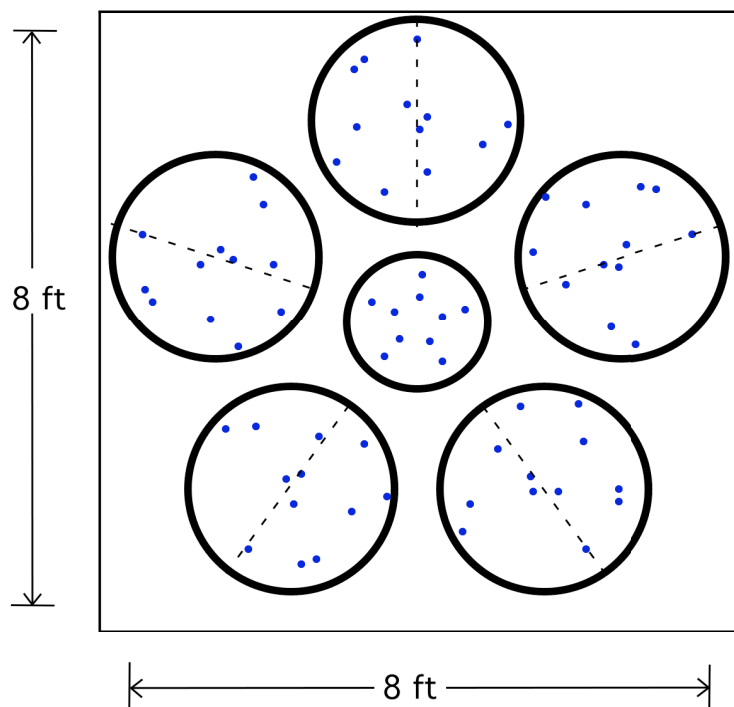


Figure 11. STAR large array pattern; the same pattern was used for each of the outer groupings of microphones.

Large Array - 5,100 Hz

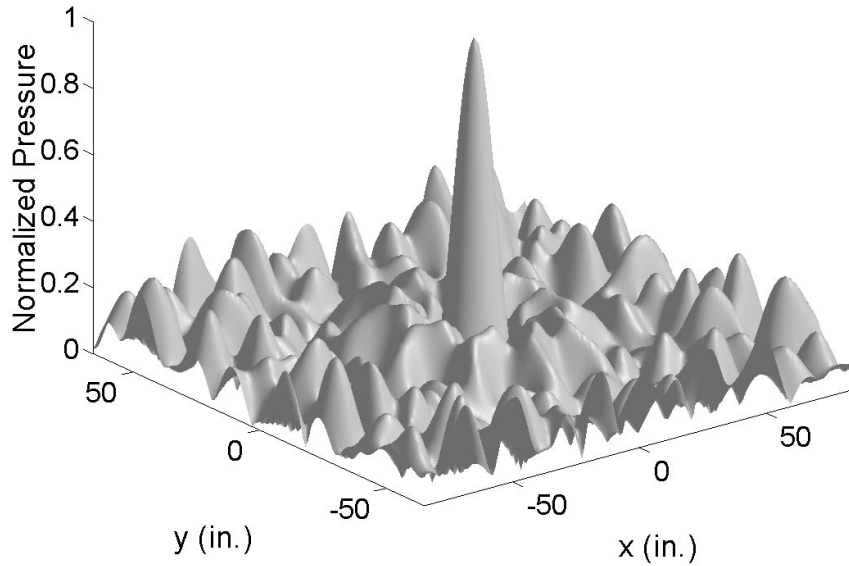


Figure 12. Simulated large array response to a source 315 in. away at 5,100 Hz; side lobes are 7.5 dB down.

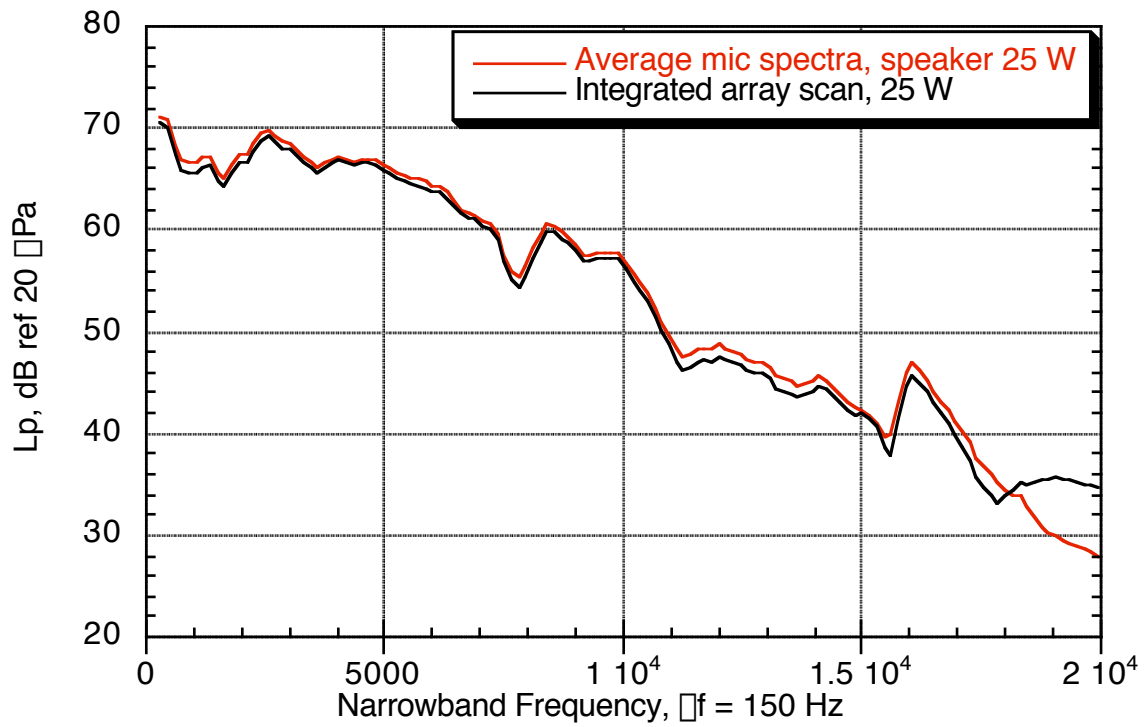


Figure 13. Large array amplitude calibration (no wind).

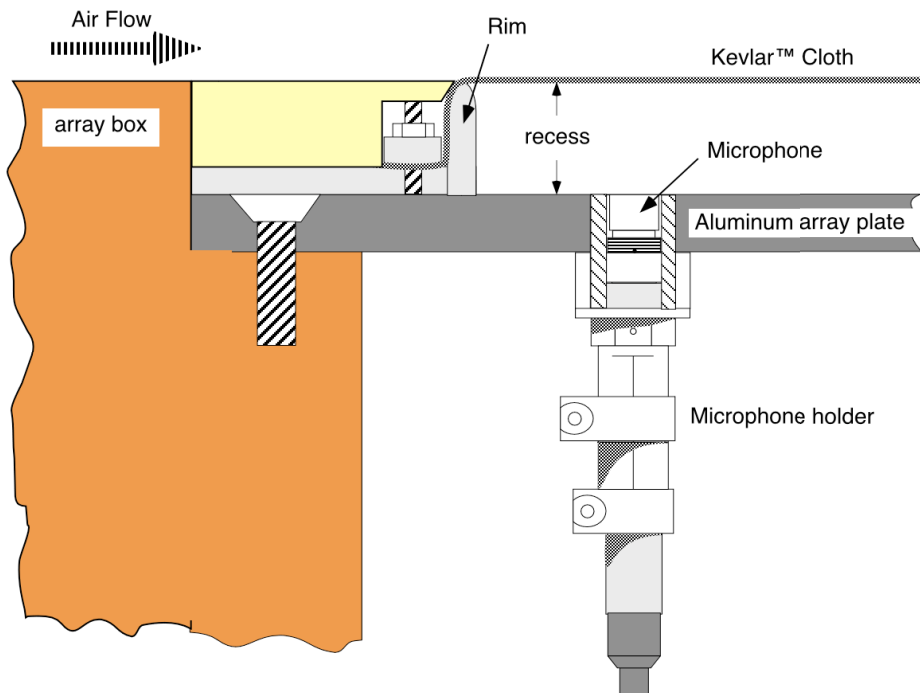


Figure 14. Kevlar recessed array design (from Jaeger et al. 2000).

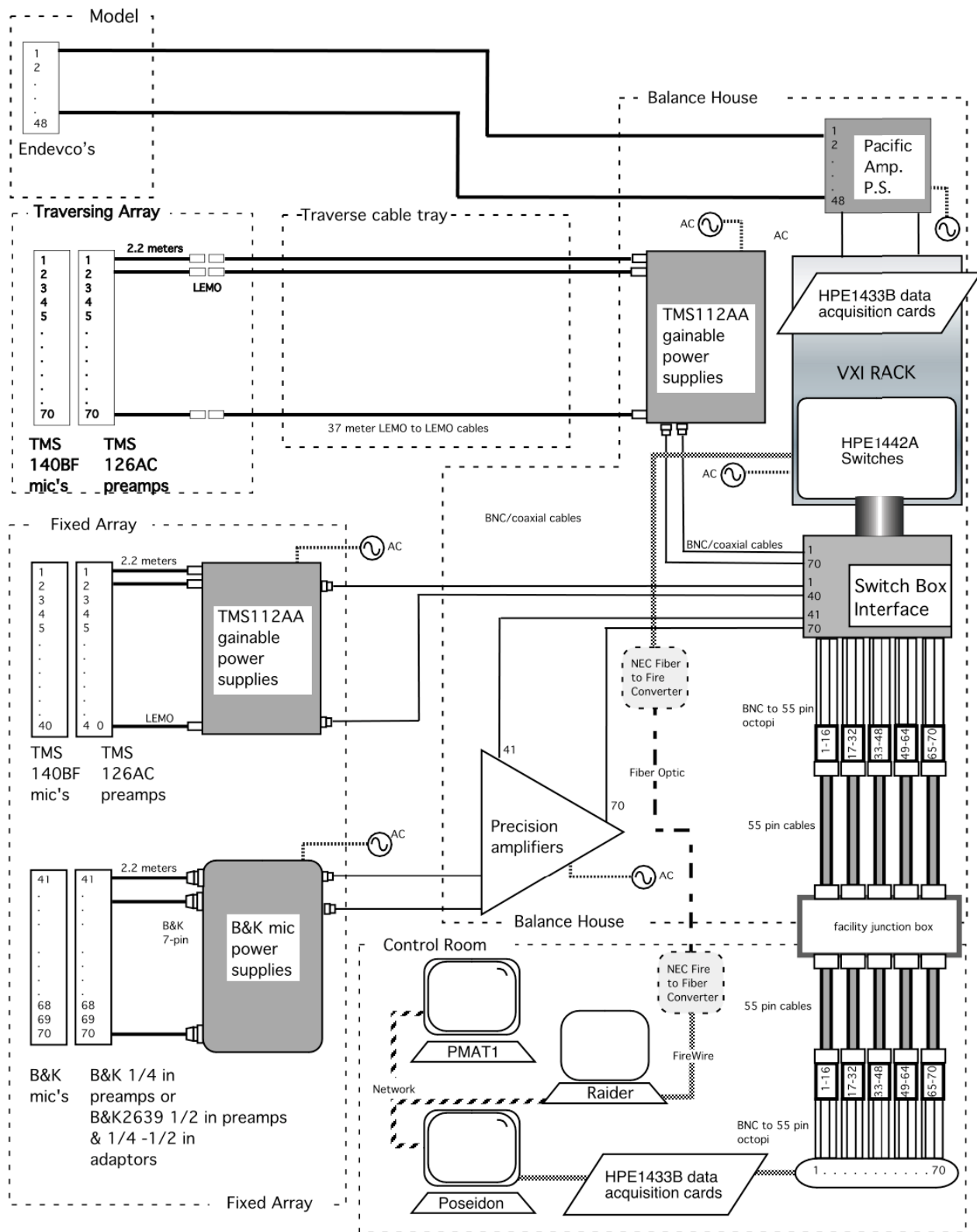


Figure 15. STAR wiring layout; dashed boxes indicated equipment location.

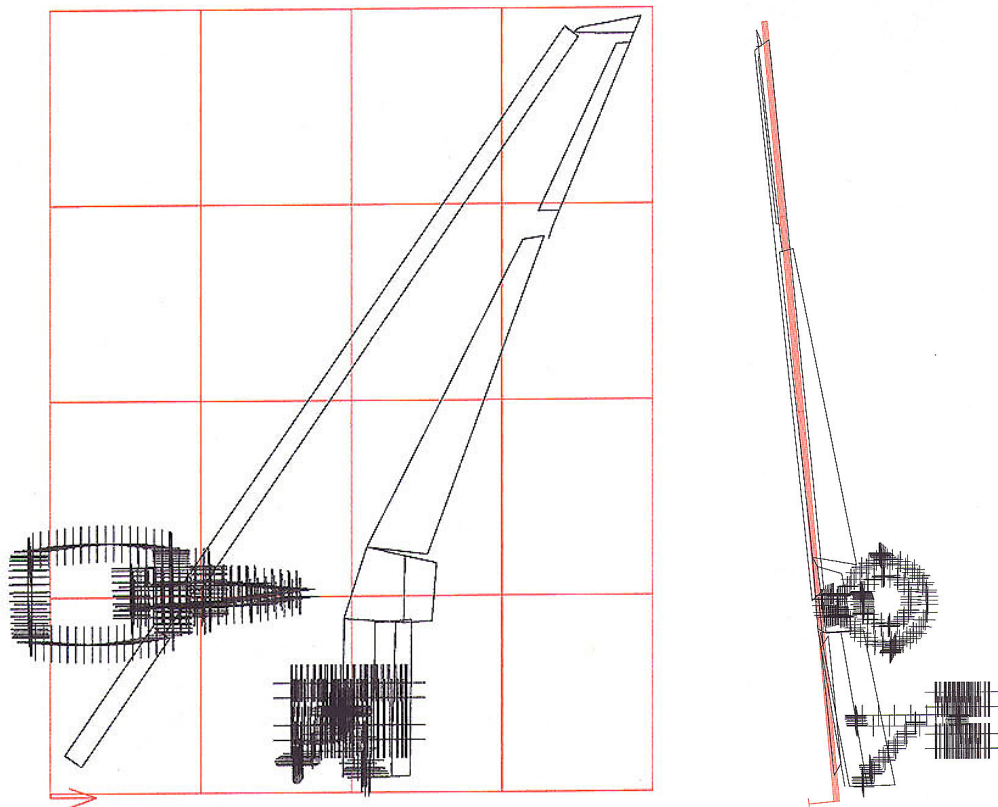


Figure 16. Plane for traversing array processes 28 and 29 and fixed array processes 38 and 39.

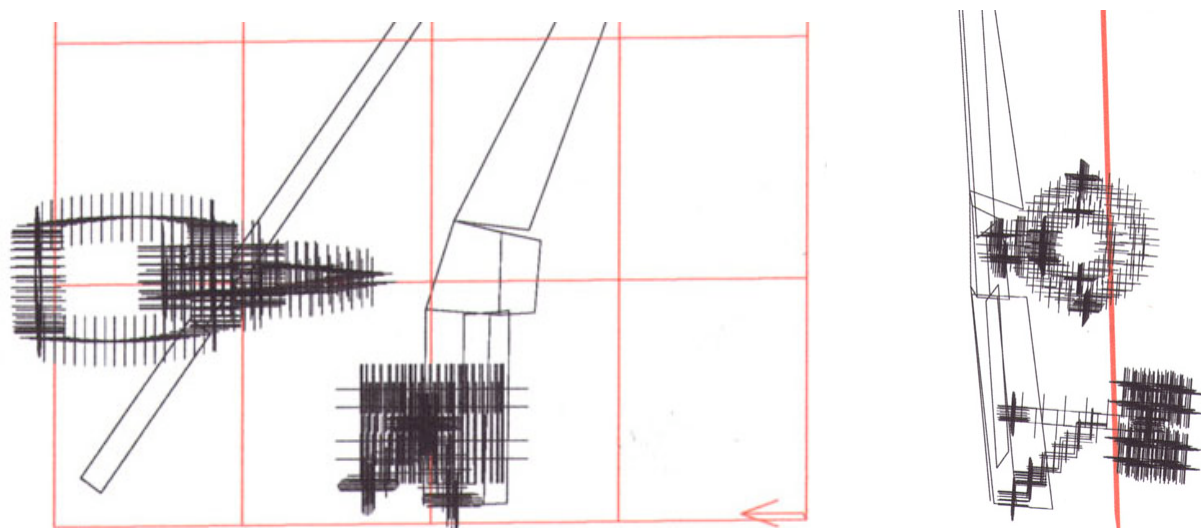


Figure 17. Plane for processes 08 and 18.

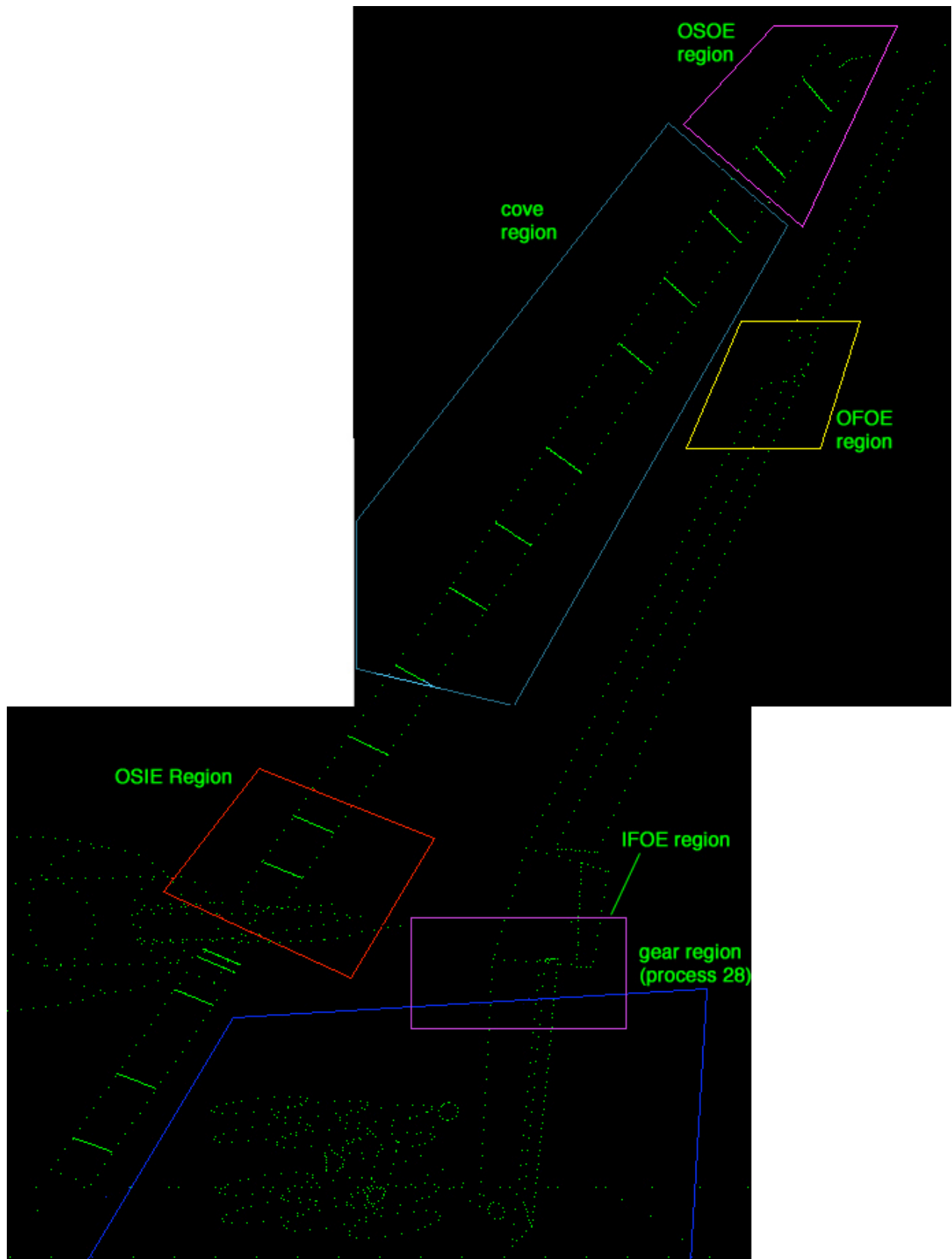


Figure 18. Integration regions used for processes 28 and 29.

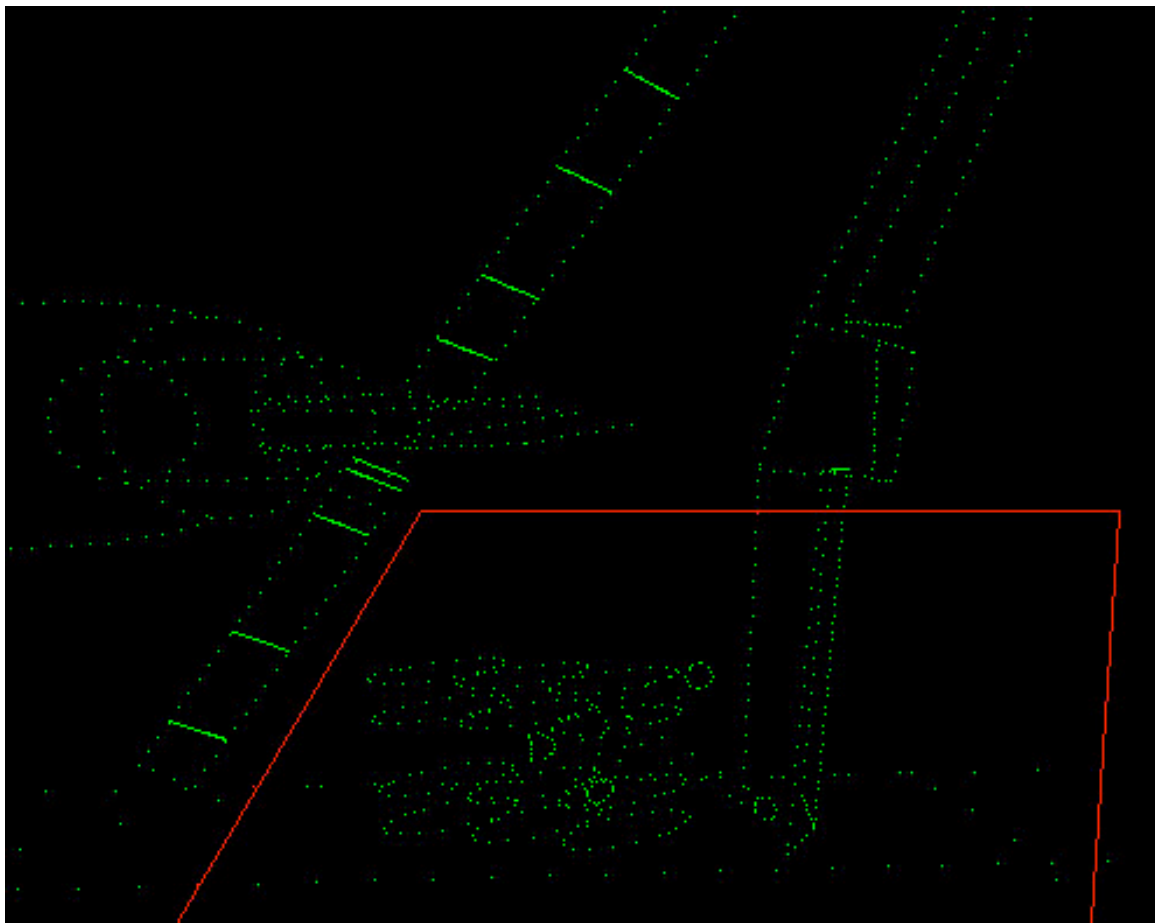


Figure 19. Process 18 landing gear integration region.

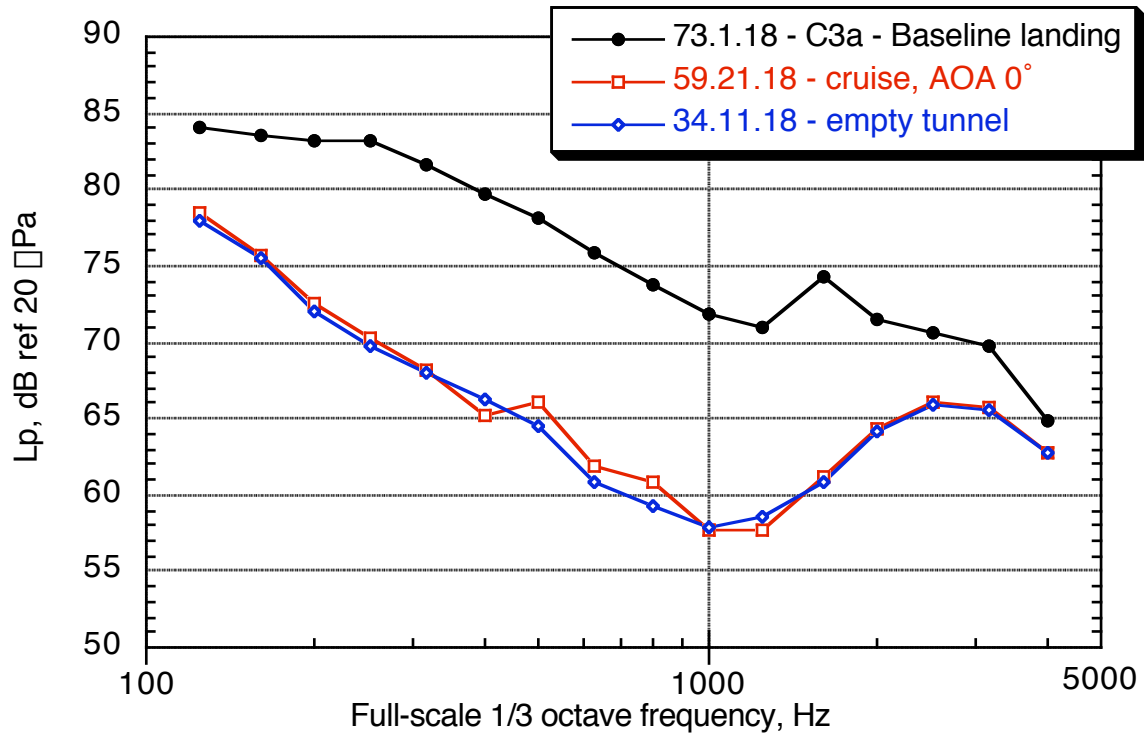


Figure 20. Landing gear integration region background noise comparison: scan plane 18,  $\square = 6^\circ$  (landing gear data),  $M = 0.21$ , traversing array at T150d.

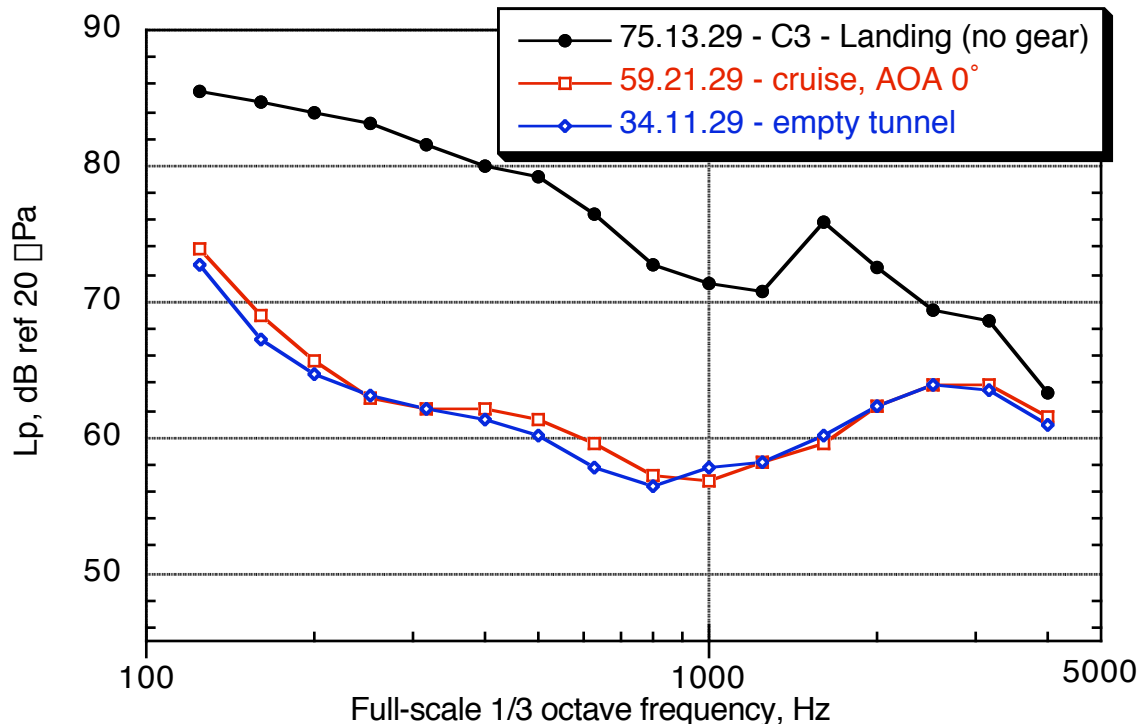


Figure 21. Slat cove integration region background noise: scan plane 29,  $\square = 6^\circ$  (cove),  $M = 0.21$ , traverse array at 150 in.

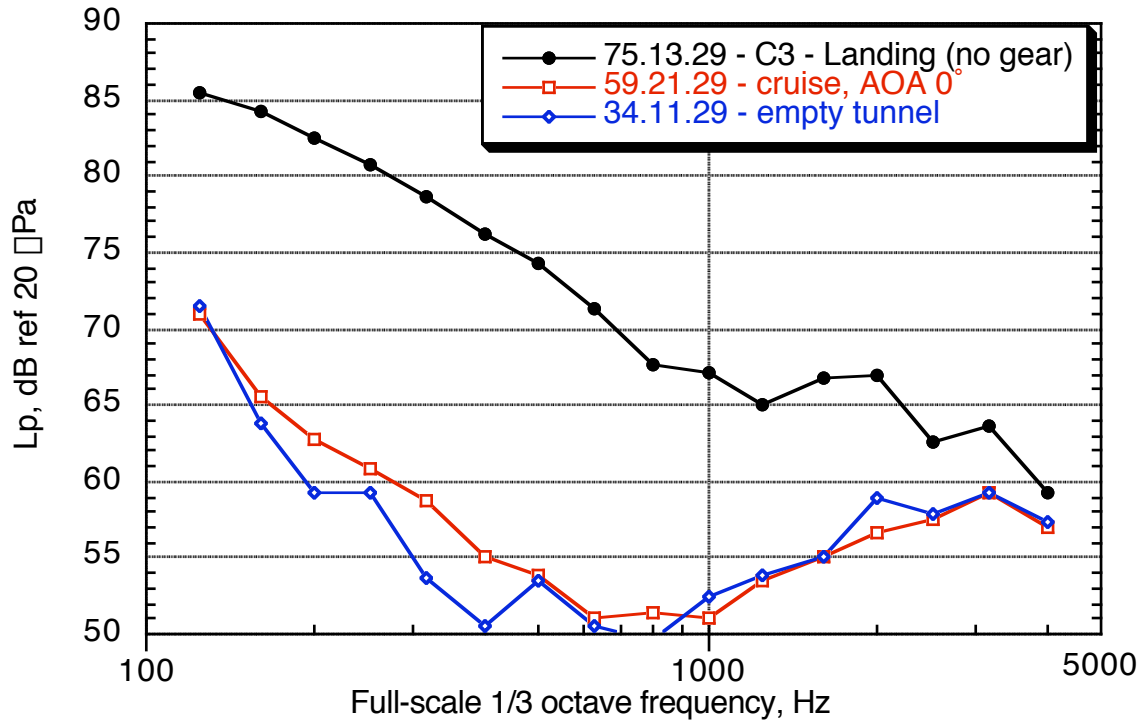


Figure 22. Outboard-slat outboard-edge (OSOE) integration region background noise: scan plane 29,  $\square = 6^\circ$  (OSOE),  $M = 0.21$ , traverse array at 150 in.

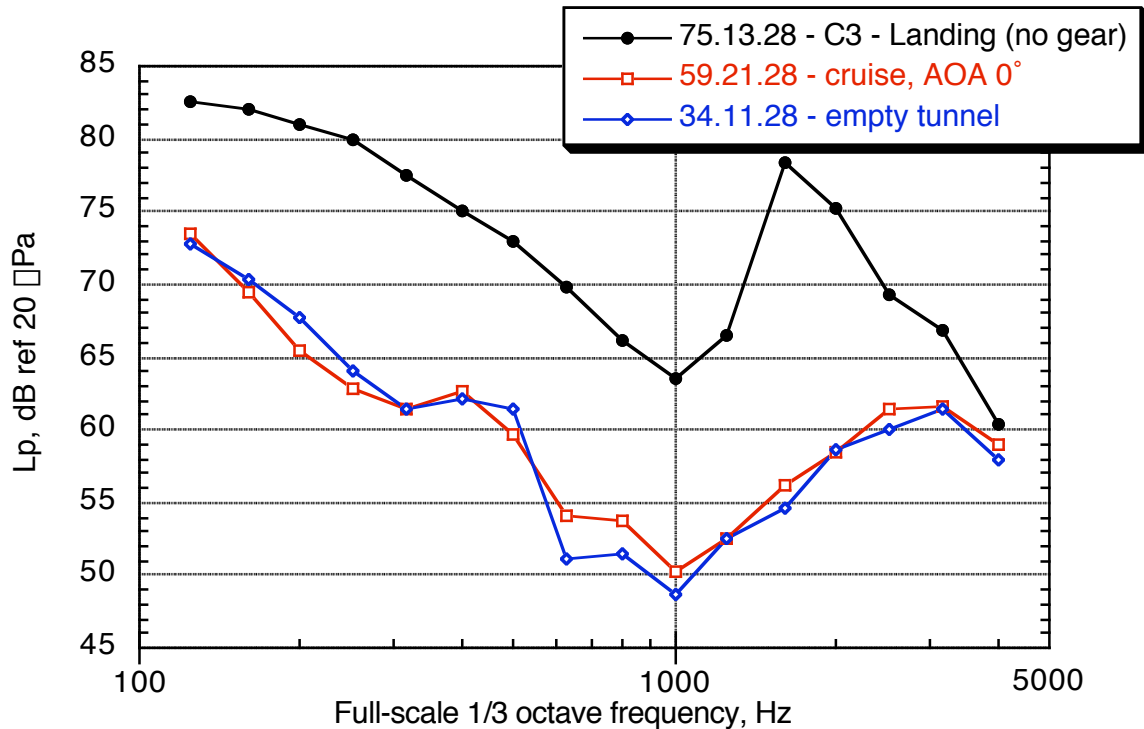


Figure 23. Outboard-slat inboard-edge (OSIE) integration region background noise: scan plane 28,  $\square = 6^\circ$  (OSIE),  $M = 0.21$ , traverse array at 150 in.

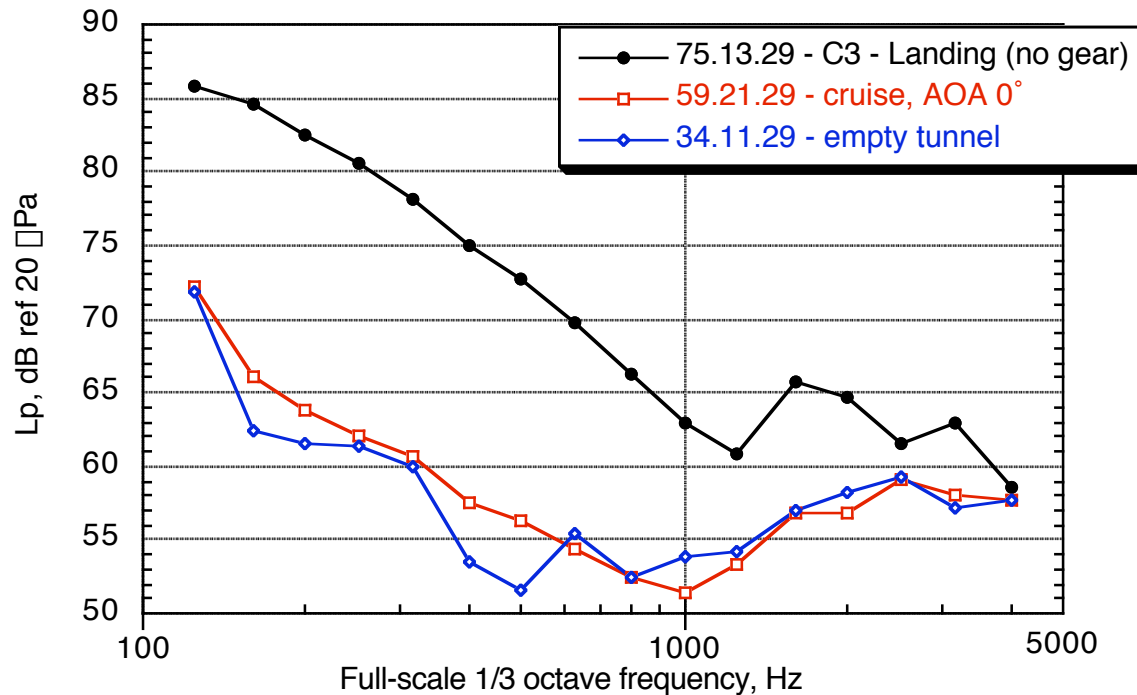
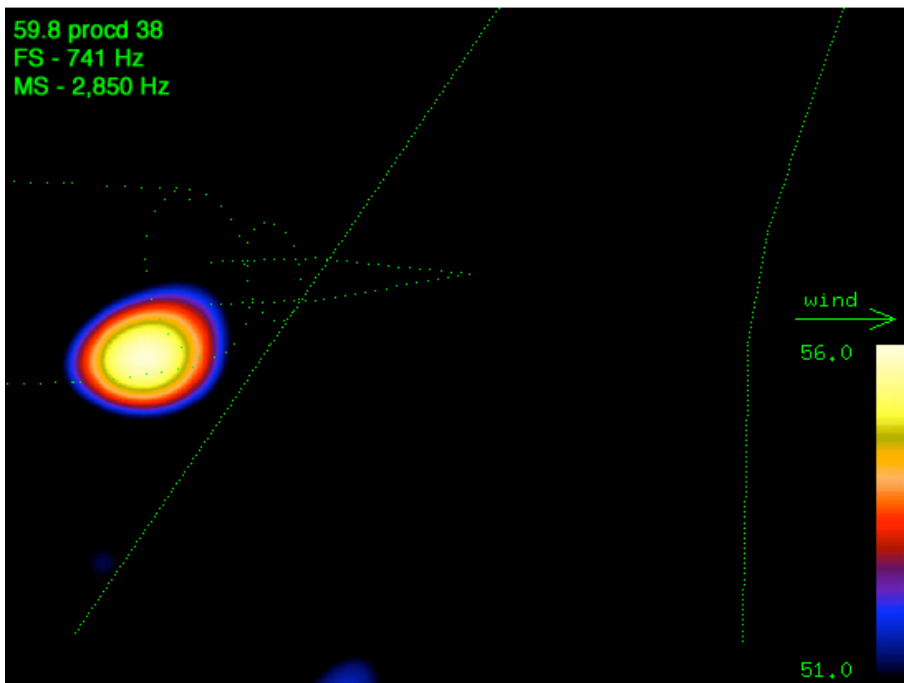
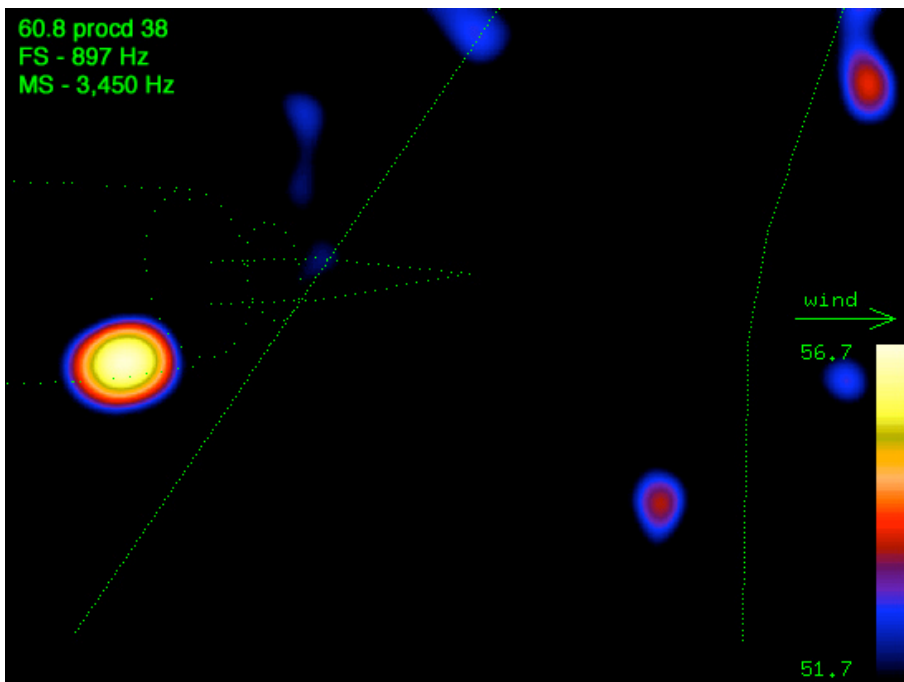


Figure 24. Outboard-flap outboard-edge (OFOE) integration region background noise: scan plane 29,  $\alpha = 6^\circ$  (OFOE),  $M = 0.21$ , traverse array at 150 in.



(a) 741 Hz,  $M = 0.21$ .



(b) 897 Hz,  $M = 0.26$ .

Figure 25. Cruise configuration nacelle source,  $\square = 4^\circ$ , fixed array, 5-dB range.

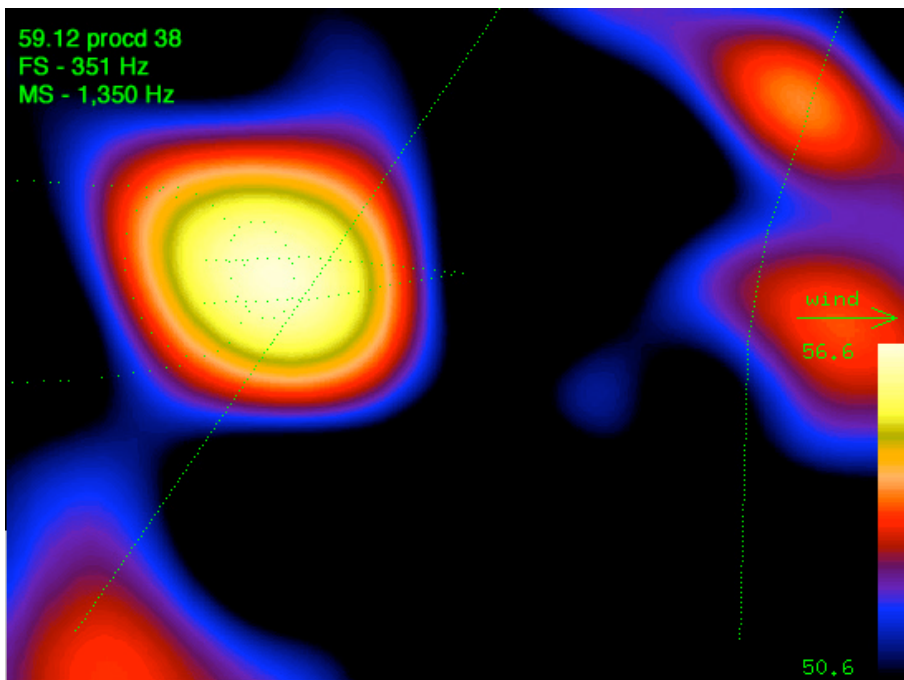


Figure 26. 351 Hz,  $M = 0.21$ ,  $\theta = 8^\circ$ , fixed array, 5-dB range.

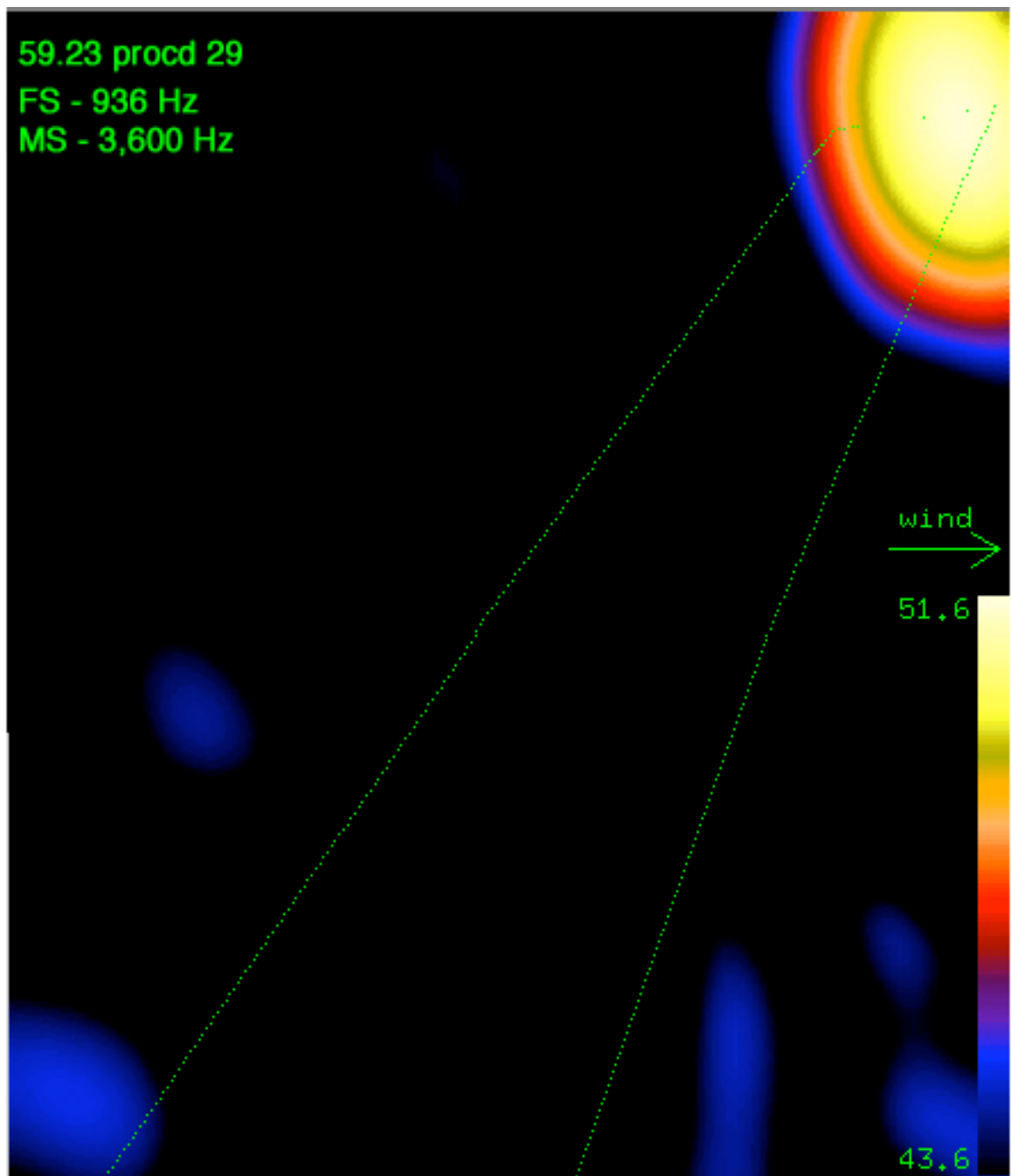


Figure 27. The broadband wing-tip source was only visible at high angles of attack: cruise,  $M = 0.21$ ,  $\alpha = 8^\circ$ , T150d.



Figure 28. STAR model inboard flap in landing configuration, gear removed.



Figure 29. The bottom edge of the inboard fairing is filled with foam and sealed.

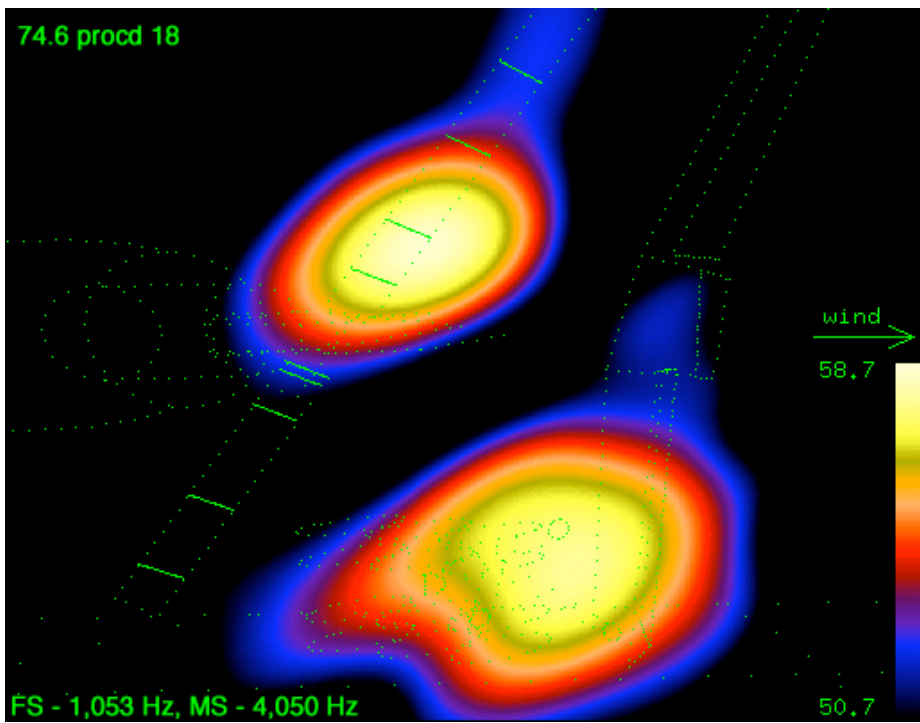


Figure 30. Below 1,053 Hz landing-gear sources dominate the source-location map:  $M = 0.18$ ,  $\Delta = 6^\circ$ , T150d, C3a, landing configuration.

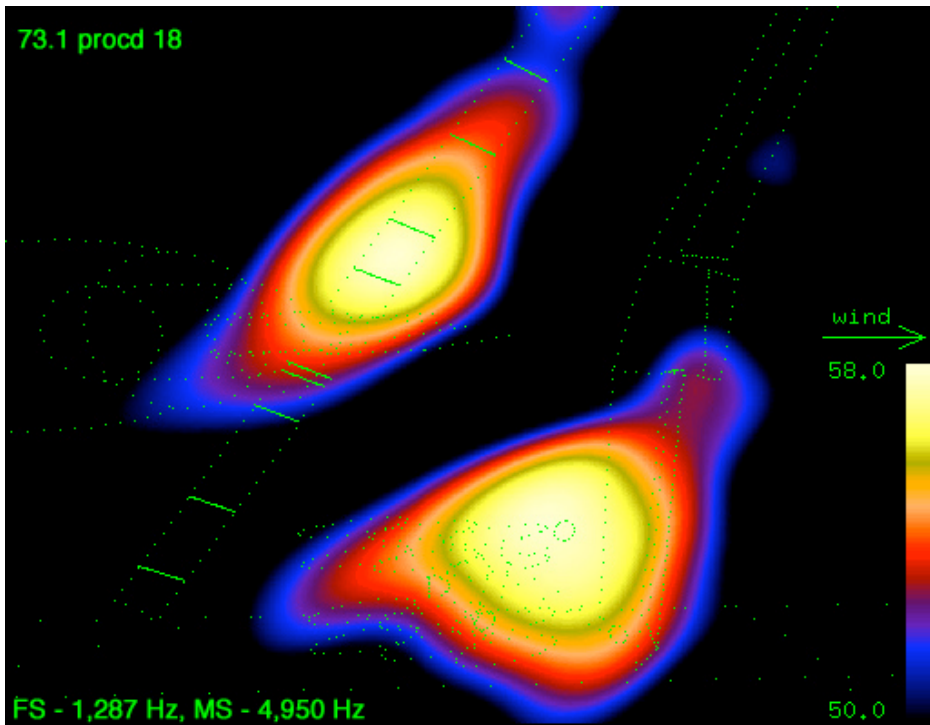


Figure 31. Slat noise becomes the loudest source above 1287 Hz at Mach 0.21:  $\Delta = 6^\circ$ ,  $M = 0.21$ , T150d, C3a, landing configuration.

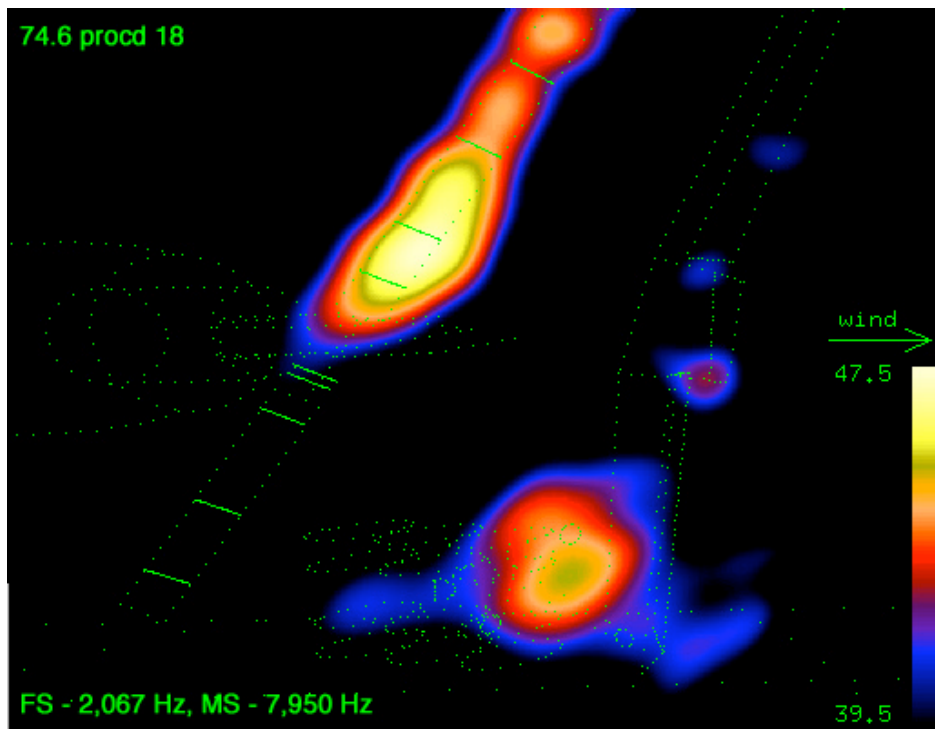


Figure 32. Landing-gear noise becomes visible again at the high end of the mid-range frequencies:  
 $\Delta = 6^\circ$ ,  $M = 0.18$ , C3a, T150d.

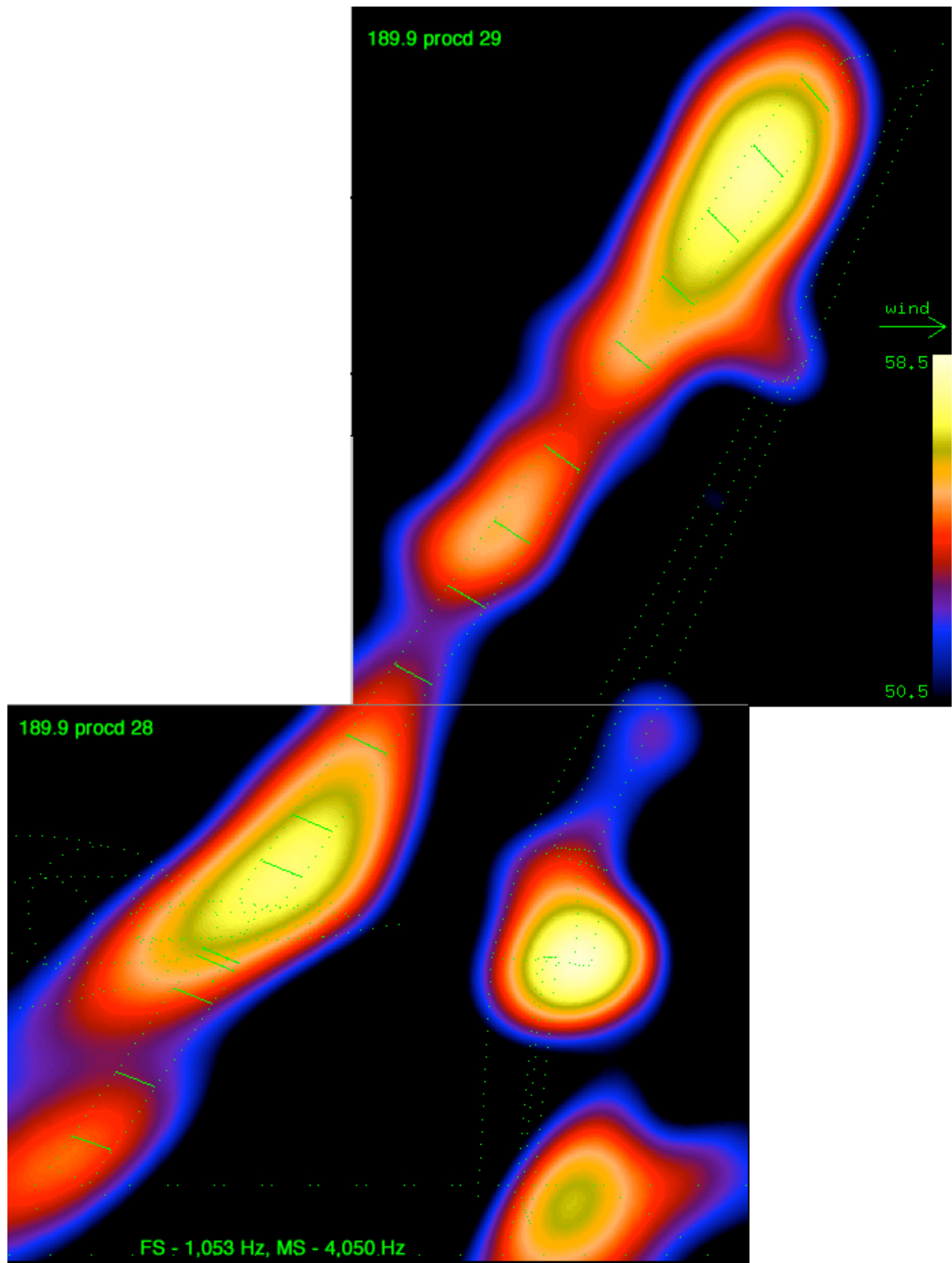


Figure 33.  $\Delta = 6^\circ$ , T150d, gear removed. Strong sources are present on the flap side-edges and in the slat-cove region.

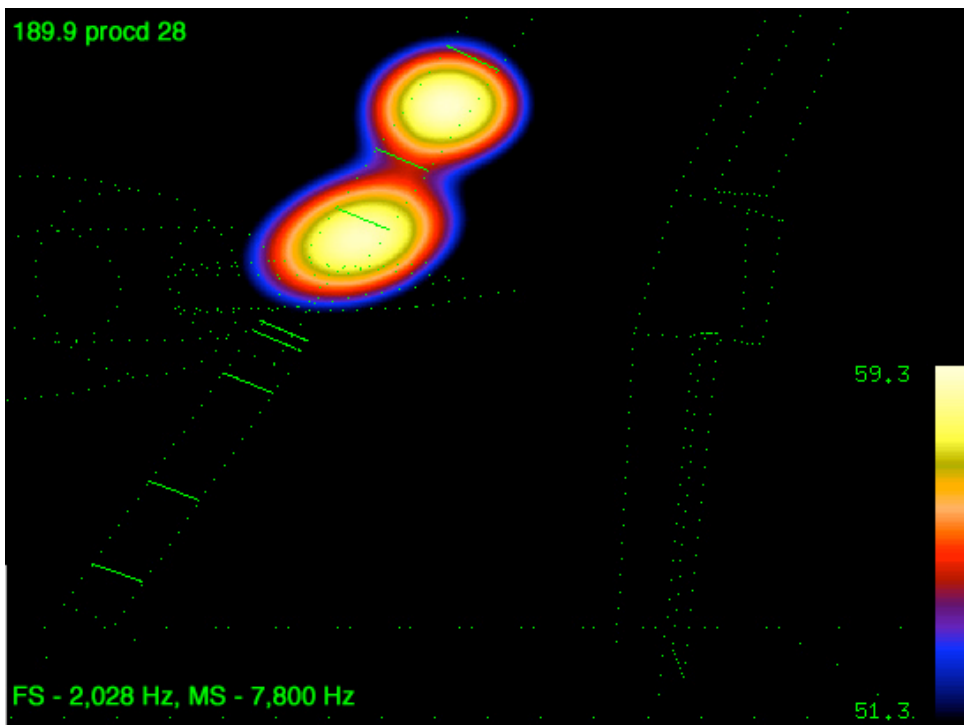


Figure 34.  $M = 0.22$ ,  $\Delta = 6^\circ$ , C37, strong sources in the slat gap and on the slat side-edge.

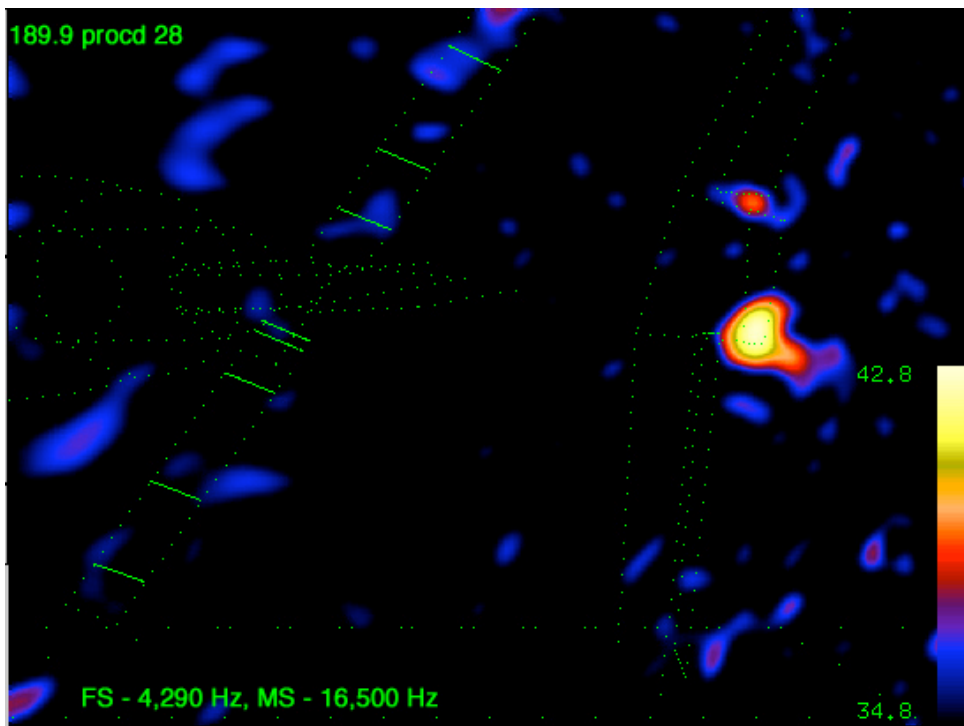


Figure 35. High-frequency sources were visible on the inboard edges of the inboard and outboard flap:  $M = 0.22$ ,  $\Delta = 6^\circ$ , C37, landing configuration, no gear.

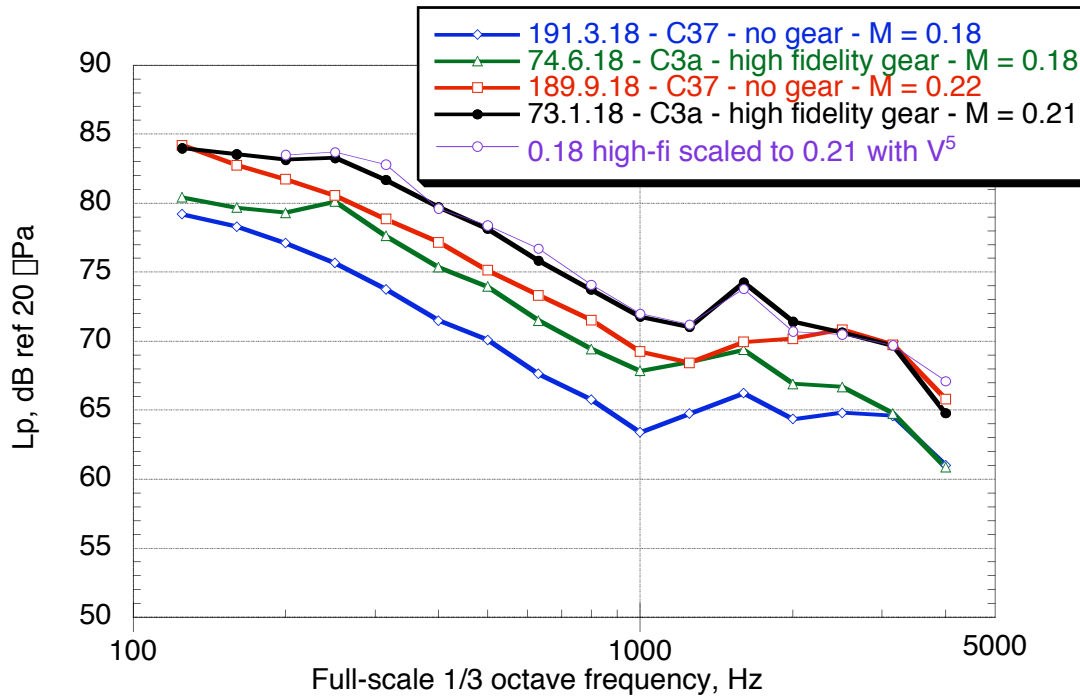


Figure 36. Mach variation with and without high-fidelity landing-gear; data at Mach 0.18 are frequency and amplitude scaled to Mach 0.21.

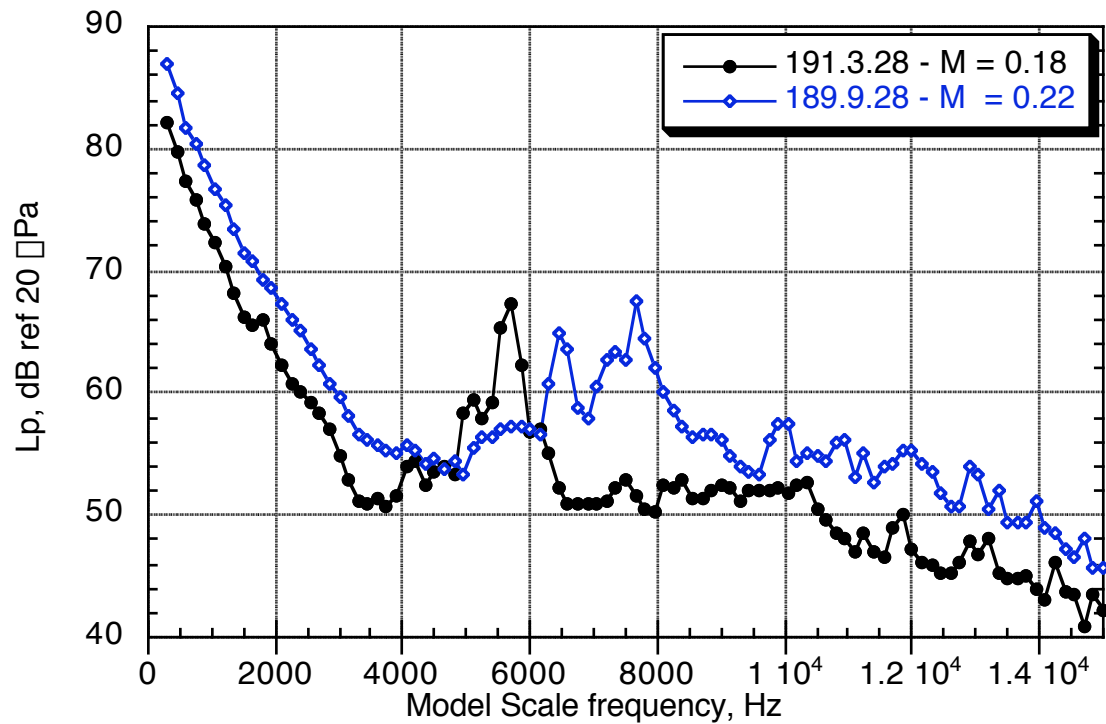
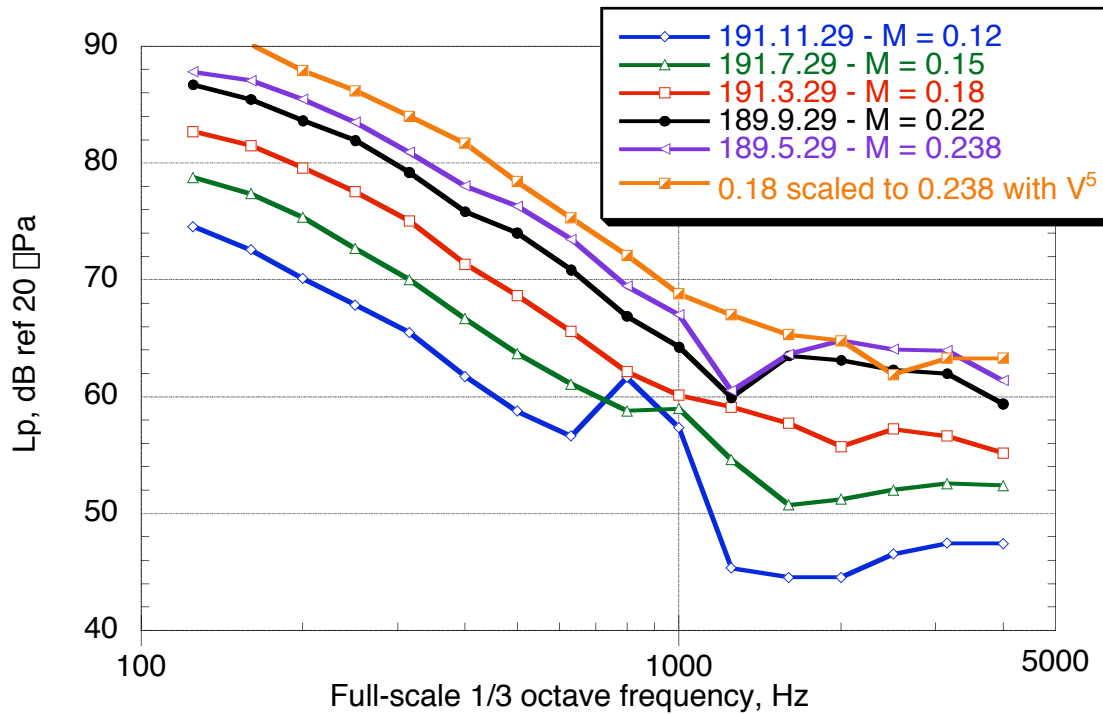
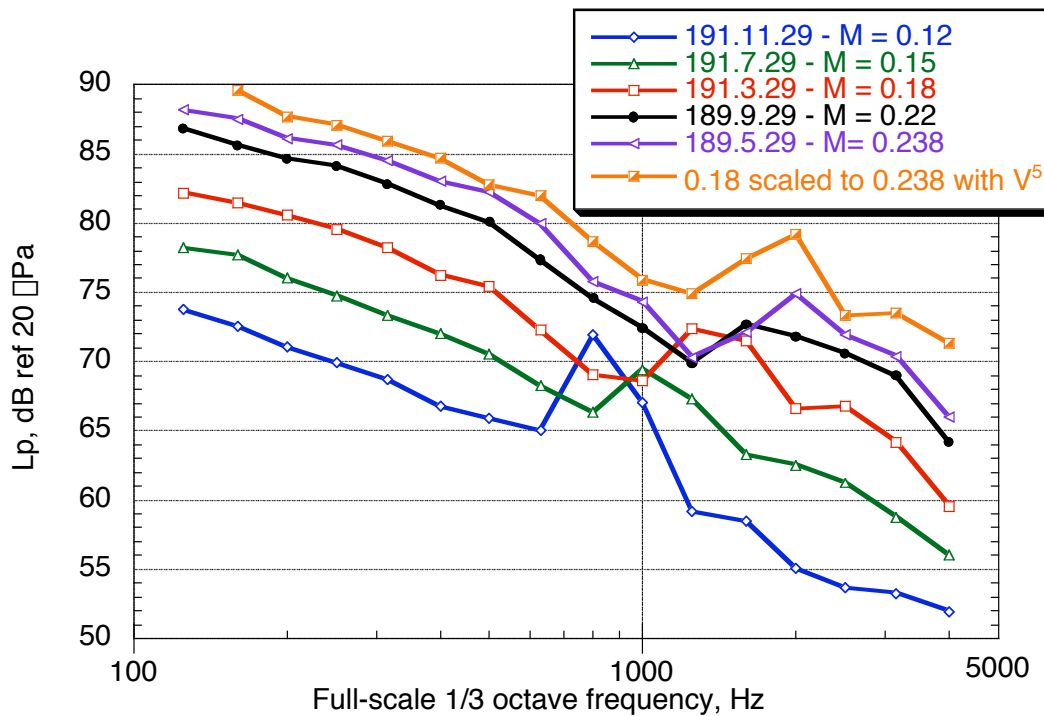


Figure 37. The OSIE tone frequency shifts with velocity, C37.

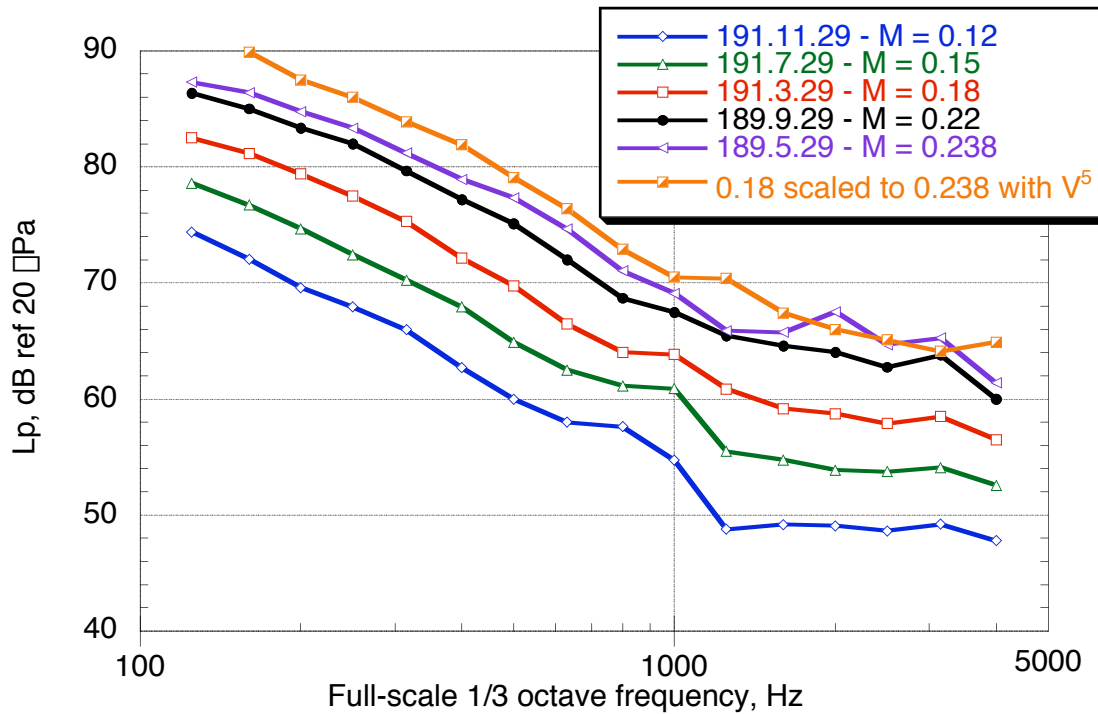


(a) Outboard-flap outboard-edge (OFOE).

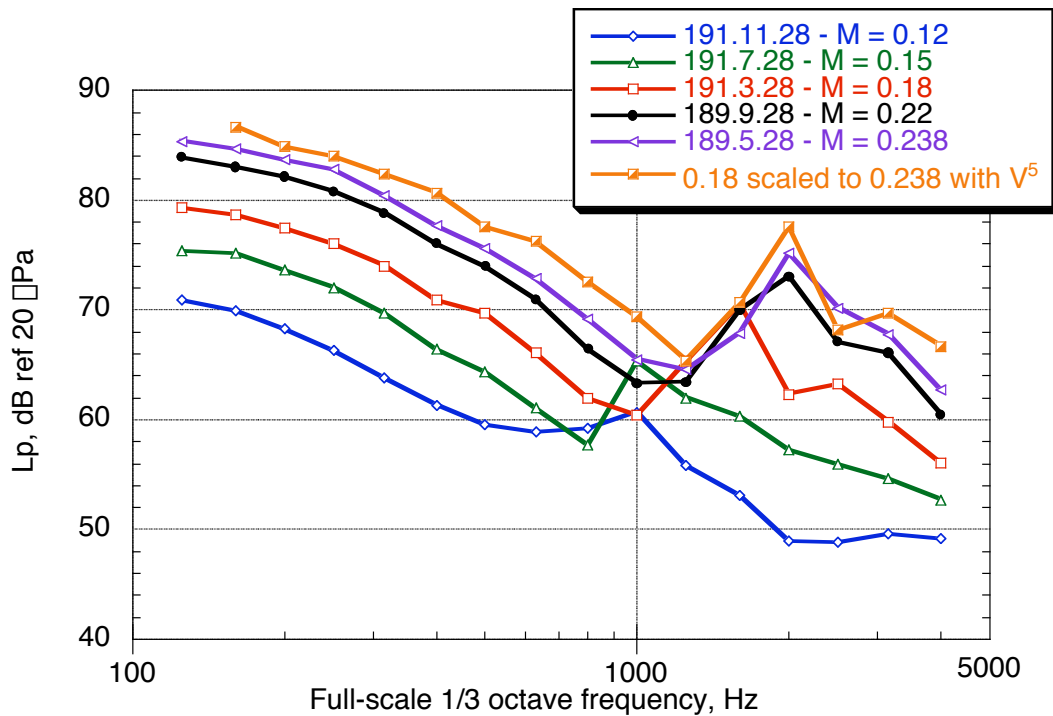


(b) Slat-cove integration.

Figure 38. Mach sweep in baseline-landing configuration C37.



(c) Outboard-slat outboard-edge (OSOE).



(d) Outboard slat inboard edge (OSIE).

Figure 38. Concluded.

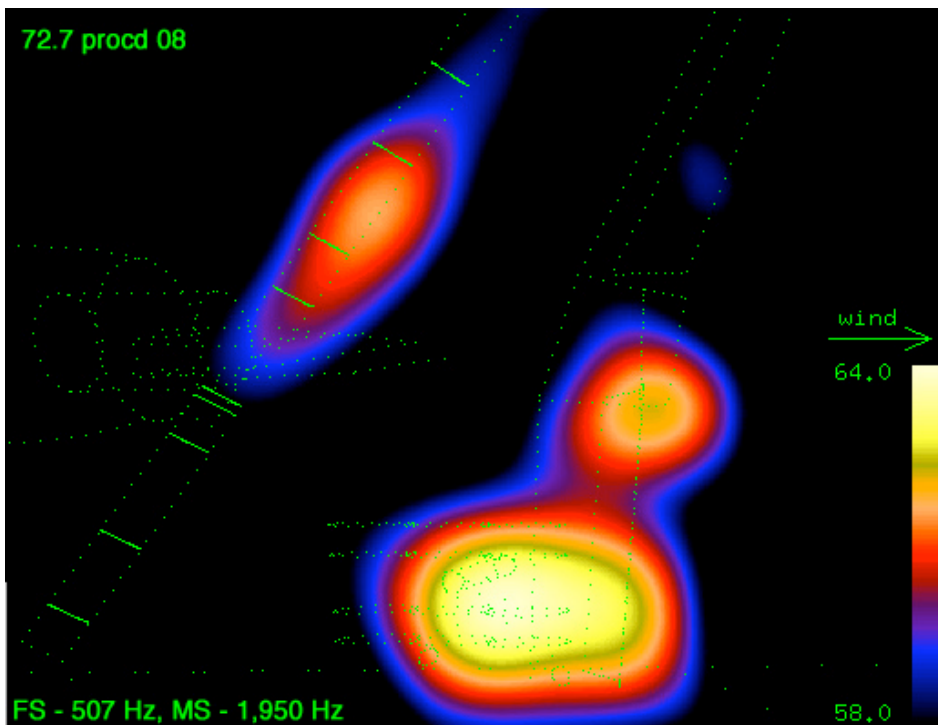


Figure 39.  $M = 0.21$ ,  $\alpha = 4^\circ$ , C3a, Fixed array; low-frequency landing gear noise.

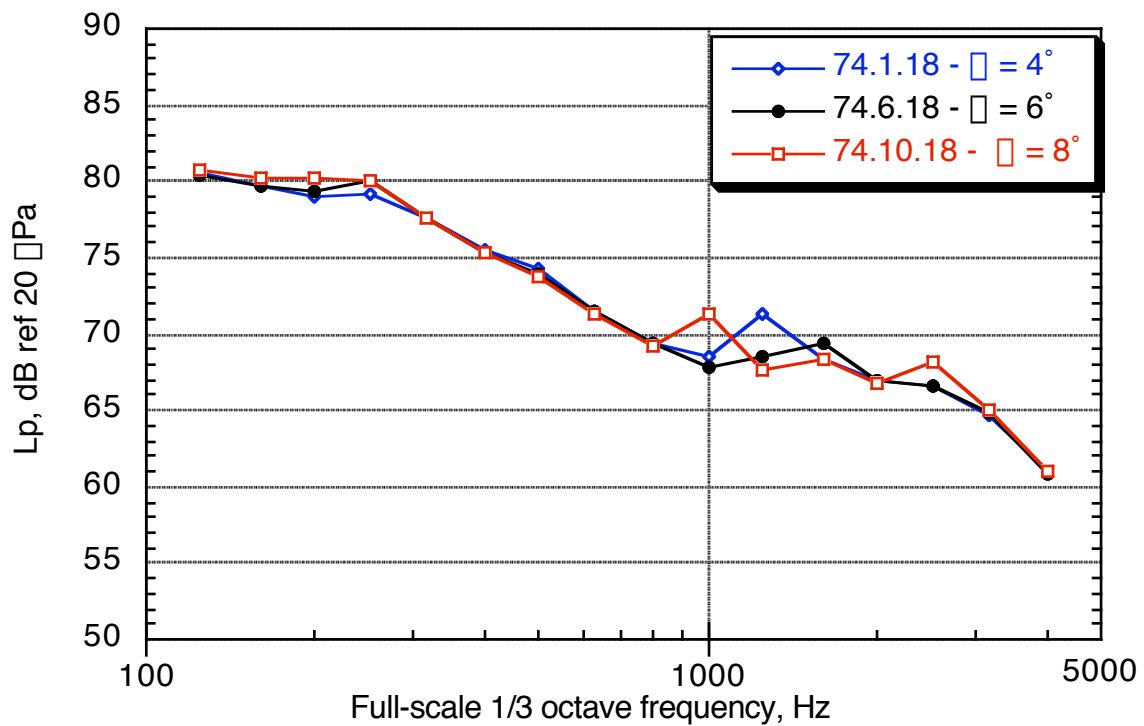


Figure 40. Angle-of-attack variation of the landing-gear region in baseline-landing configuration: C3a at Mach 0.18.

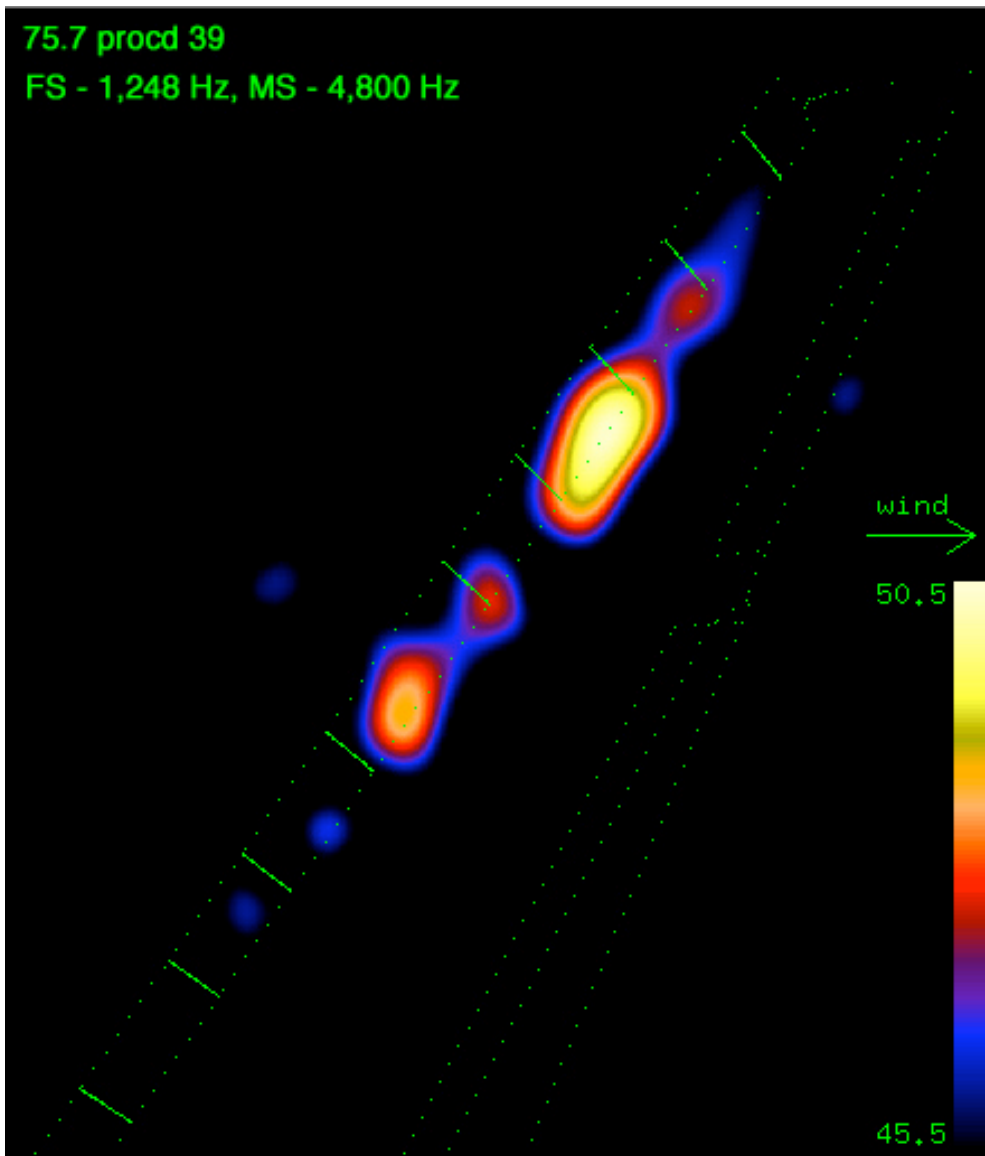


Figure 41.  $M = 0.21$ ,  $\alpha = 6^\circ$ ; the lines in the slat section represent the slat brackets.

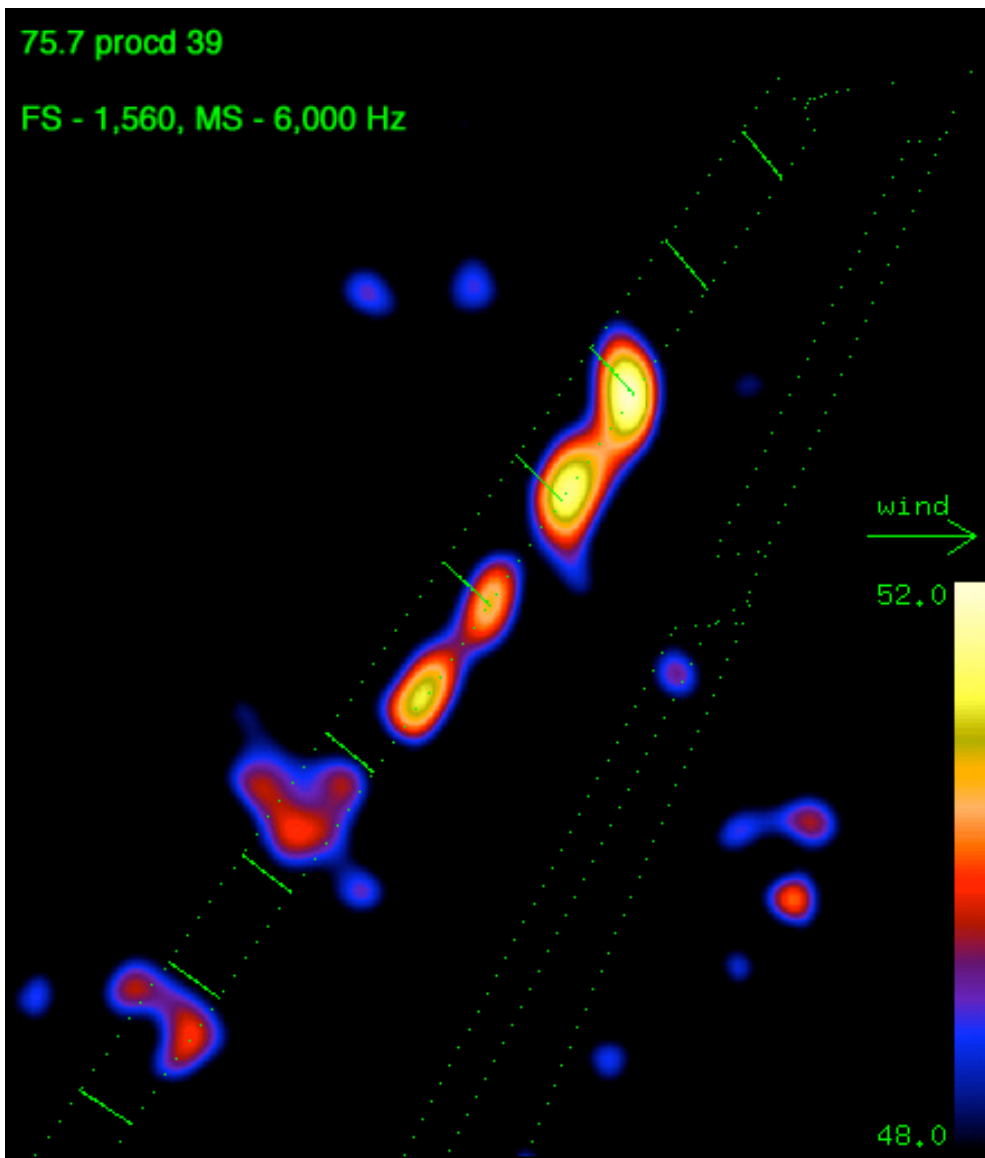
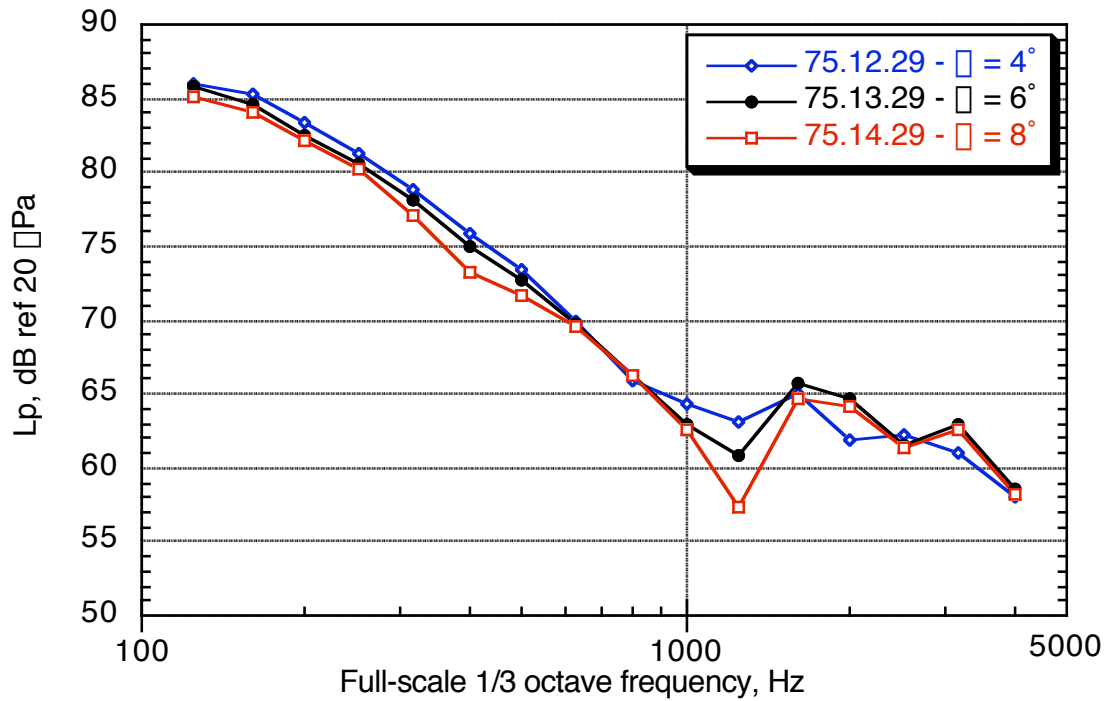
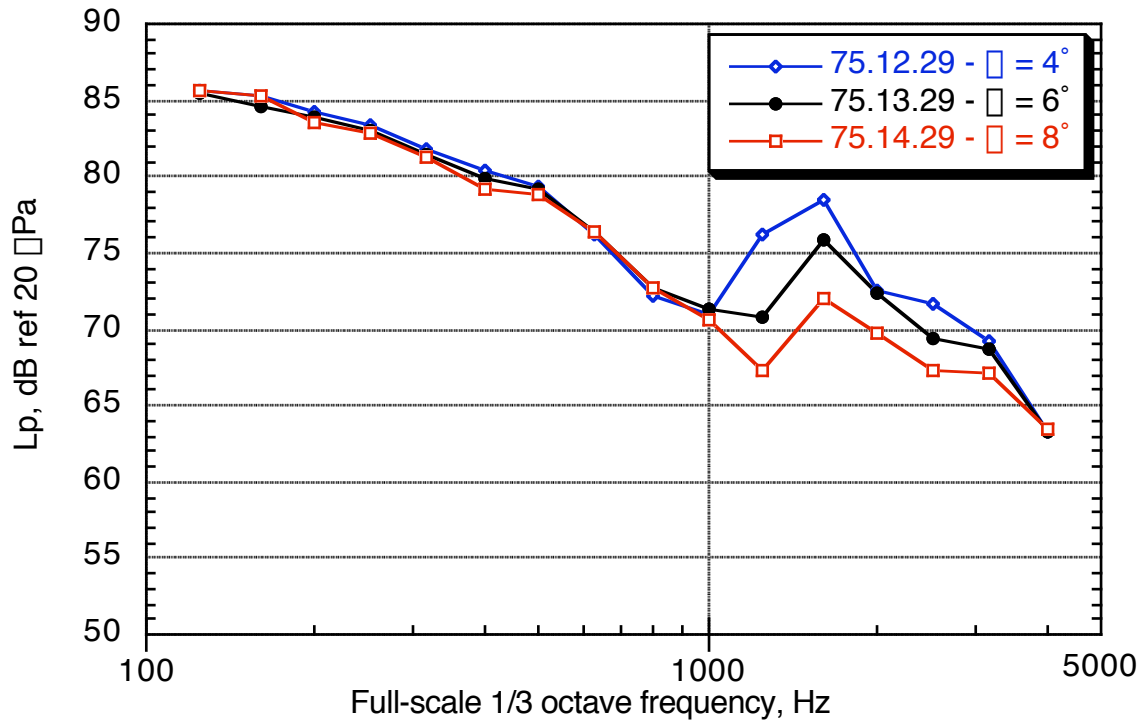


Figure 42.  $M = 0.21$ ,  $\alpha = 6^\circ$ , C3, fixed array.

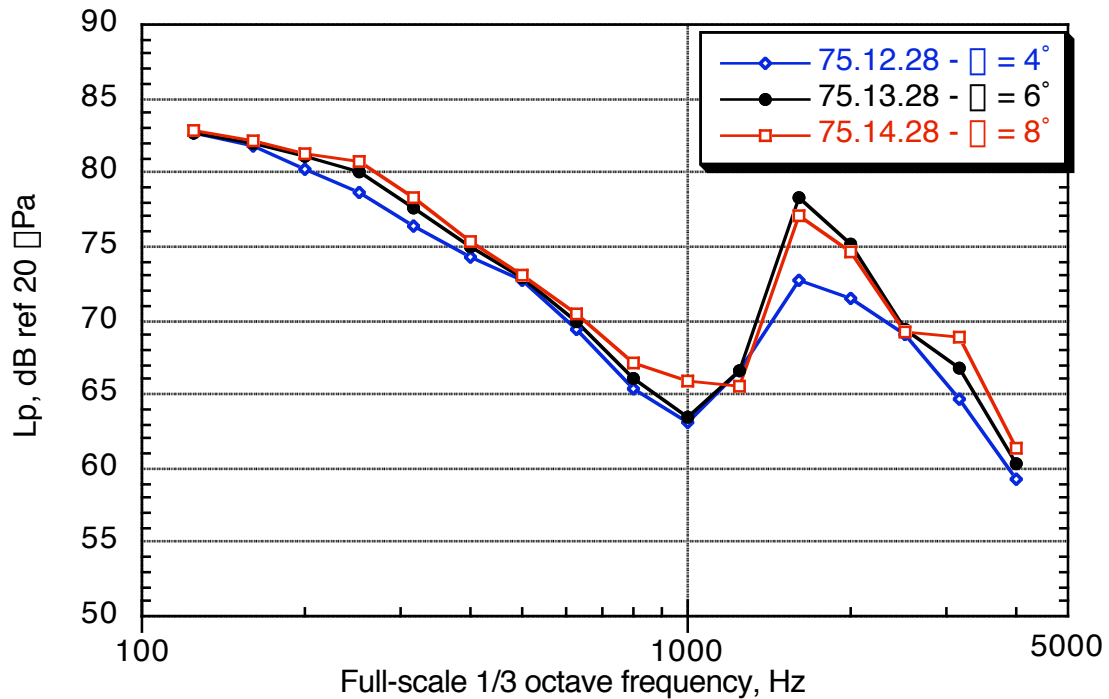


(a) OFOE.

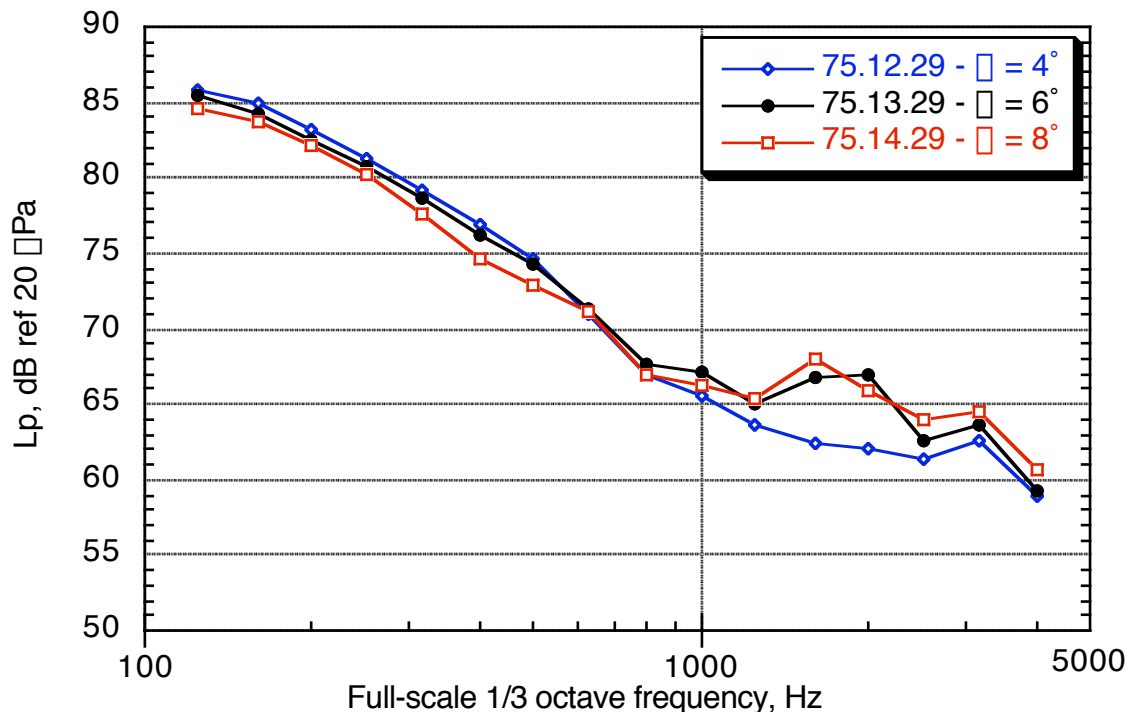


(b) Slat cove.

Figure 43. Angle-of-attack variation in baseline-landing configuration C3 with the landing gear removed,  $M = 0.21$ .

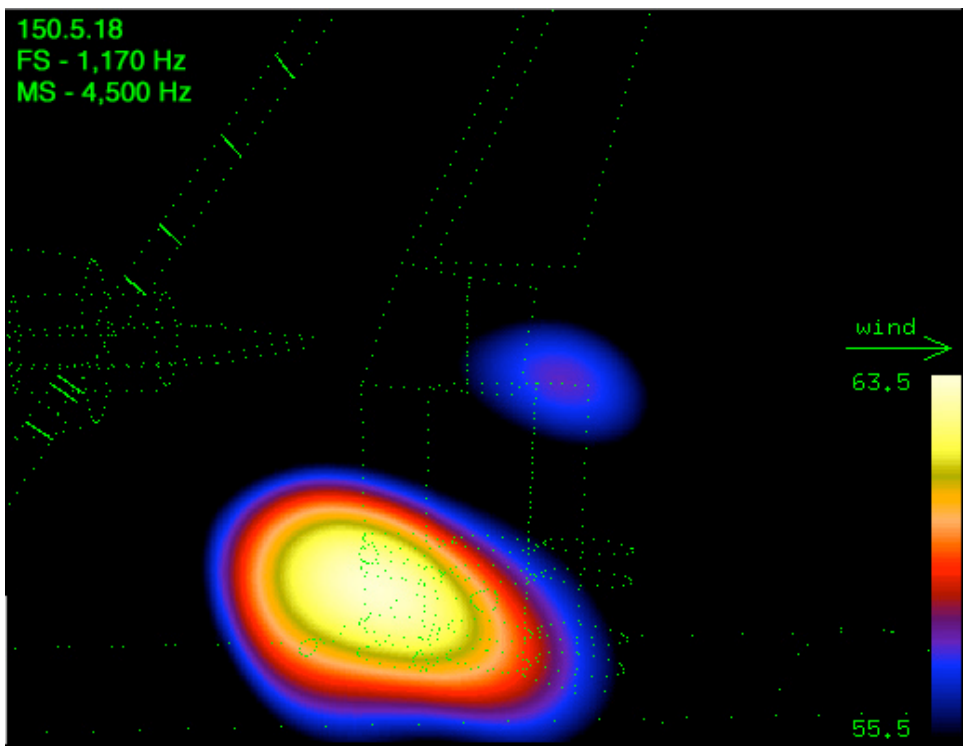


(c) OSIE.

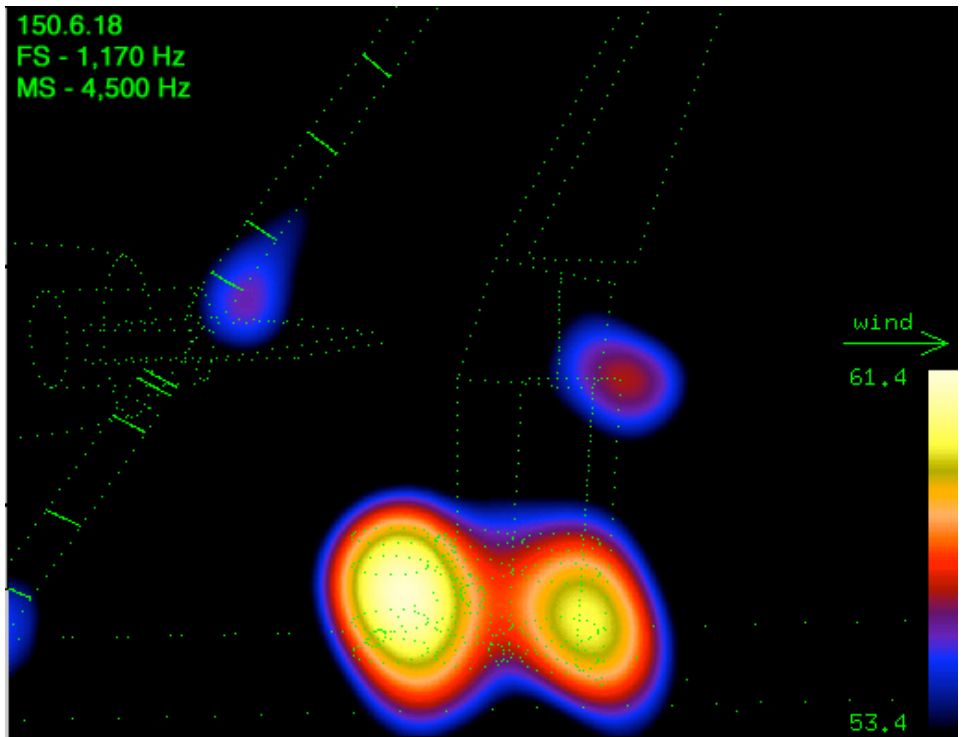


(d) OSOE.

Figure 43. Concluded.

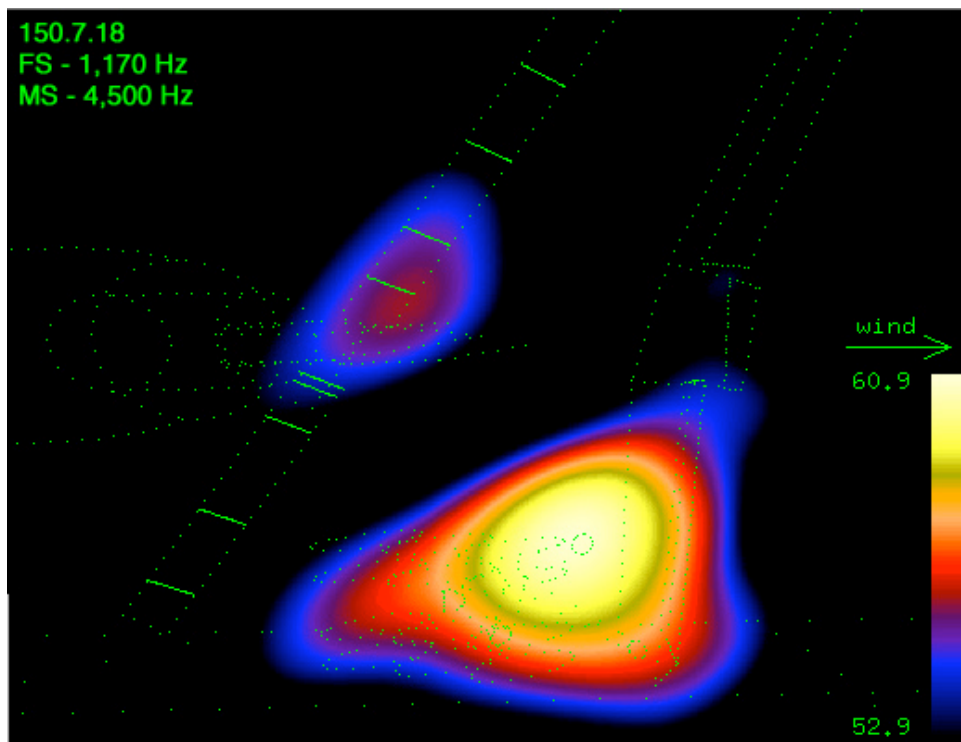


(a) T100u.

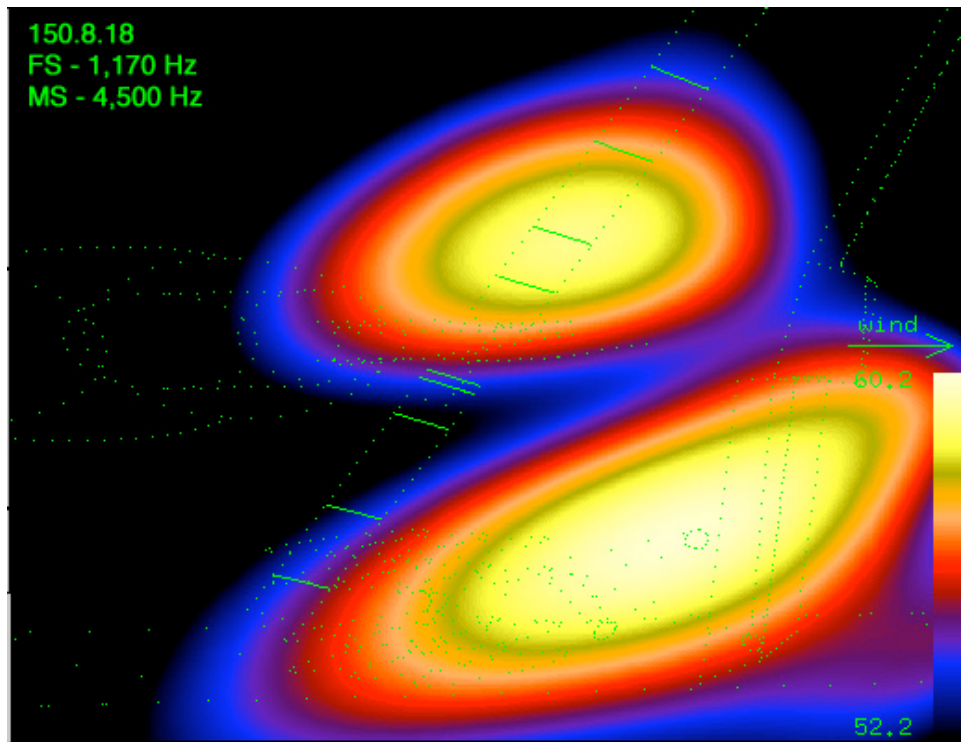


(b) T0.

Figure 44. High-fidelity landing gear traverse.



(c) T150d.



(d) T250d.

Figure 44. Concluded.

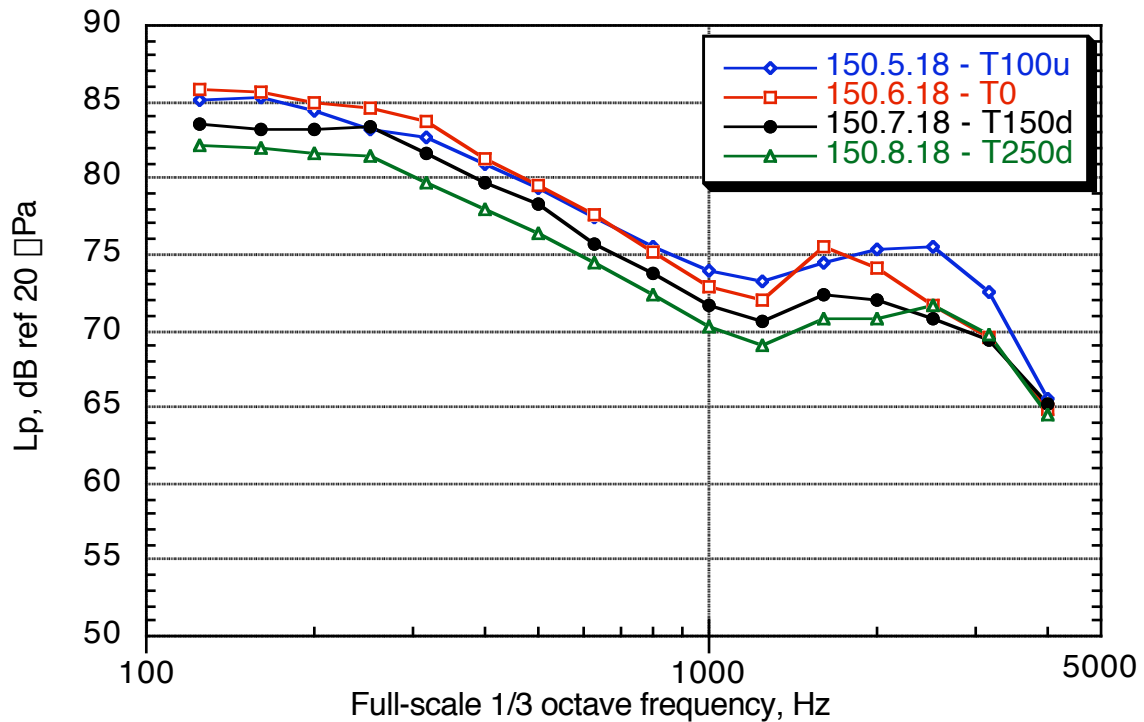


Figure 45. Landing gear region array traverse of the high-fidelity baseline-landing configuration C3a, at Mach 0.21.

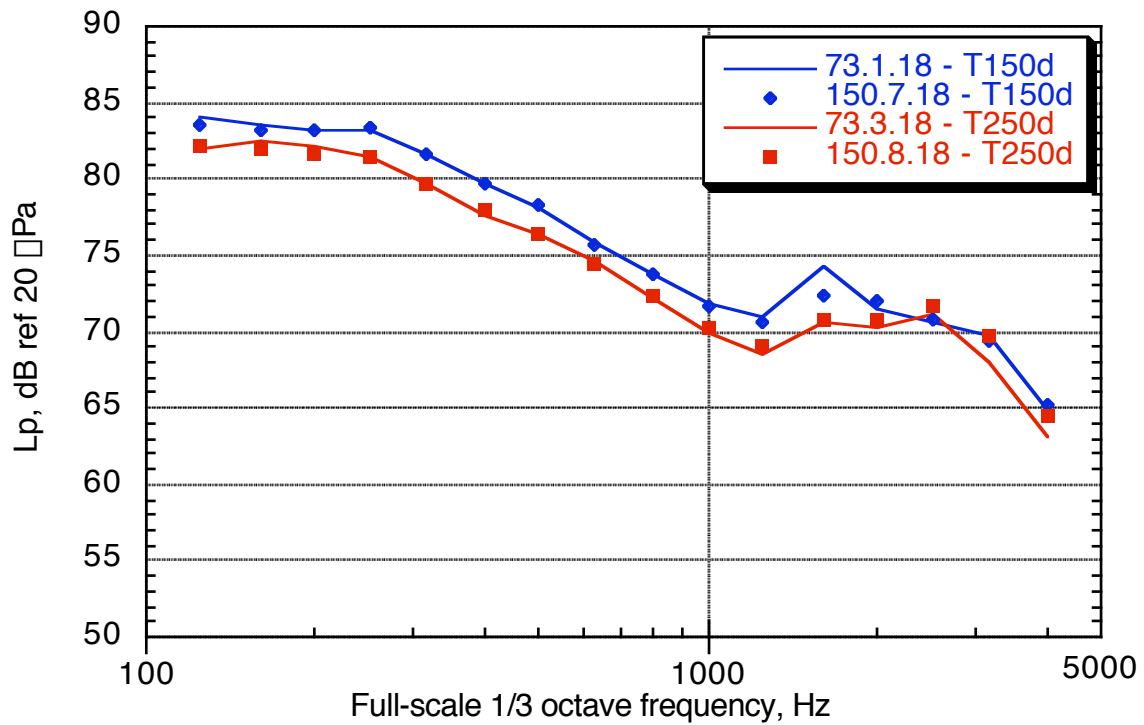
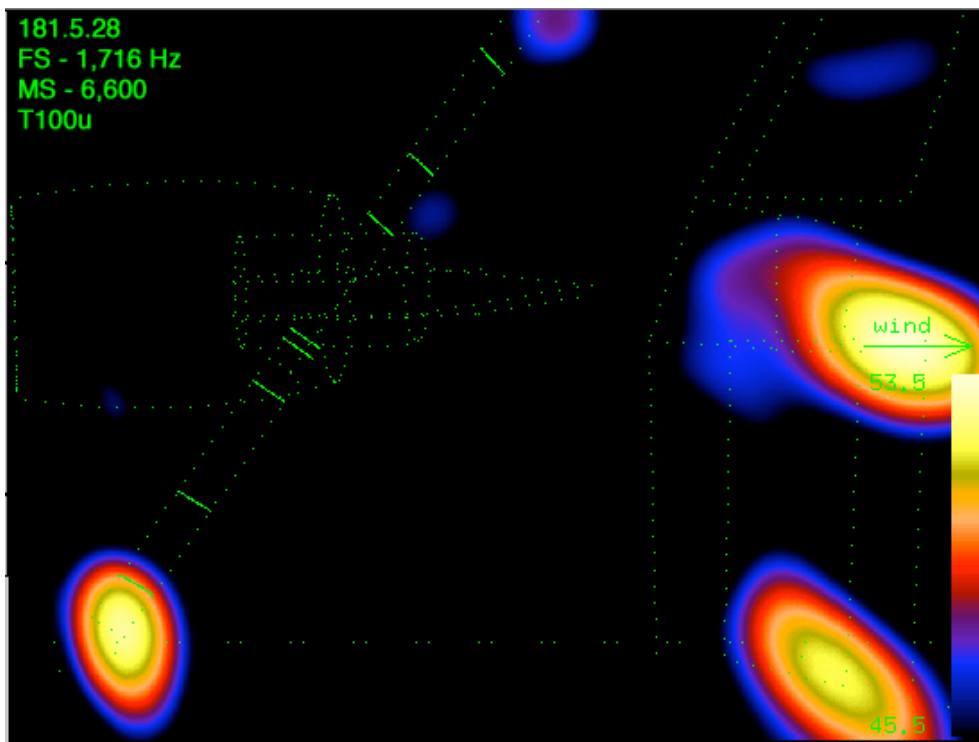
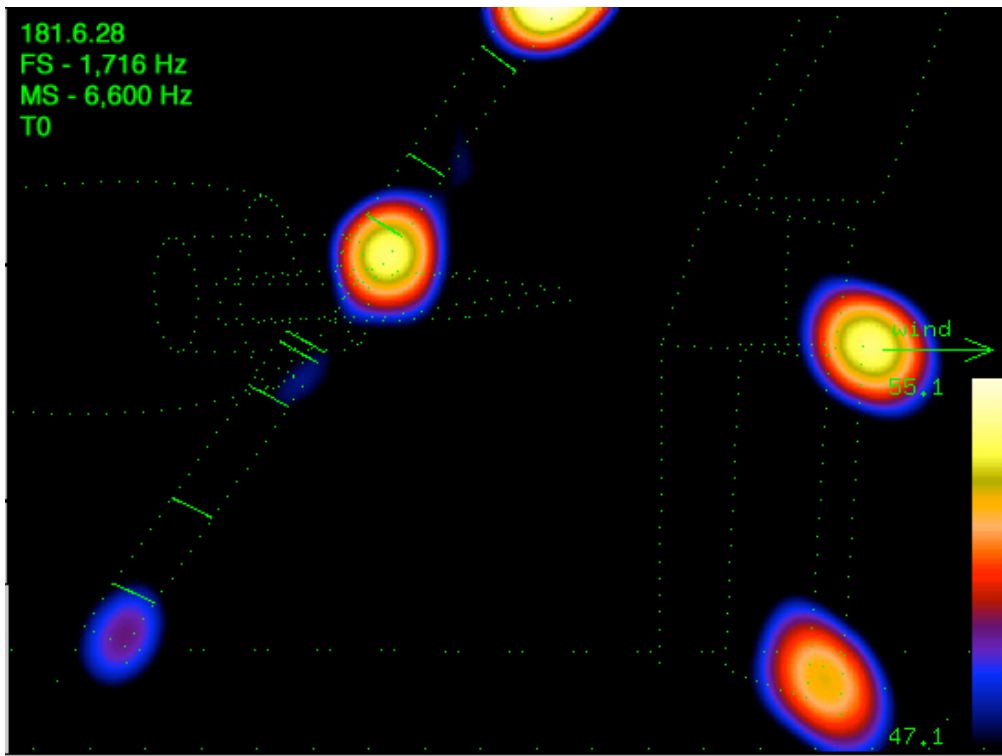


Figure 46. Landing gear region, configuration C3a repeatability; repeat points are shown as solid symbols,  $M = 0.21$ .

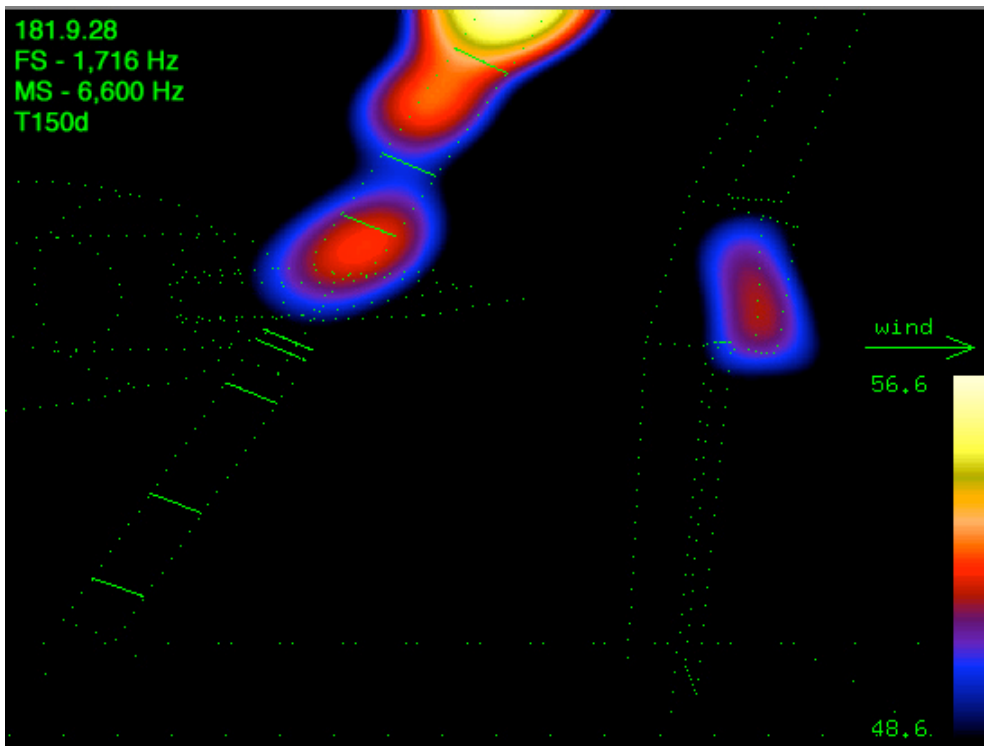


(a) T100u.

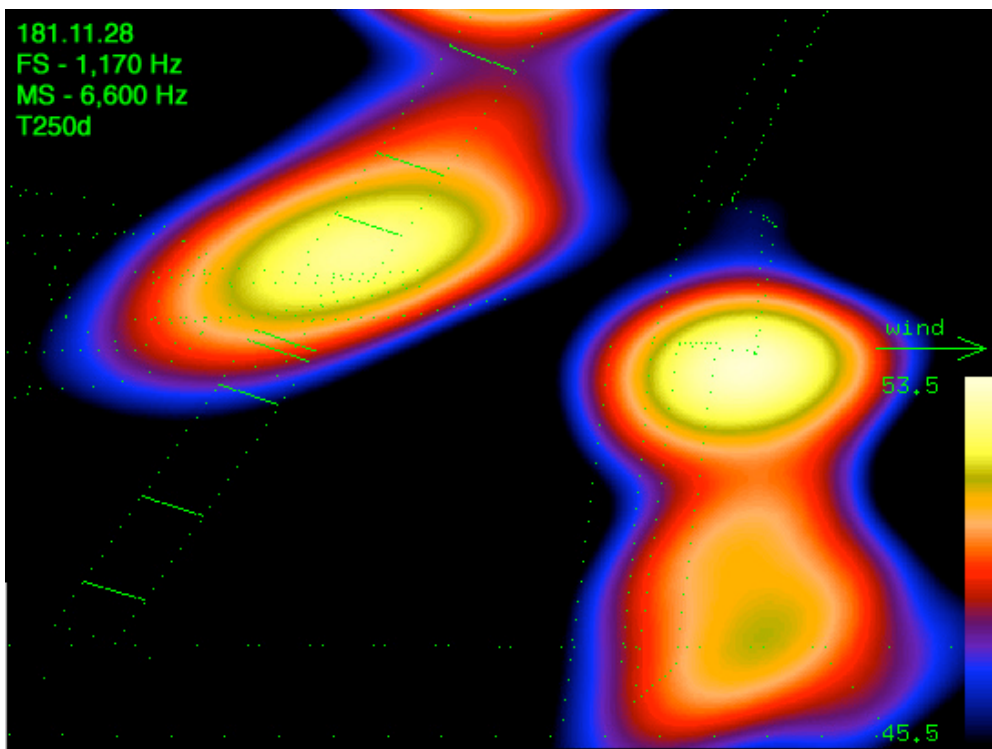


(b) T0.

Figure 47. 1716 Hz, configuration 35 array traverse at Mach 0.21 and  $\Delta = 6^\circ$ .



(c) T150d.



(d) T250d.

Figure 47. Concluded.

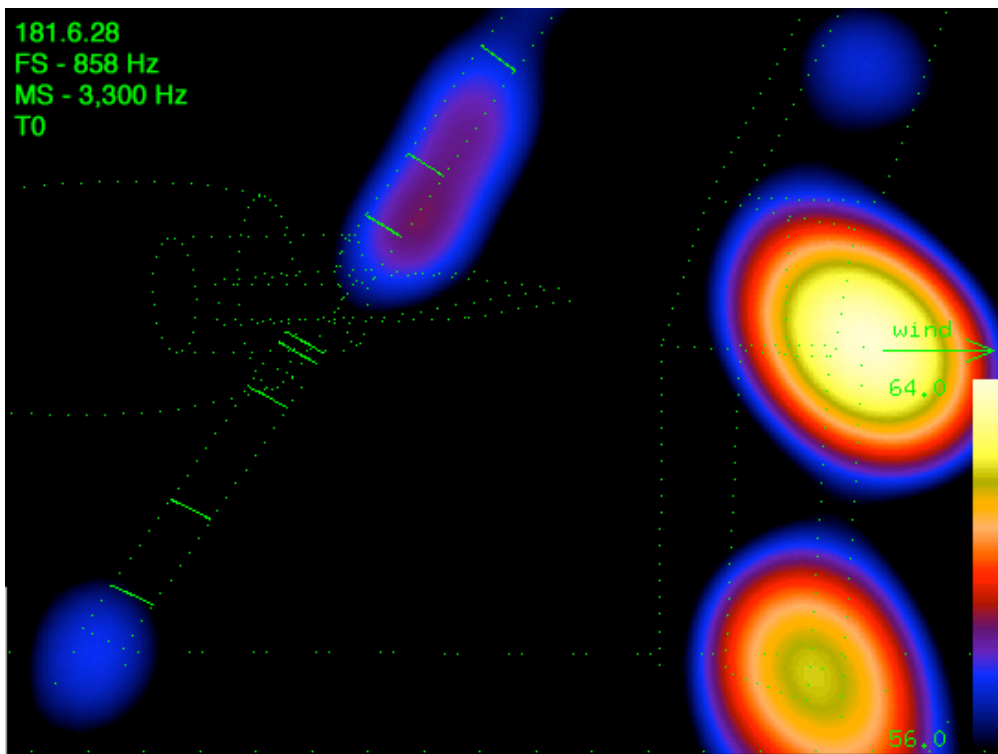


Figure 48. Noise sources were present on the inboard and outboard edges of the inboard-aft flap at traverse position T0, C35.

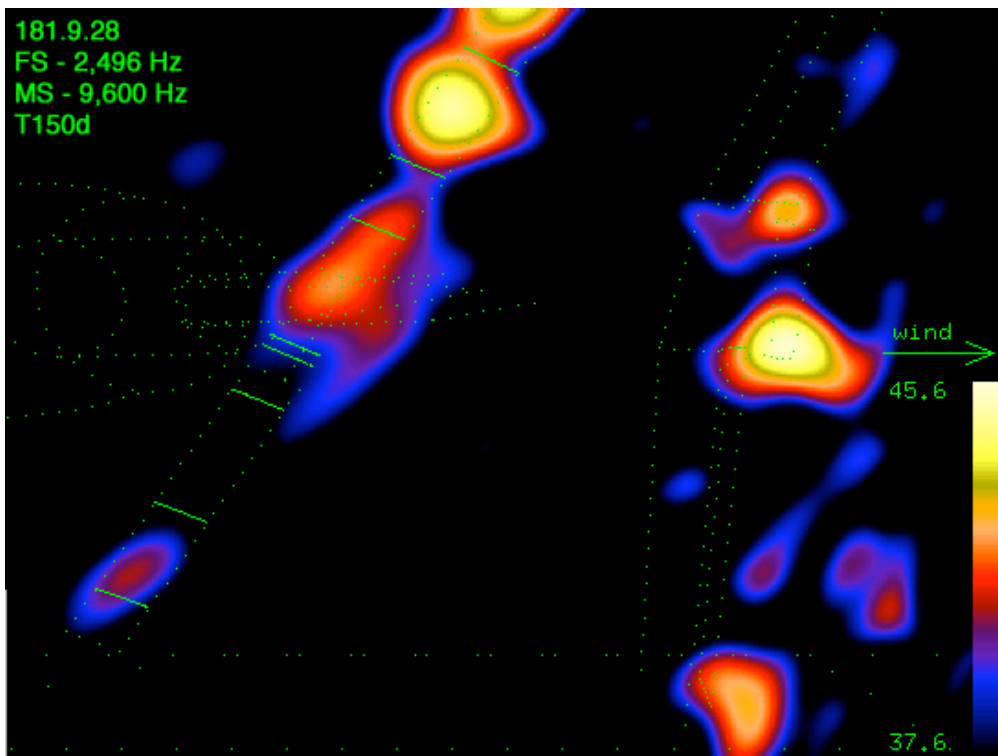
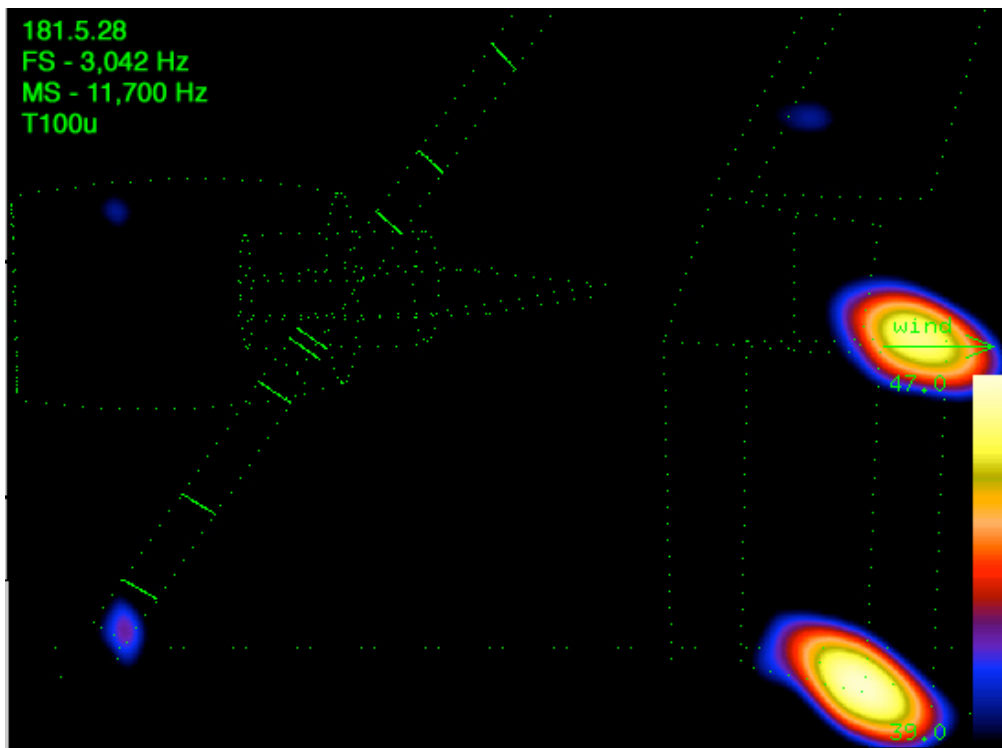
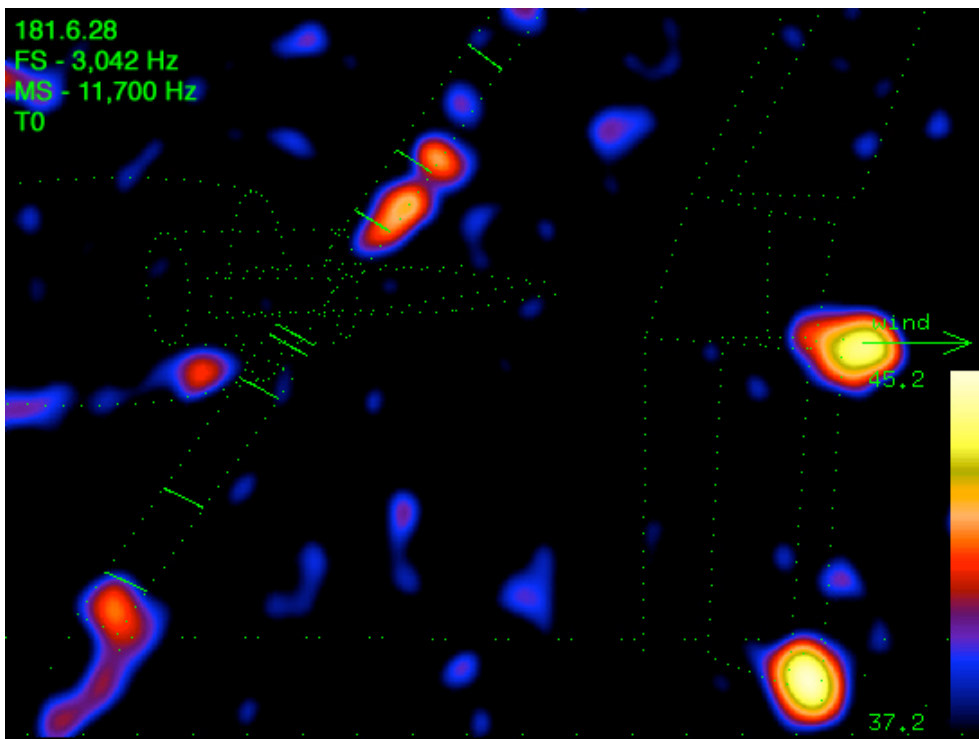


Figure 49. The IFIE was visible over a broad range of frequencies; shown here at 2,496 Hz at traverse position T150d, C35.

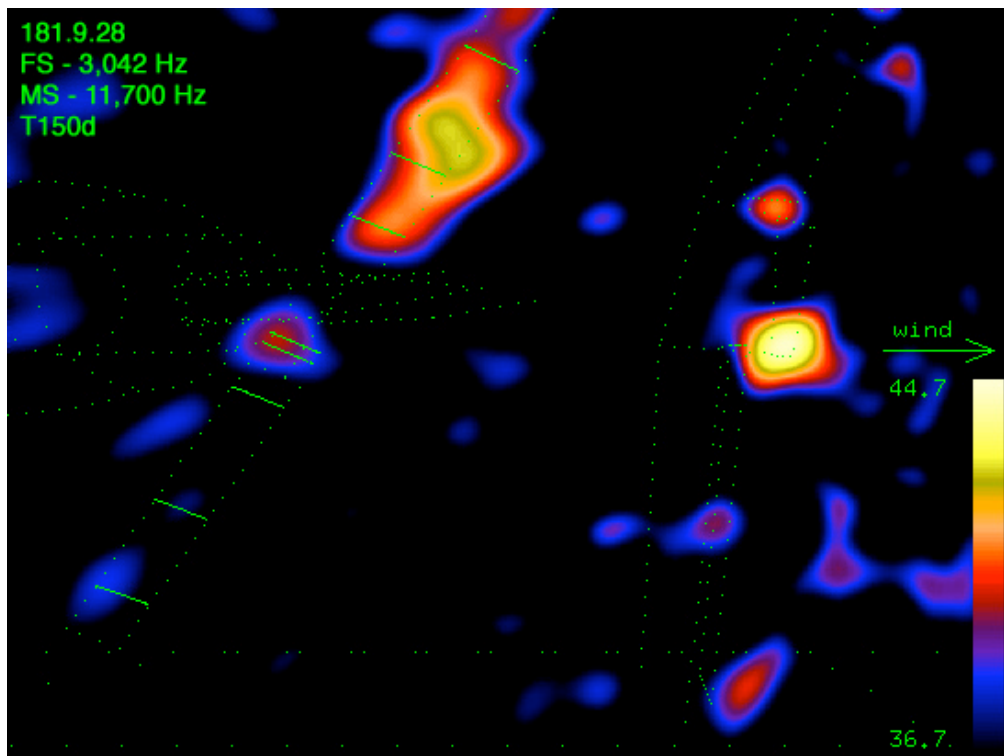


(a) T100u.

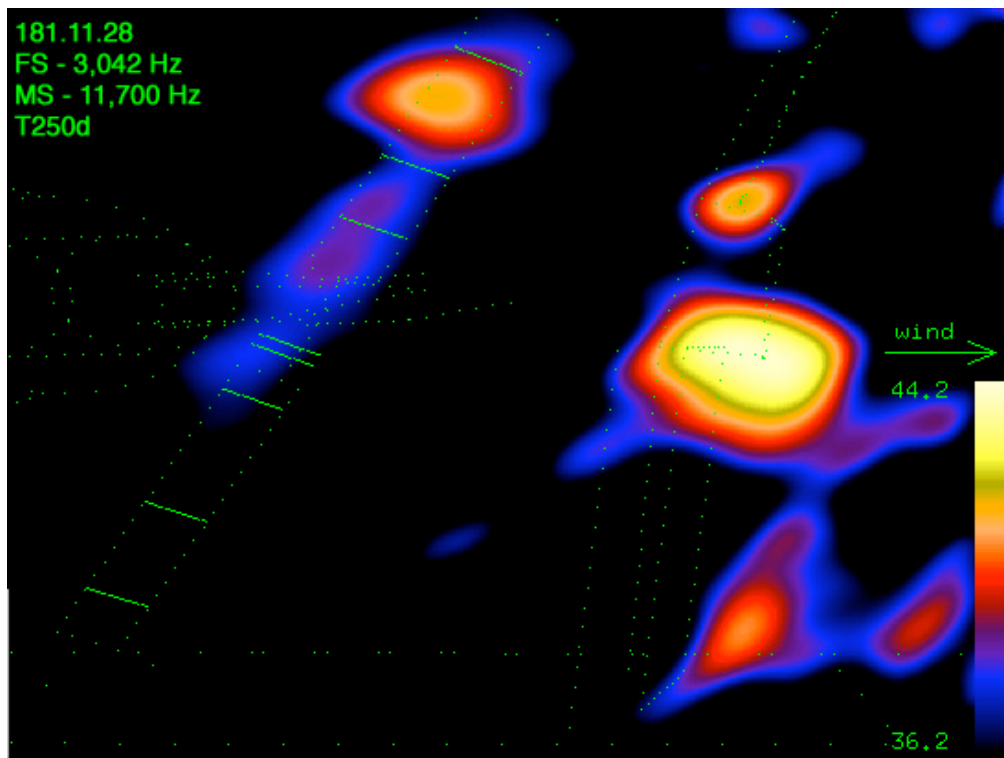


(b) T0.

Figure 50. Array traverse of landing configuration C35 at 3,042 Hz, gear removed,  $M = 0.21$ .



(c) T150d.



(d) T250D

Figure 50. Concluded.

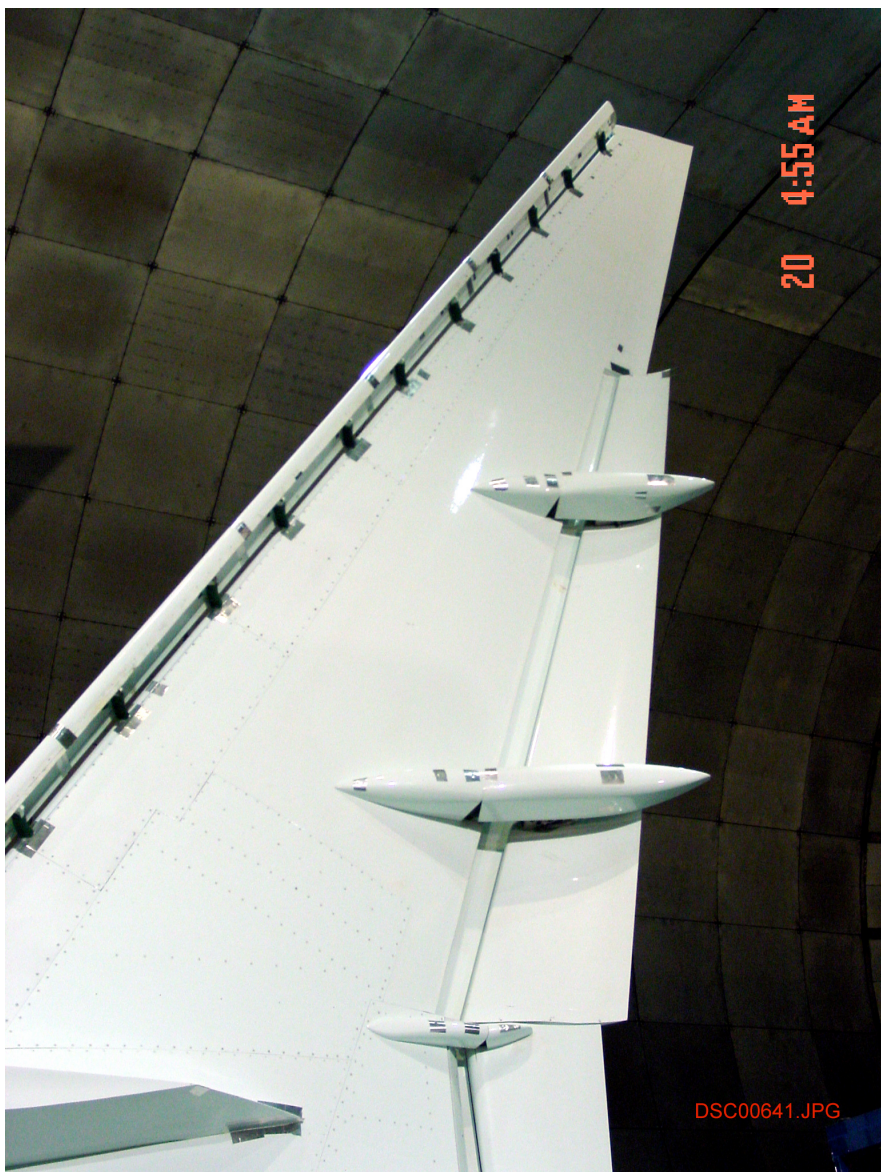


Figure 51. STAR outboard high-lift-system in landing configuration.

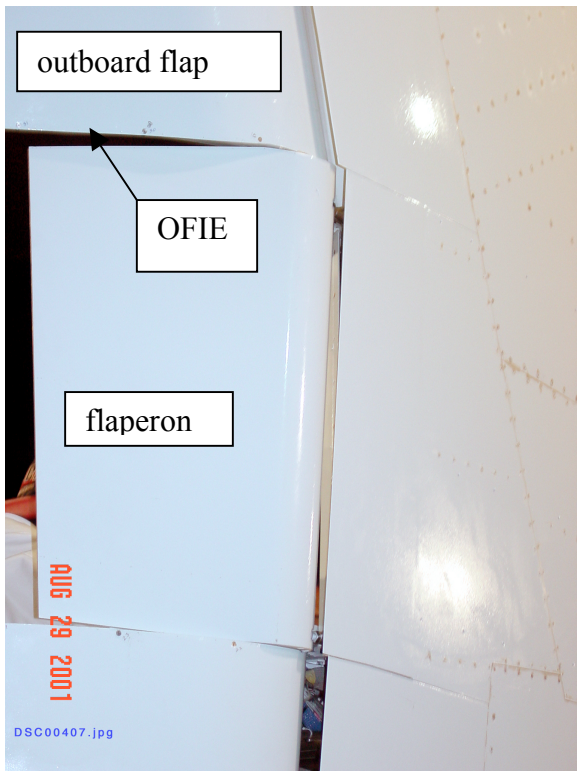
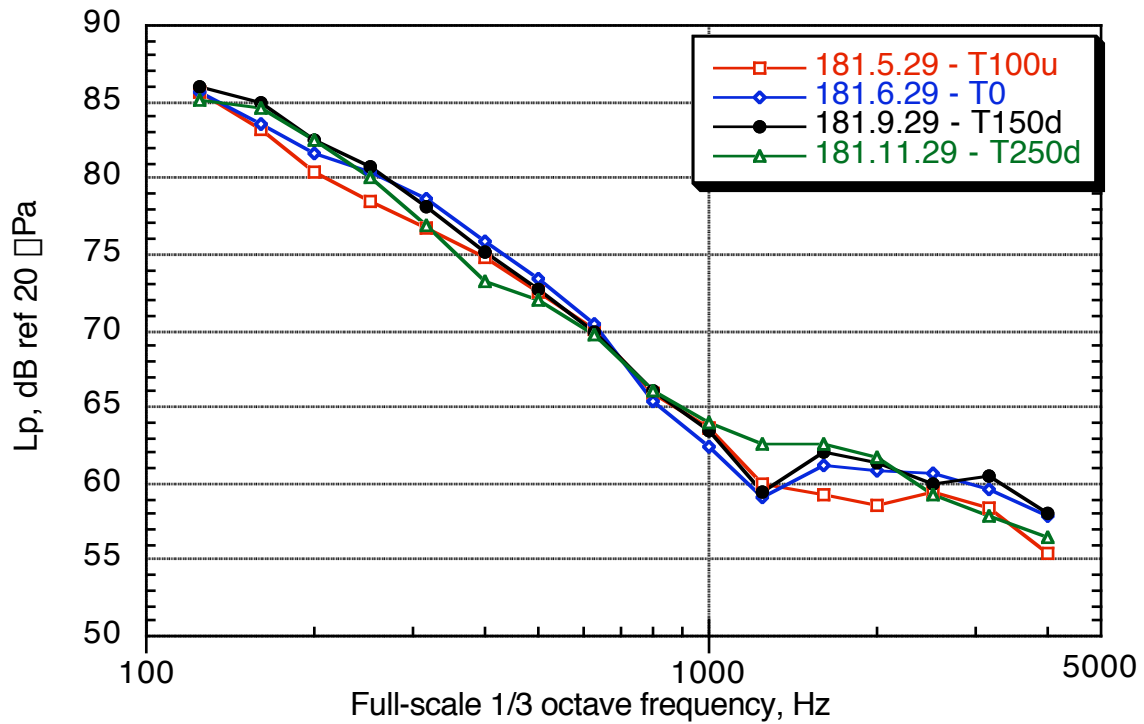


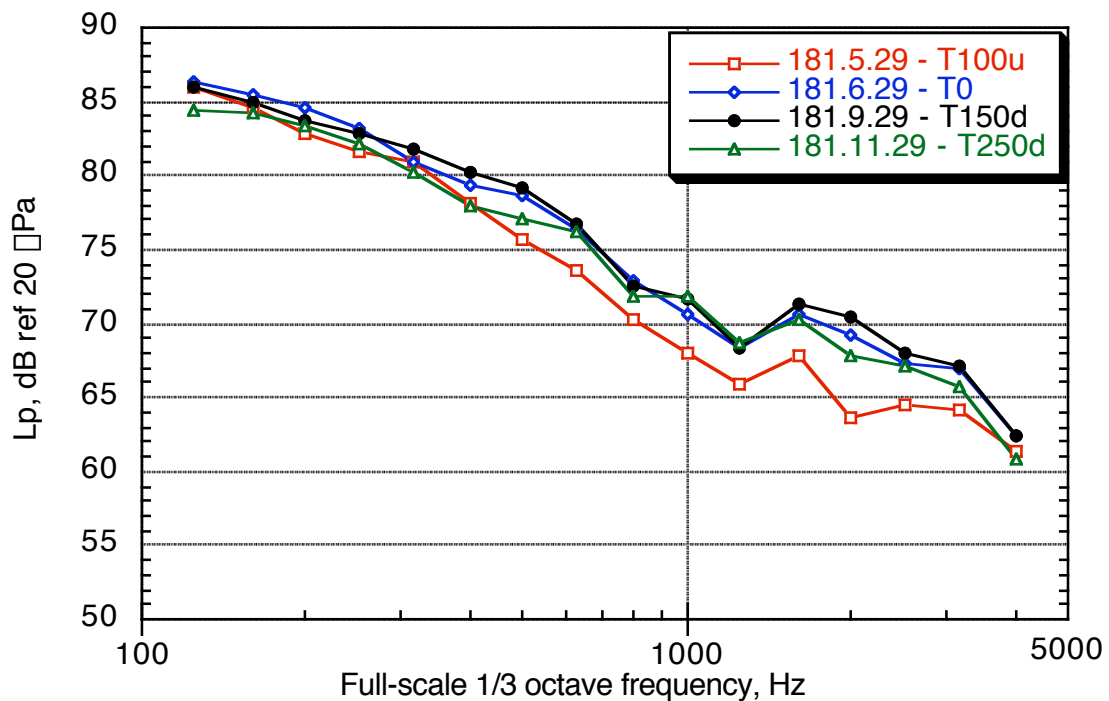
Figure 52. Upper-surface of the flaperon in landing configuration.



Figure 53. Gap between the flaperon and the outboard-flap.

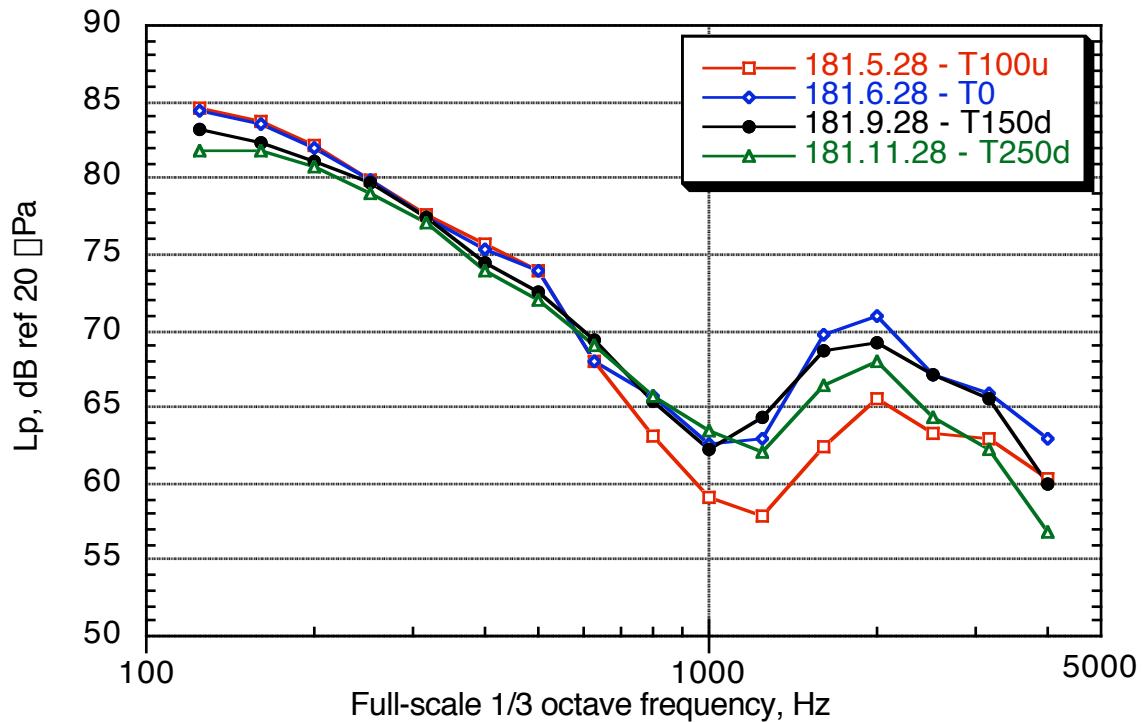


(a) OFOE.

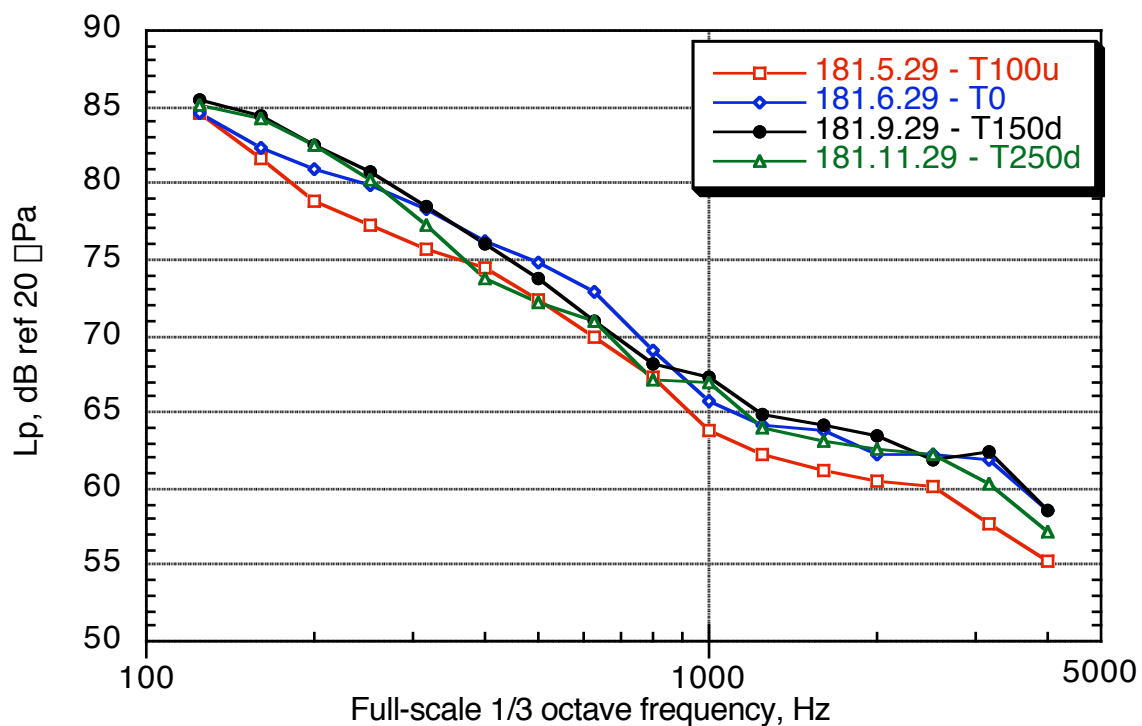


(b) Slat cove.

Figure 54. C35 array traverse,  $\alpha = 6^\circ$ , Mach 0.21.

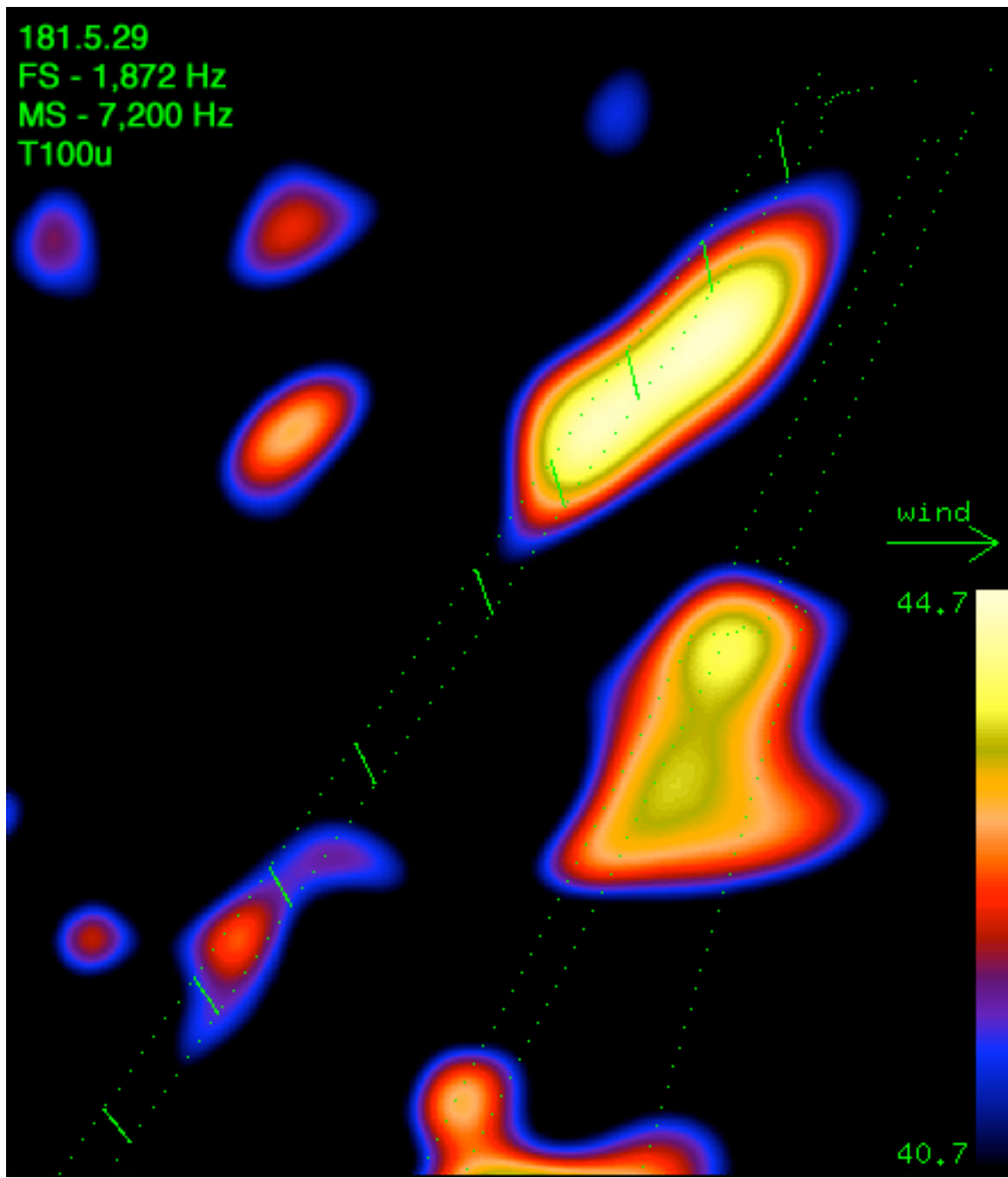


(c) OSIE.



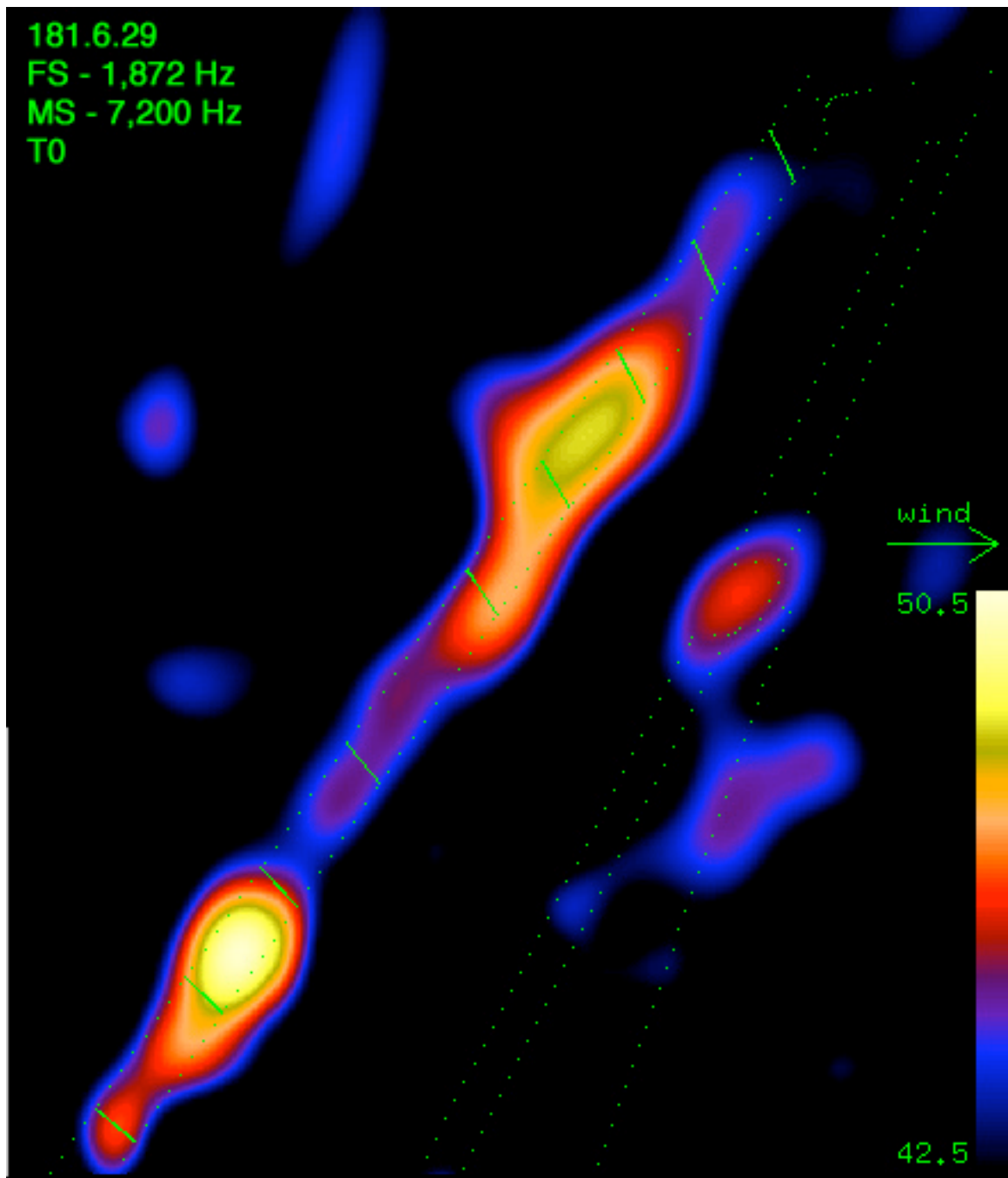
(d) OSOE.

Figure 54. Concluded.



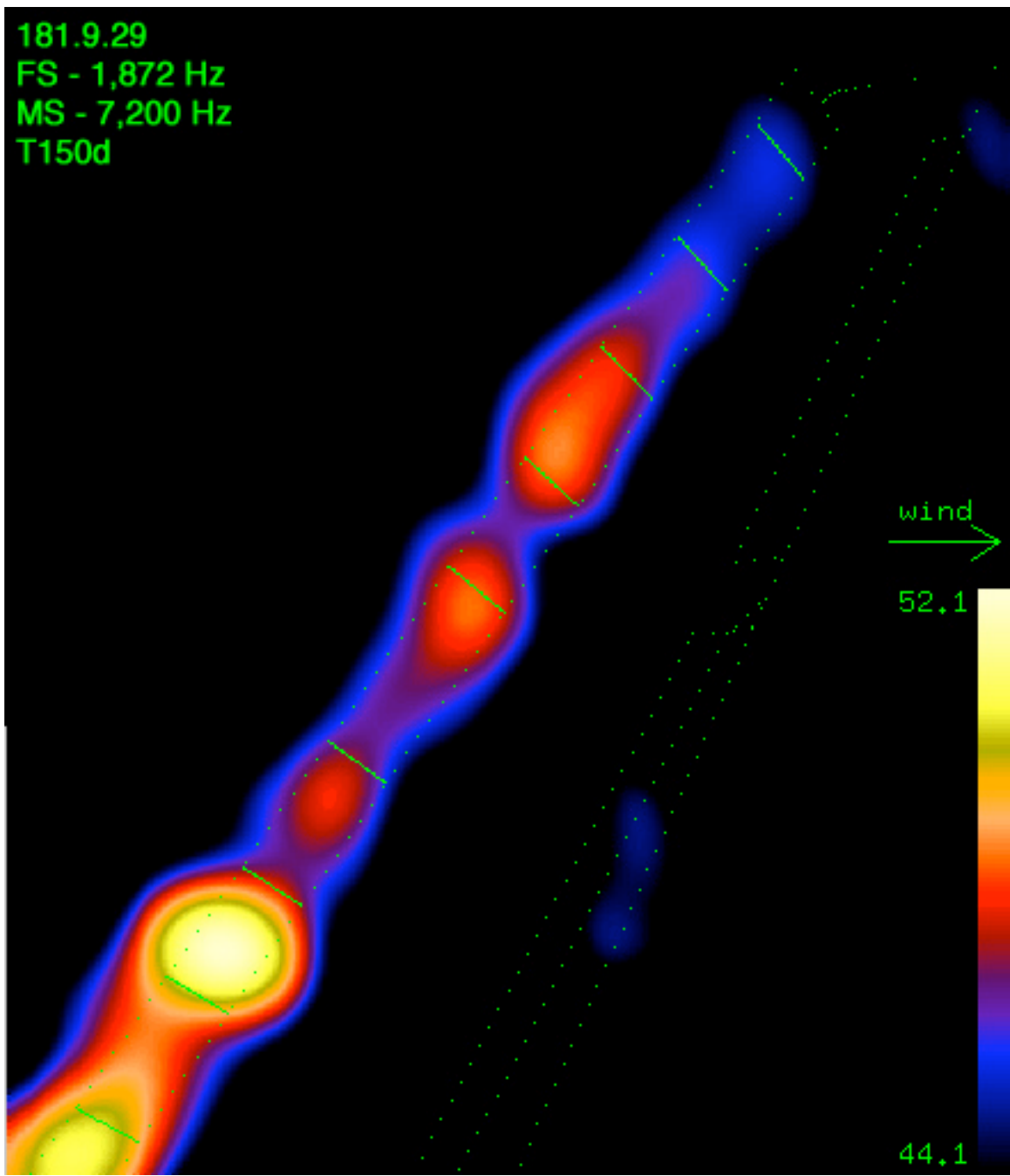
(a) T100u – note the 4 dB contour range.

Figure 55. Landing configuration C35 at 1,872 Hz.



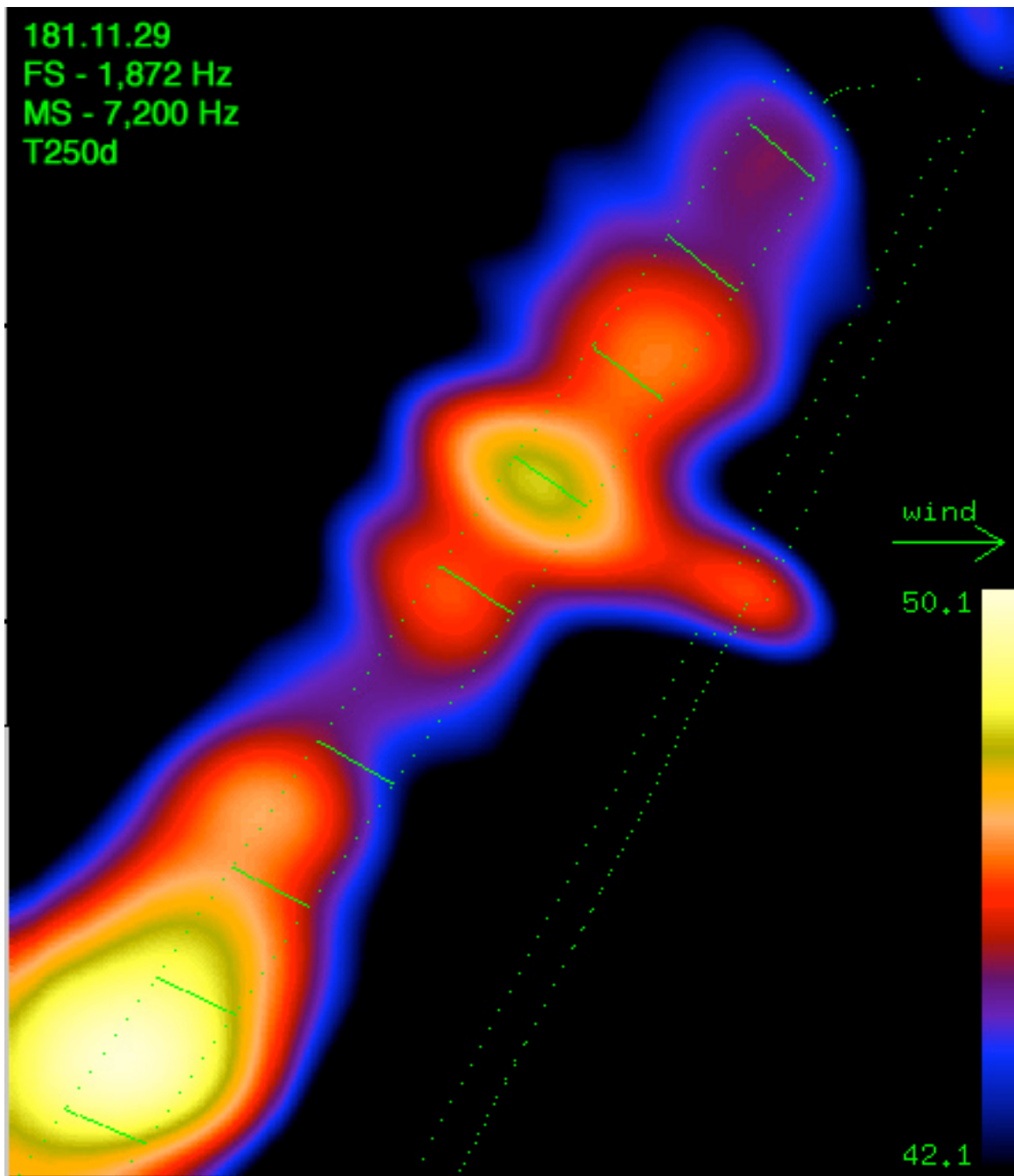
(b) T0.

Figure 55. Continued.



(c) T150d.

Figure 55. Continued.



(d) T250d.

Figure 55. Concluded.

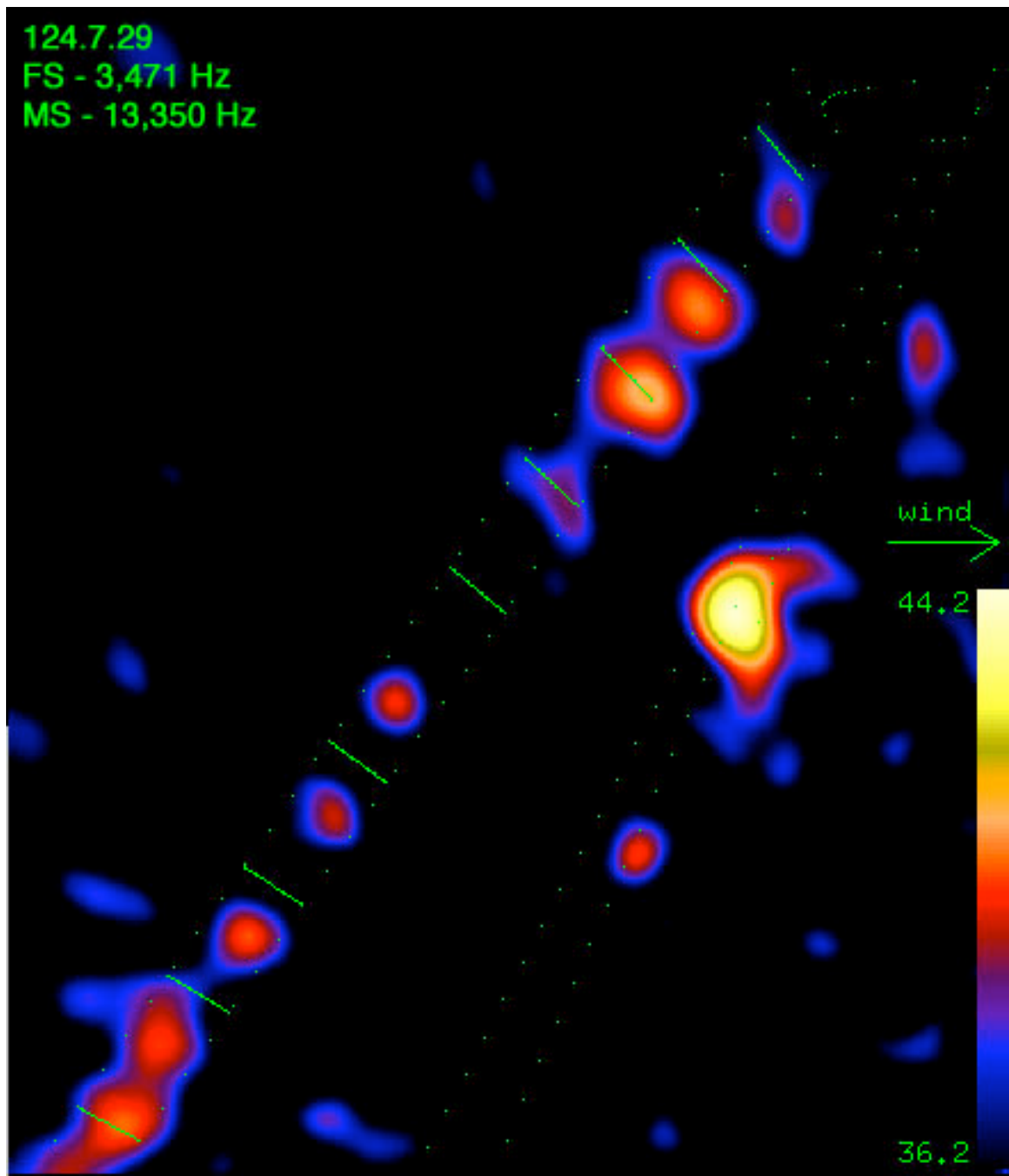
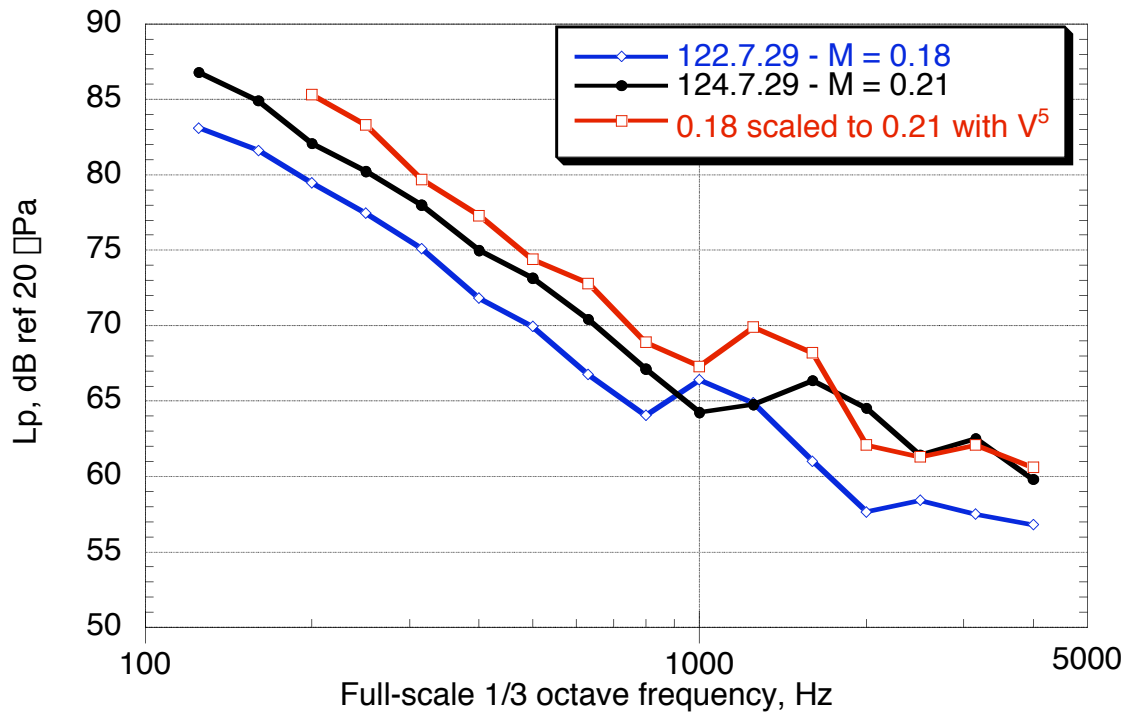
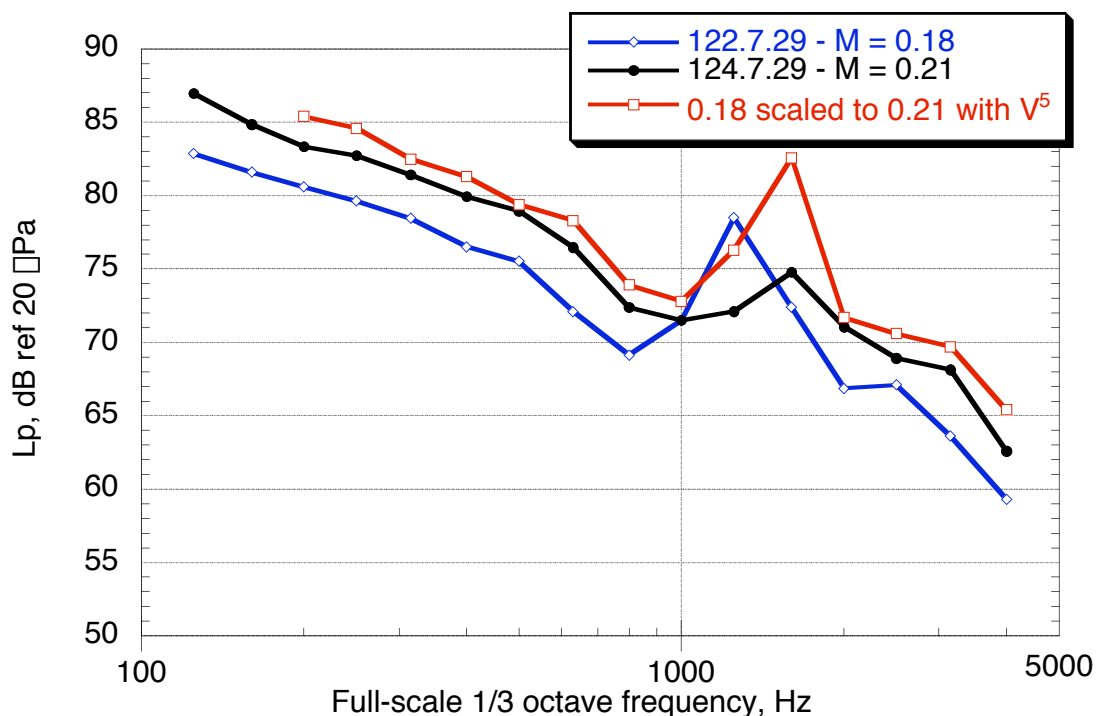


Figure 56. Approach baseline C14,  $\square = 6^\circ$ , T150d, 3,471 Hz.

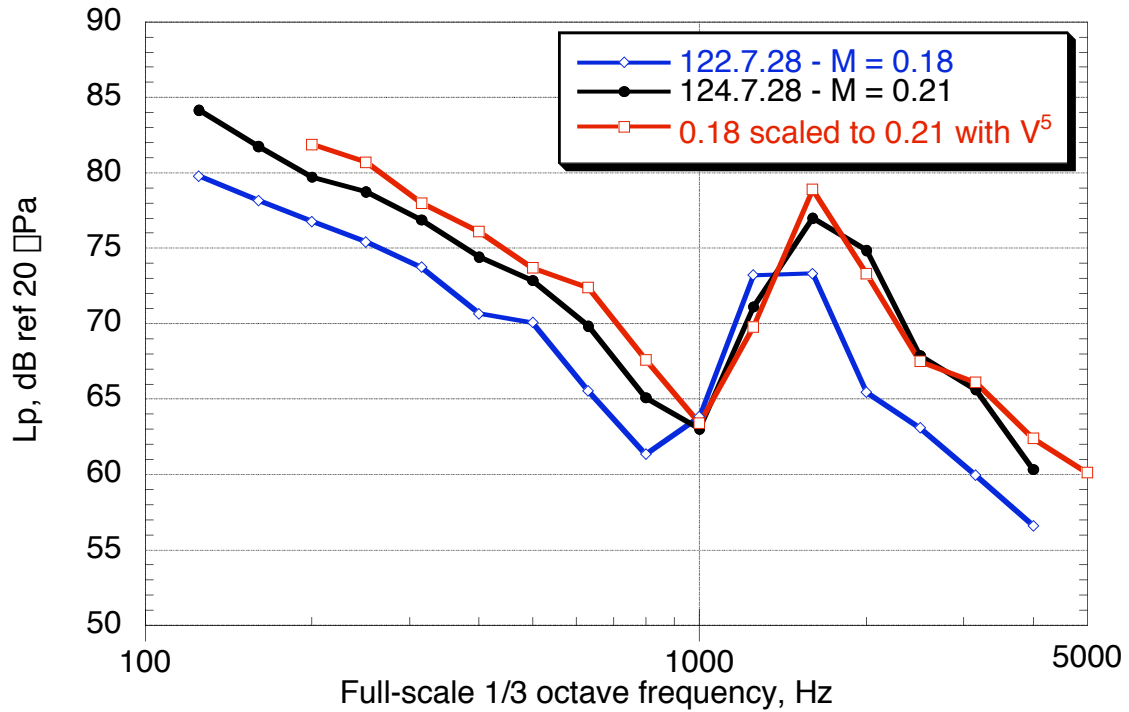


(a) OFOE.

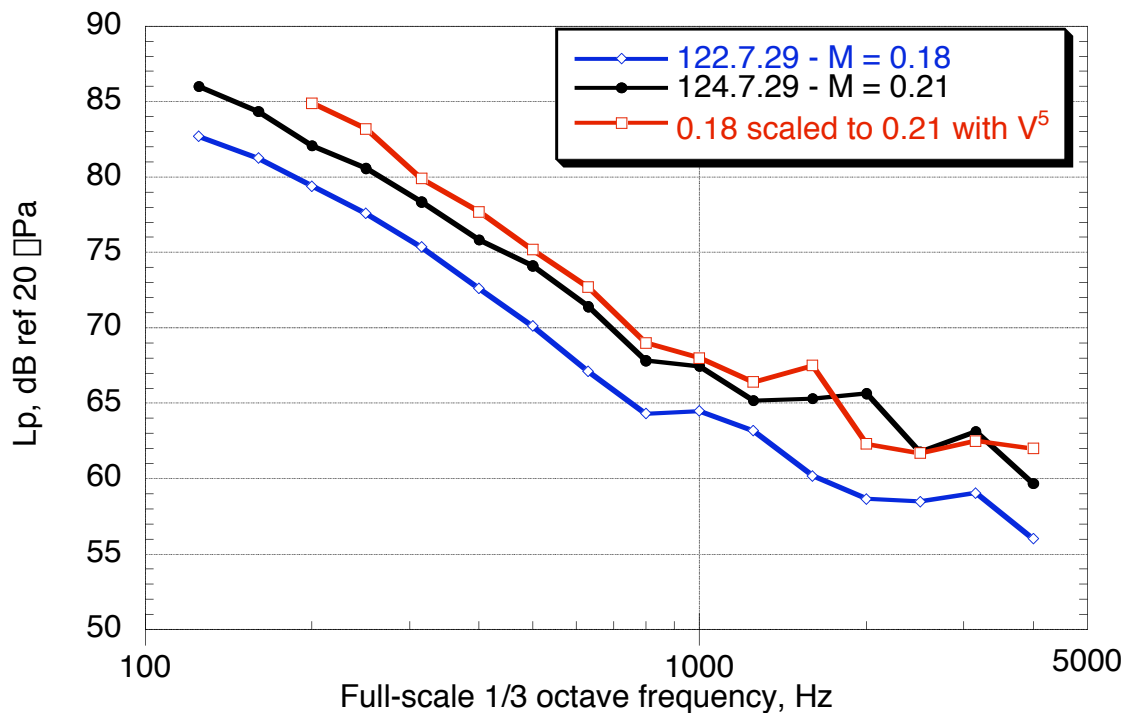


(b) Slat cove.

Figure 57. Mach variation in baseline-approach configuration C14.



(c) OSIE.



(d) OSOE.

Figure 57. Concluded.

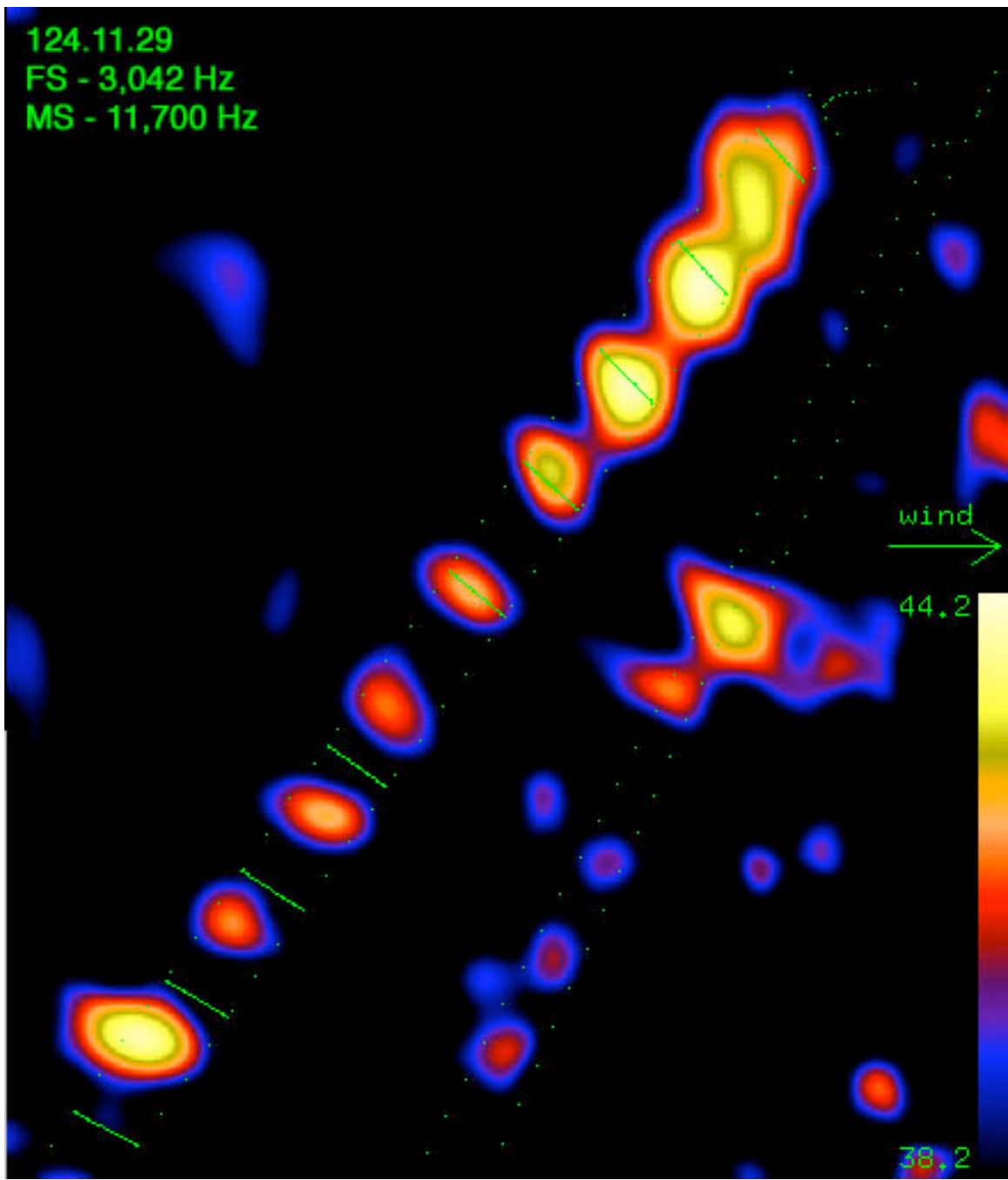
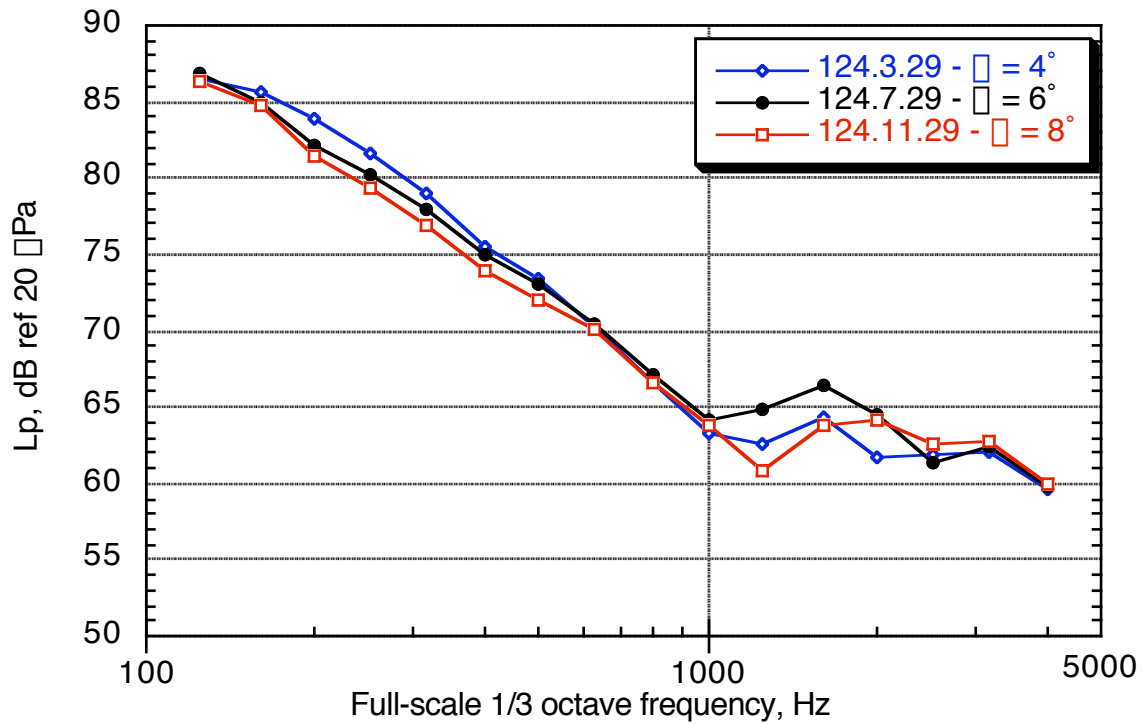
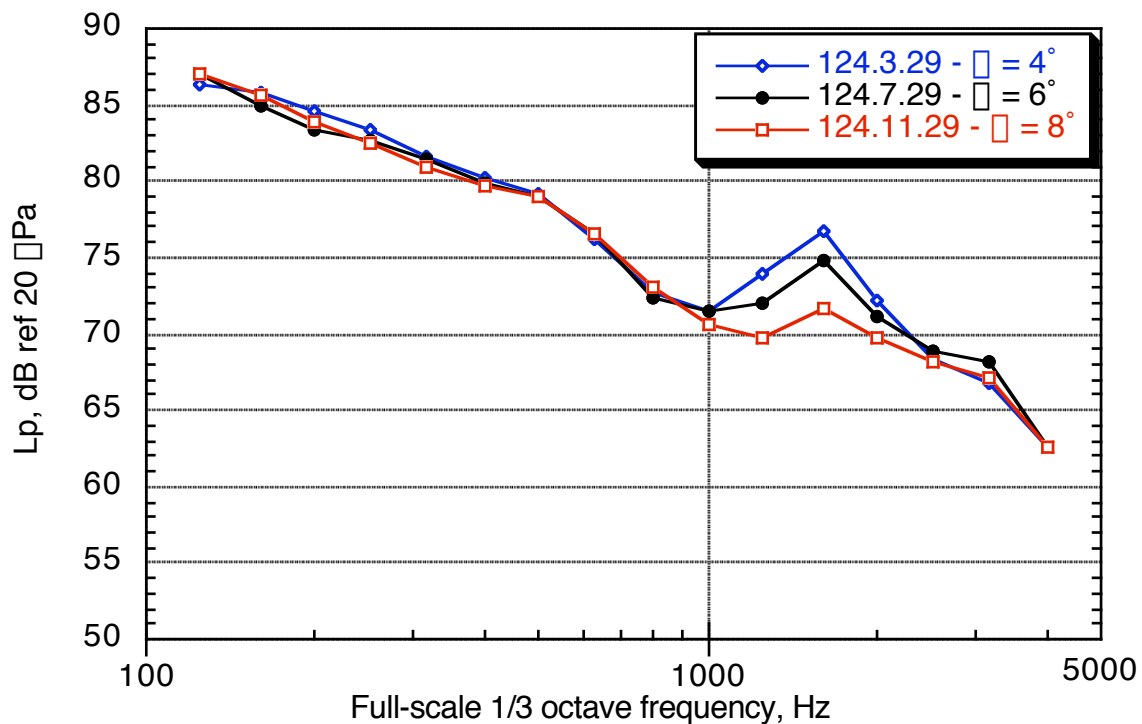


Figure 58. Approach configuration C14,  $\square = 8^\circ$ , T150d,  $M = 0.21$ .

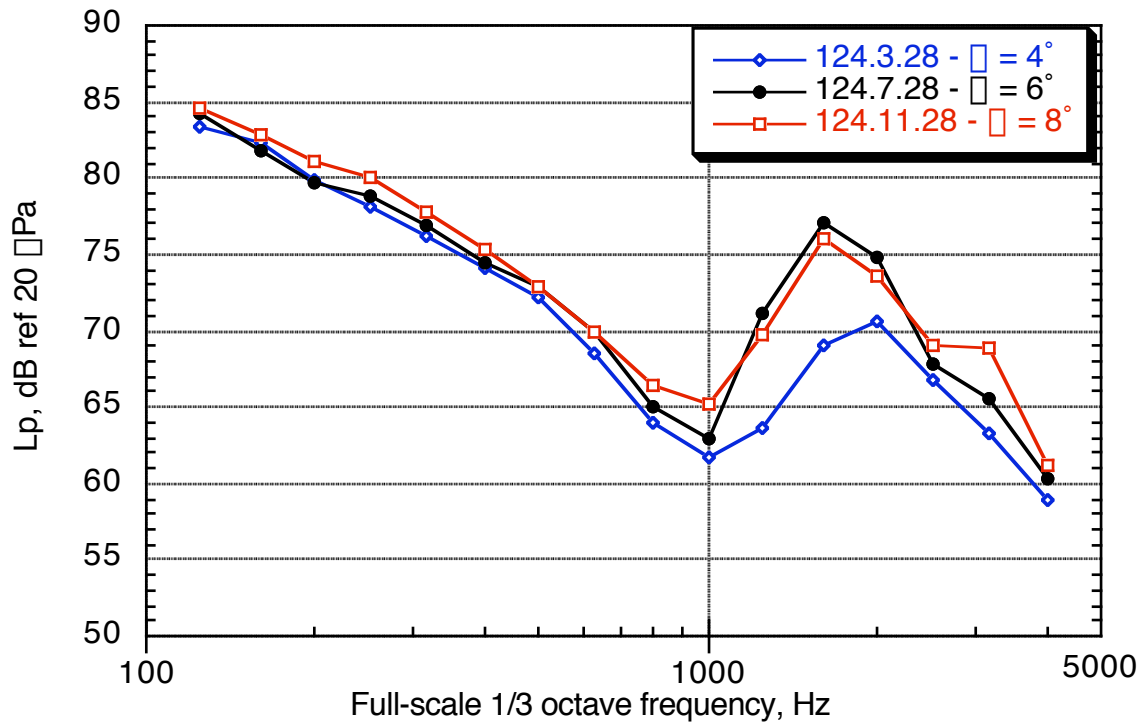


(a) OFOE.

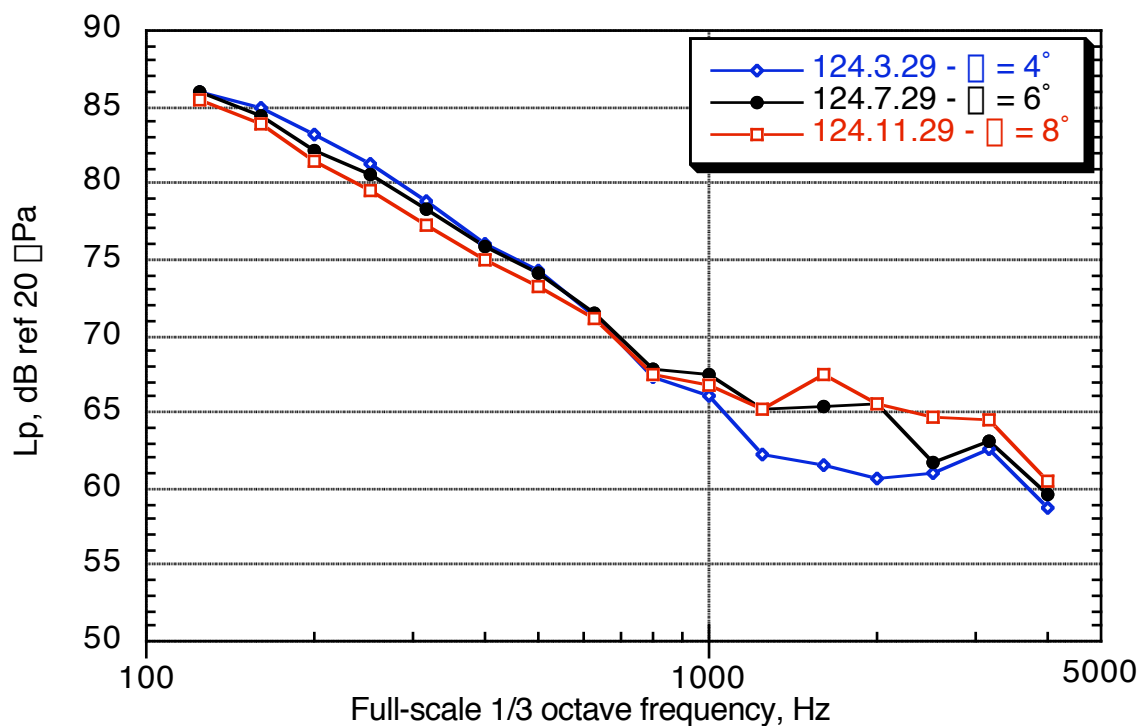


(b) Slat cove.

Figure 59. Angle-of-attack effect on baseline approach C14.

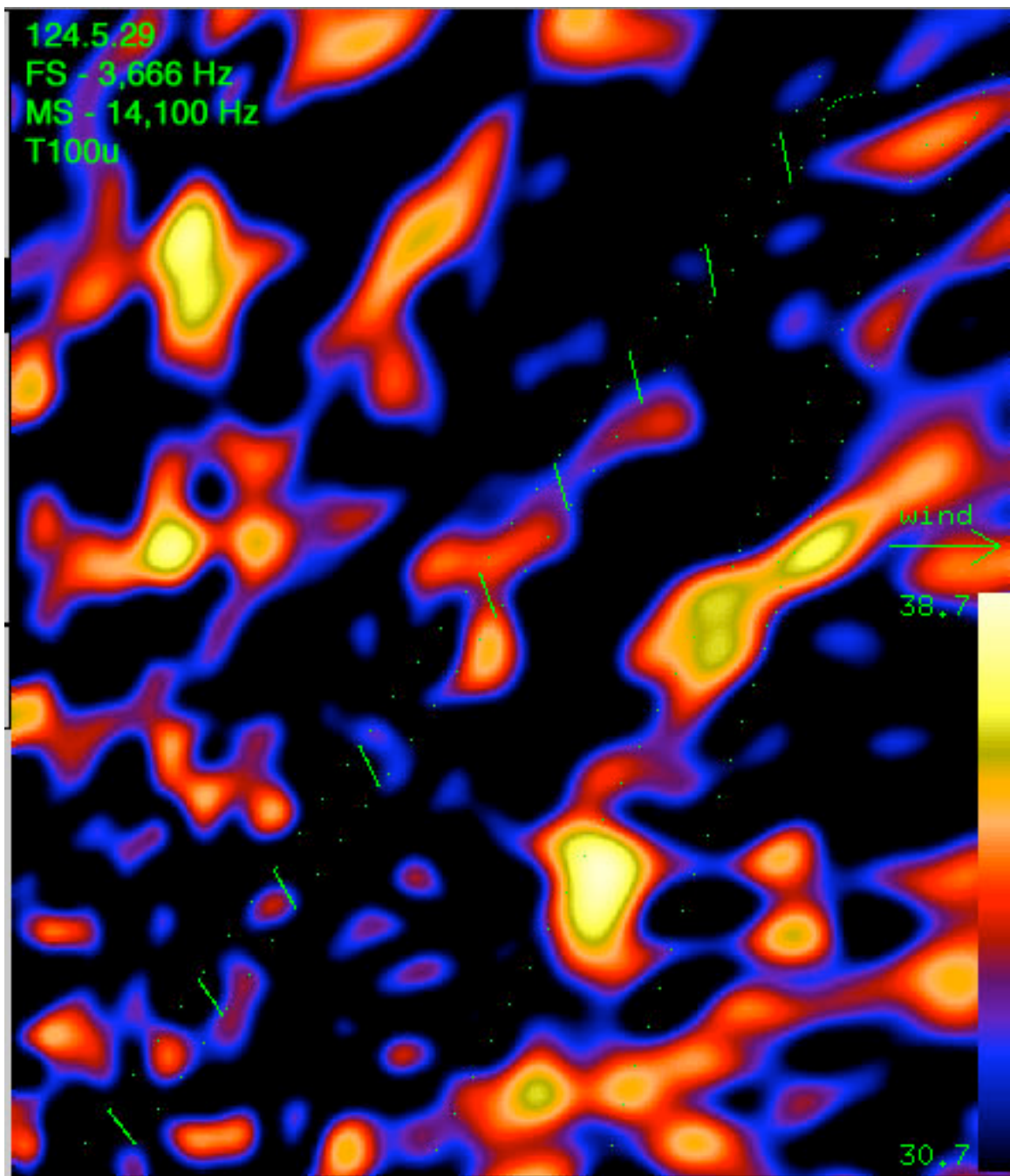


(c) OSIE.



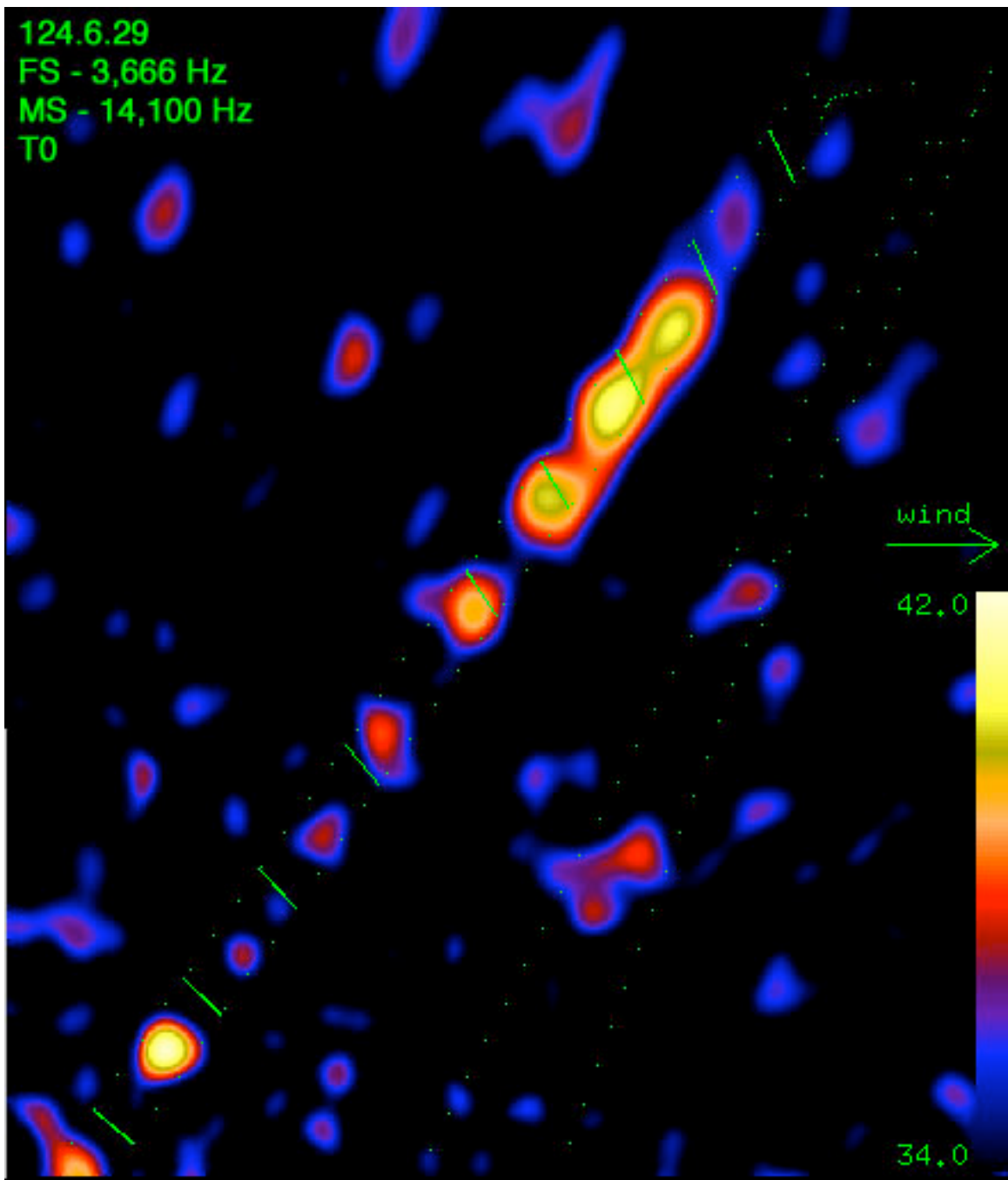
(d) OSOE.

Figure 59. Concluded.



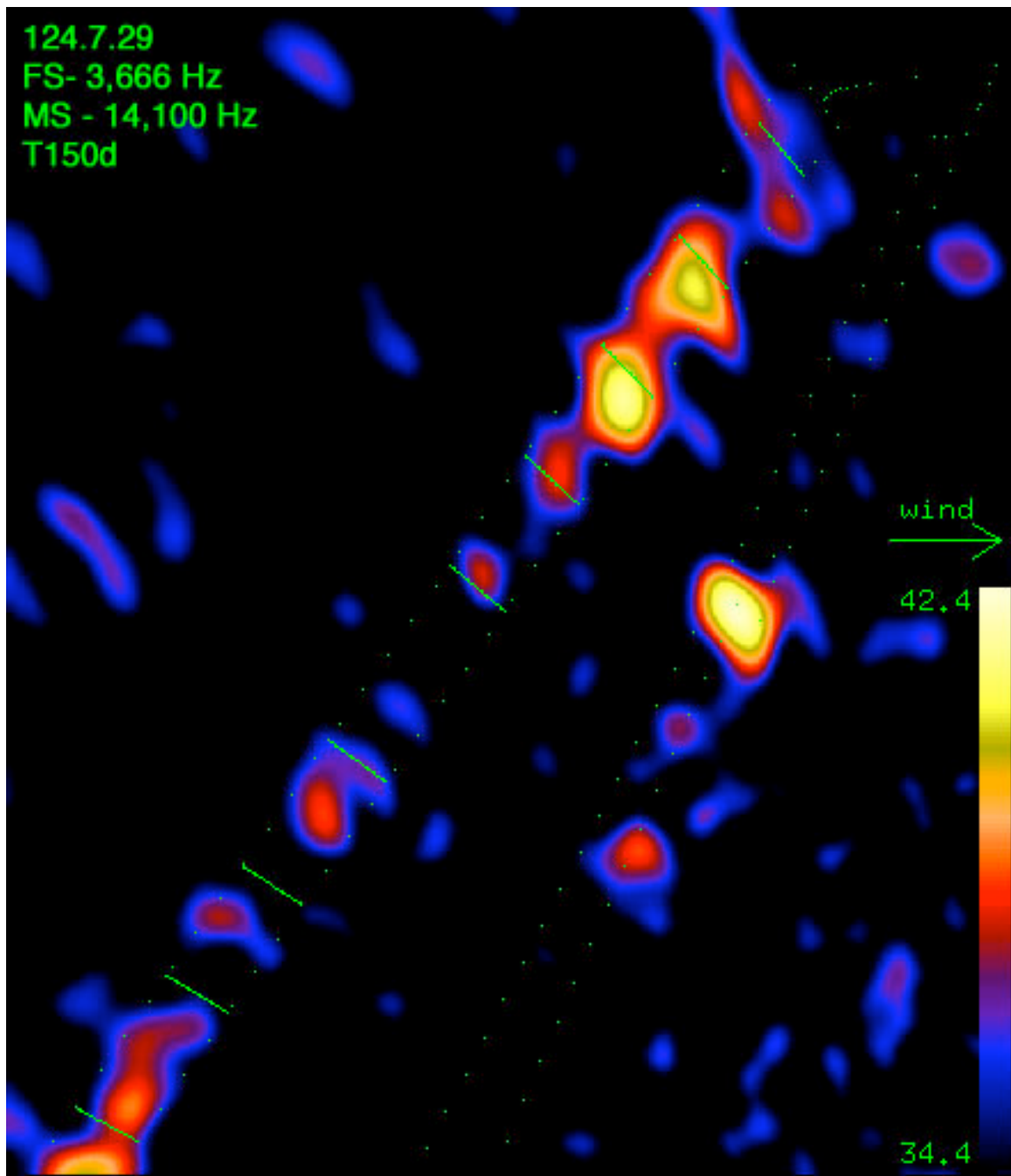
(a) T100u—Source map is cluttered with side lobes.

Figure 60. Baseline approach, 3,666 Hz,  $\square = 6^\circ$ ,  $M = 0.21$ .



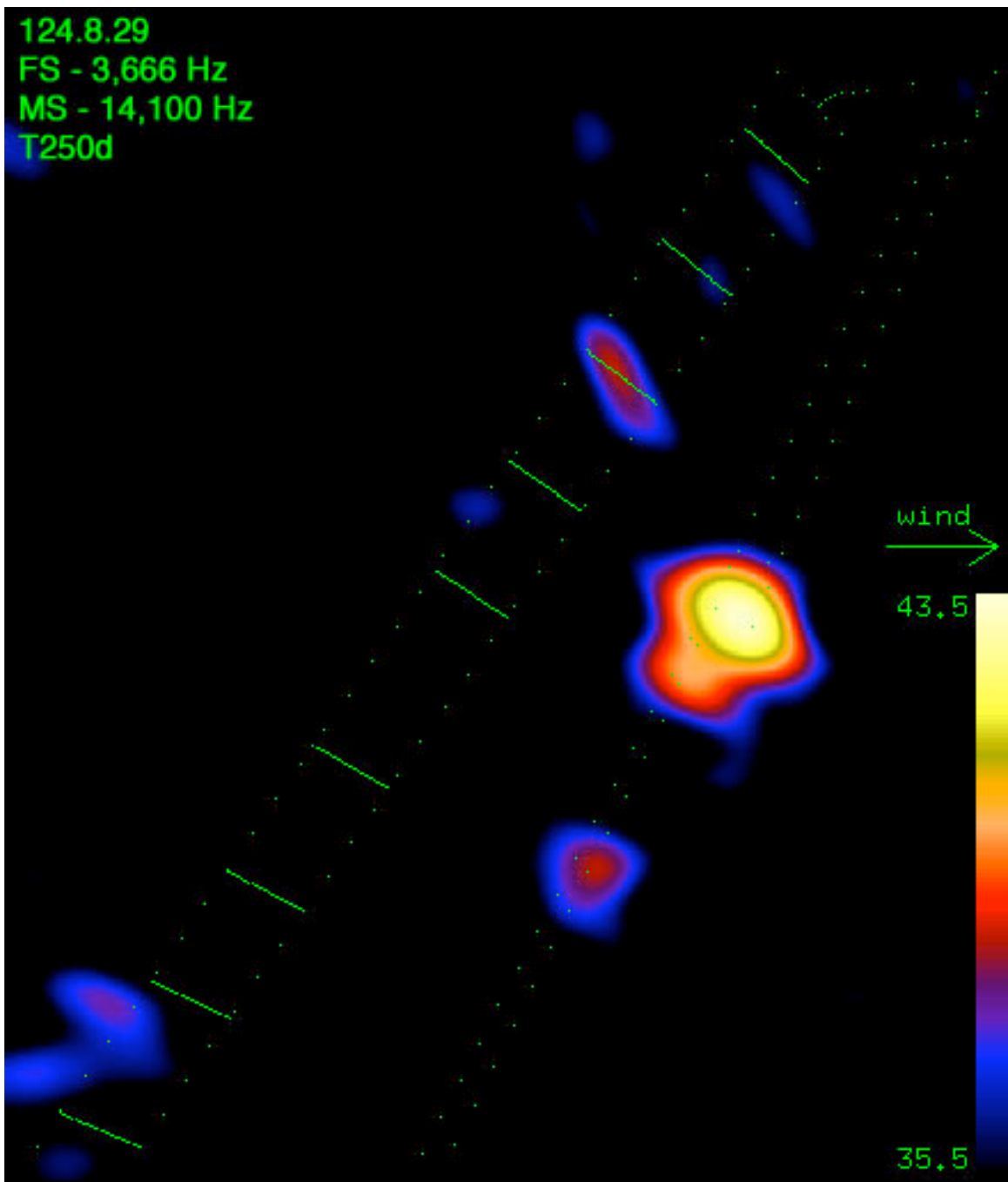
(b) T0.

Figure 60. Continued.



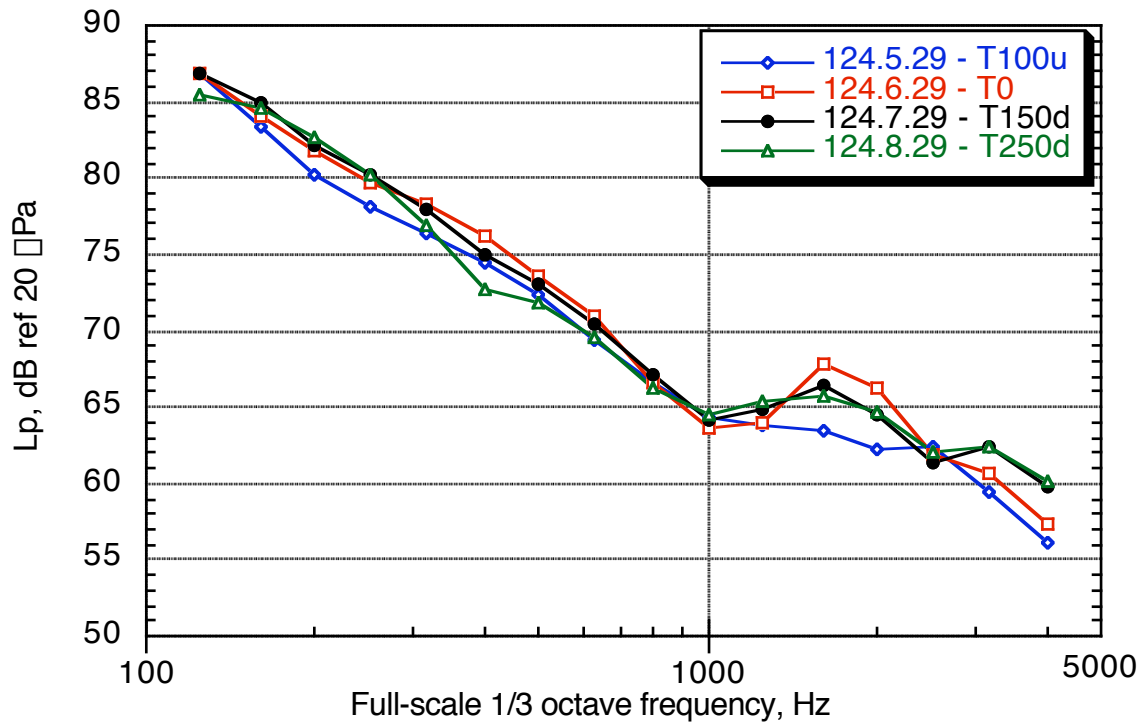
(c) T150d.

Figure 60. Continued.

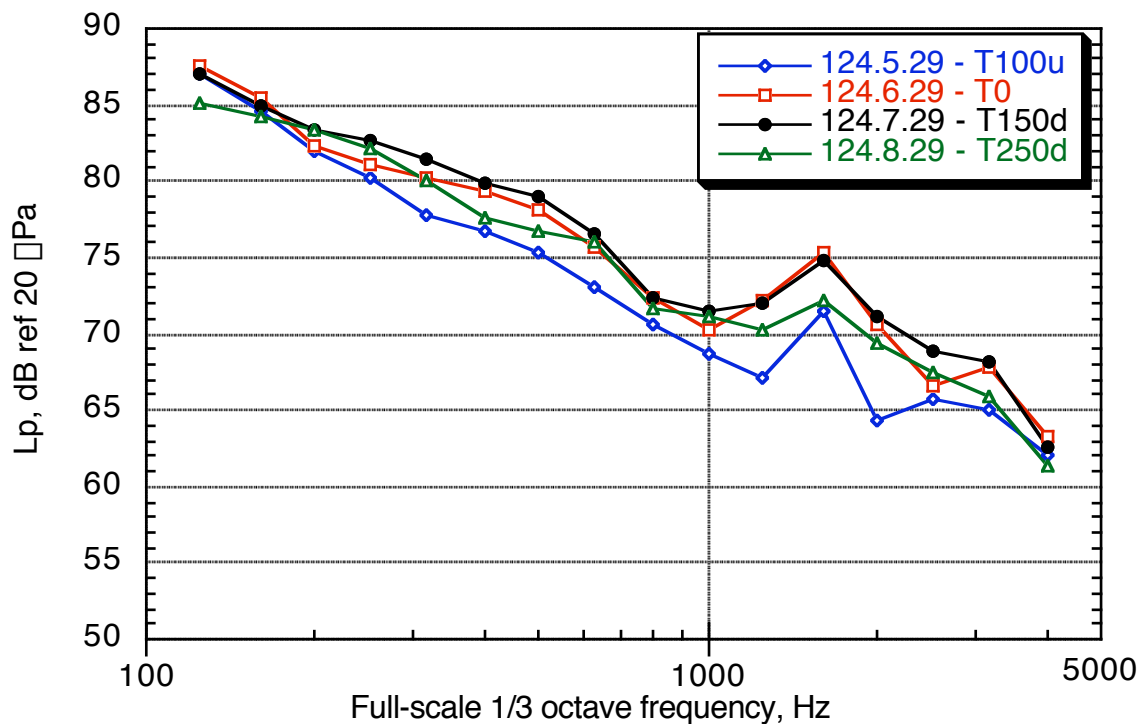


(d) T250d.

Figure 60. Concluded.

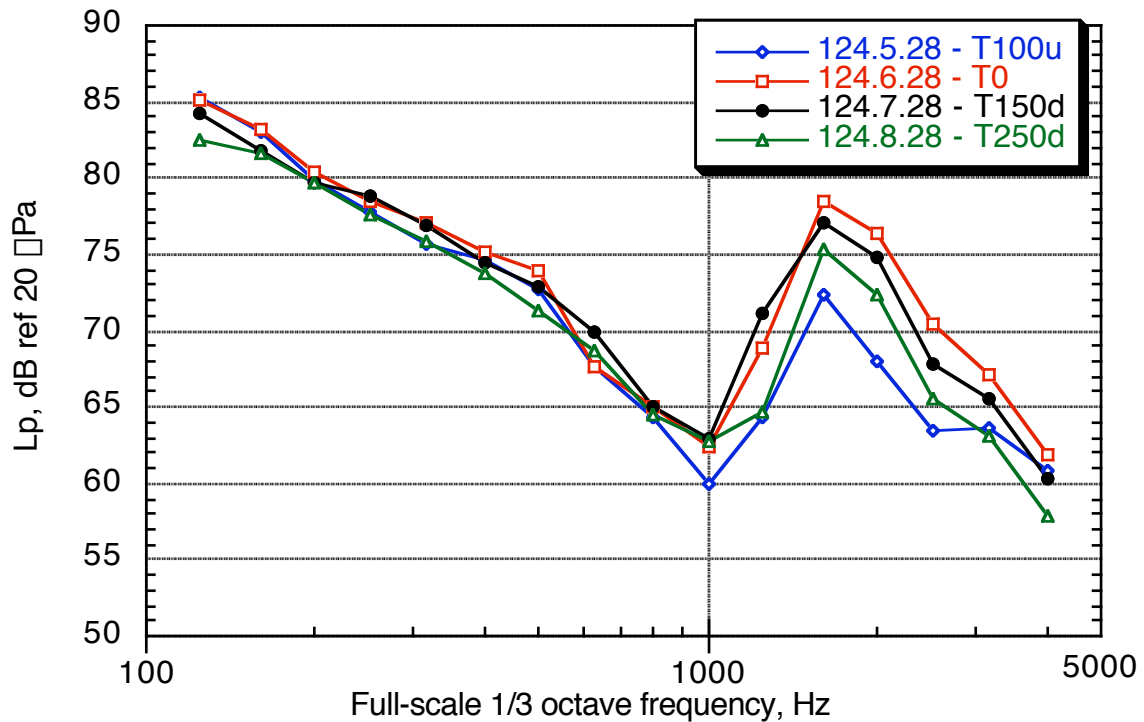


(a) OFOE.

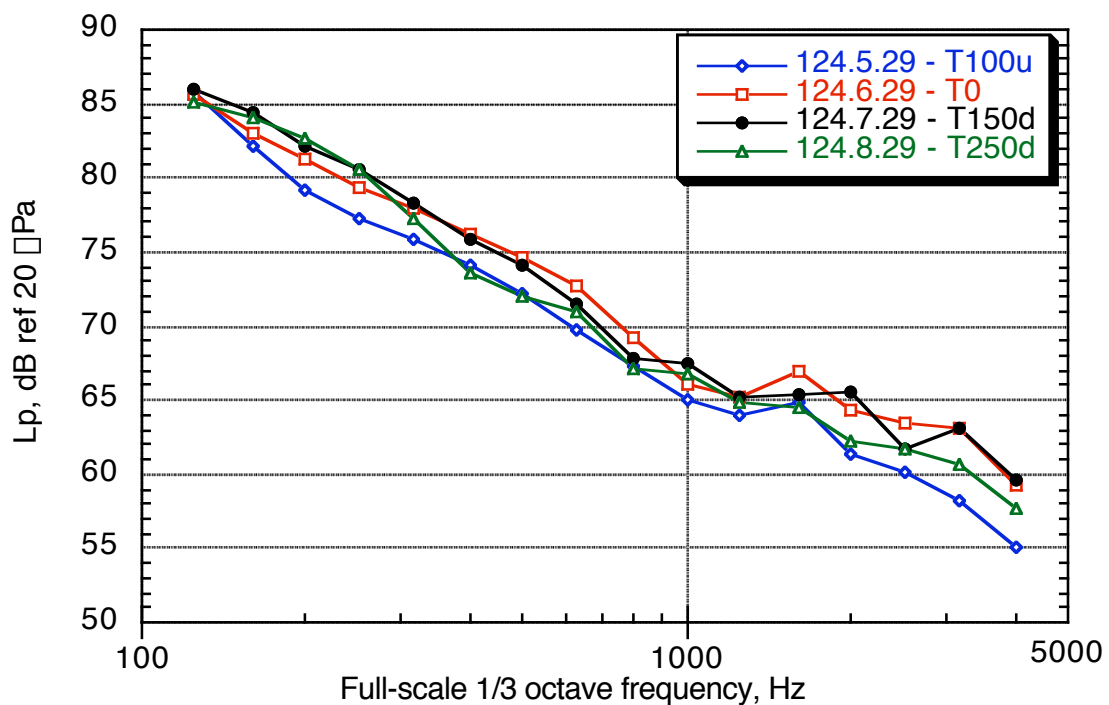


(b) Slat cove.

Figure 61. Baseline-approach configuration C14,  $\square = 6^\circ$ ,  $M = 0.21$ .



(c) OSIE.



(d) OSOE.

Figure 61. Concluded.



Figure 62. High-fidelity gear, view toward fuselage, flow from top to bottom; note inboard flap system in lower right corner. Torque link and wire harnesses are visible between middle tire and gear door.



Figure 63. High-fidelity gear, looking downstream and away from fuselage; inboard flap fairing is removed, tire treads untaped, lock links removed. Note brake links and rock guards on truck lower surface (flaps removed).



Figure 64. Simple-geometry gear with door, simple side braces and lock links, looking downstream; wheel hub cover plates are also installed.

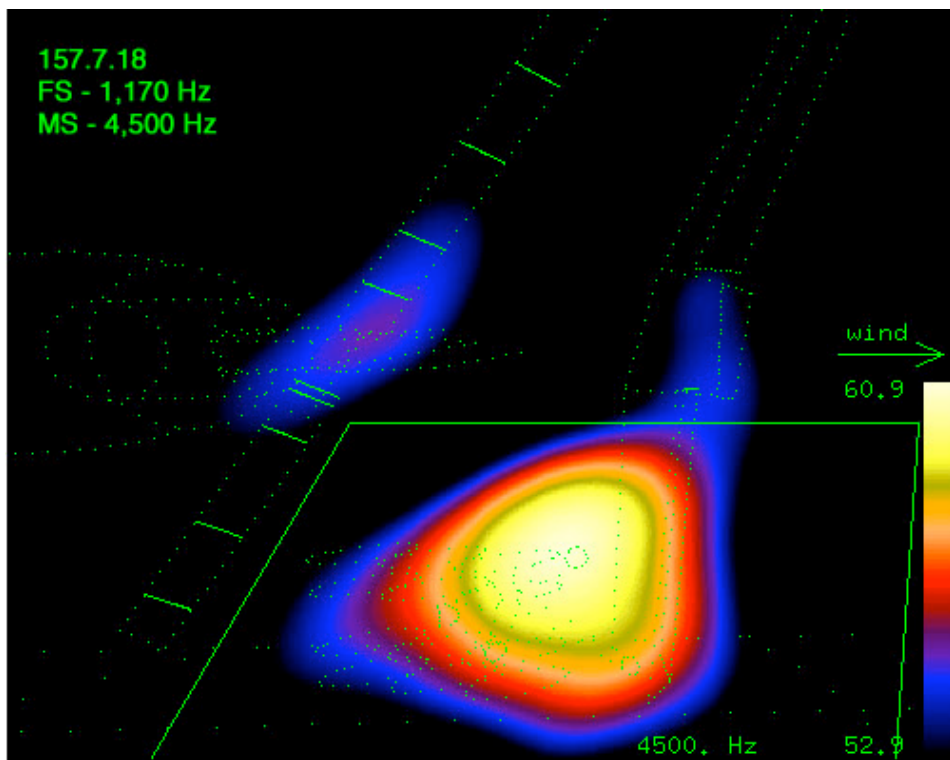


Figure 65. Source location plot for scan region 18; scan plane near lower wheel surface.

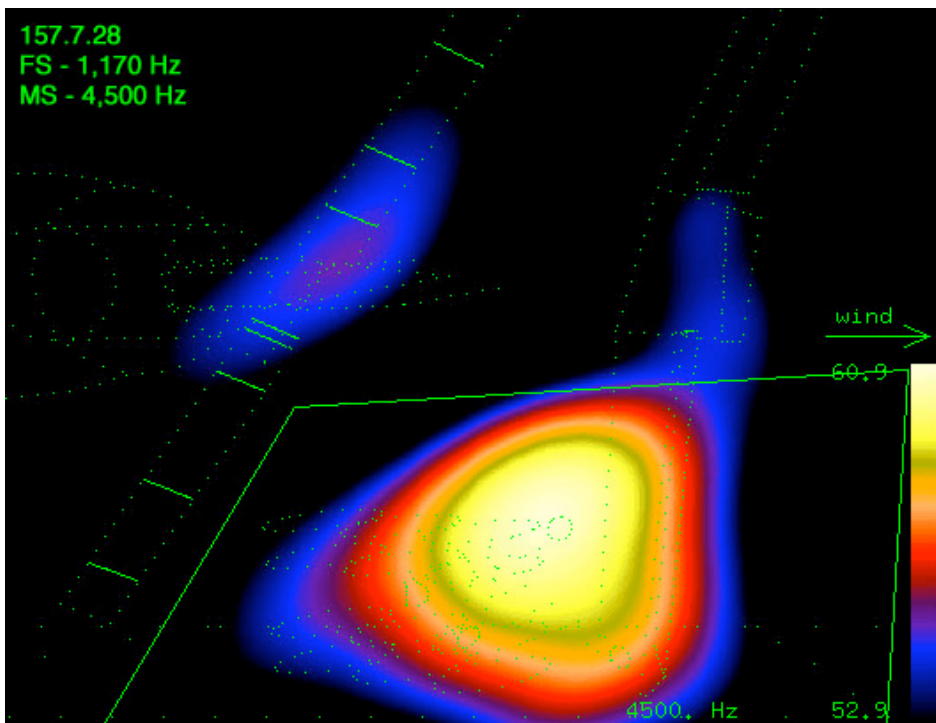


Figure 66. Source location map for landing gear region, scan region 28, coincident with wing plane.

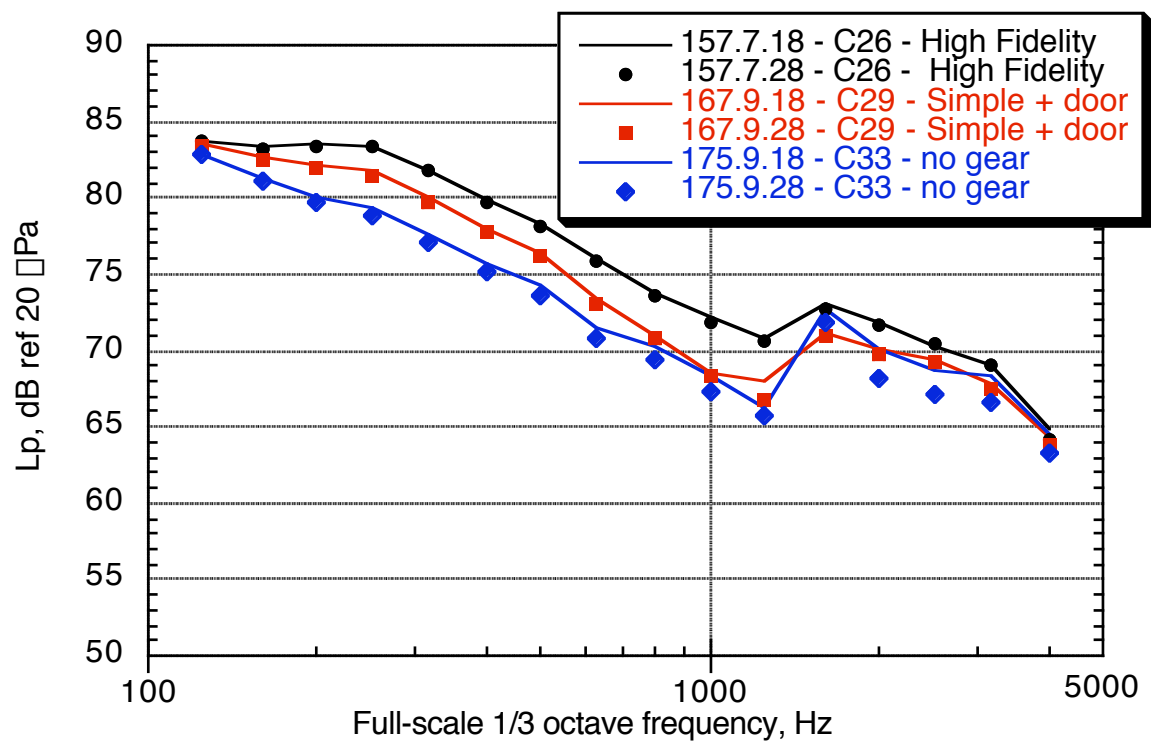


Figure 67. Comparison of integrated levels (scan region 18 and 28) for three configurations: no gear, simple gear with door, and high-fidelity gear:  $M = 0.21$ ,  $\alpha = 6^\circ$ , traverse = 150 in. downstream.

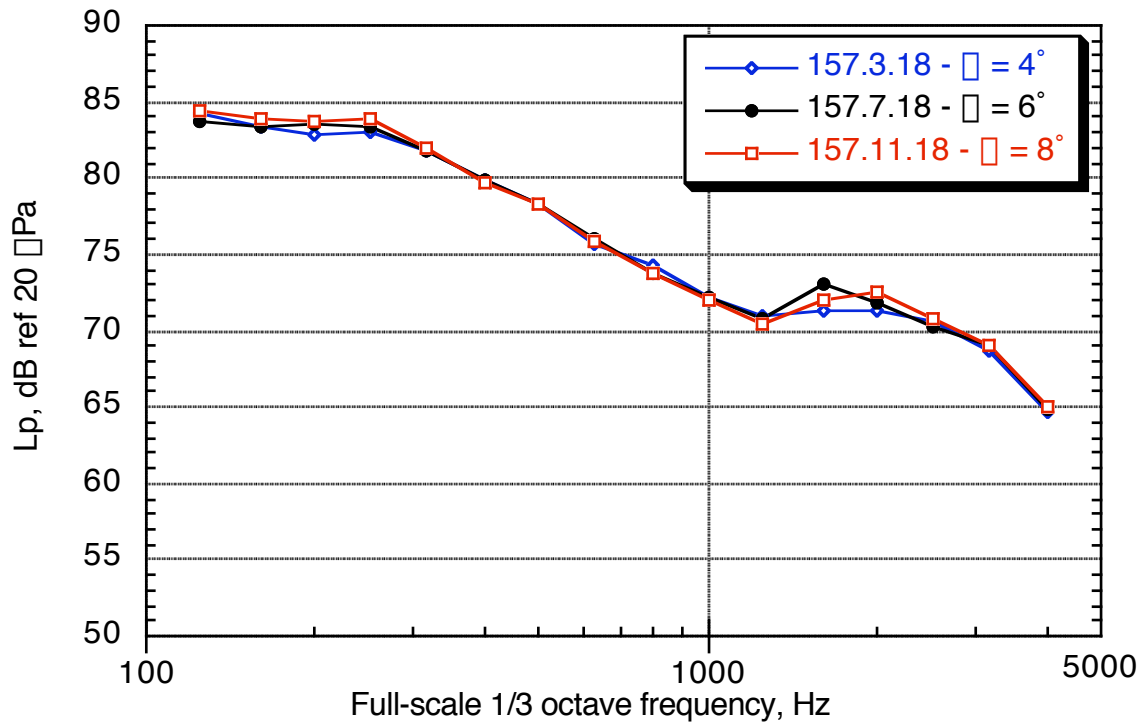


Figure 68. Effect of angle of attack on high-fidelity gear noise:  $M = 0.21$ , traverse = 150 in. downstream, scan region 18.

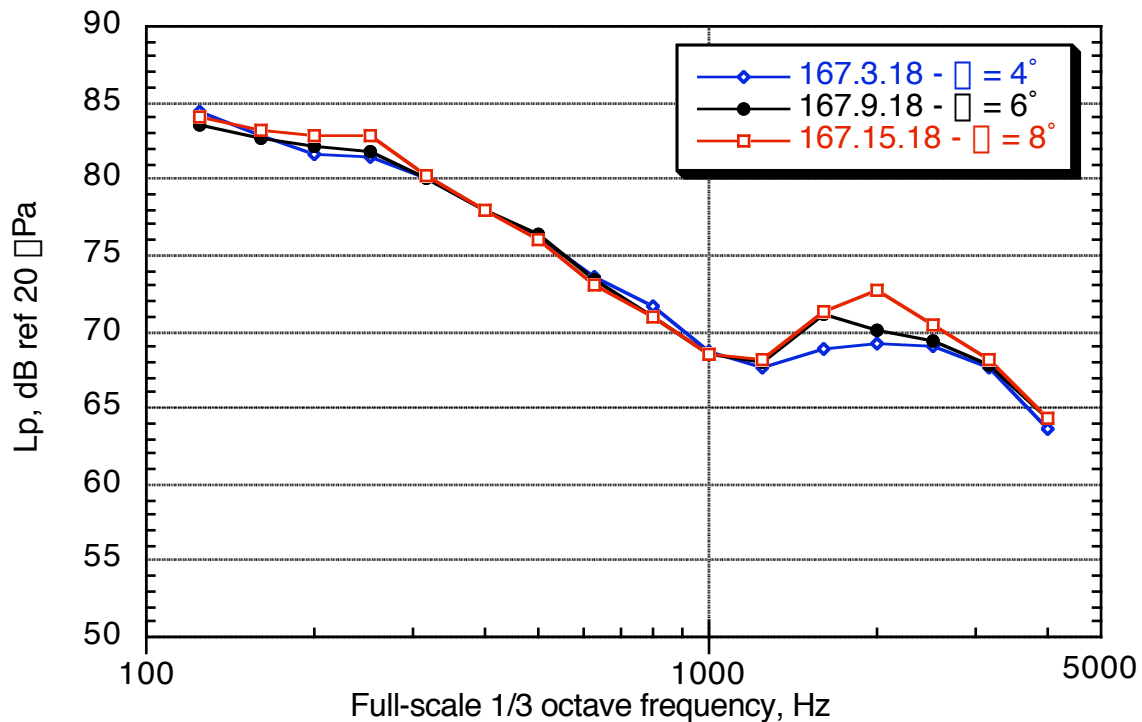


Figure 69. Effect of angle of attack variation on integrated gear noise (simple geometry with door):  $M = 0.21$ , traverse = 150 in. downstream, scan region 18.

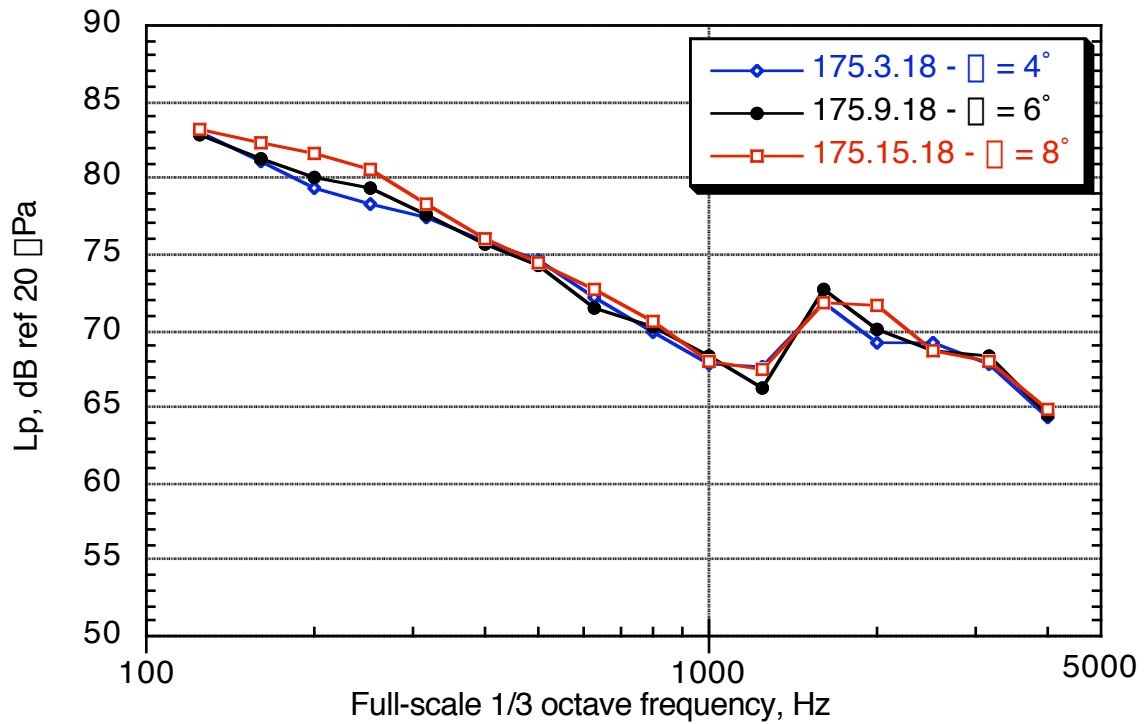


Figure 70. Effect of angle of attack variation on integrated noise from gear region with gear removed and cavity sealed:  $M = 0.21$ , traverse = 150 in. downstream, scan region 18.

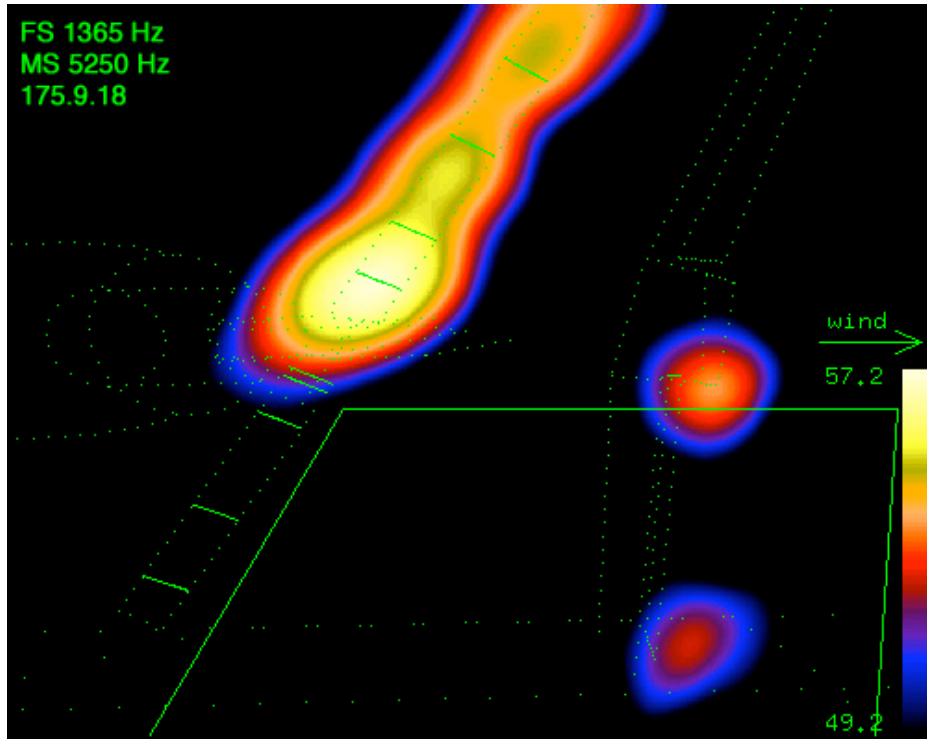


Figure 71. Source location plot with gear removed; notice the inboard flap noise in landing gear region.

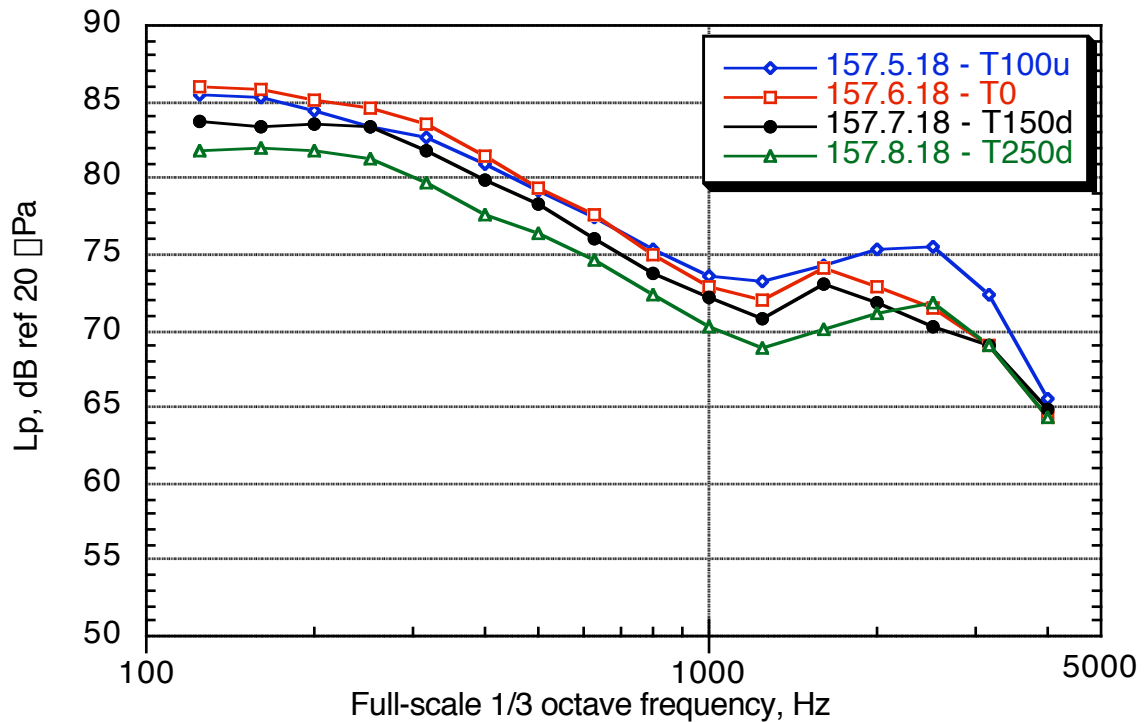


Figure 72. Variation of noise from high-fidelity gear with traverse position:  $M = 0.21$ ,  $\theta = 6^\circ$ , scan region 18.

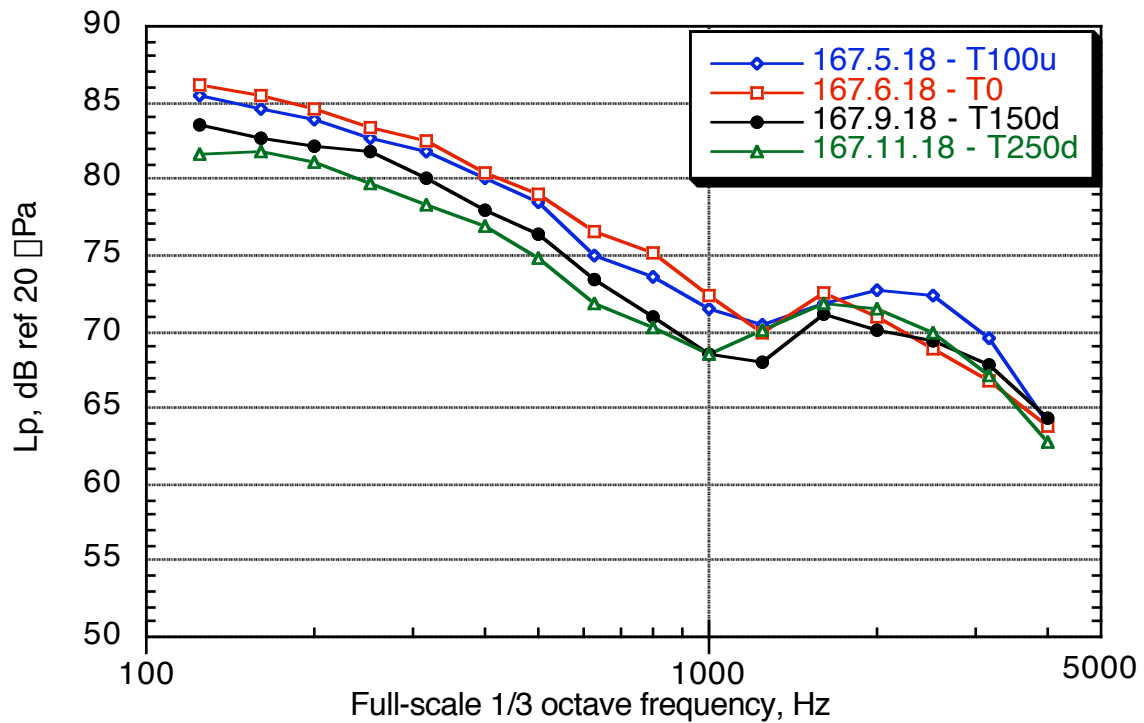


Figure 73. Variation of noise from simple-geometry gear with traverse position:  $M = 0.21$ ,  $\theta = 6^\circ$ , scan region 18.

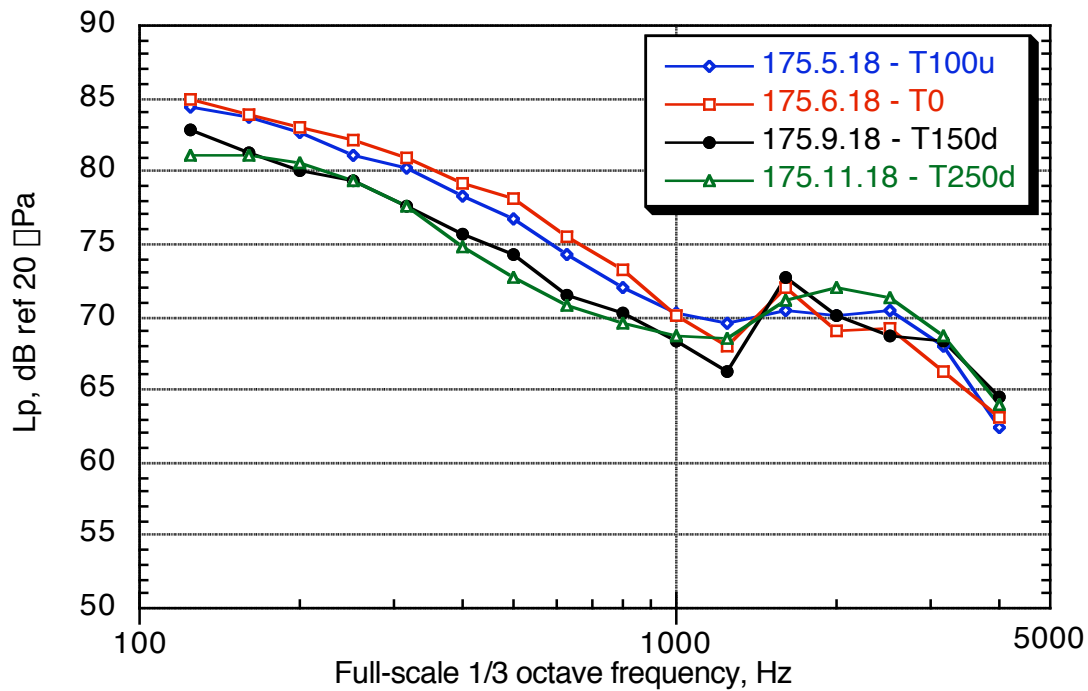


Figure 74. Variation of noise from landing gear region (gear removed, cavity sealed) with traverse position:  $M = 0.21$ ,  $\alpha = 6^\circ$ , traverse sweep, scan region 18.

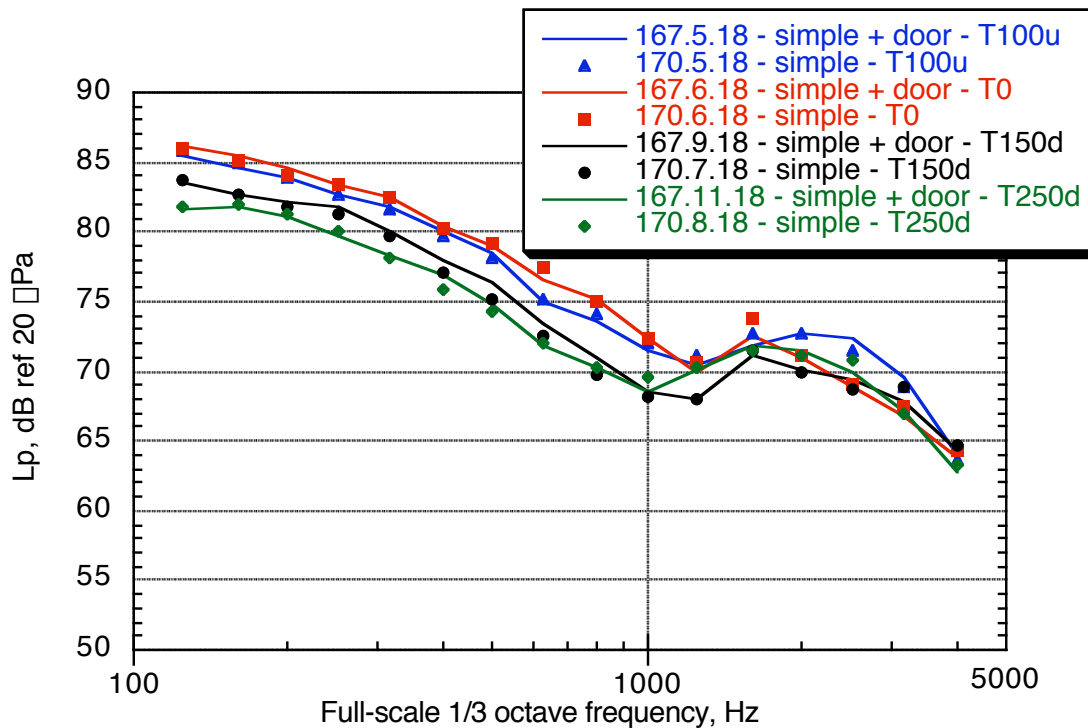


Figure 75. Variation of noise from simple-geometry gear with traverse position:  $M = 0.21$ ,  $\alpha = 6^\circ$ , traverse = 100 in. upstream, 0 in., 150 in. downstream, 250 in. downstream, scan region 18.

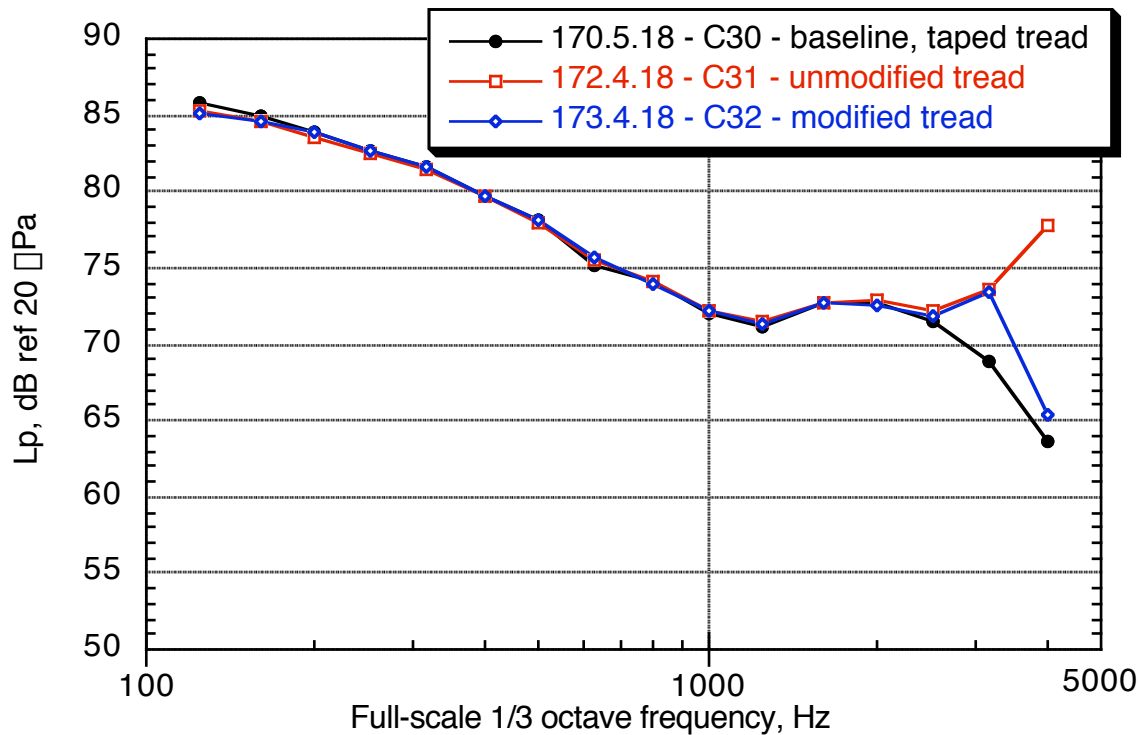


Figure 76. Effect of tire tread treatment, simple-geometry gear with doors removed:  $M = 0.21$ ,  $\Delta = 6^\circ$ , traverse = 100 in. upstream.

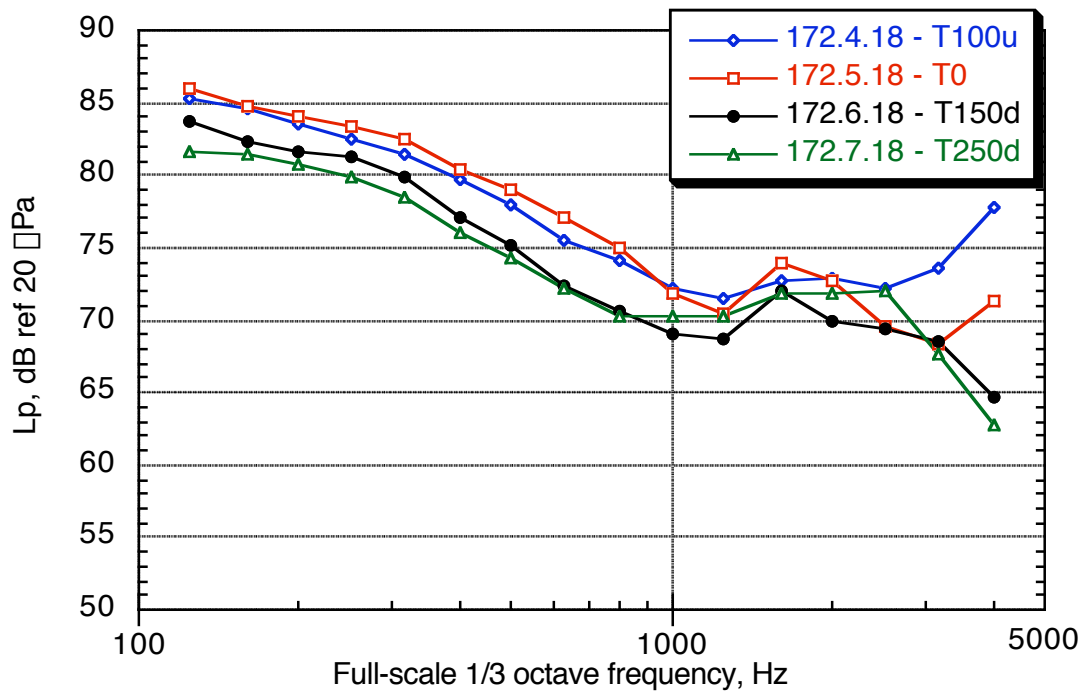
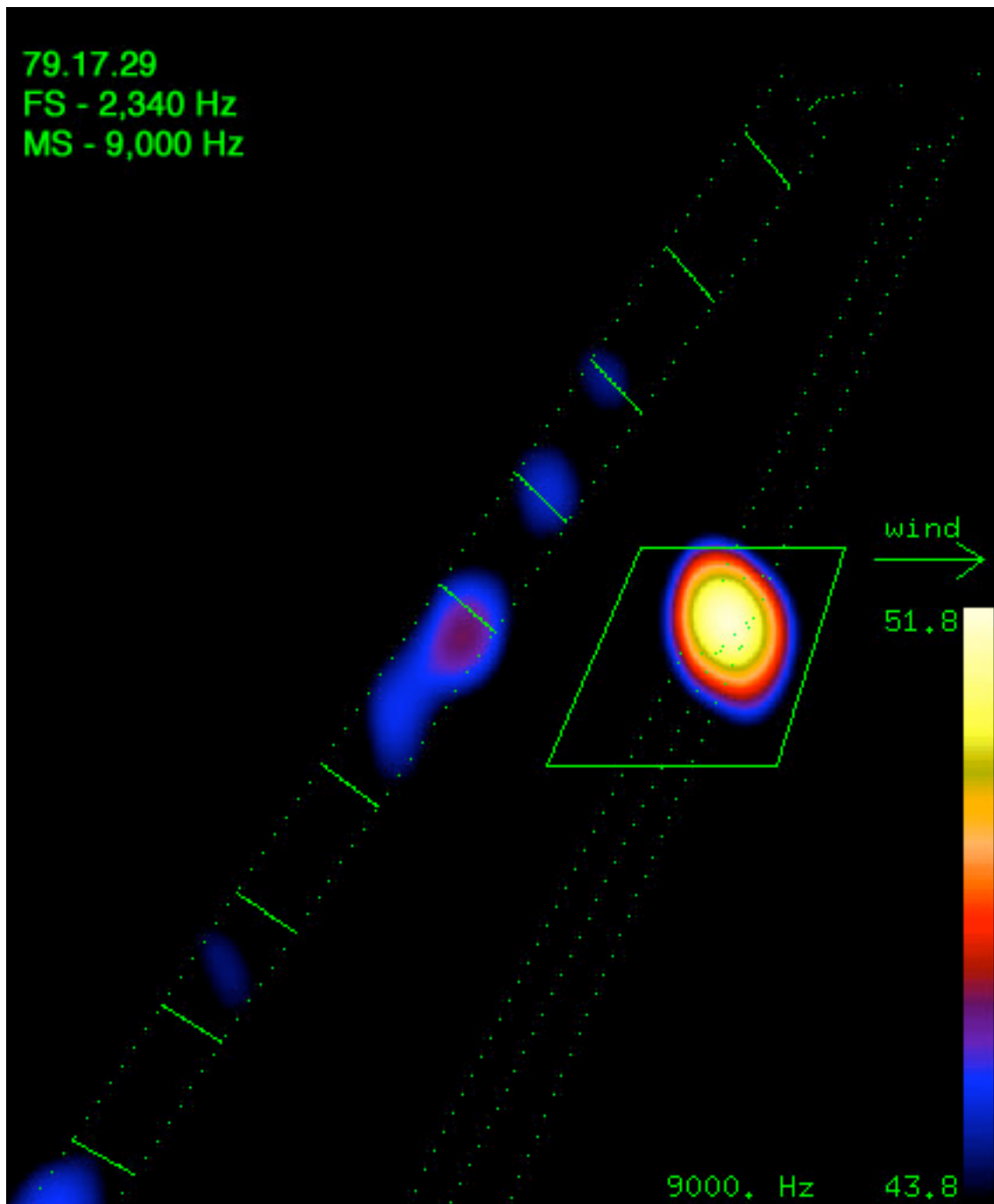
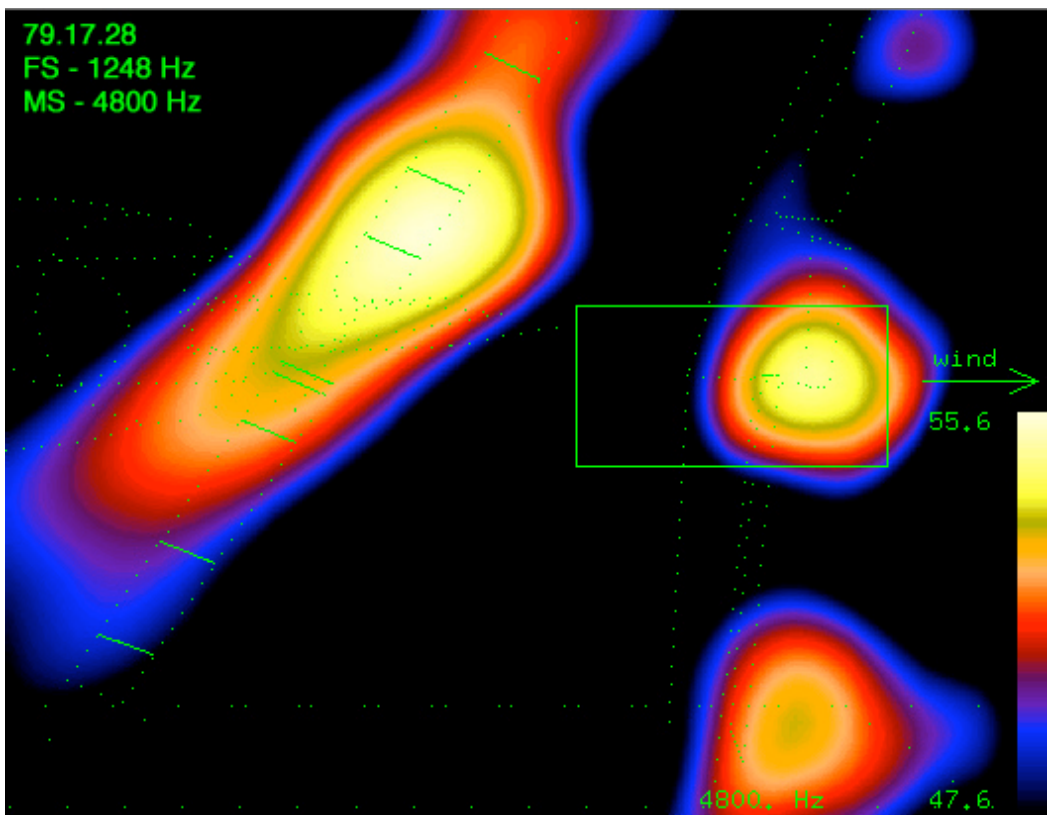


Figure 77. Traverse study of simple-geometry gear, no doors, unmodified tire tread,  $M = 0.21$ ,  $\Delta = 6^\circ$ .



(a) Outboard-flap outboard-edge (OFOE) integration region.

Figure 78. Source location plot with flap integration regions.

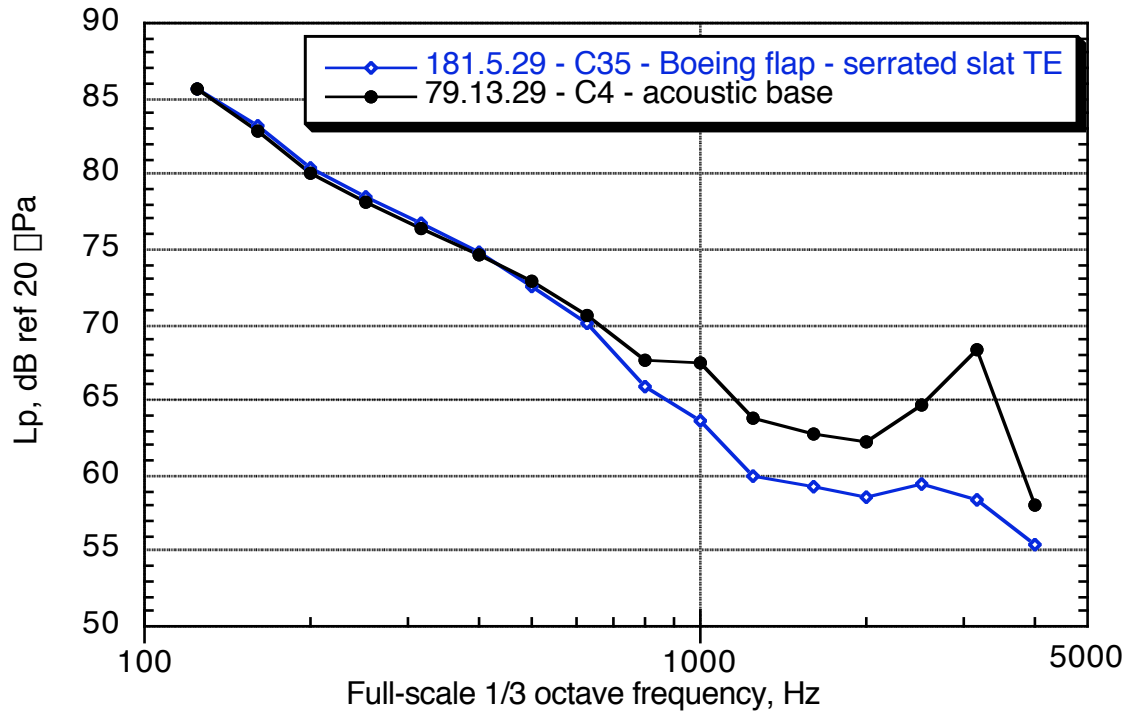


(b) Integration region for the outboard-edge of the inboard-aft flap.

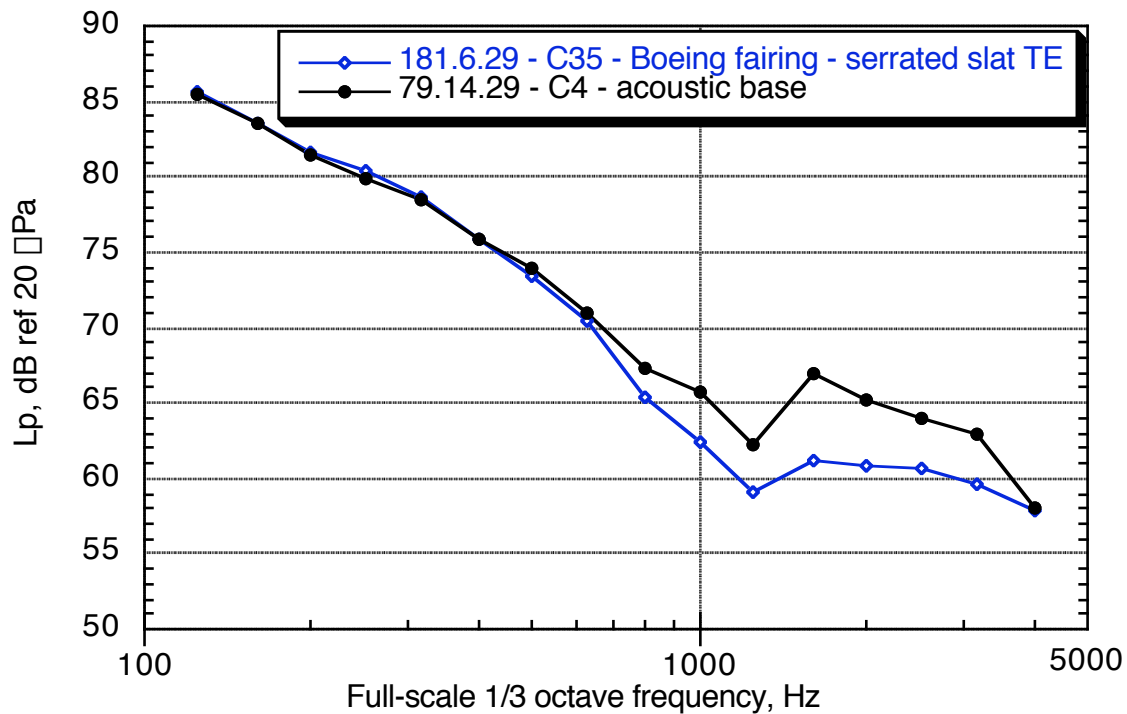
Figure 78. Concluded.



Figure 79. Lower surface detail of outboard edge of outboard flap, with bulb-seal fairing used on Boeing 777.

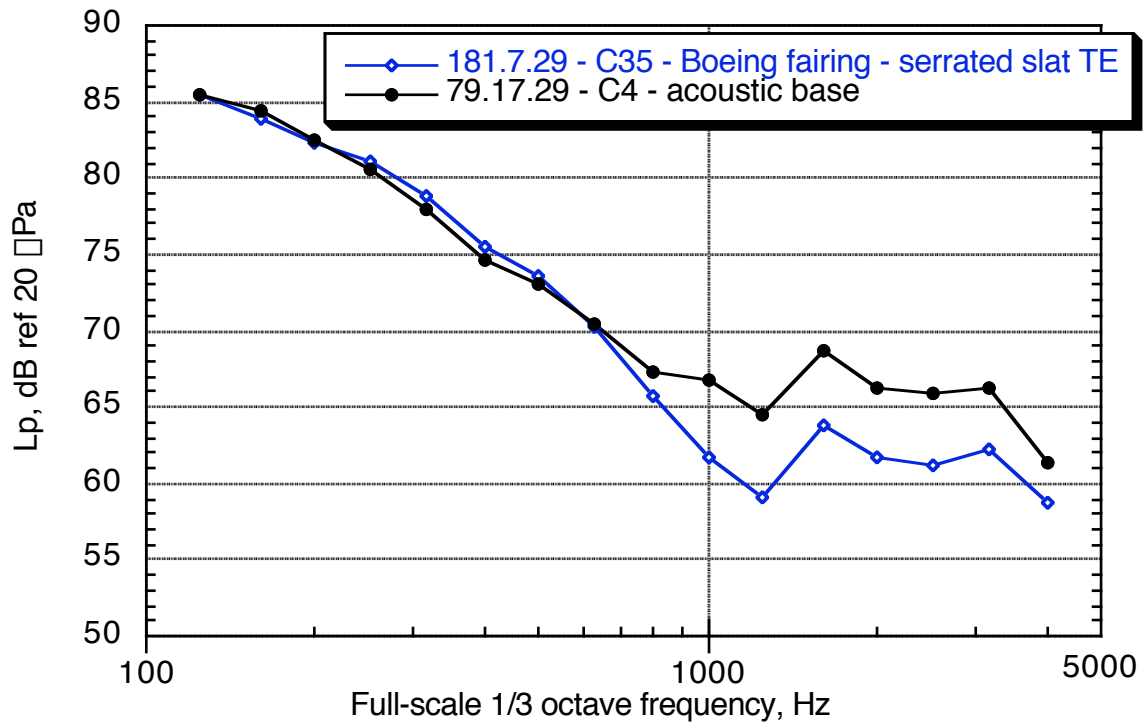


(a) Traverse = 100 in. upstream.

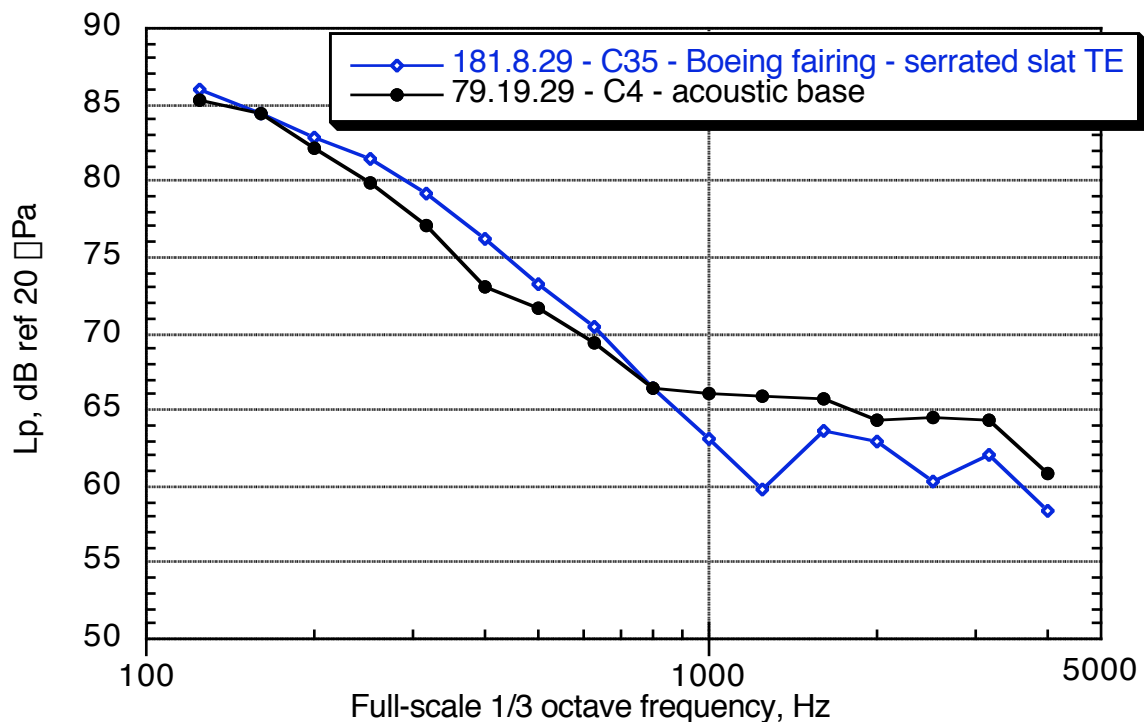


b) Traverse = 0 in.

Figure 80. Landing configuration (flap 30°, slat 20°), no gear, flap-edge region 29:  $M = 0.21$ ,  $\alpha = 6^\circ$ , Boeing fairing vs. no treatment.

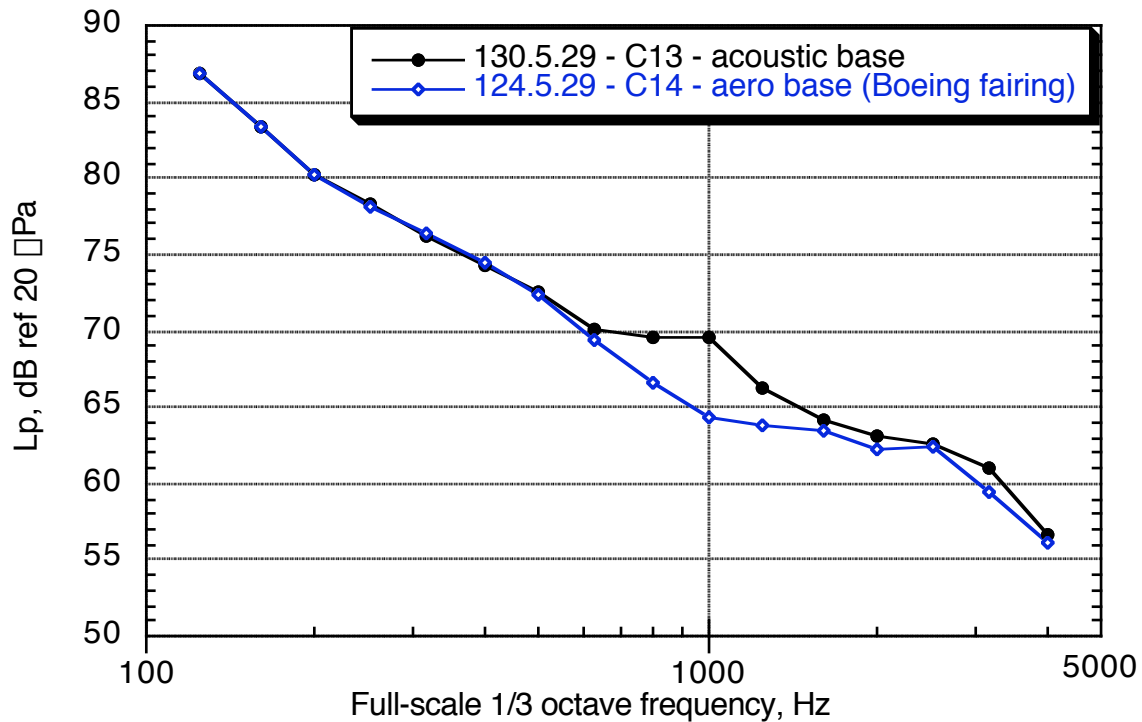


(c) Traverse = 150 in. downstream.

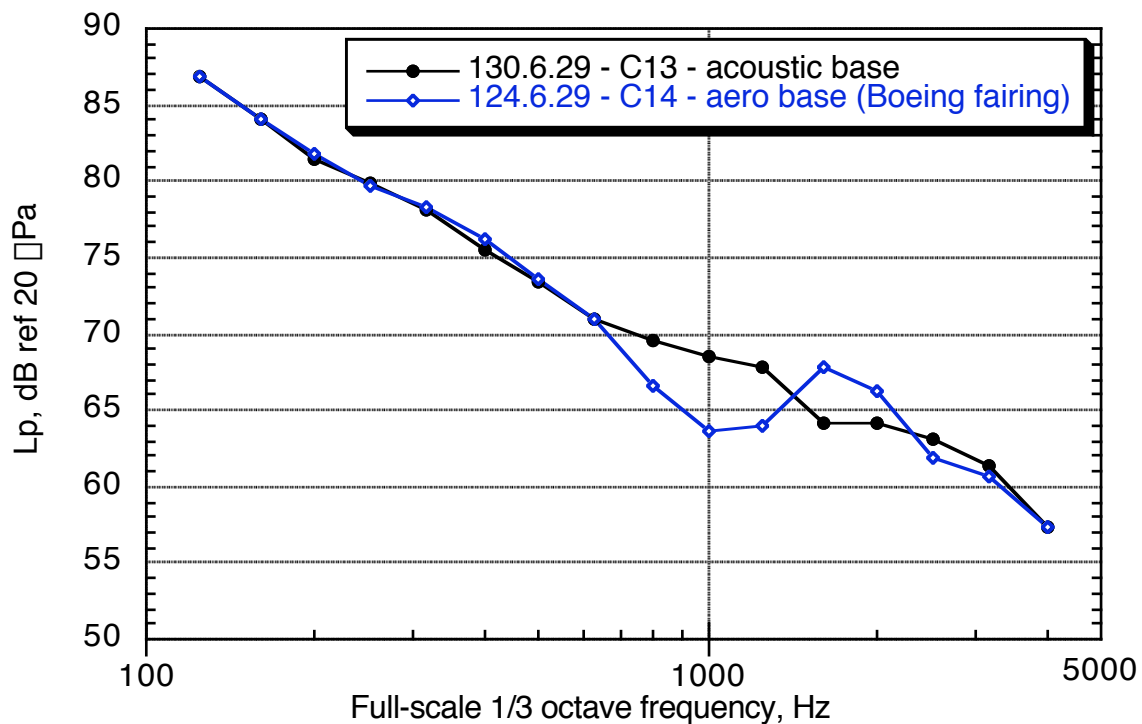


(d) Traverse = 250 in. downstream.

Figure 80. Concluded.

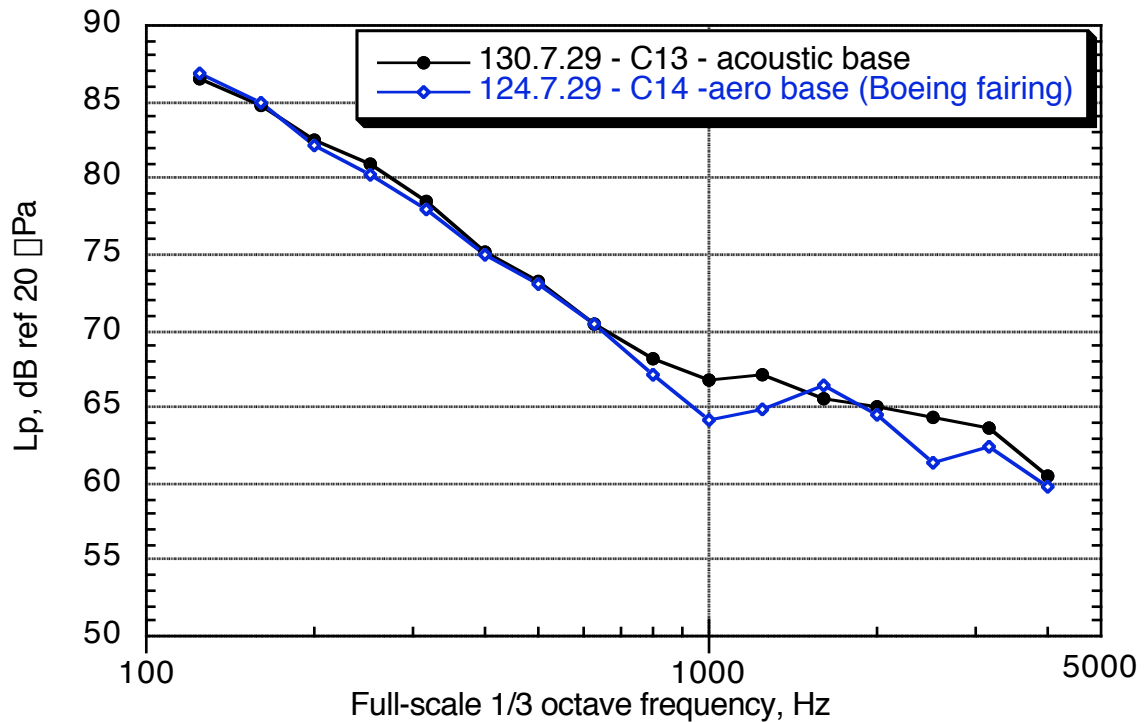


(a) Traverse = 100 in. upstream.

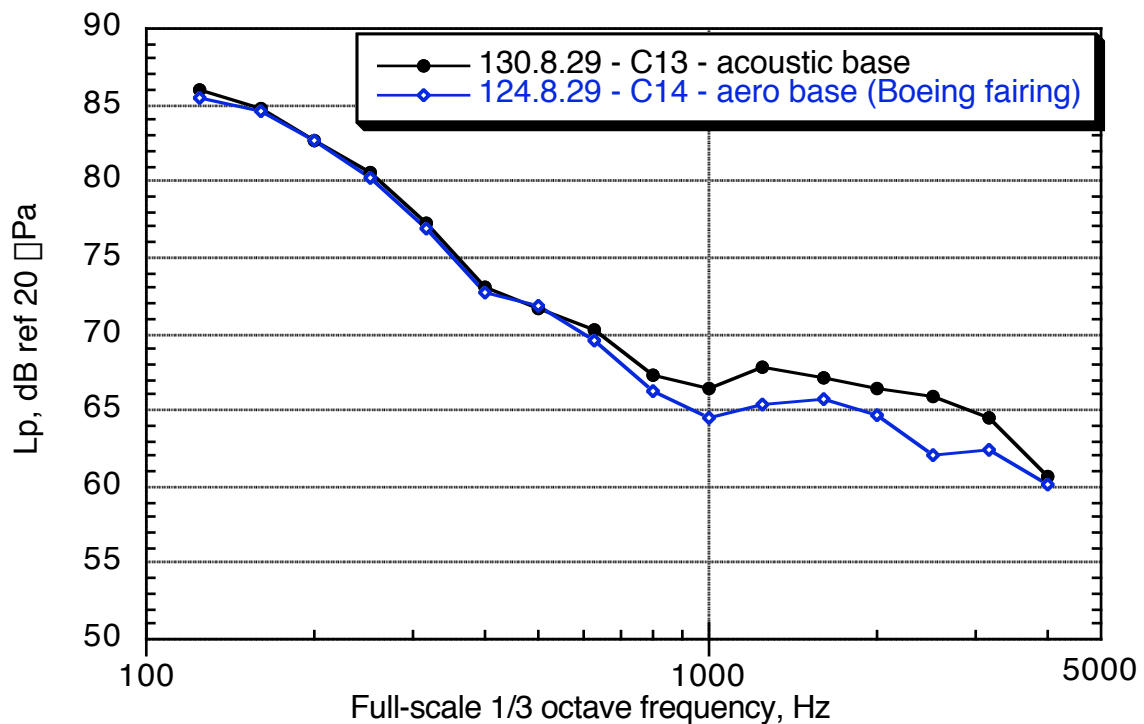


(b) Traverse = 0 in.

Figure 81. Approach configuration (flap 20°, slat 20°), no gear, flap-edge region 29:  $M = 0.21$ ,  $\Delta = 6^\circ$ , Boeing fairing vs. no treatment.



(c) Traverse = 150 in. downstream.

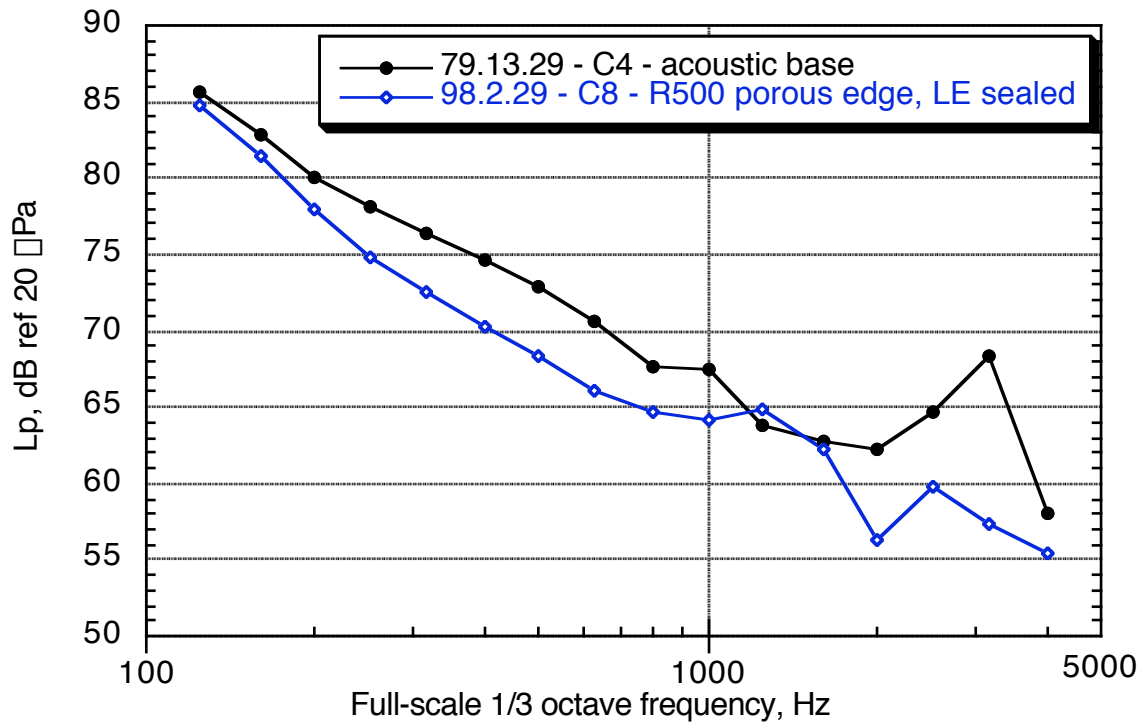


(d) Traverse = 250 in. downstream.

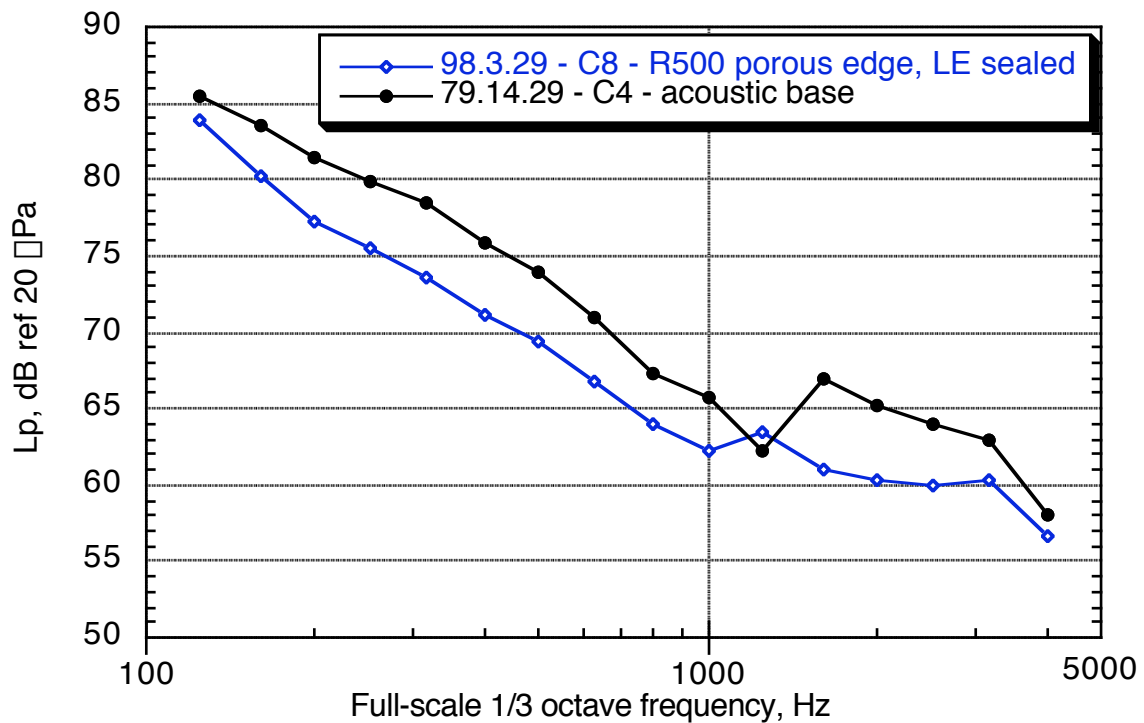
Figure 81. Concluded.



Figure 82. Outboard-flap outboard-edge lower surface view of porous edge treatment; porous treatment also extended to flap side edge and flap edge upper surface.

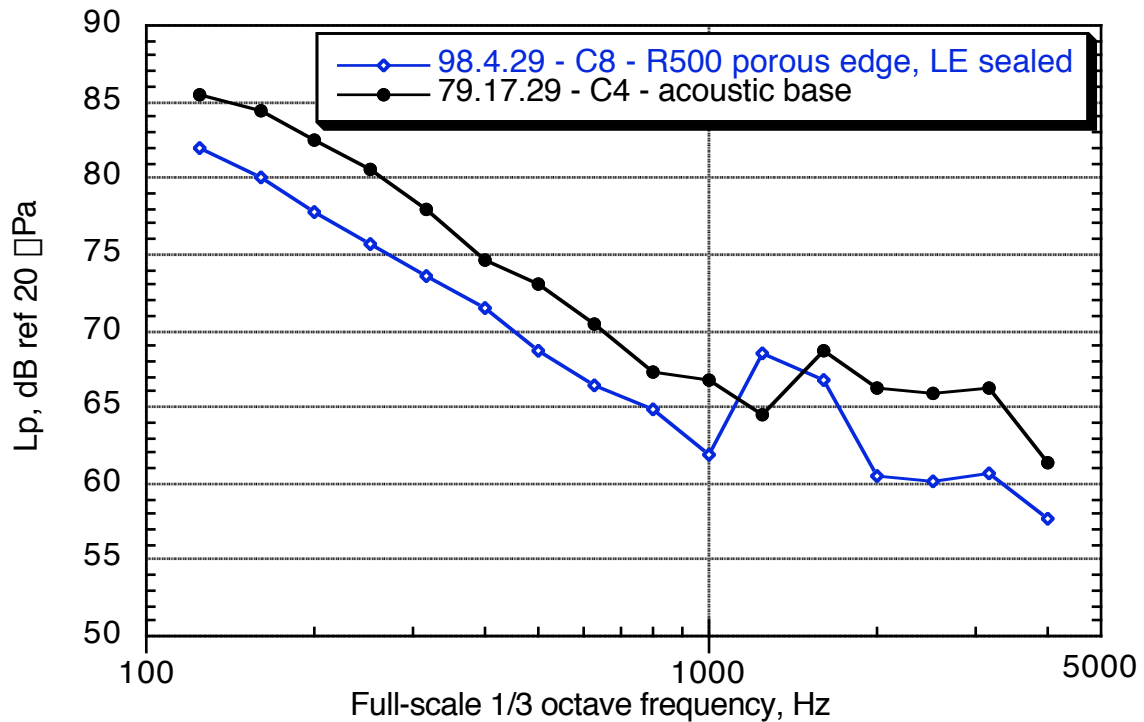


(a) Traverse = 100 in. upstream.

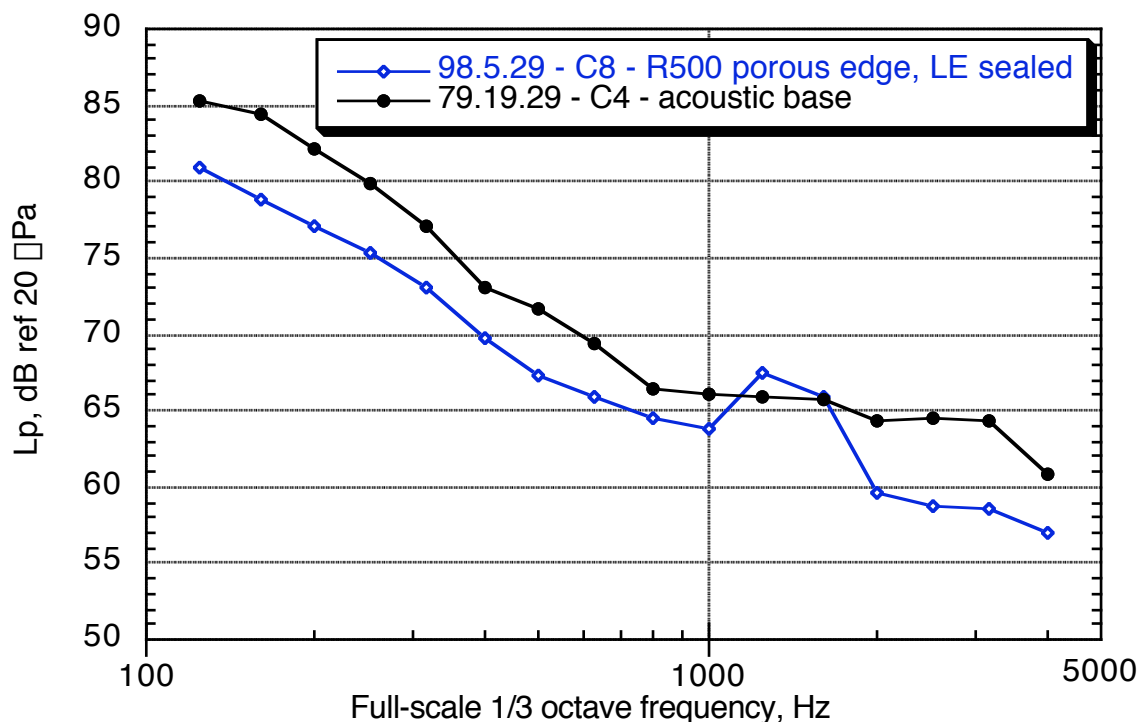


(b) Traverse = 0 in.

Figure 83. Comparison of porous flap edge (outboard flap, outboard edge) and untreated flap edge:  $M = 0.21$ ,  $\Delta = 6^\circ$ , flap  $30^\circ$ , slat  $20^\circ$ .

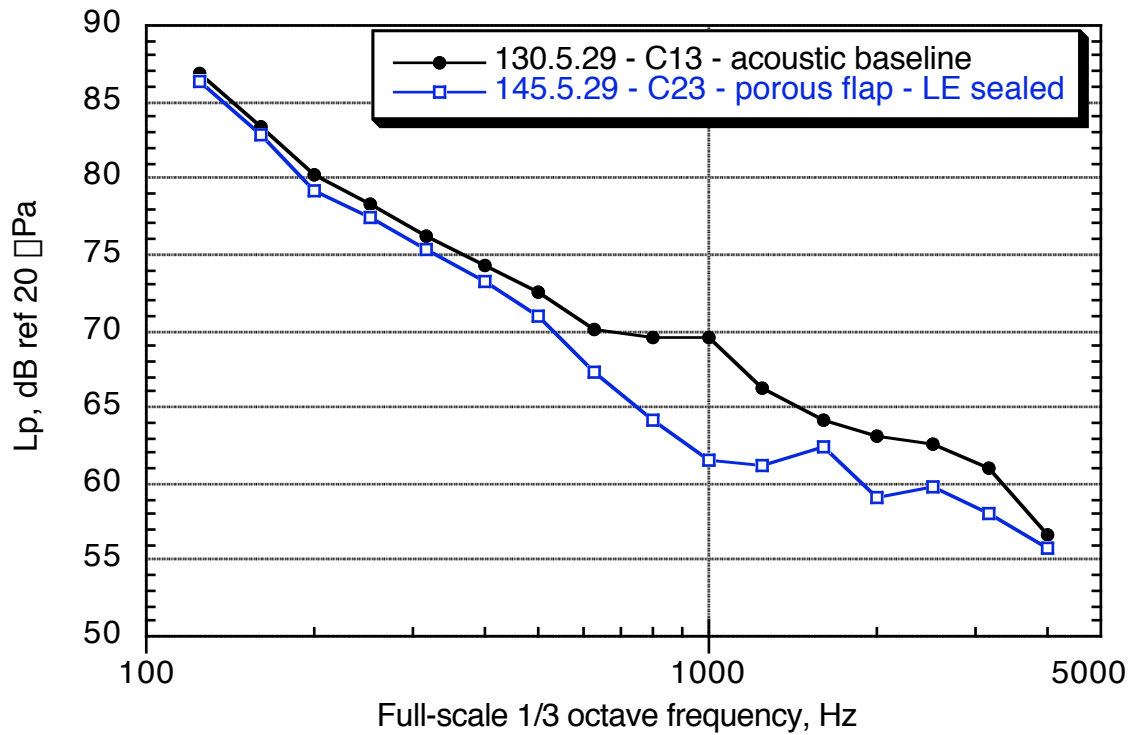


(c) Traverse = 150 in. downstream.

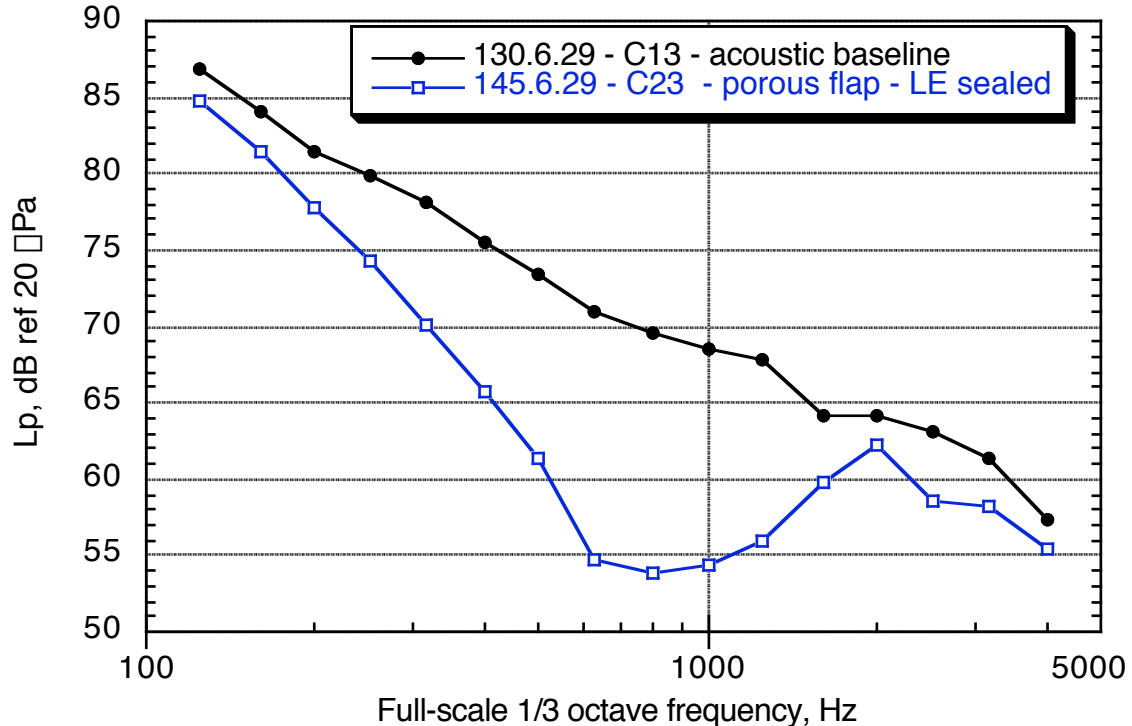


(d) Traverse = 250 in. downstream.

Figure 83. Concluded.

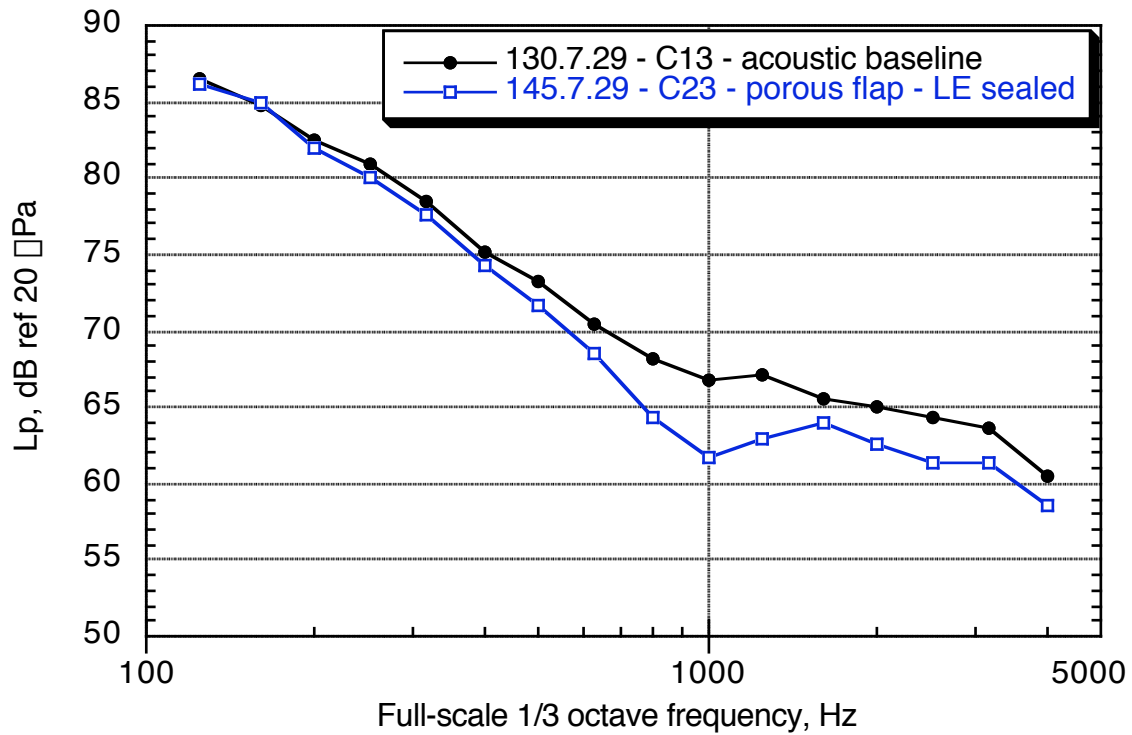


(a) Traverse = 100 in. upstream.

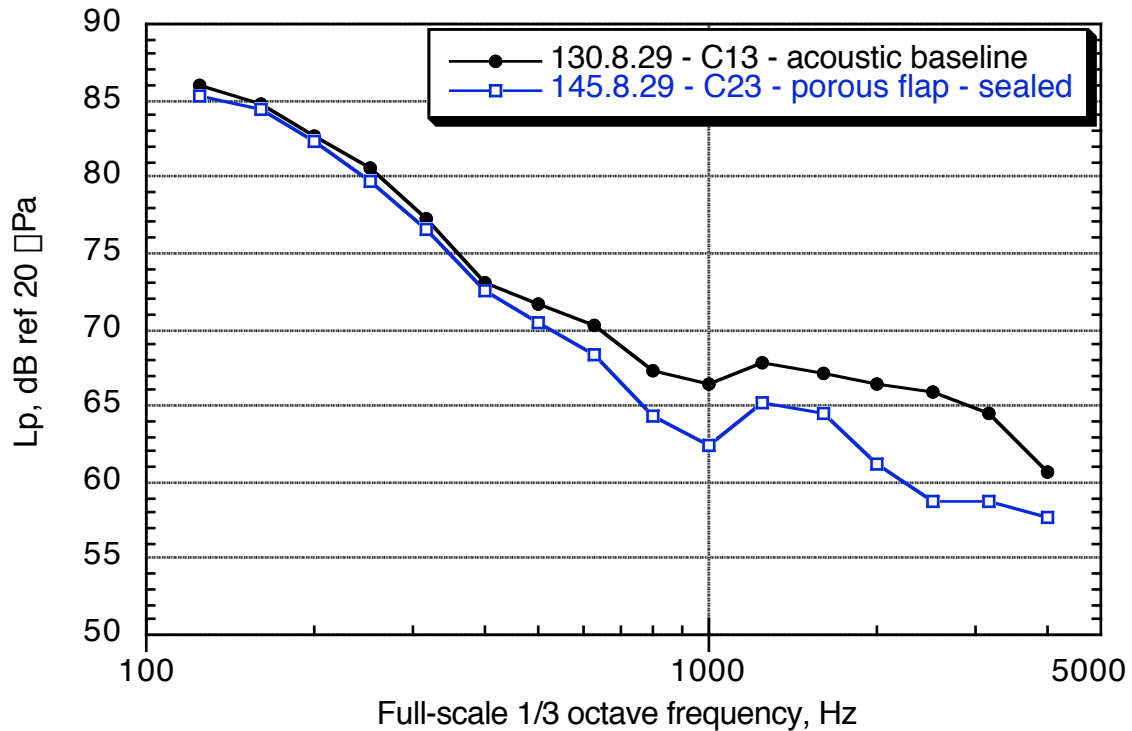


(b) Traverse = 0.

Figure 84. Comparison of porous flap edge (outboard flap, outboard edge) and untreated flap edge:  $M = 0.21$ ,  $\Delta = 6^\circ$ , flap  $20^\circ$ , slat  $20^\circ$ .



(c) Traverse = 150 in. downstream.



(d) Traverse = 250 in. downstream.

Figure 84. Concluded.

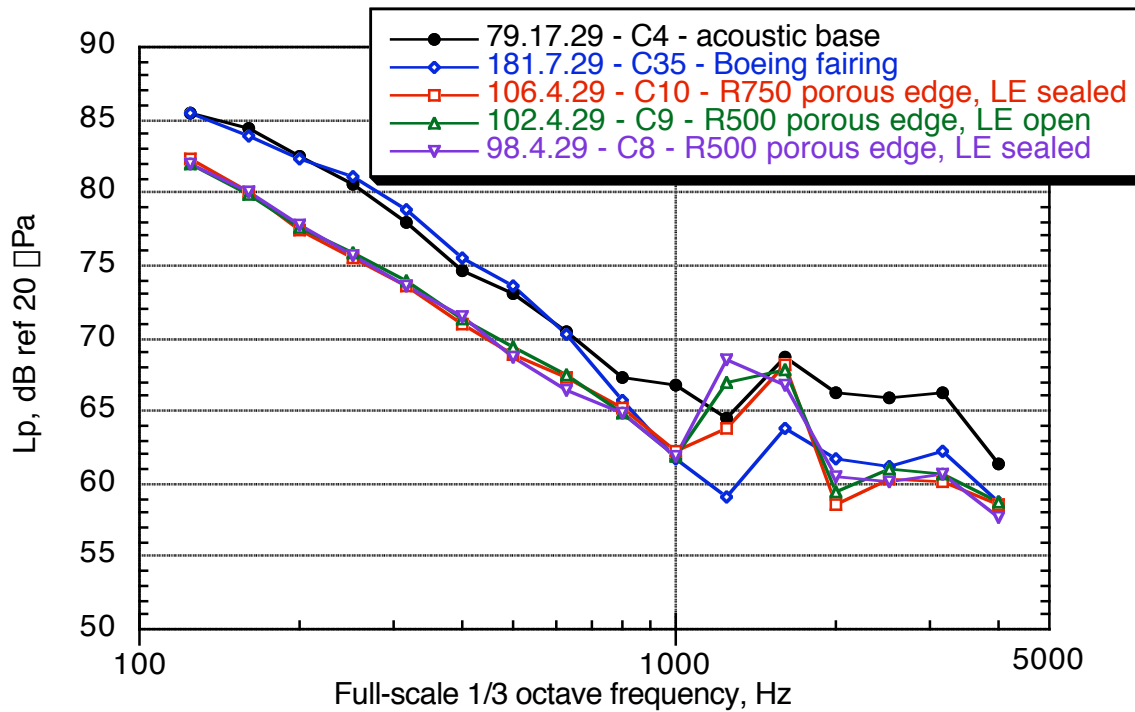


Figure 85. Comparison of various porous flap edge treatments with untreated and Boeing fairing treatments, landing configuration: traverse = 150 in. downstream,  $M = 0.22$ ,  $\alpha = 6^\circ$ .

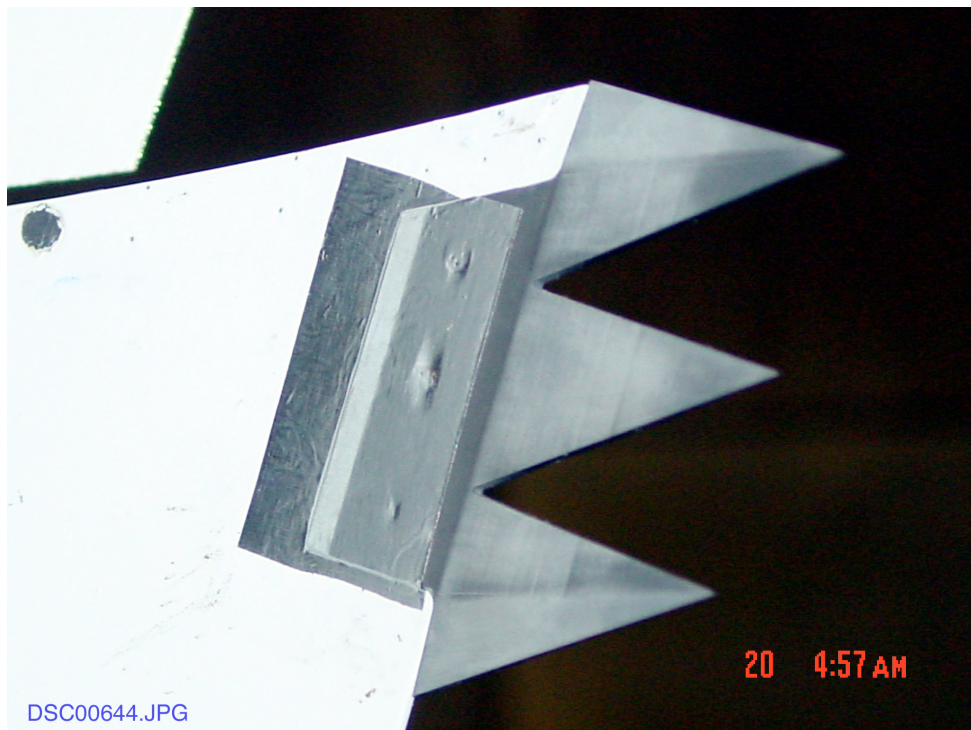


Figure 86. Detail of outboard flap, outboard edge with trailing-edge serrations.

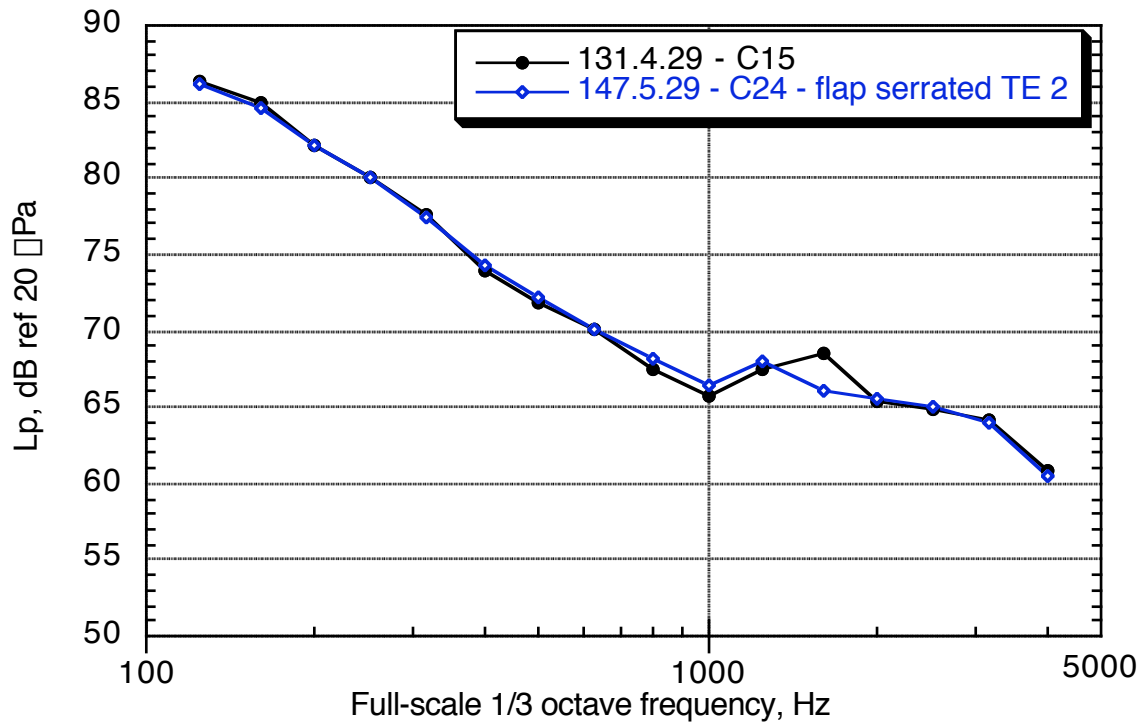


Figure 87. Comparison of spectra for serrated flap trailing edge with untreated flap edge: traverse = 150 in. downstream,  $M = 0.22$ ,  $\alpha = 6^\circ$ .



Figure 88. Detail of outboard flap, outboard edge with microtabs ( $70^\circ$ ) on lower flap surface.

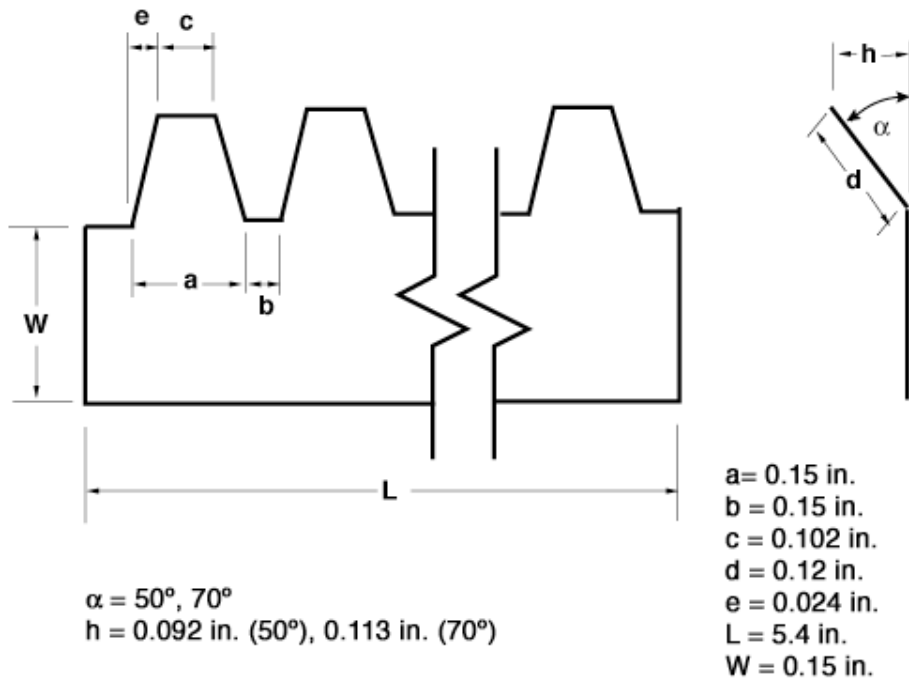


Figure 89. Microtab sketch with dimensions for both the  $50^\circ$  and  $70^\circ$  treatments.

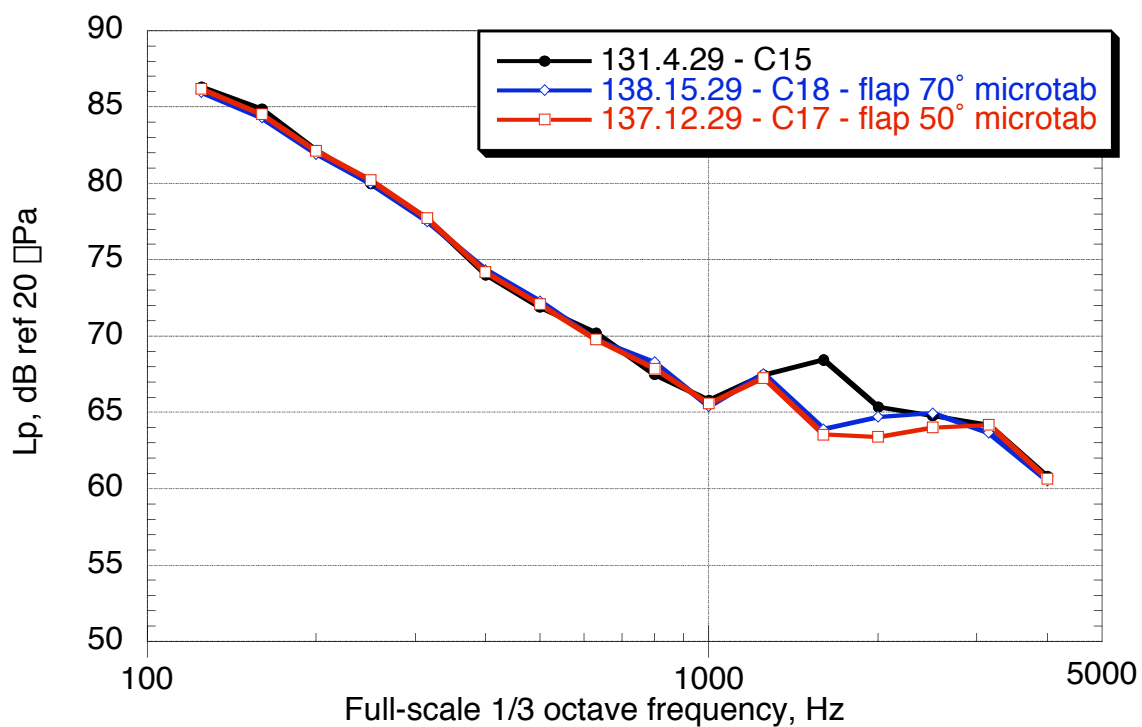


Figure 90. Comparison of spectra from OFOE; microtab 1 ( $50^\circ$ ) and 2 ( $70^\circ$ ), and untreated flap edge: approach configuration, traverse position = 150 in. downstream,  $M = 0.22$ ,  $\alpha = 6^\circ$ .

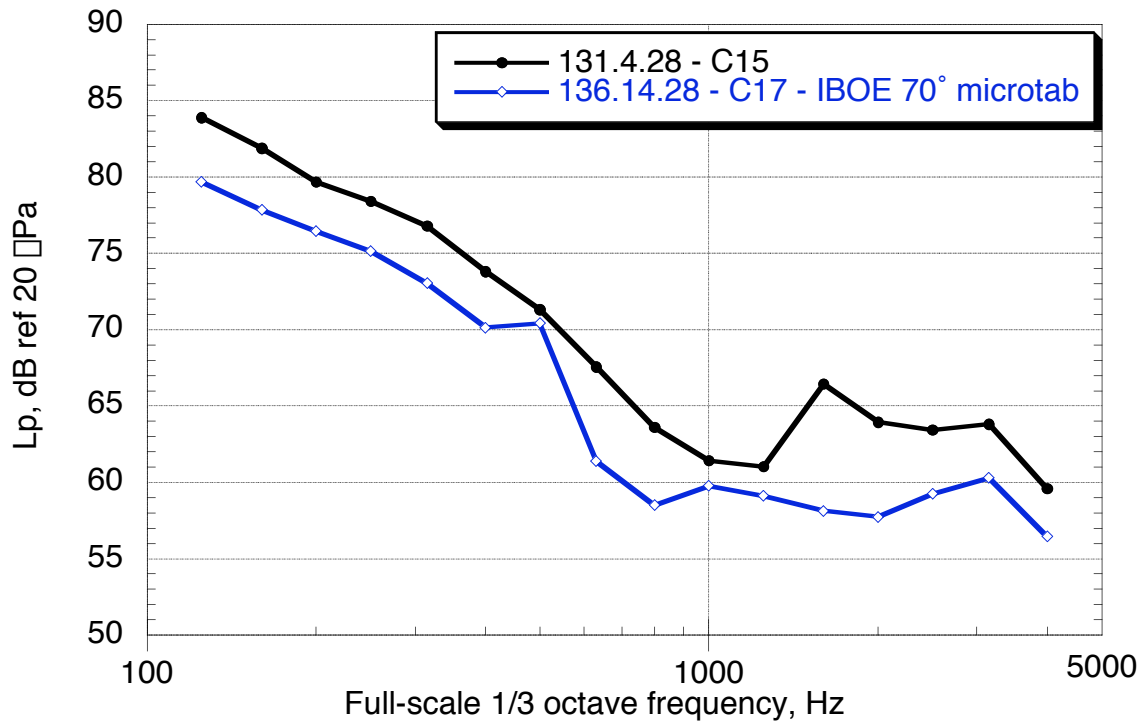


Figure 91. Effect of microtabs on the outboard edge of the aft flap; microtab 1 and 2 configurations both used 70° tabs on the IBOE: approach configuration, traverse position = 150 in. downstream,  $M = 0.22$ ,  $\alpha = 6^\circ$ .

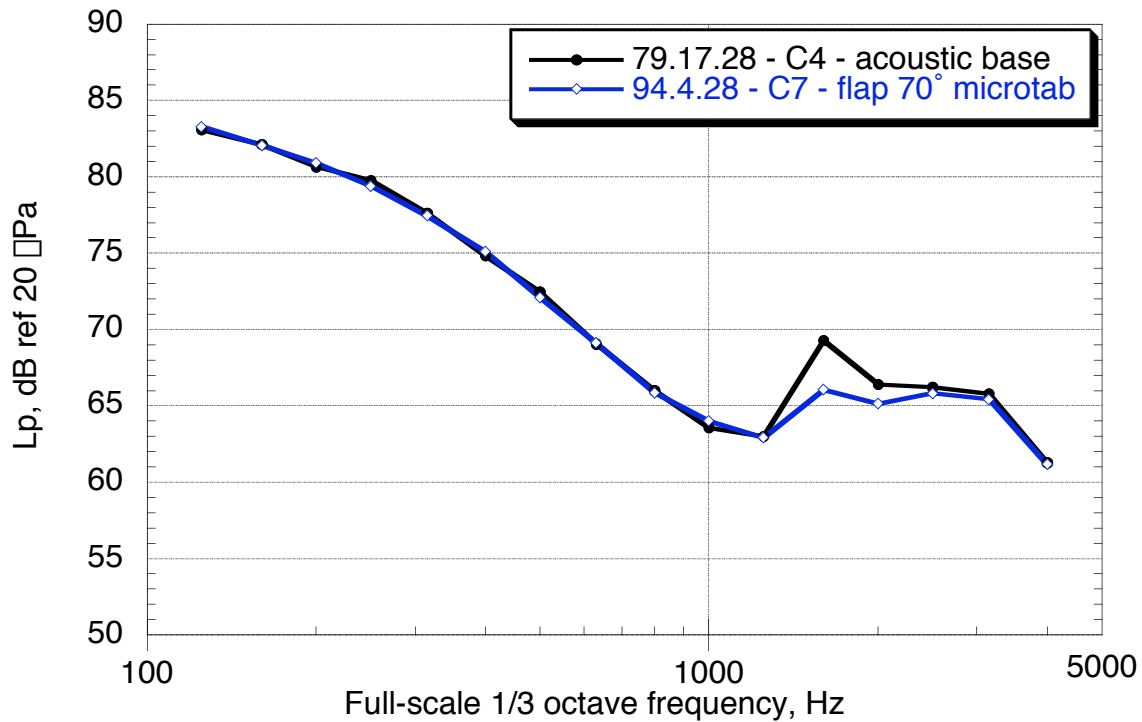
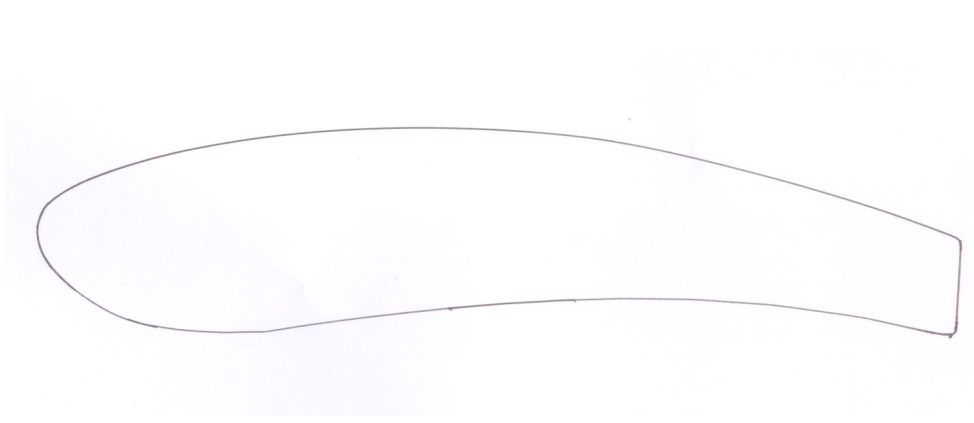


Figure 92. IBOE microtabs for the landing configuration: traverse position = 150 in. downstream,  $M = 0.22$ ,  $\alpha = 6^\circ$ .

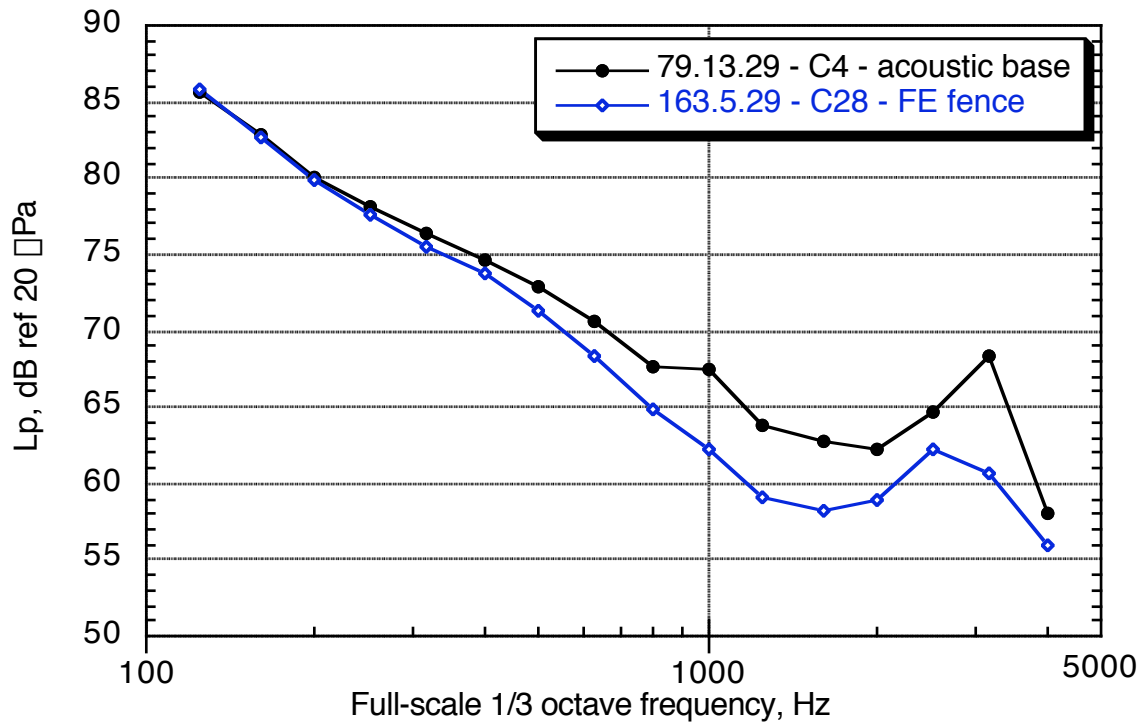


(a) OFOE fence photo.

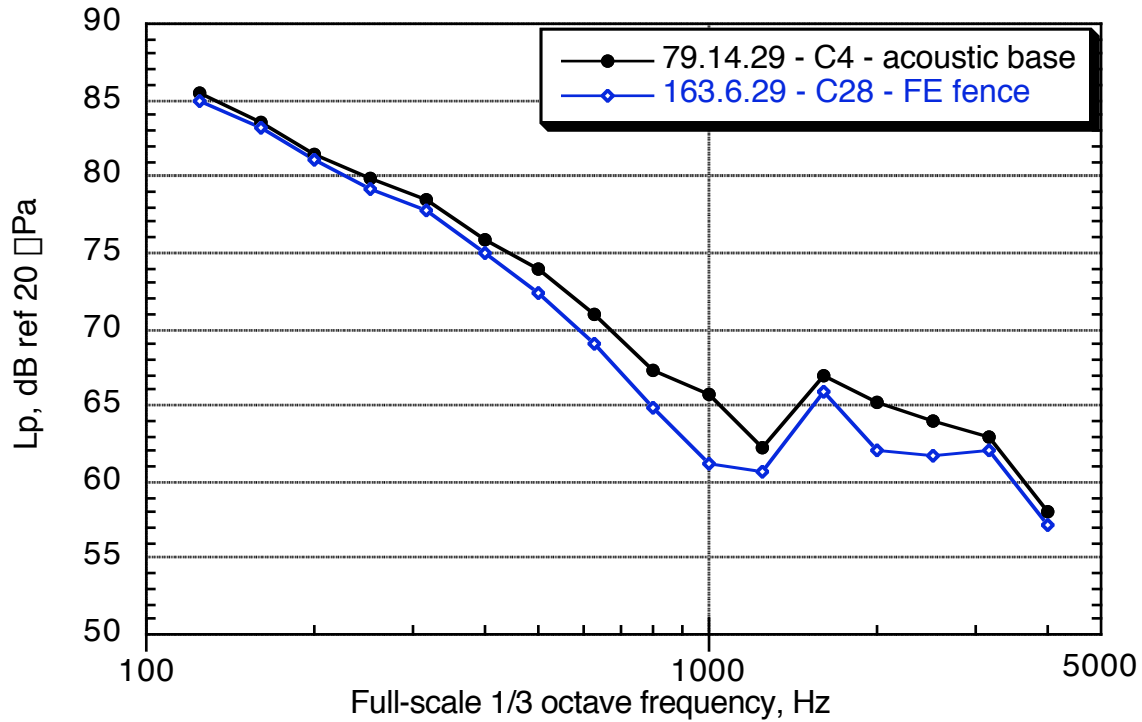


(b) Sketch of the OFOE fence.

Figure 93. Detail of outboard edge of outboard flap with flap-edge fence.

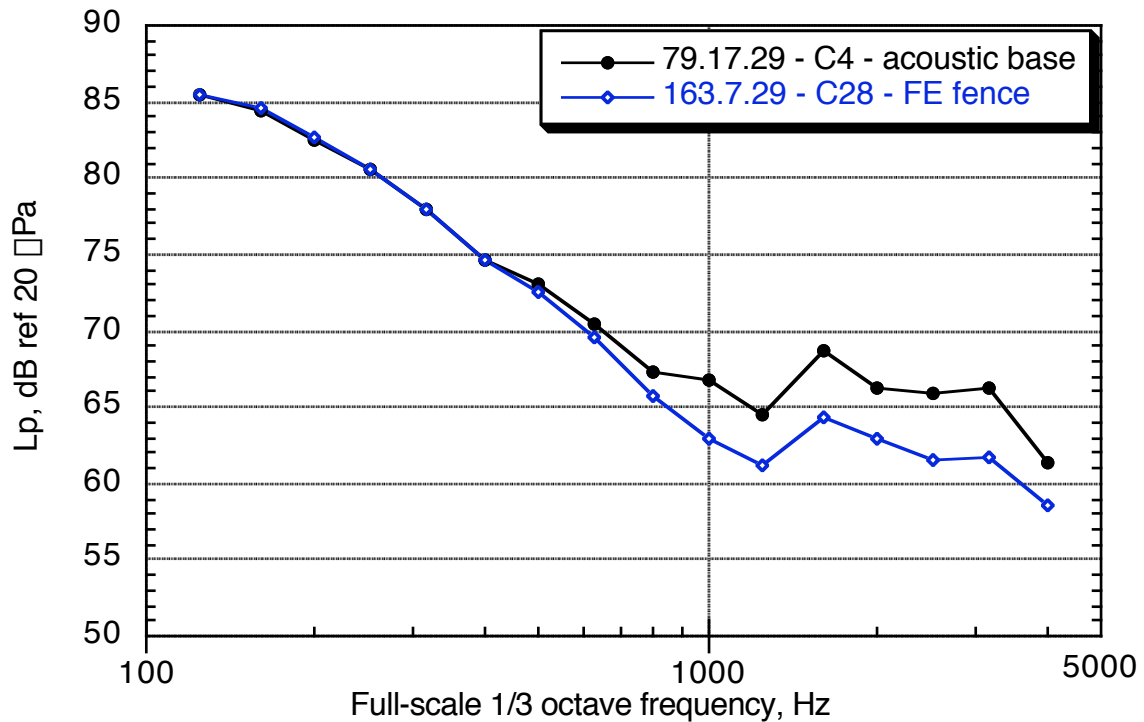


(a) Traverse = 100 in. upstream.

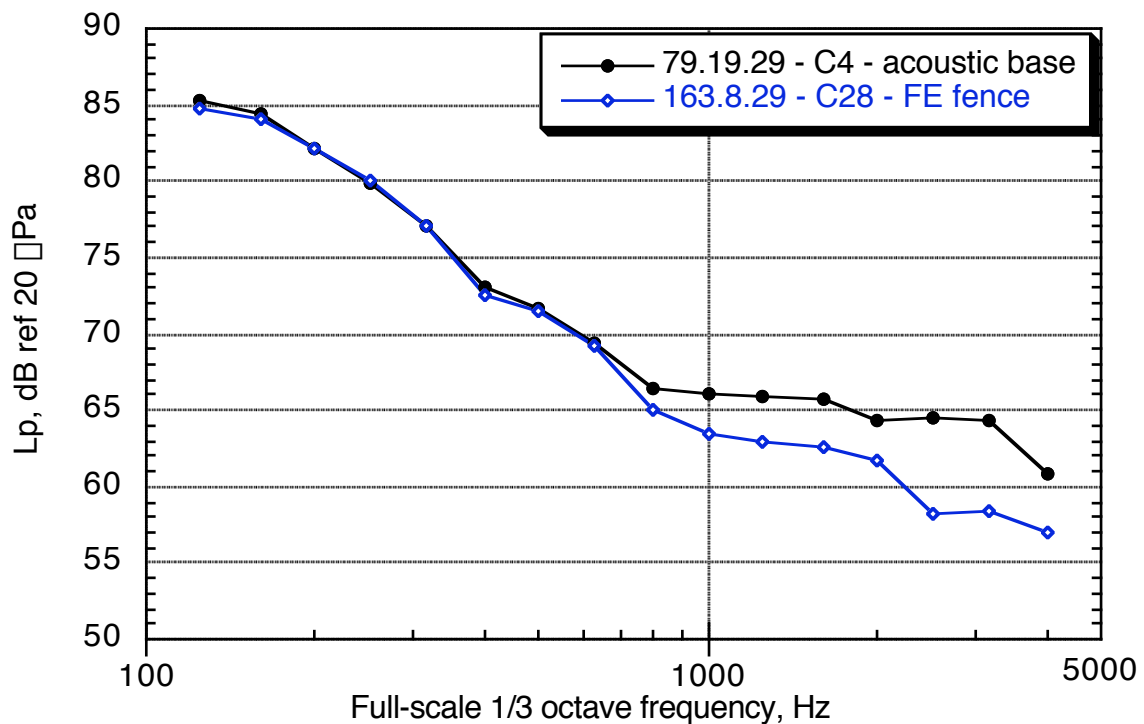


(b) Traverse = 0 in.

Figure 94. Comparison of spectra from outboard flap outboard edge, flap-edge fence vs. untreated flap edge: landing configuration,  $M = 0.22$ ,  $\square = 6^\circ$ .



(c) Traverse = 150 in. downstream.



(d) Traverse = 250 in. downstream.

Figure 94. Concluded.

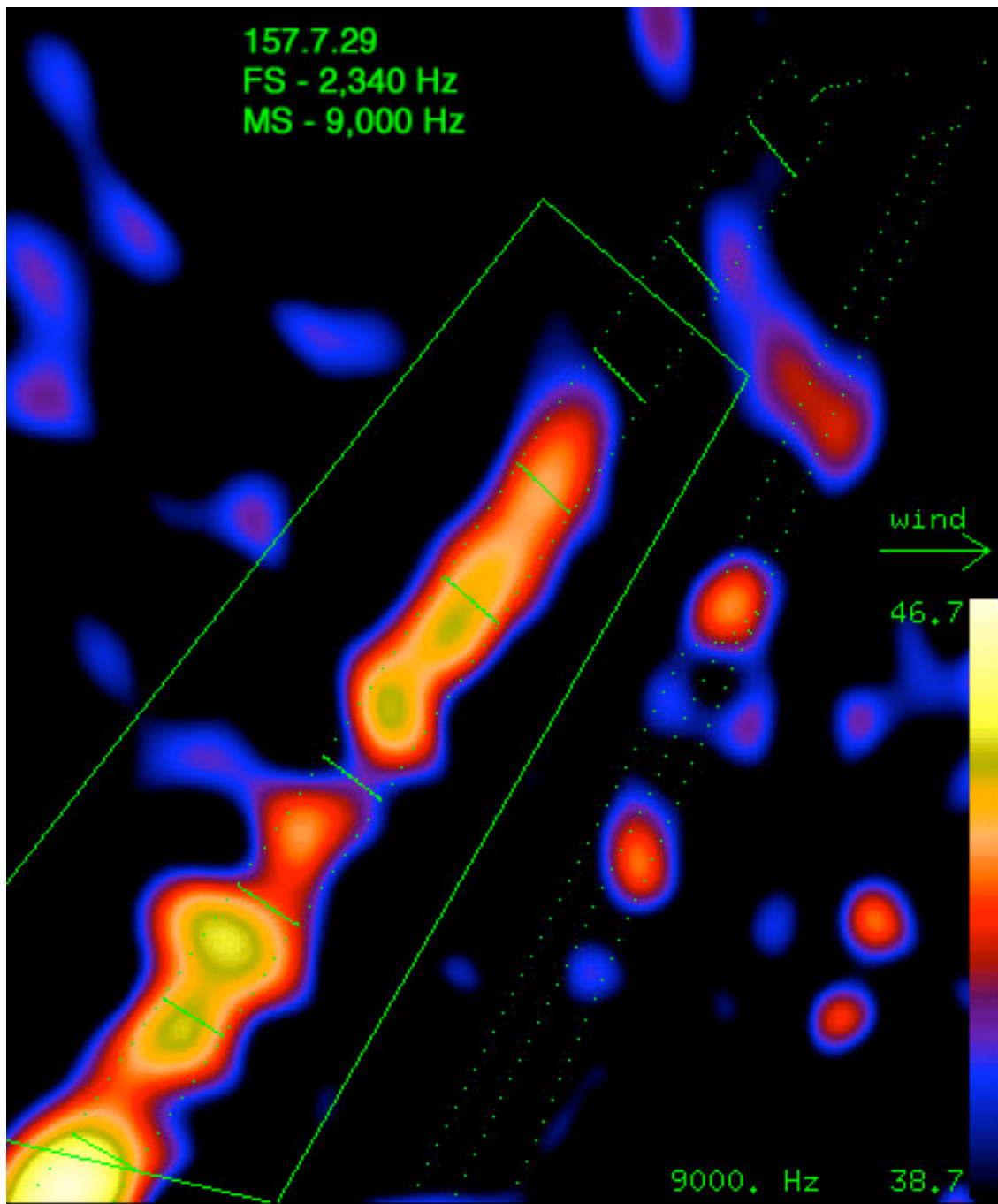
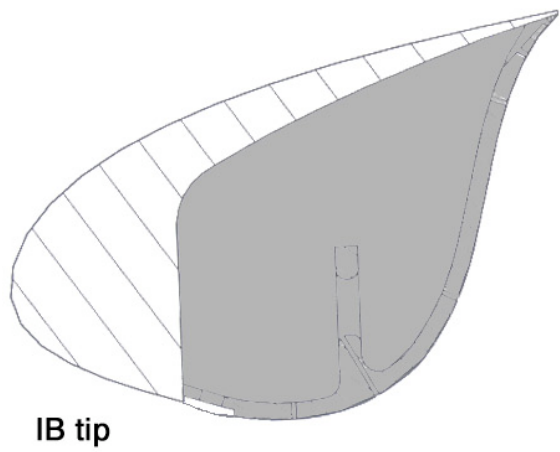


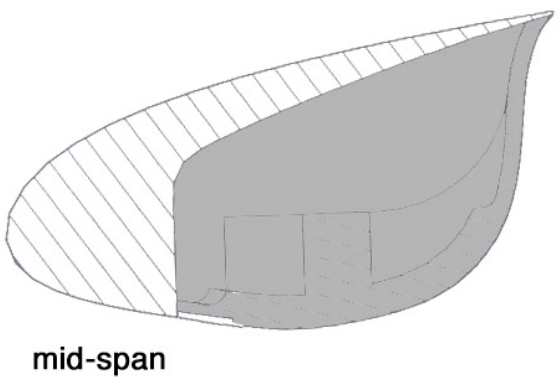
Figure 95. Typical source location plot of outer wing region (scan/integration process 29) showing boundary of outboard slat cove integration region (solid line polygon); slat brackets are shown as short line segments, wing outline as dots.



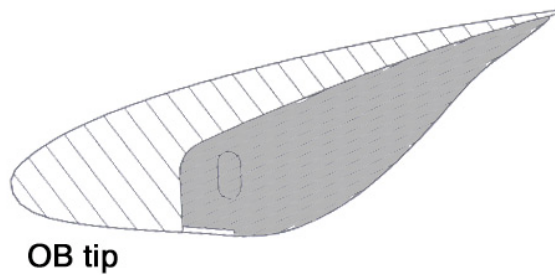
Figure 96. Outboard slat with full span cove filler, also showing partially covered slat brackets; the outboard slat bracket is covered with a fiber mat, and a bracket fairing is applied to the lowest visible bracket.



IB tip



mid-span



OB tip

Figure 97. Cove-filler profiles at three points along slat cove; the cove-filler region is shaded.

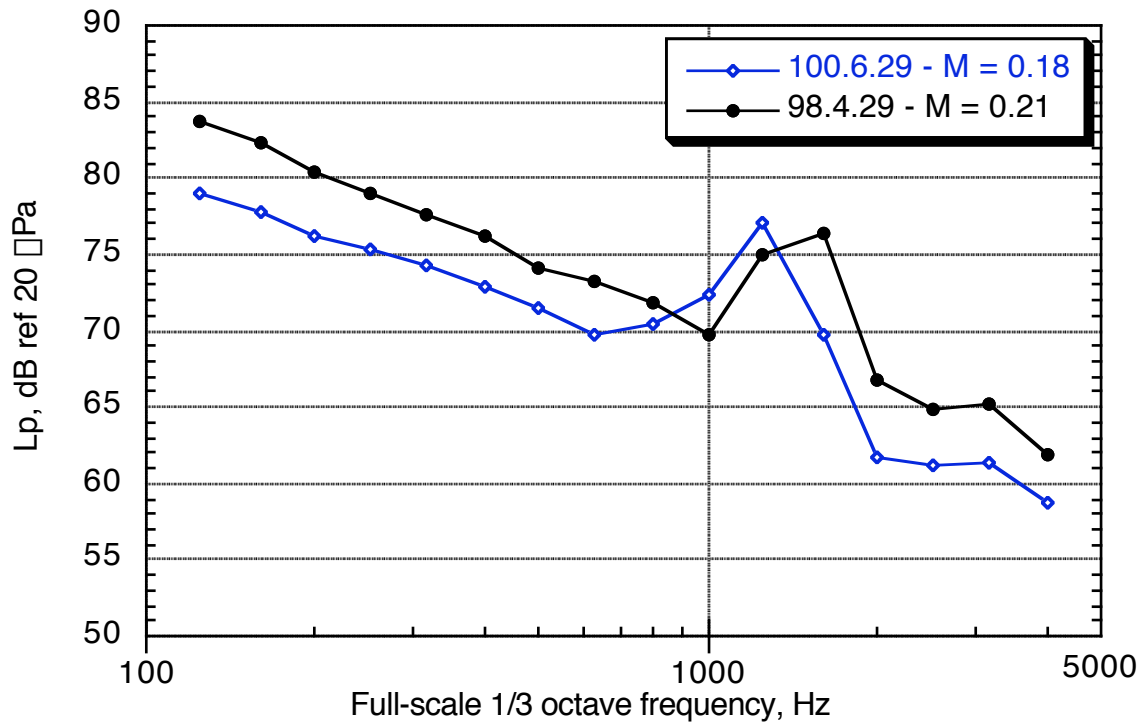


Figure 98. Effect of Mach number on slat cove noise: landing configuration, traverse = 150 in. downstream,  $\square = 6^\circ$ .

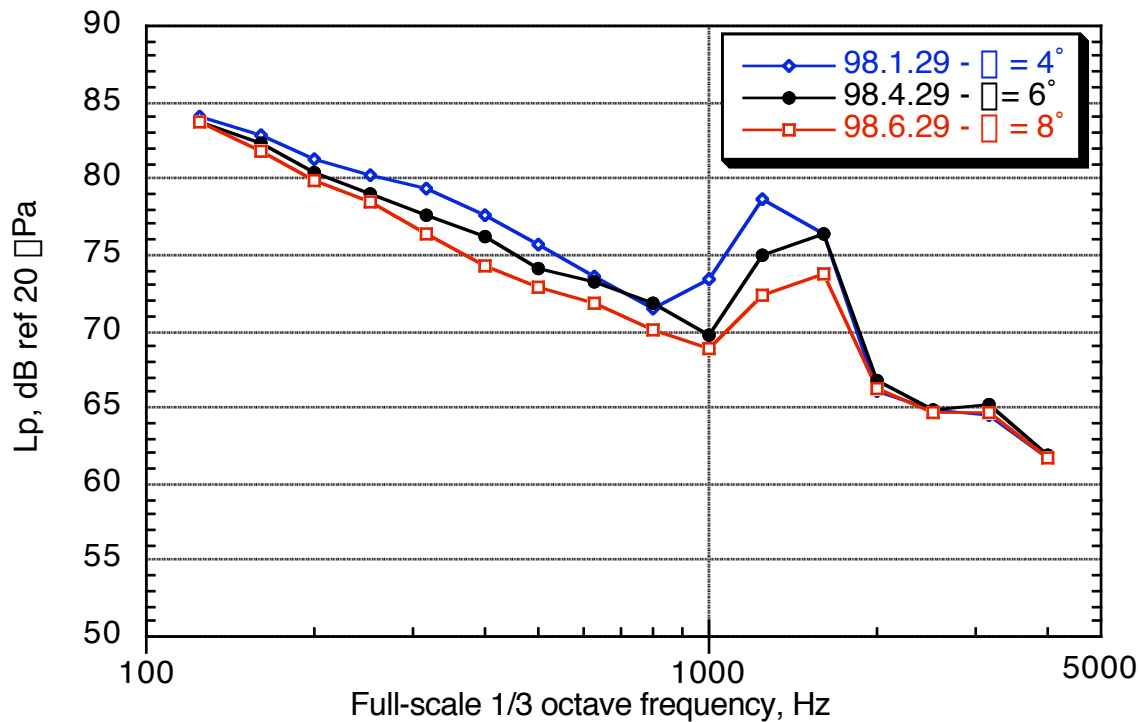
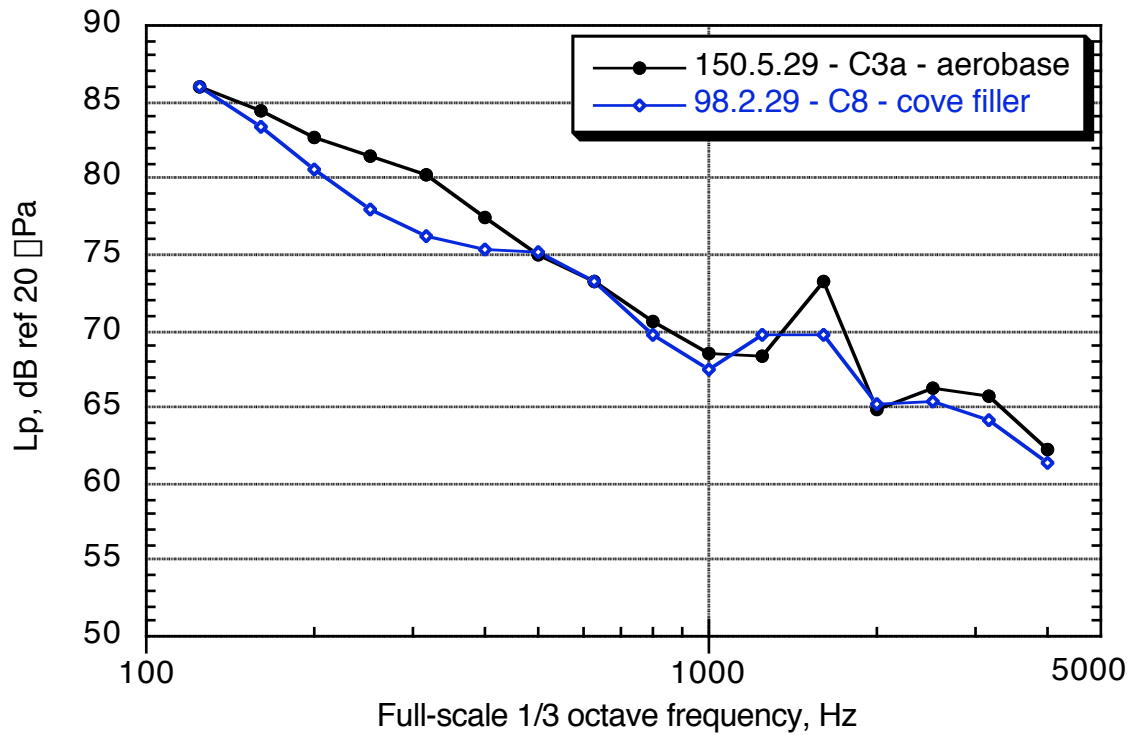
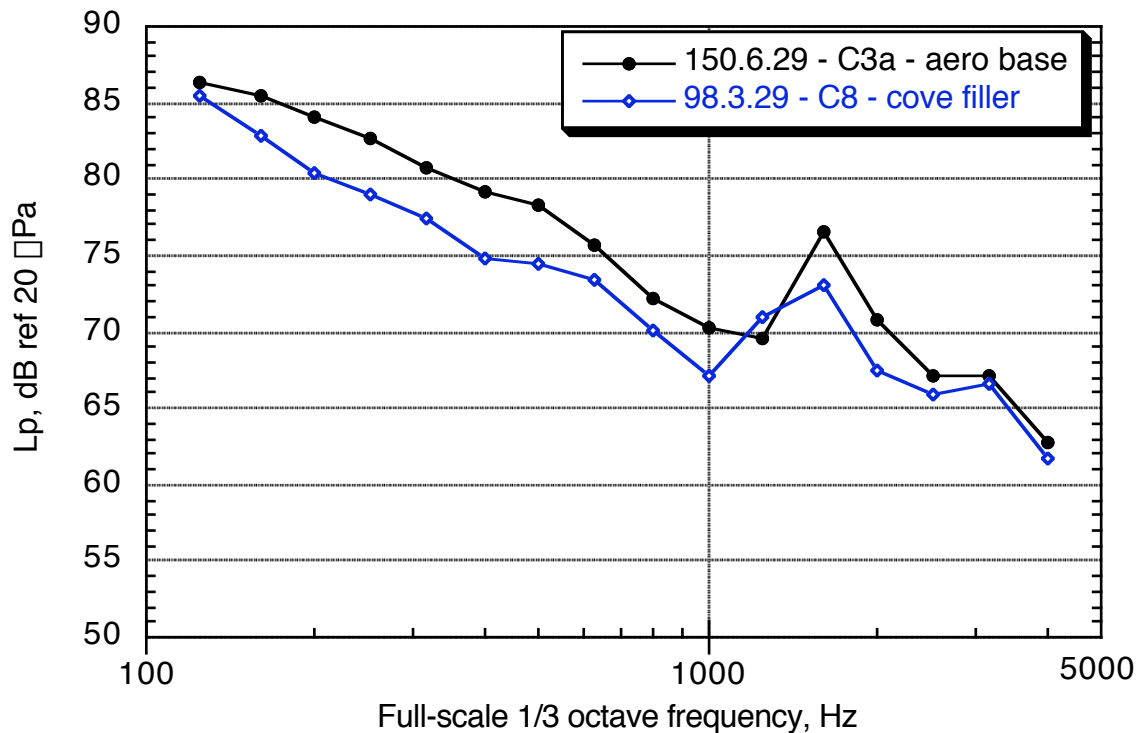


Figure 99. Effect of angle of attack on slat cove noise: landing configuration, traverse = 150 in. downstream,  $M = 0.21$ .

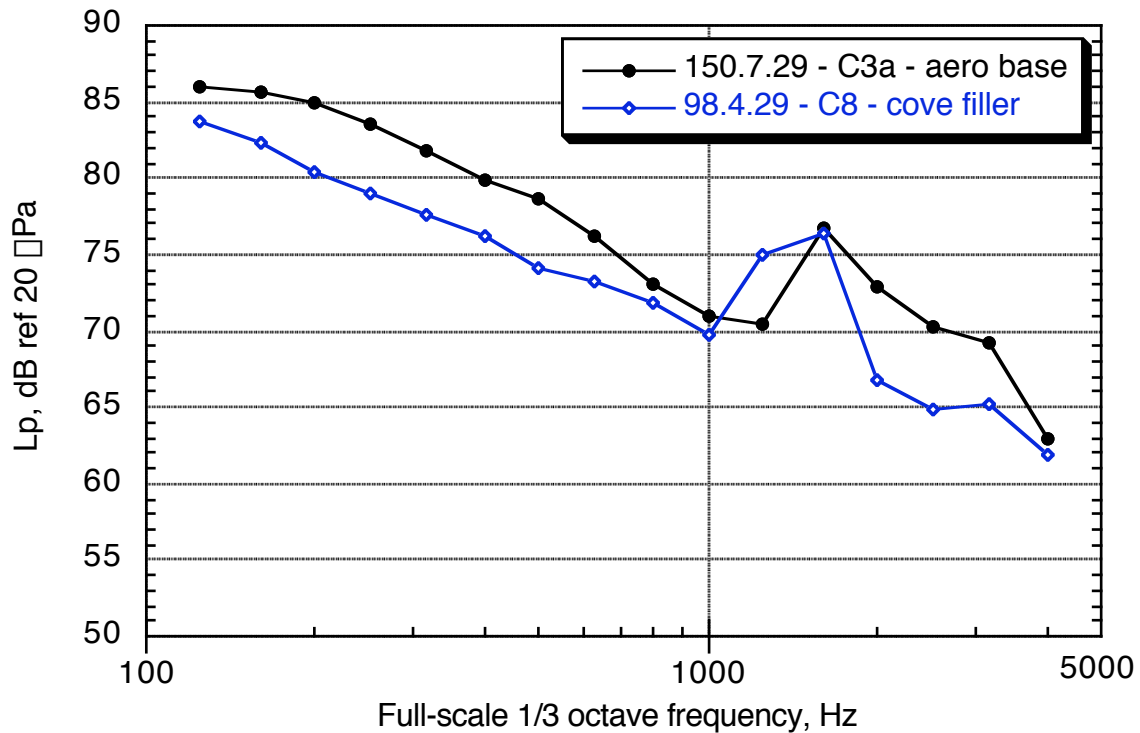


(a) Traverse position = 100 in. upstream.

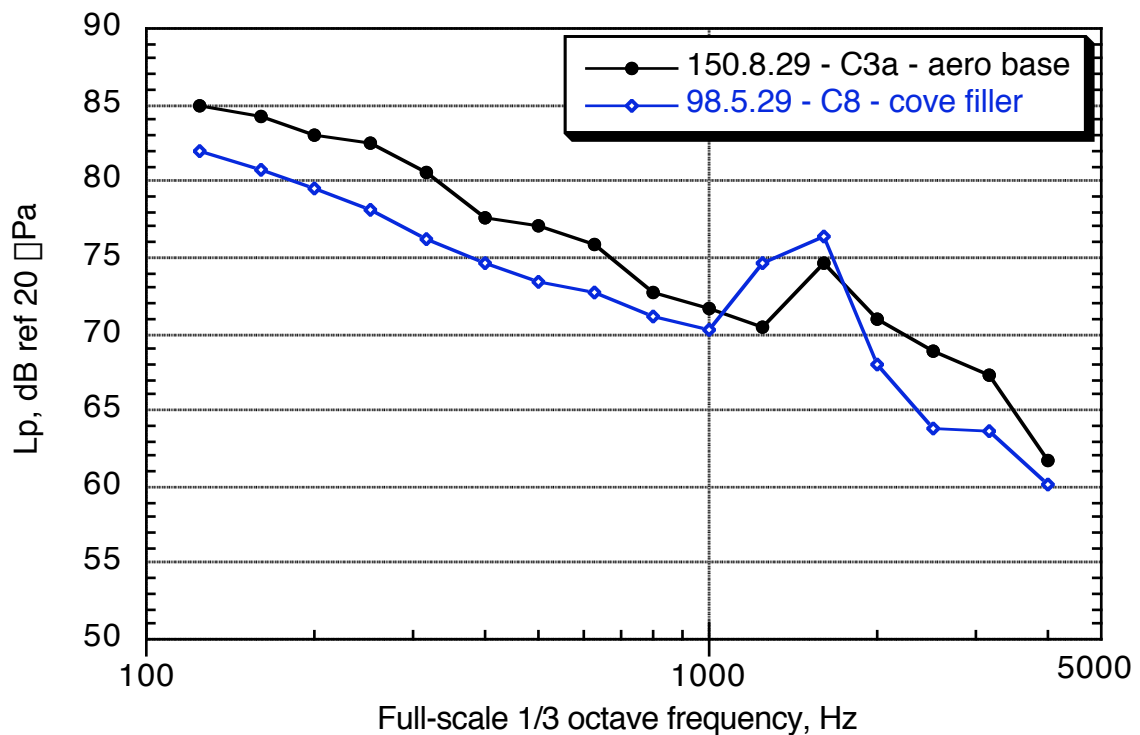


(b) Traverse position = 0 in.

Figure 100. Effect of cove filler on slat cove noise: landing configuration,  $M = 0.21$ ,  $\alpha = 6^\circ$ .



(c) Traverse position = 150 in. downstream.



(d) Traverse position = 250 in. downstream.

Figure 100. Concluded.

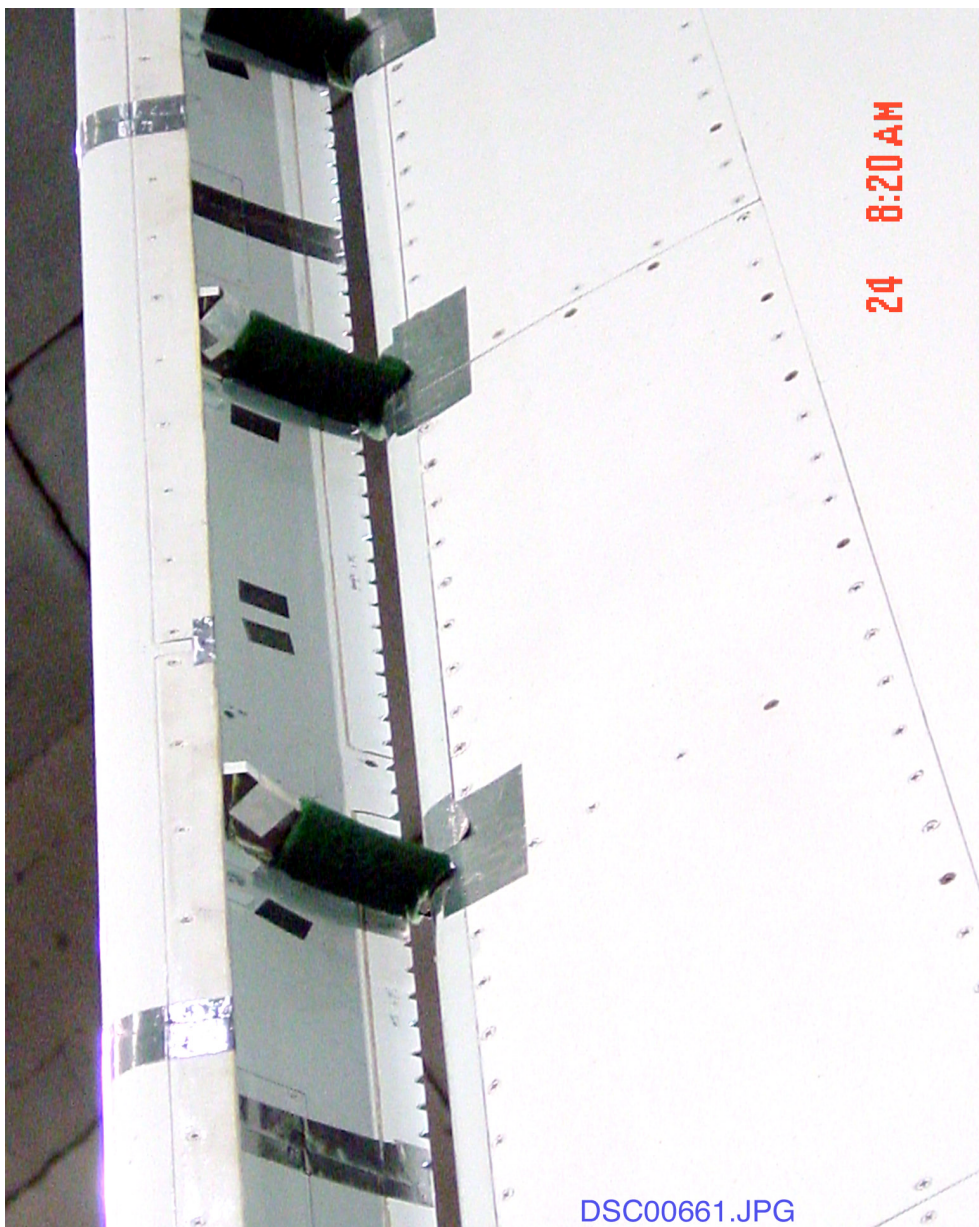


Figure 101. Slat serrated trailing edge; fiber pad (Scotchbrite) treatment on slat brackets.

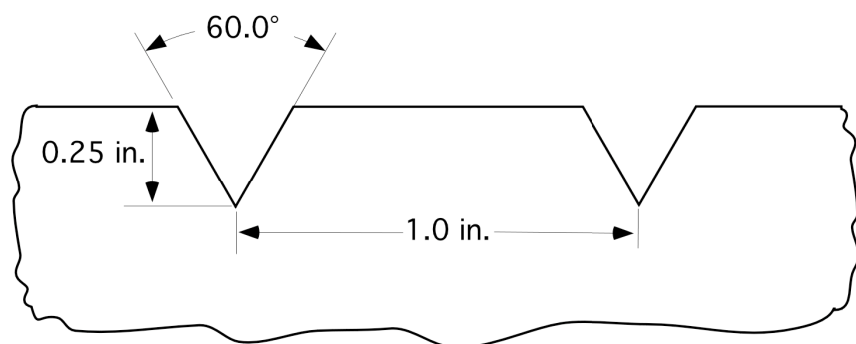
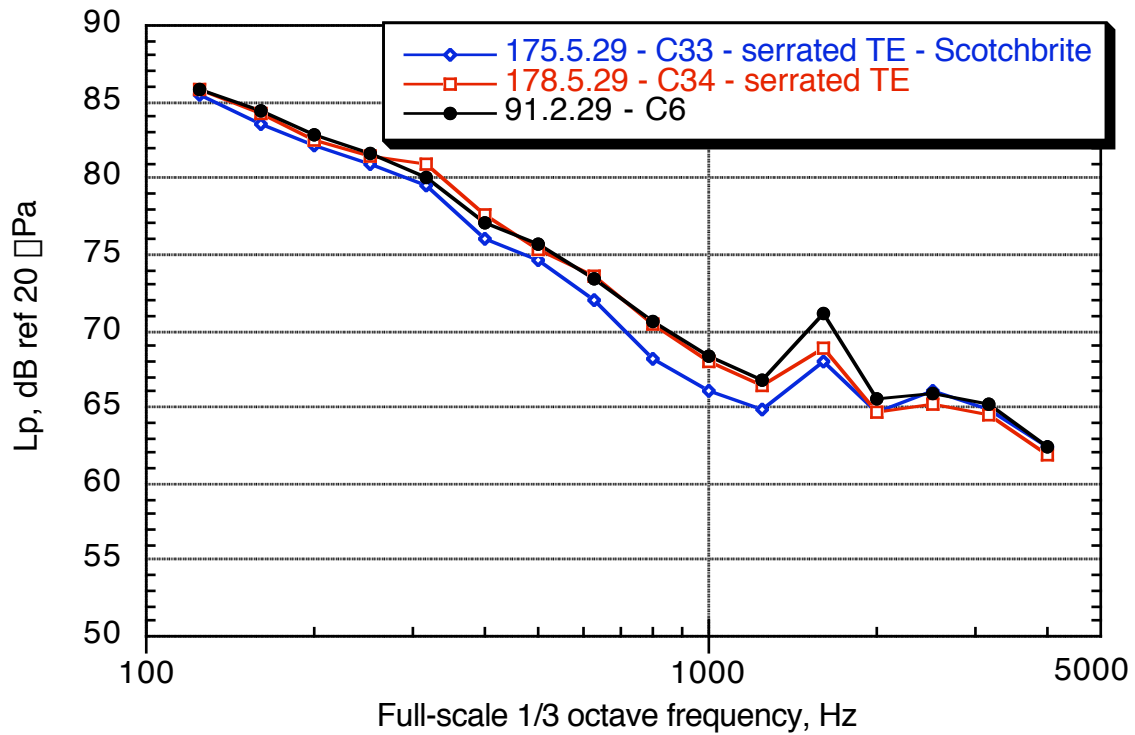
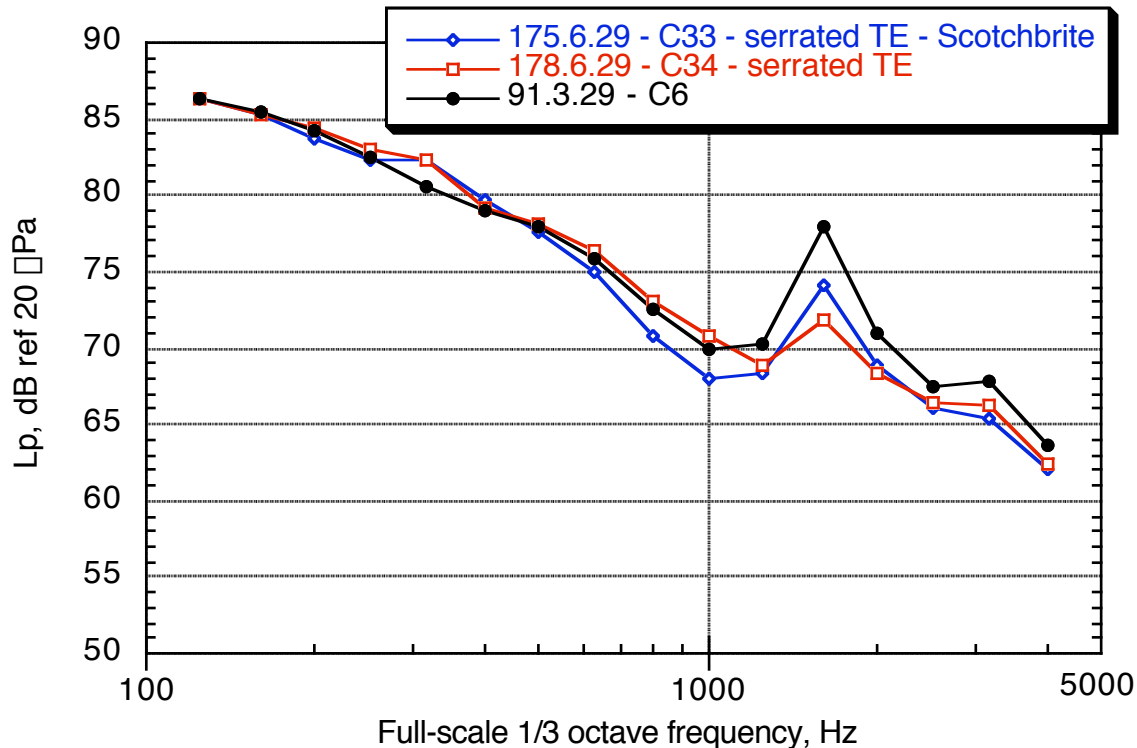


Figure 102. Slat serration geometry.

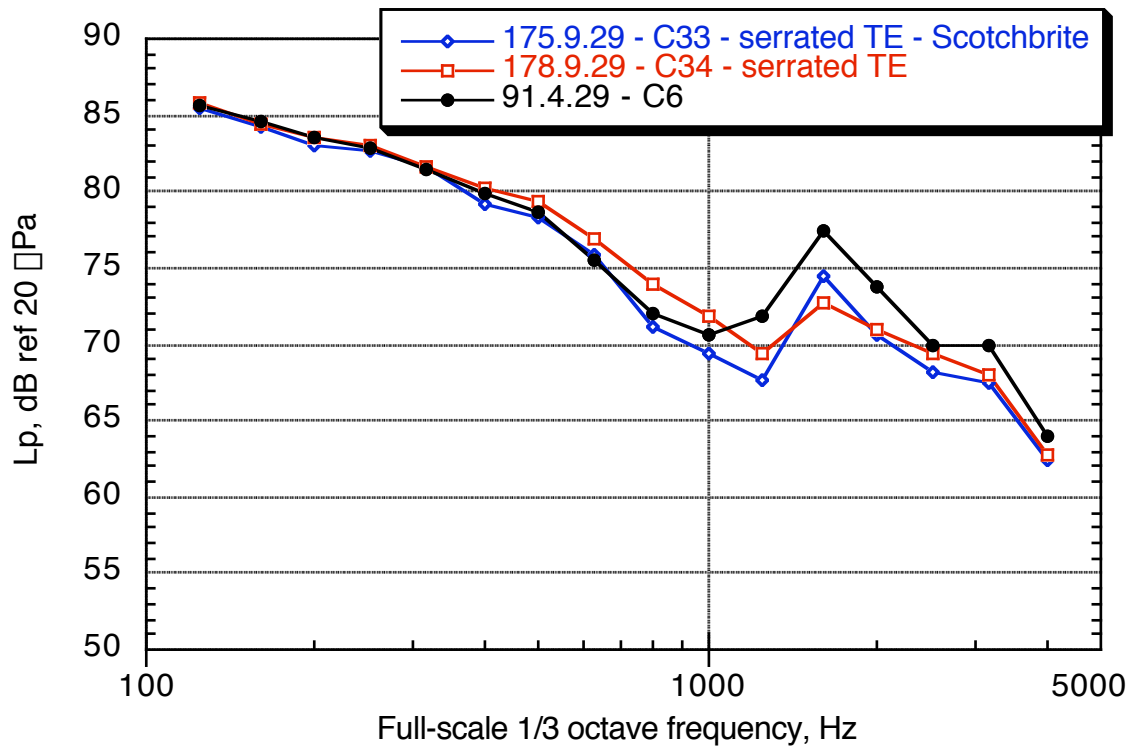


(a) Traverse position = 100 in. upstream.

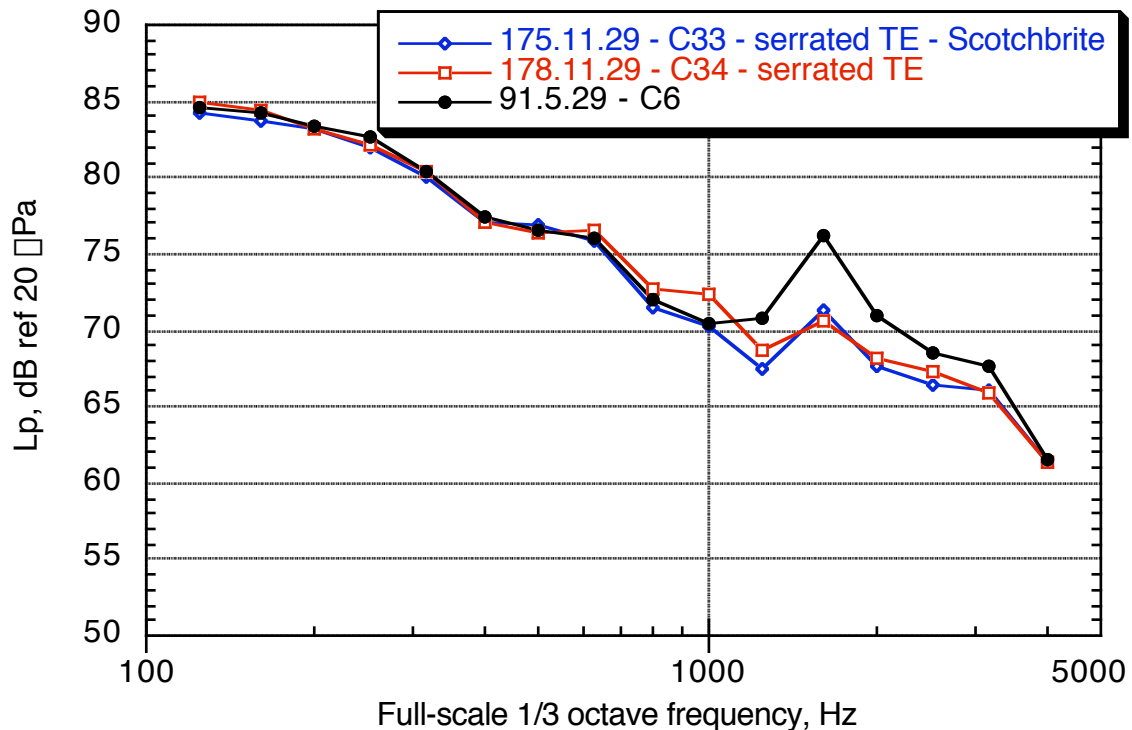


(b) Traverse position = 0 in.

Figure 103. Effect of serrated slat TE with and without fiber pad treatment on slat brackets: landing configuration,  $\alpha = 6^\circ$ ,  $M = 0.21$ .

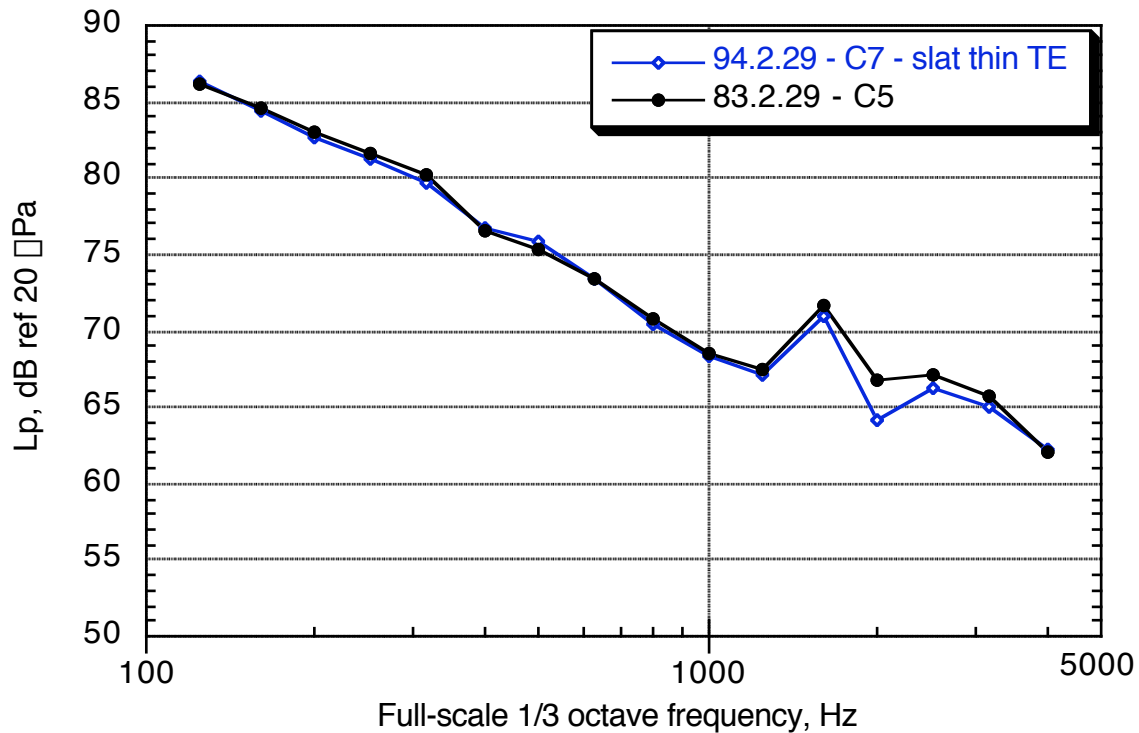


(c) Traverse position = 150 in. downstream.

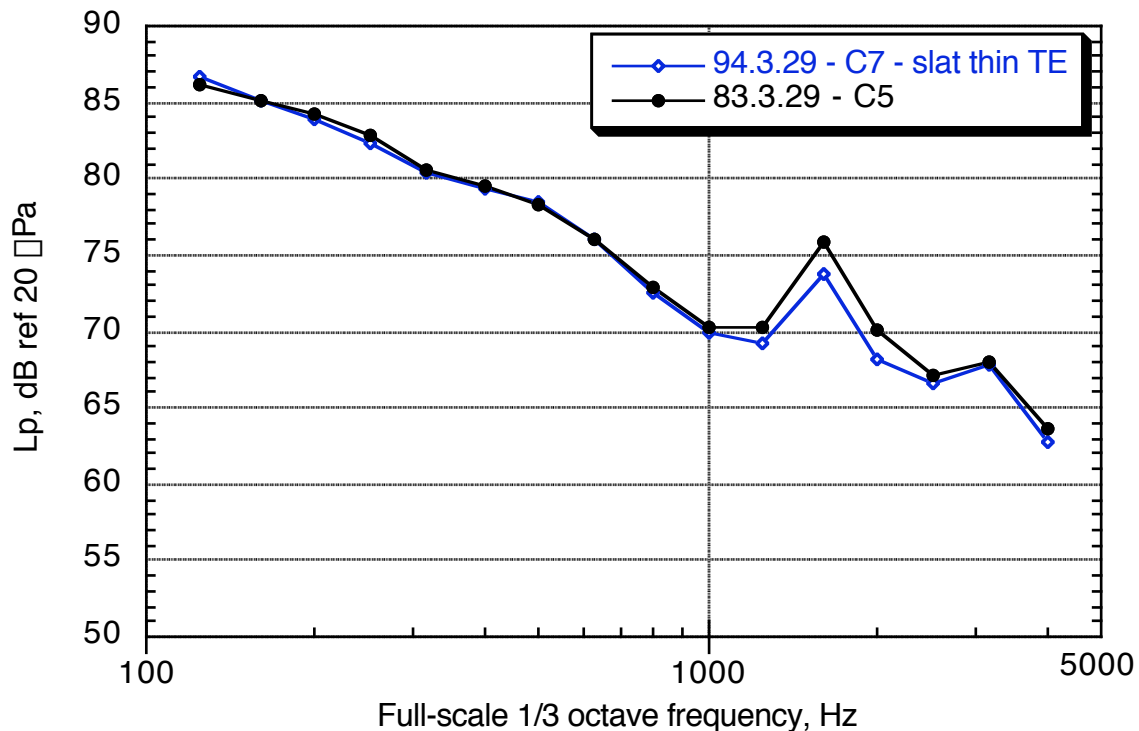


(d) Traverse position = 250 in. downstream.

Figure 103. Concluded.

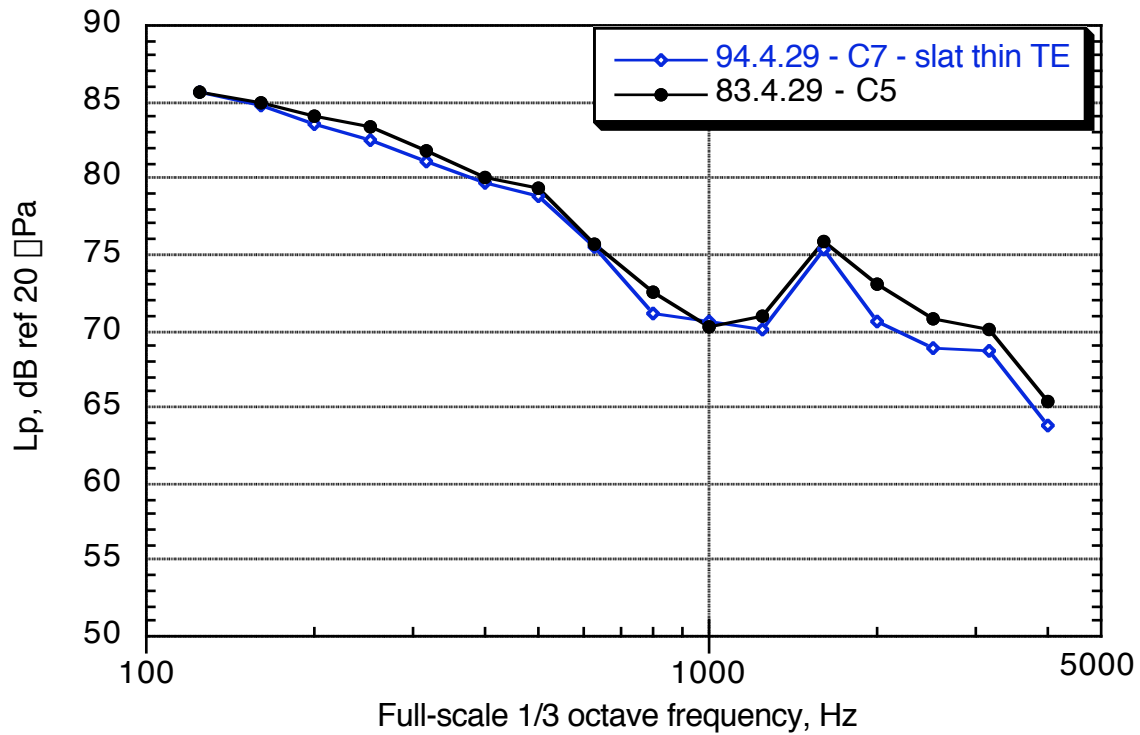


(a) Traverse position = 100 in. upstream.

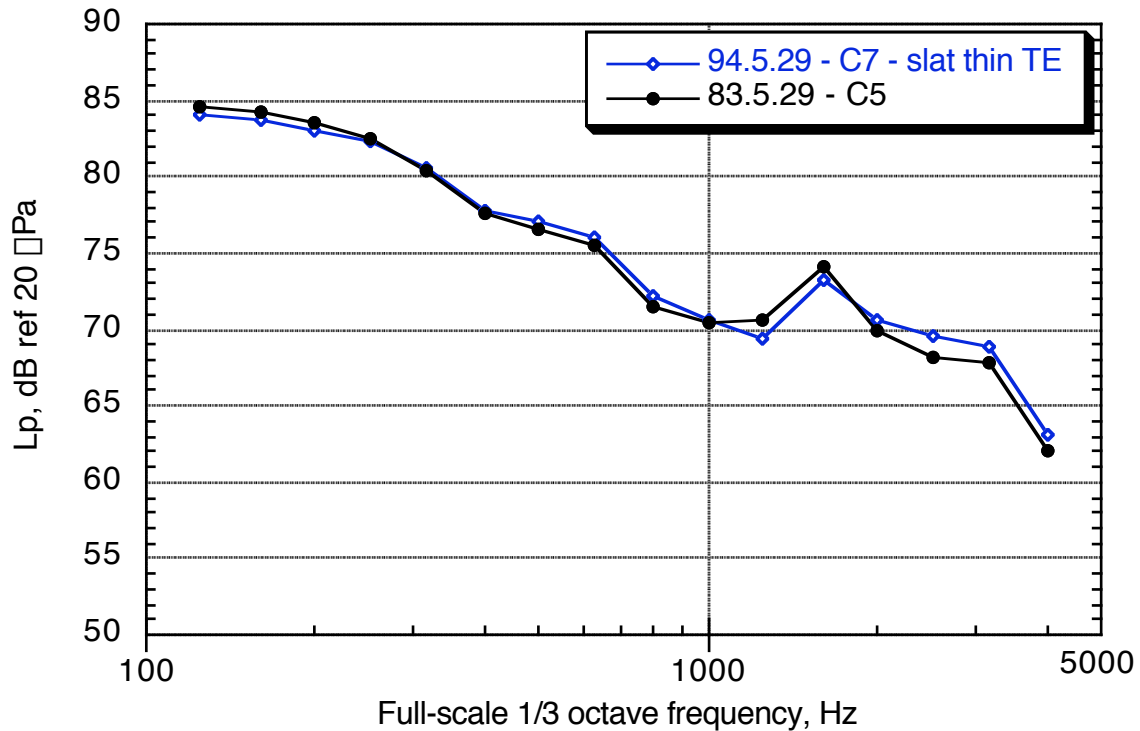


(b) Traverse position = 0 in.

Figure 104. Effect of thin slat trailing edge: landing configuration,  $\alpha = 6^\circ$ ,  $M = 0.21$ .



(c) Traverse position = 150 in. downstream.



(d) Traverse position = 250 in. downstream.

Figure 104. Concluded.

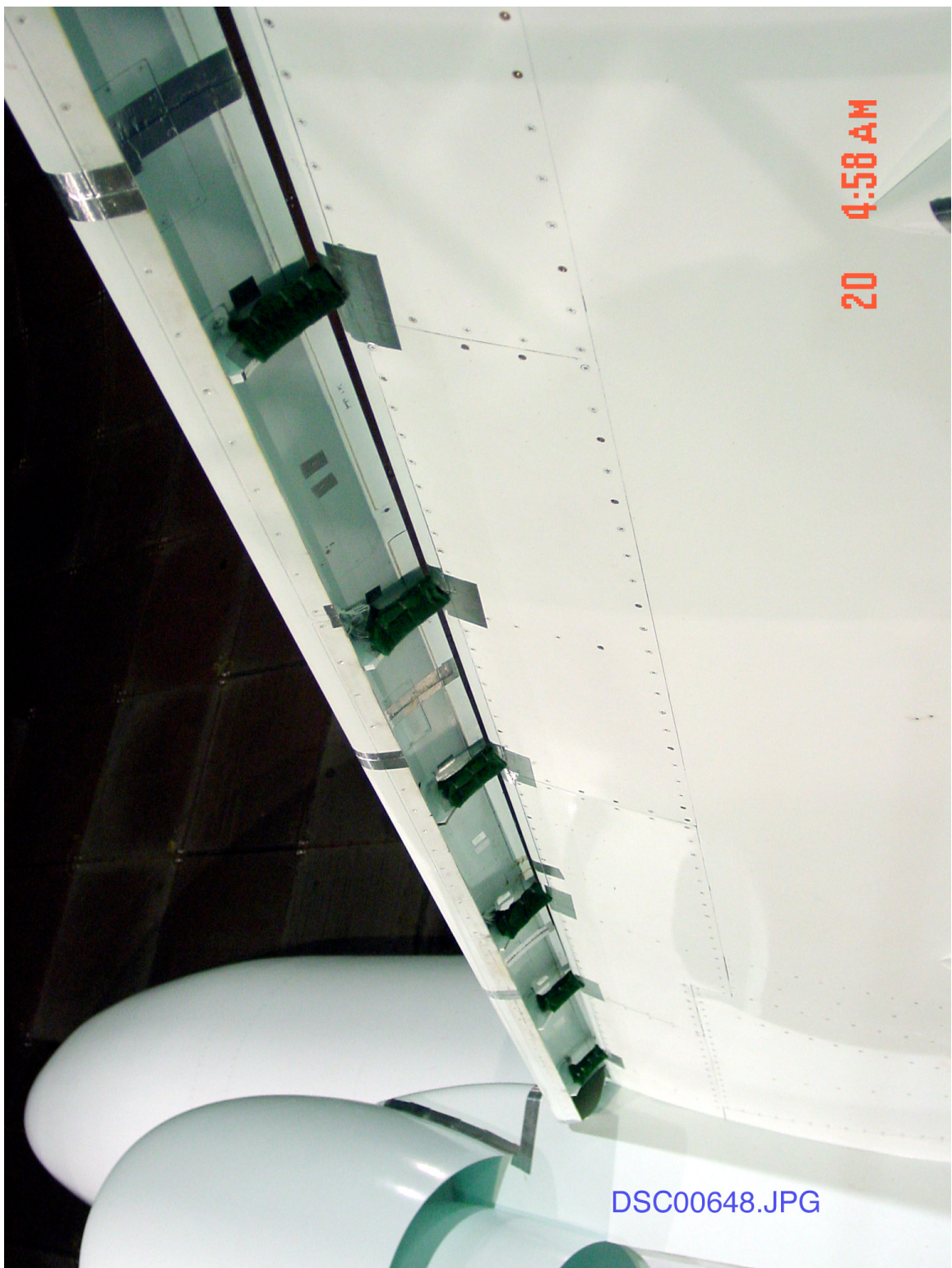
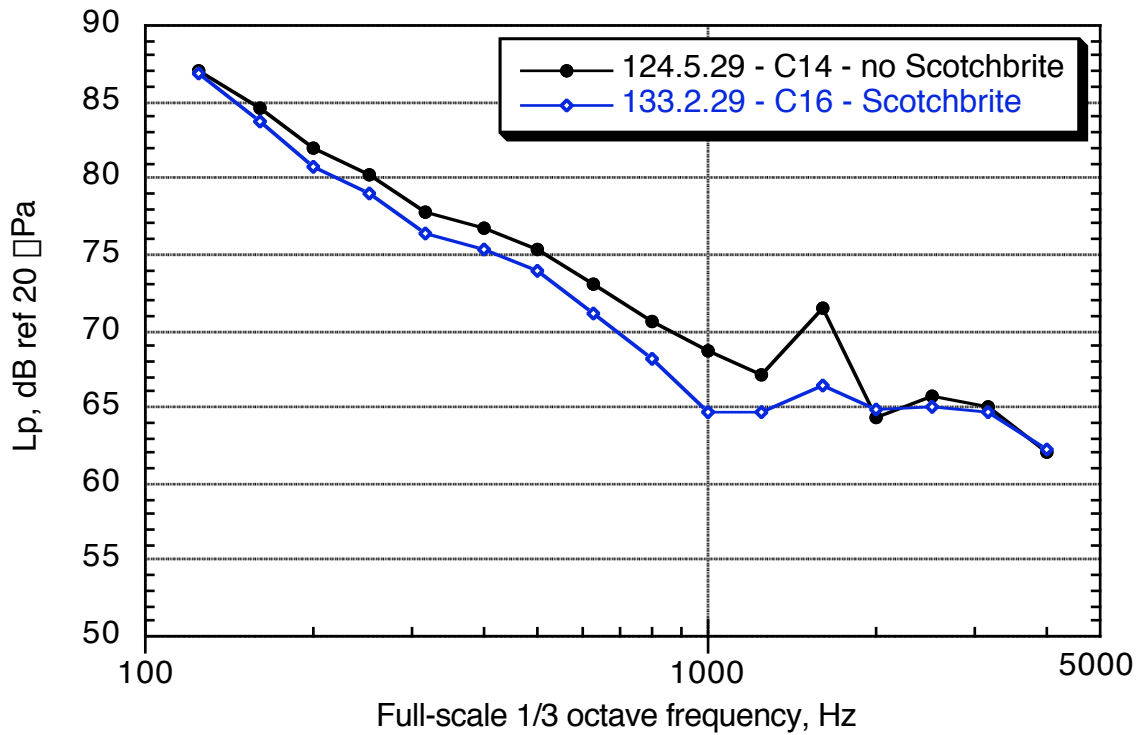
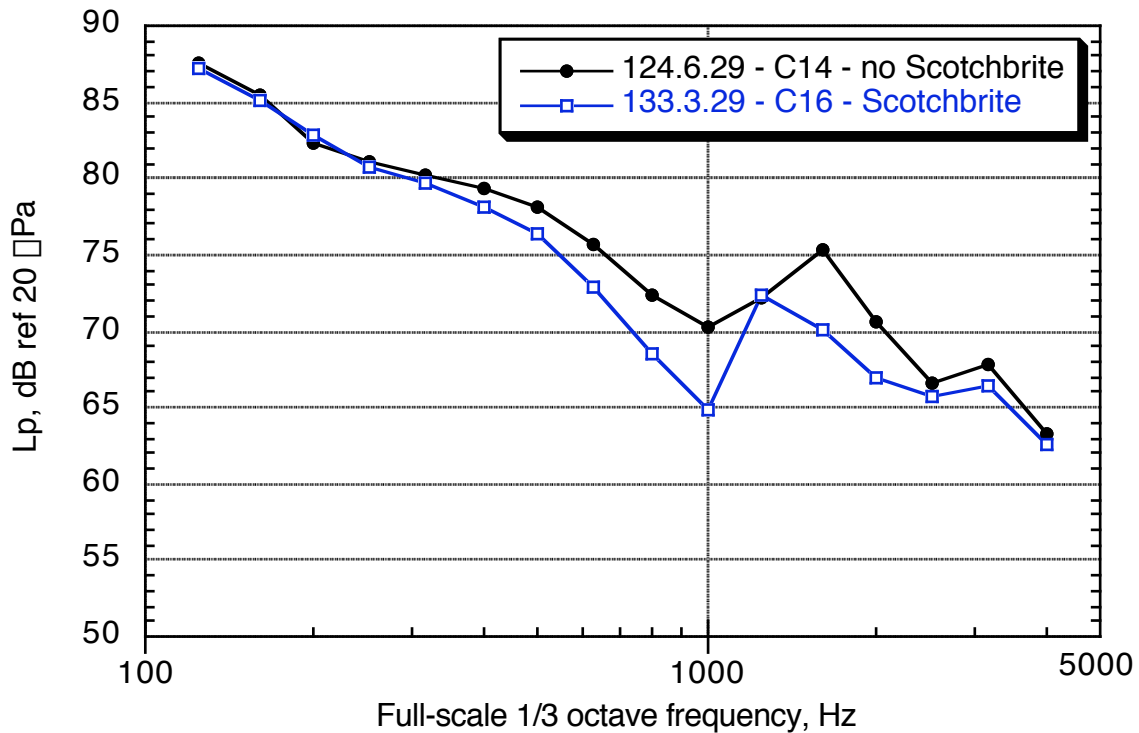


Figure 105. Porous pad (Scotchbrite) sleeve on slat brackets.

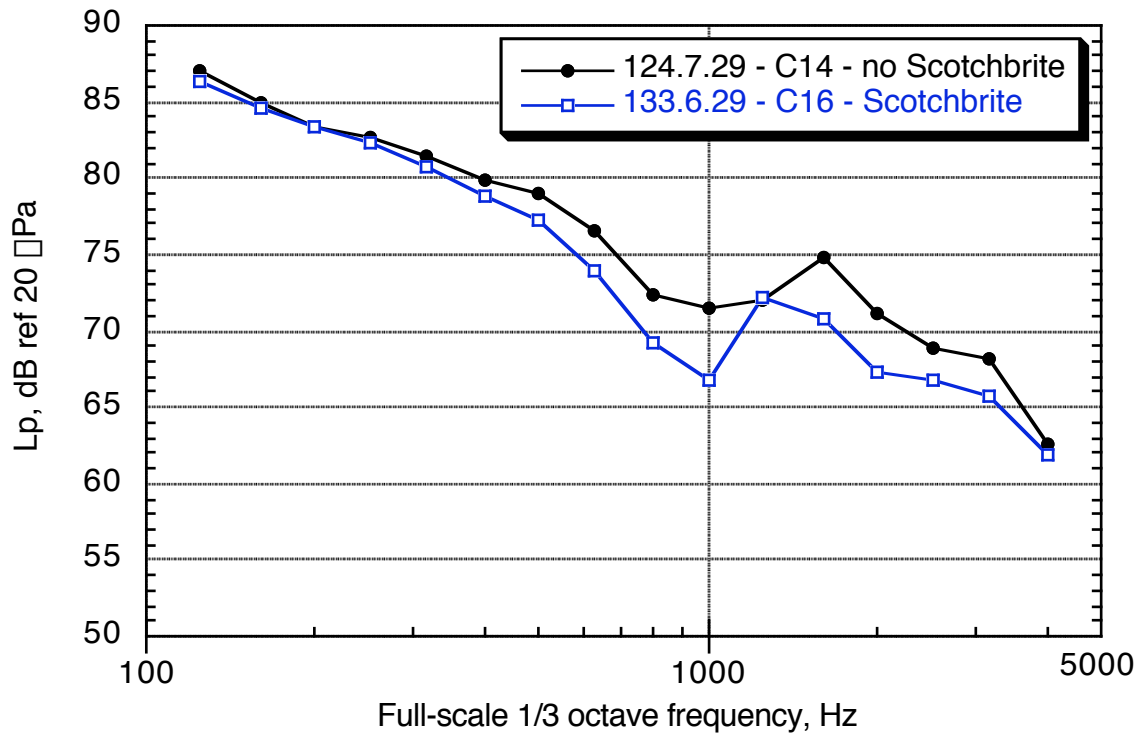


(a) Traverse position = 100 in. upstream.

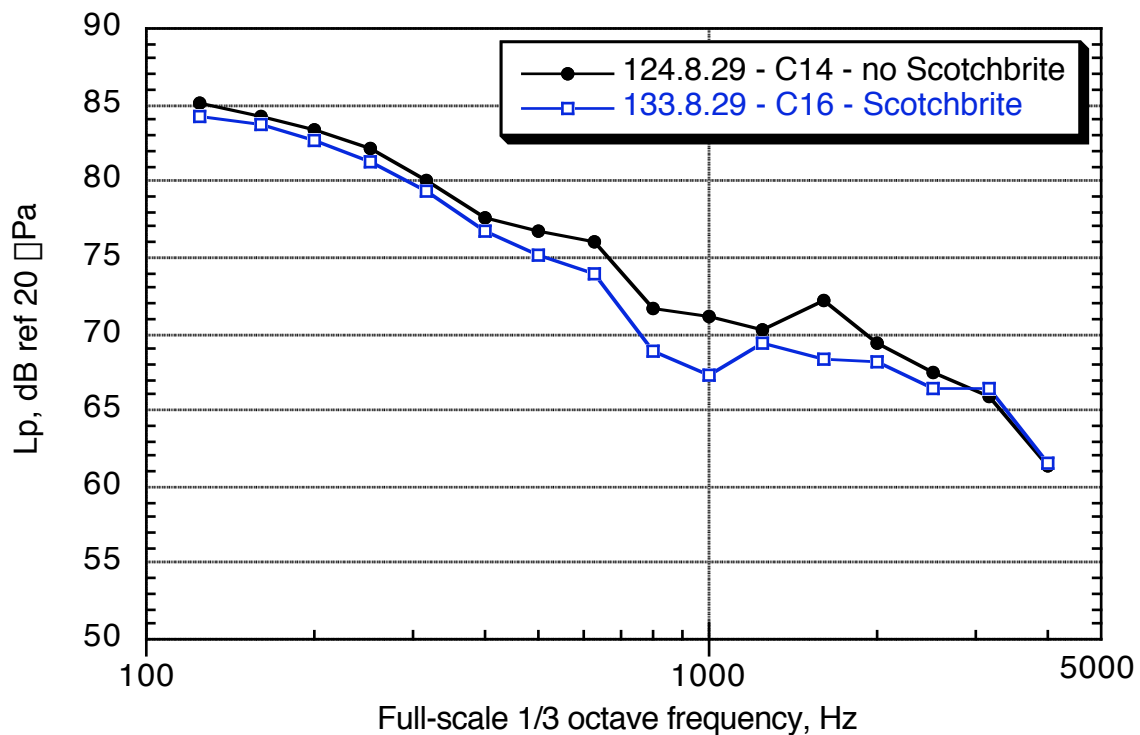


(b) Traverse position = 0 in.

Figure 106. Effect of porous pad (Scotchbrite) treatment of slat brackets on slat cove noise: approach configuration,  $M = 0.21$ ,  $\alpha = 6^\circ$ .



(c) Traverse position = 150 in. downstream.



(d) Traverse position = 250 in. downstream.

Figure 106. Concluded

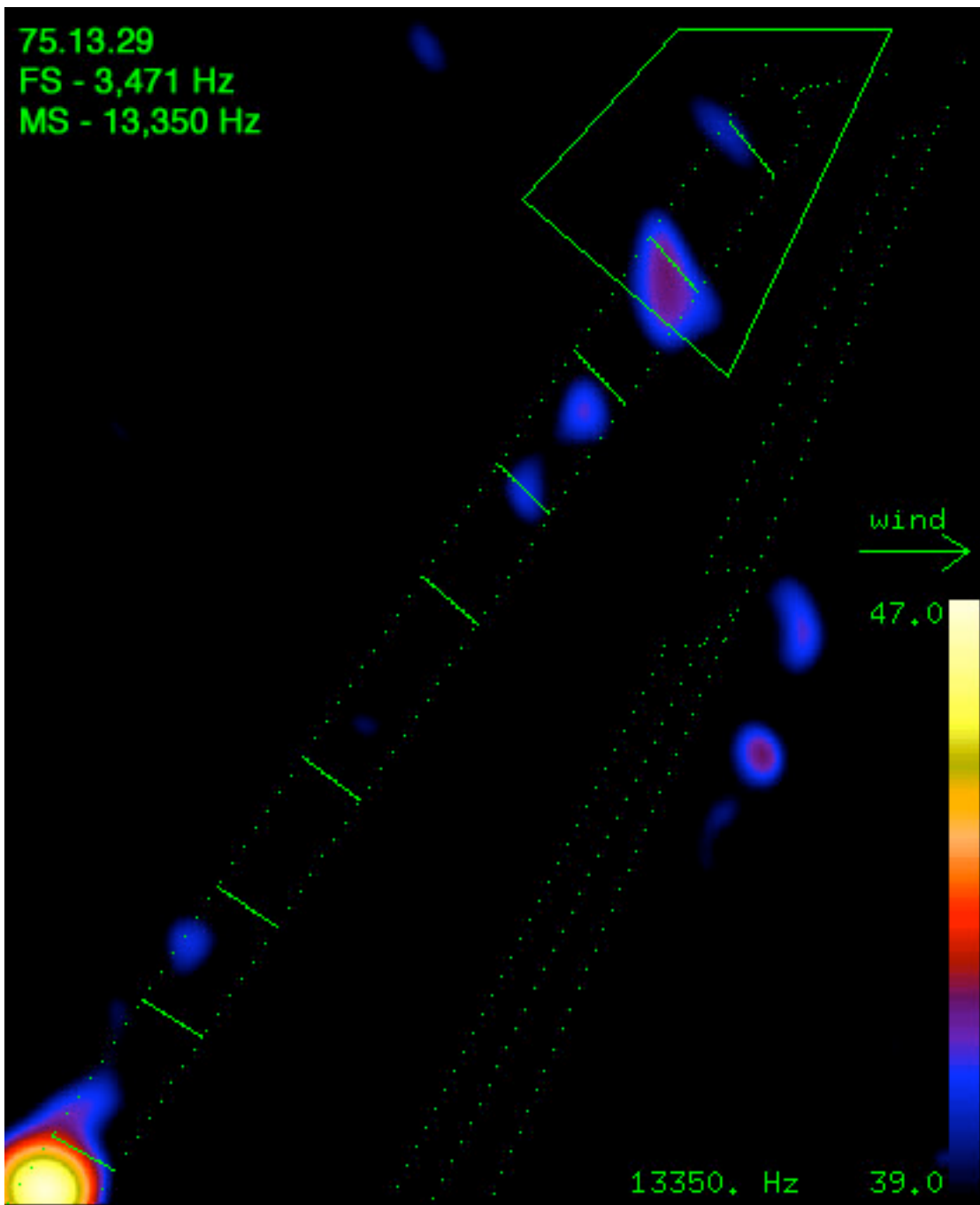


Figure 107. Integration region for outboard-slat outboard-tip.

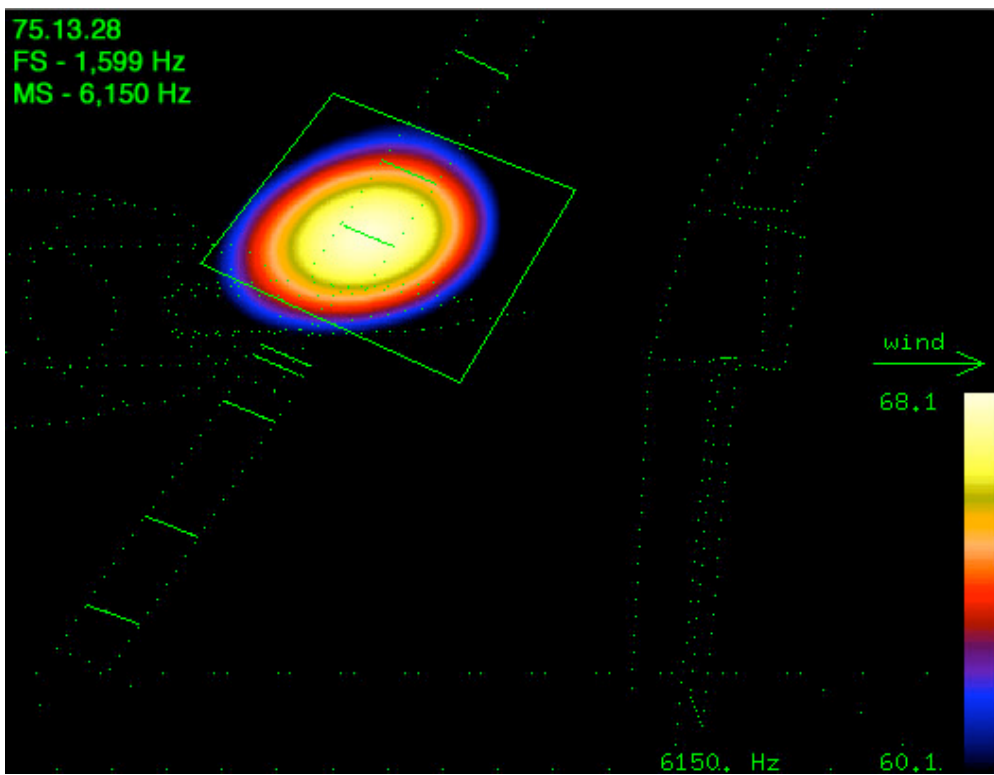


Figure 108. Integration region for inboard tip of outboard slat.

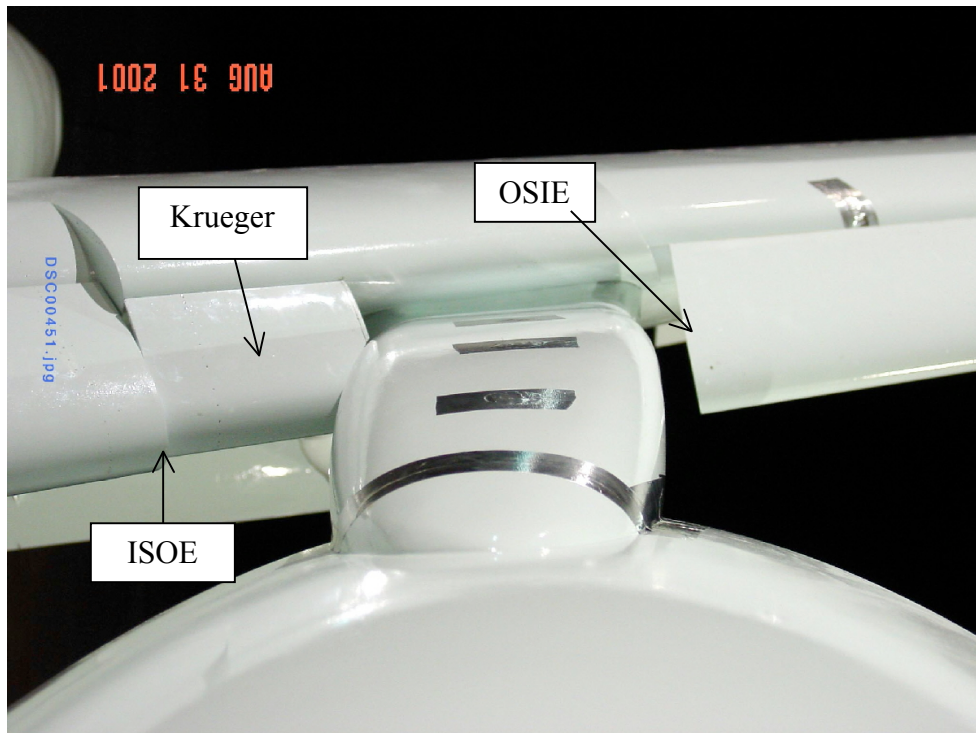
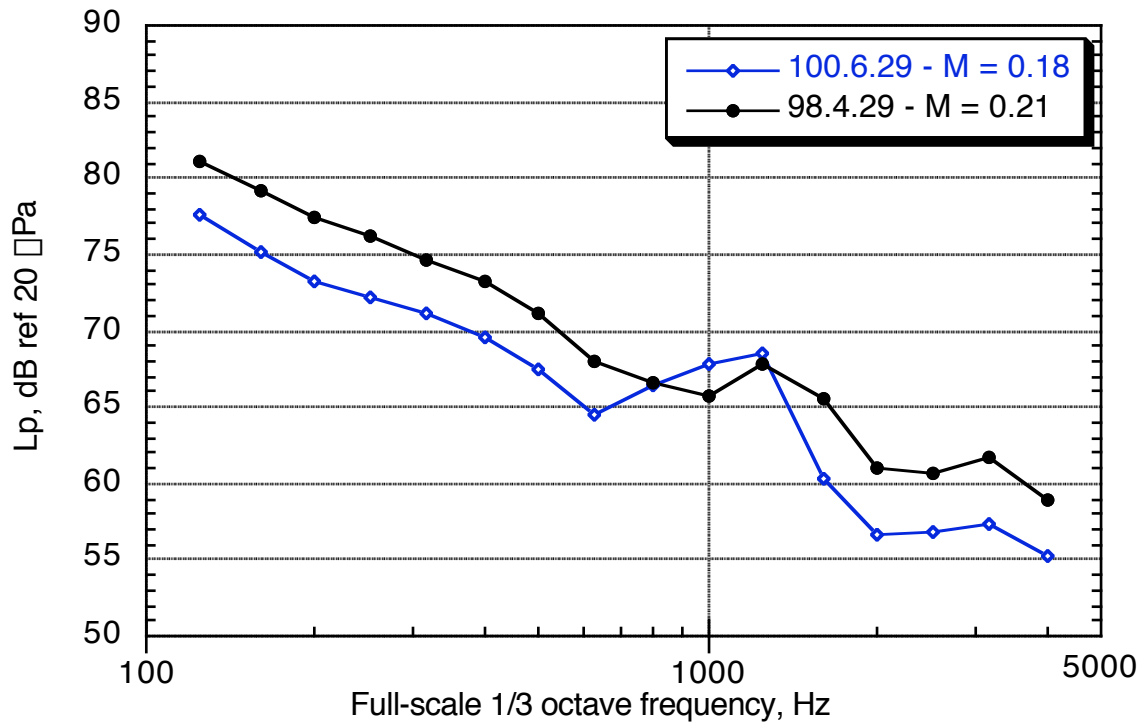
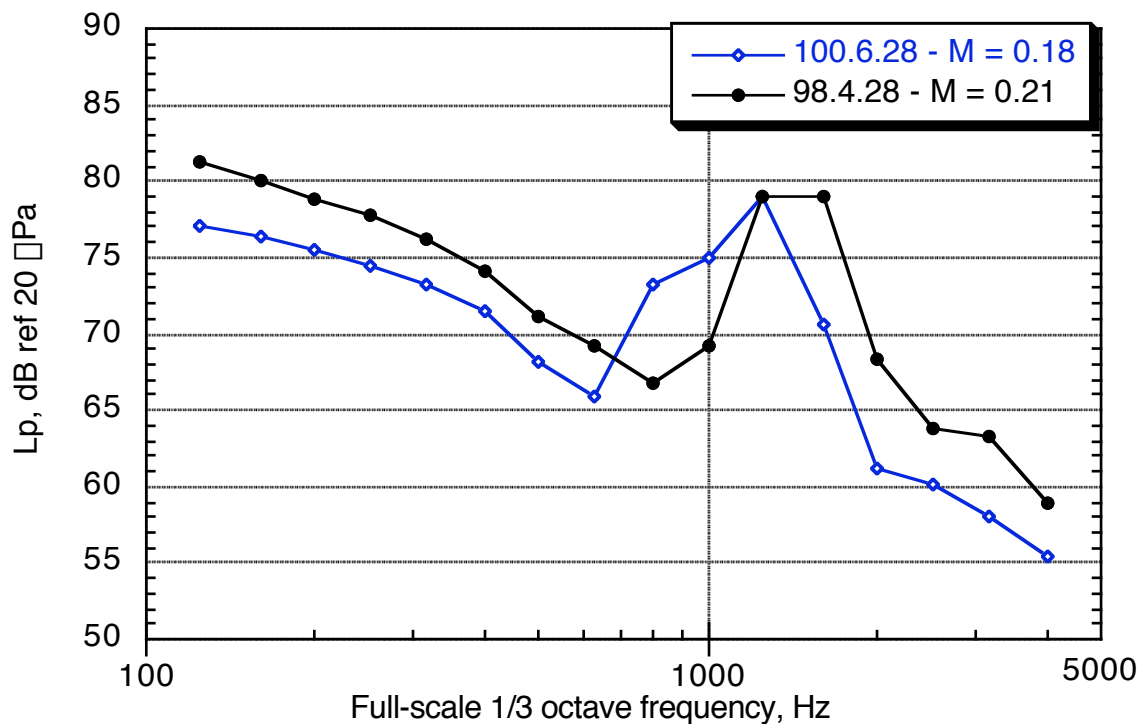


Figure 109. Front view of leading-edge high-lift system near nacelle pylon. From left to right: outboard edge of inboard slat (slotted), Krueger (non-slotted), nacelle pylon, inboard edge of outboard slat (slotted).

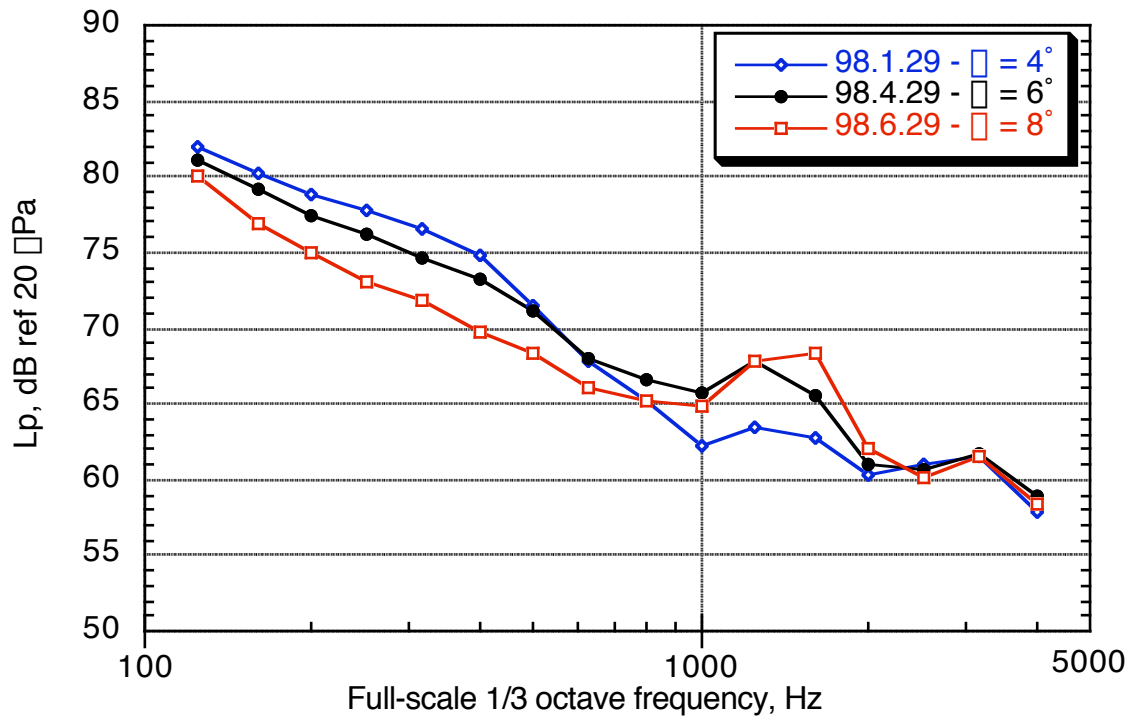


(a) Outboard slat outboard edge.

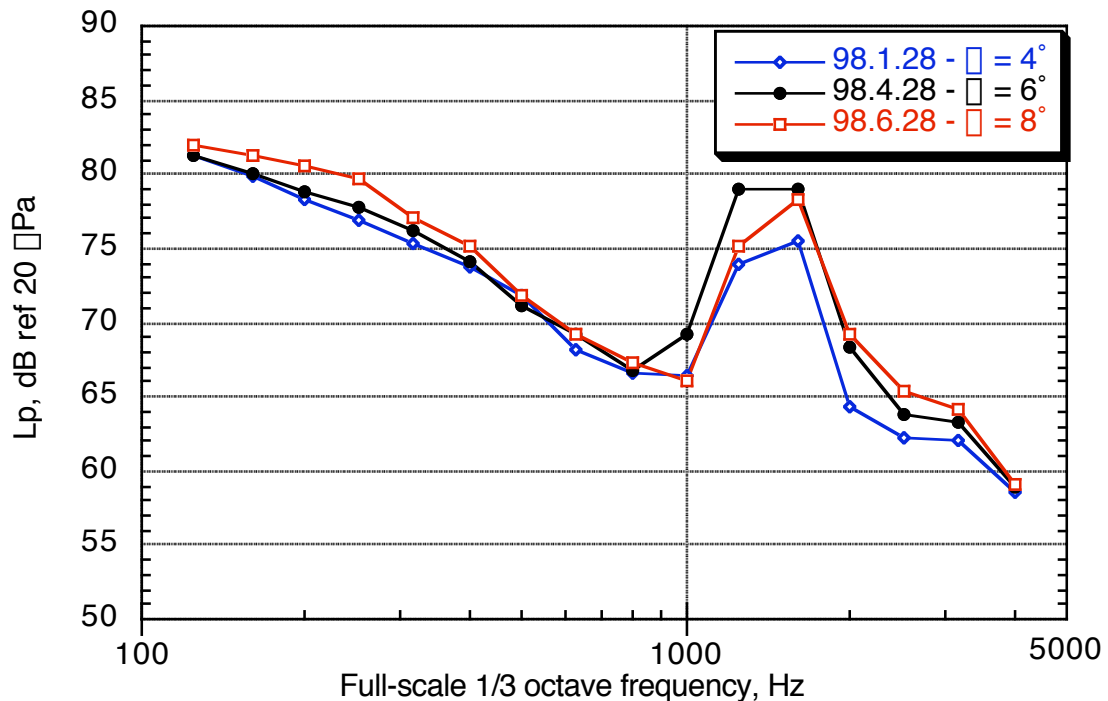


(b) Outboard slat inboard edge.

Figure 110. Mach number effect on outboard slat-tip regions: landing configuration, traverse = 150 in. downstream.

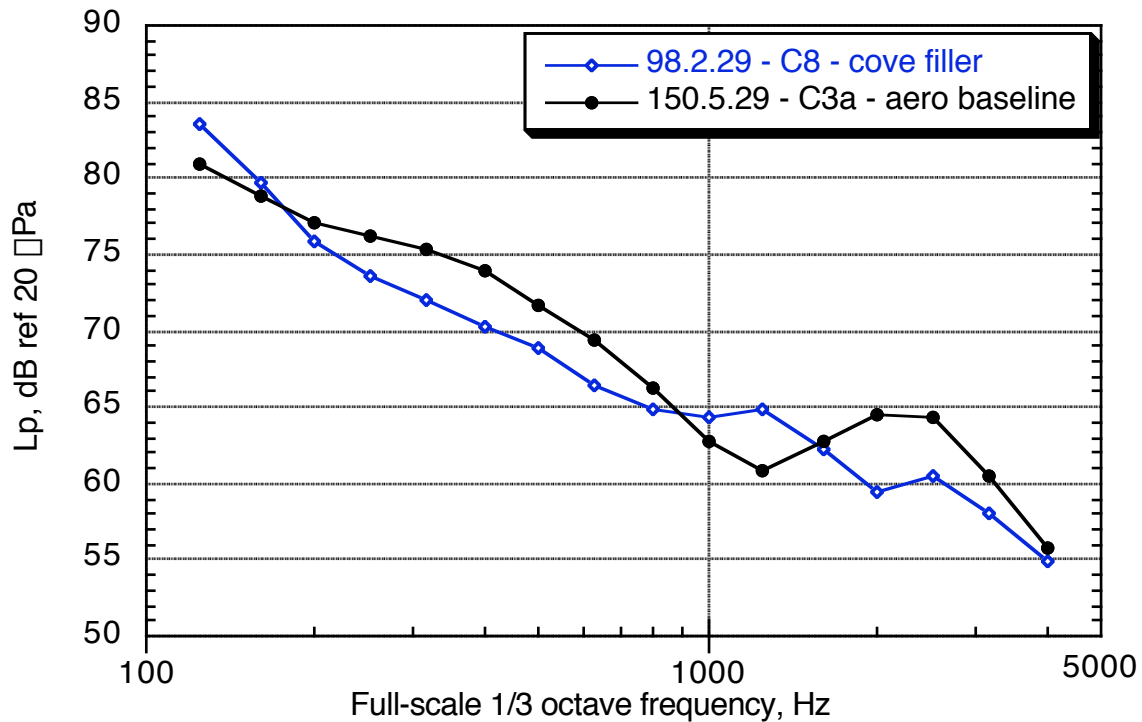


(a) Outboard slat outboard tip region.

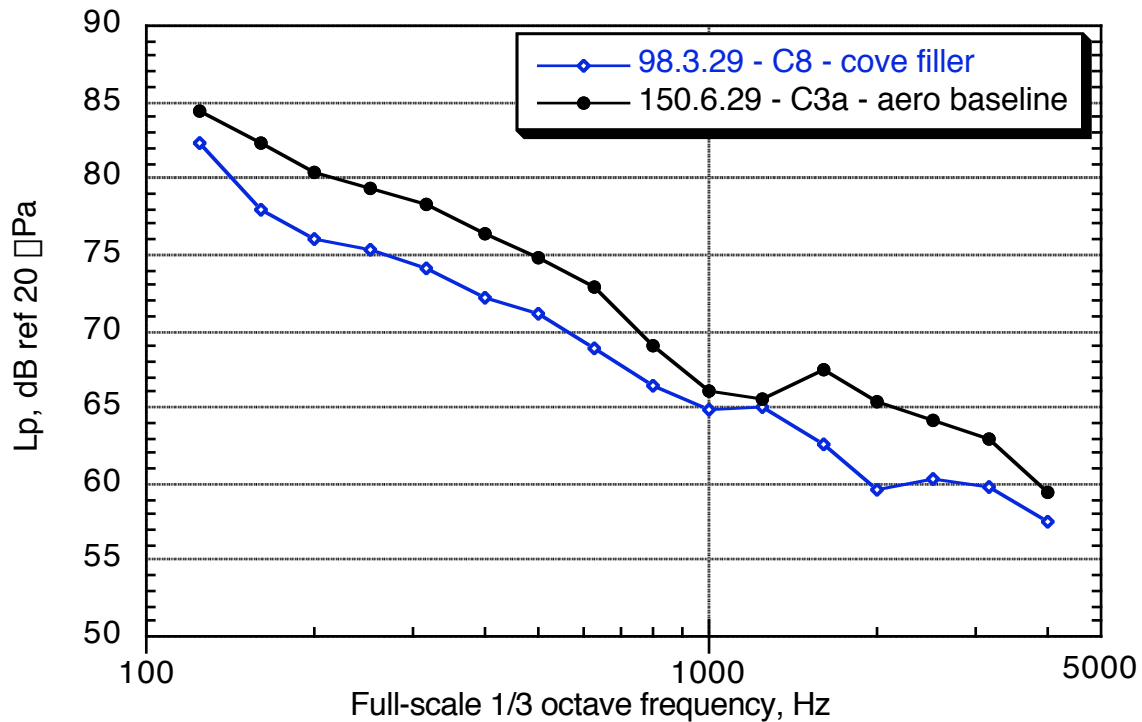


(b) Outboard slat inboard tip region.

Figure 111. Angle-of-attack effect on outboard slat-tip noise: landing configuration, traverse = 150 in. downstream,  $M = 0.21$ .

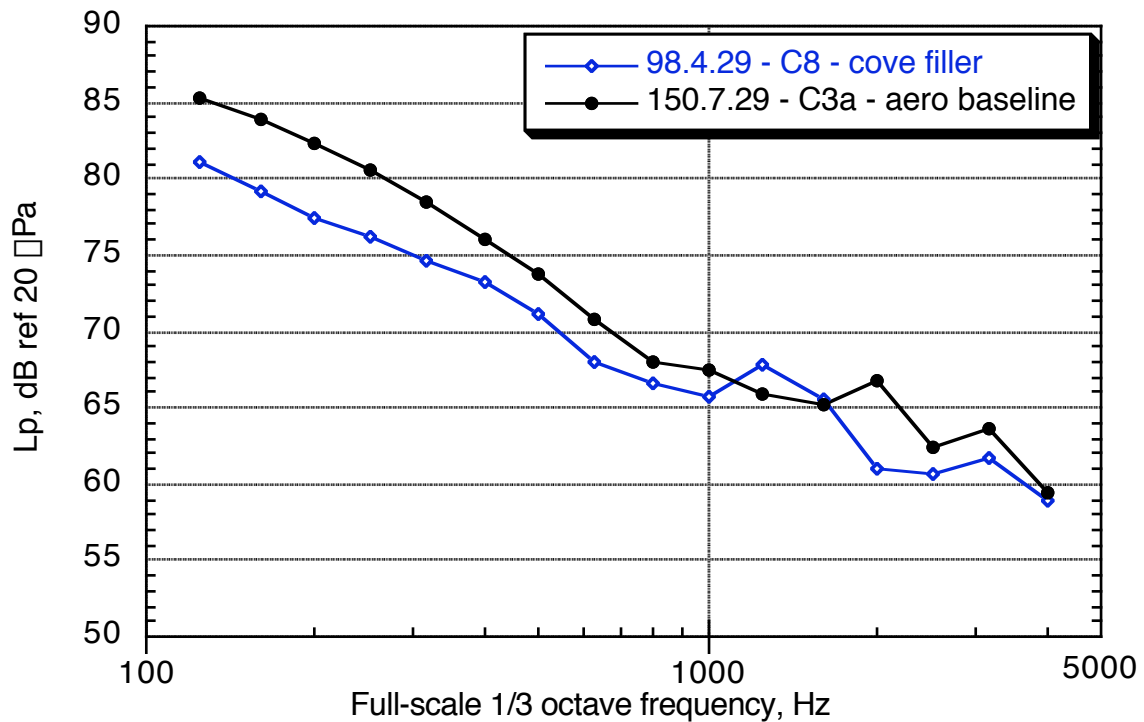


(a) Traverse = 100 in. upstream.

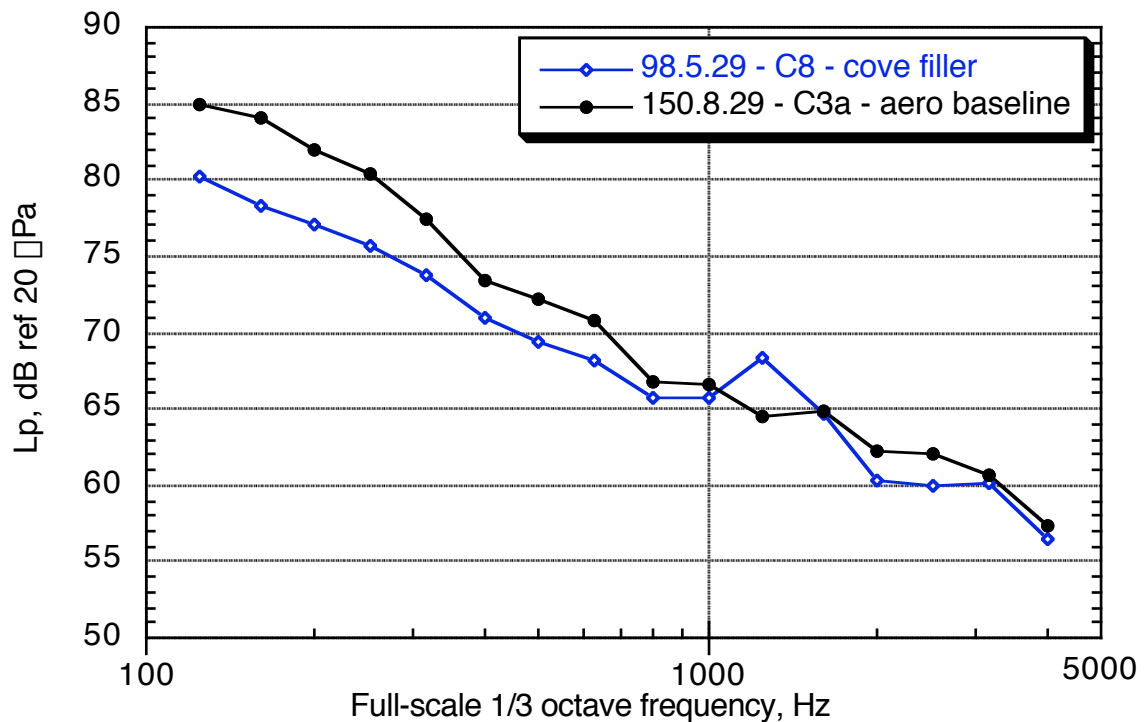


(b) Traverse = 0 in.

Figure 112. Outboard-slat outboard-tip region: landing configuration,  $M = 0.21$ ,  $\alpha = 6^\circ$ .

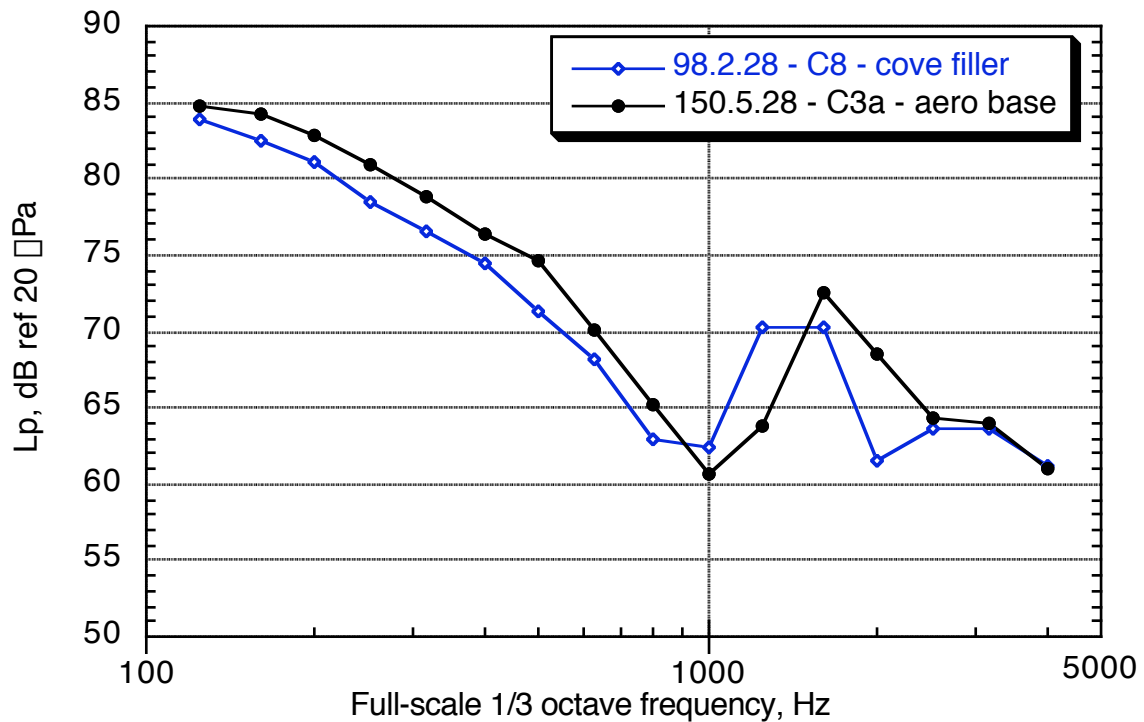


(c) Traverse = 150 in. downstream.

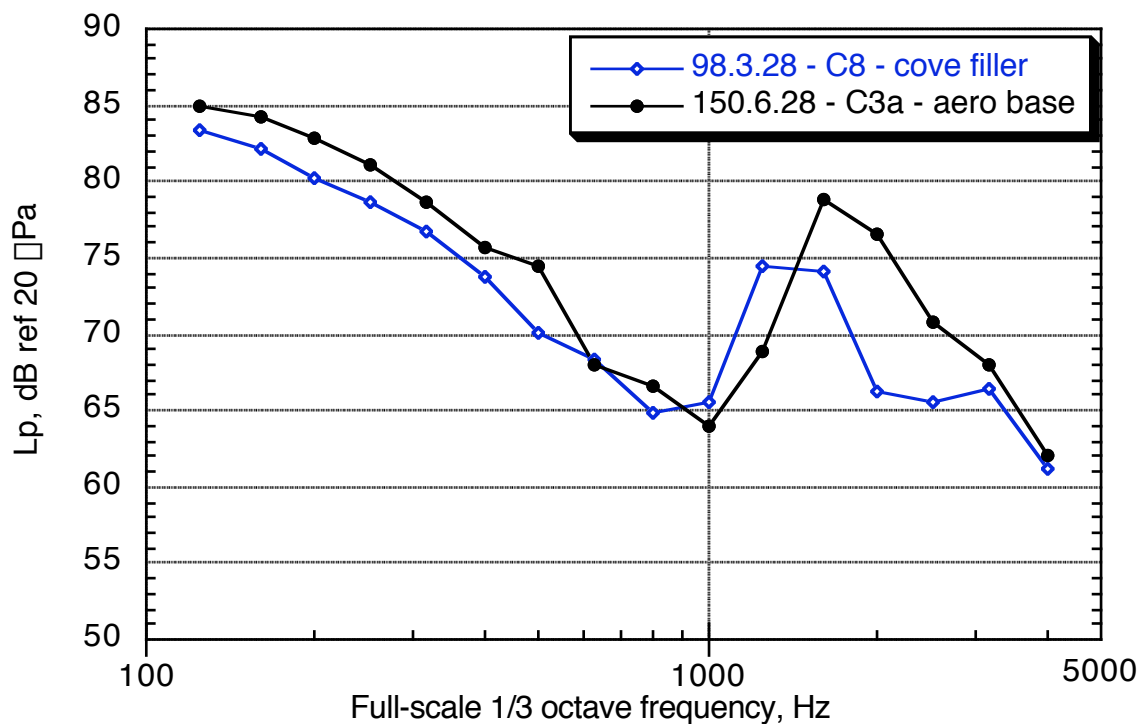


(d) Traverse = 250 in. downstream.

Figure 112. Concluded.

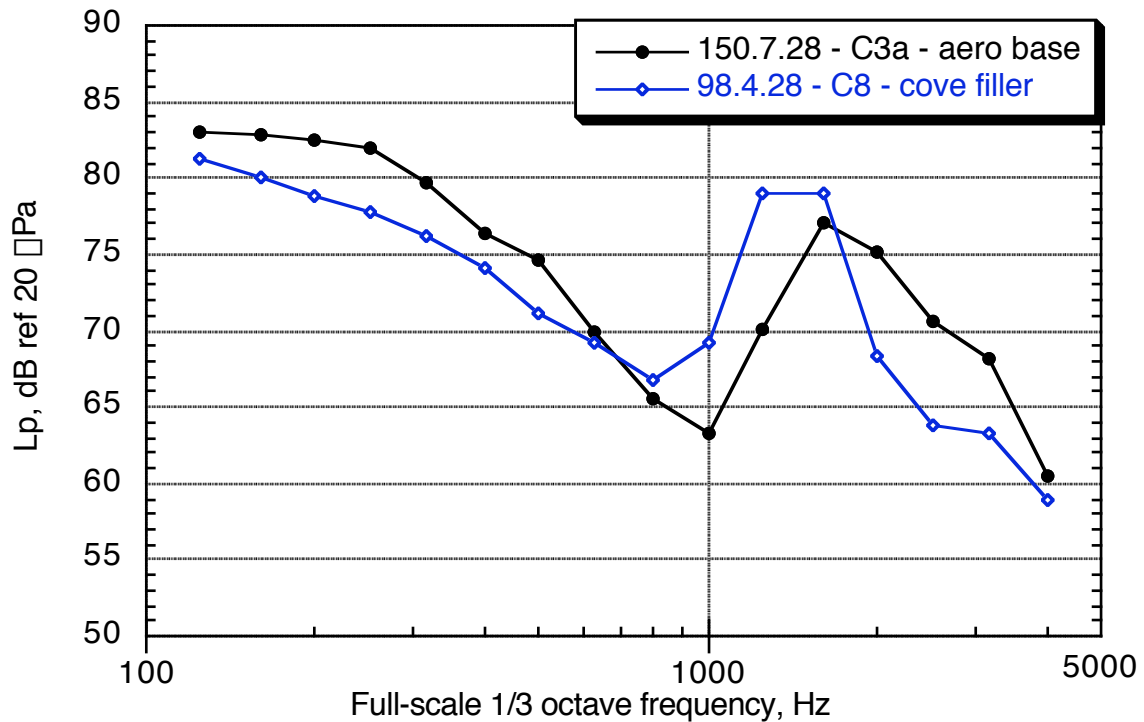


(a) Traverse = 100 in. upstream.

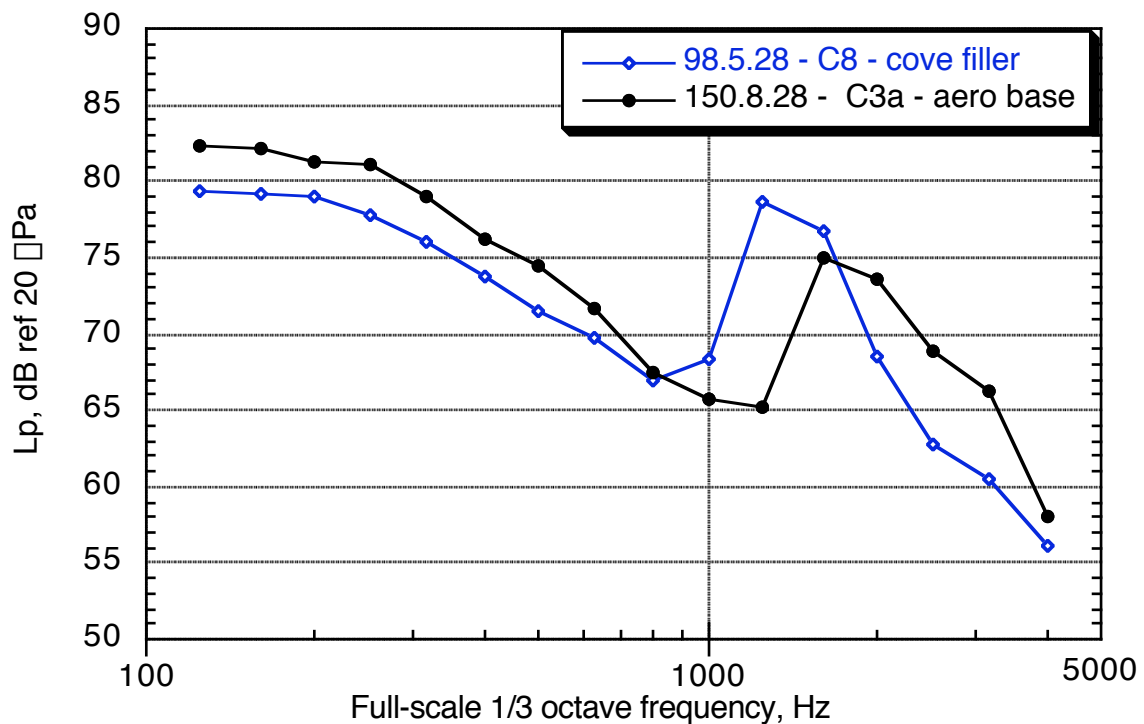


(b) Traverse = 0 in.

Figure 113. Outboard-slat inboard-tip region: landing configuration,  $M = 0.21$ ,  $\alpha = 6^\circ$ .



(c) Traverse = 150 in. downstream.

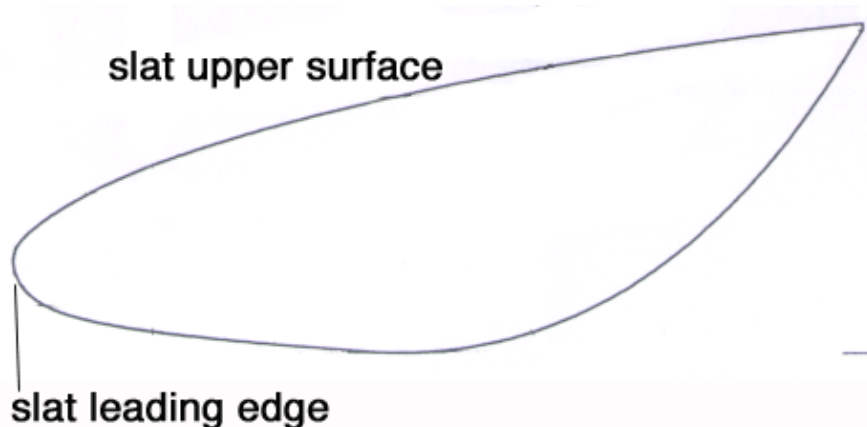


(d) Traverse = 250 in. downstream.

Figure 113. Concluded.



(a) Outboard slat-tip fence photo.



(b) Outboard-slat outboard-edge fence sketch.

Figure 114. Slat-tip fence placed on the outboard edge of outboard slat.

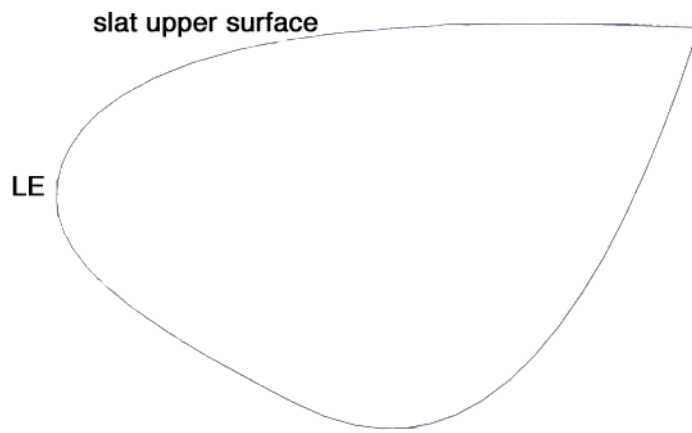
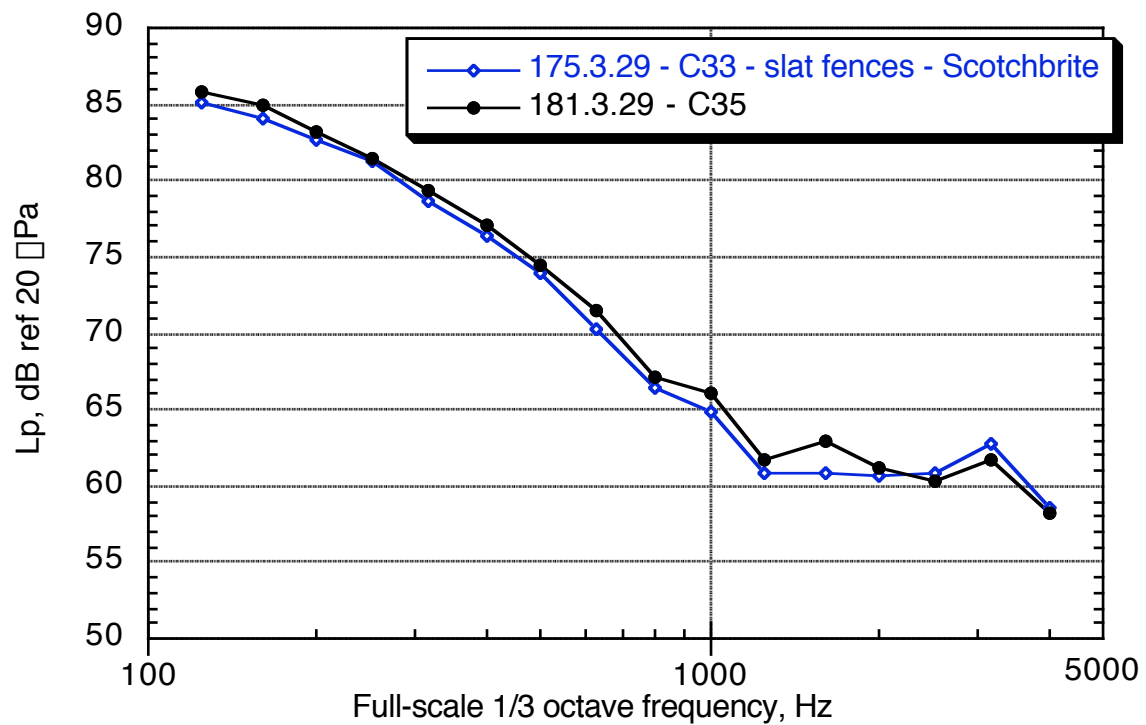
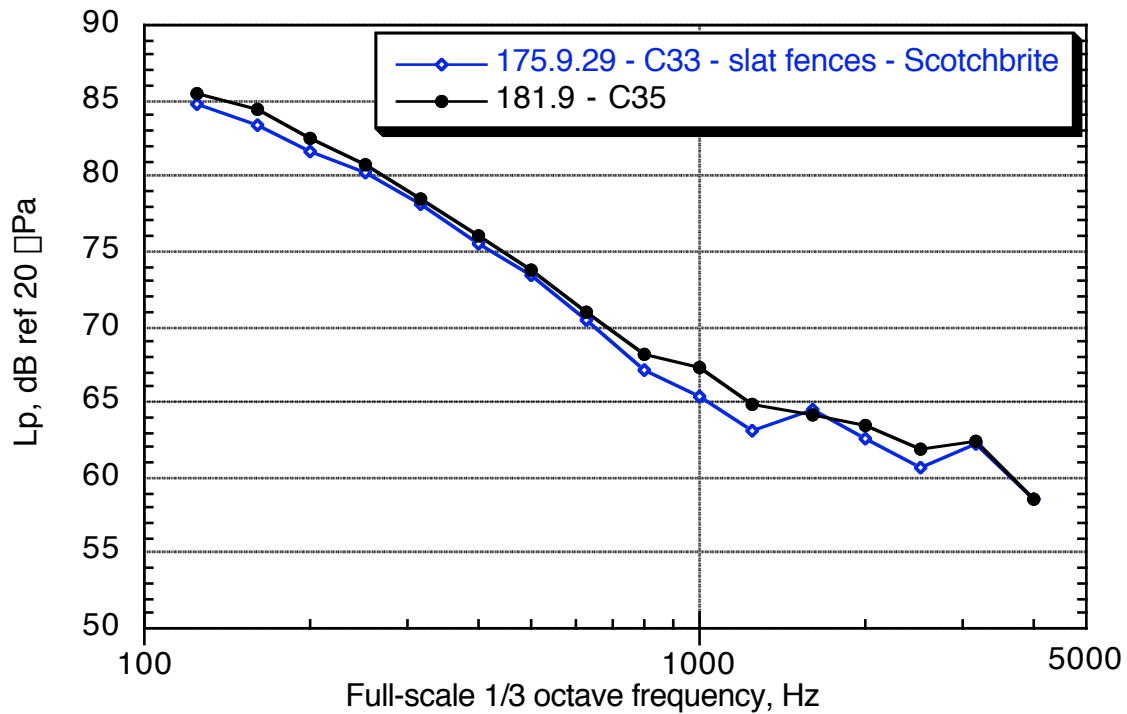


Figure 115. Outboard-slat inboard-edge fence.

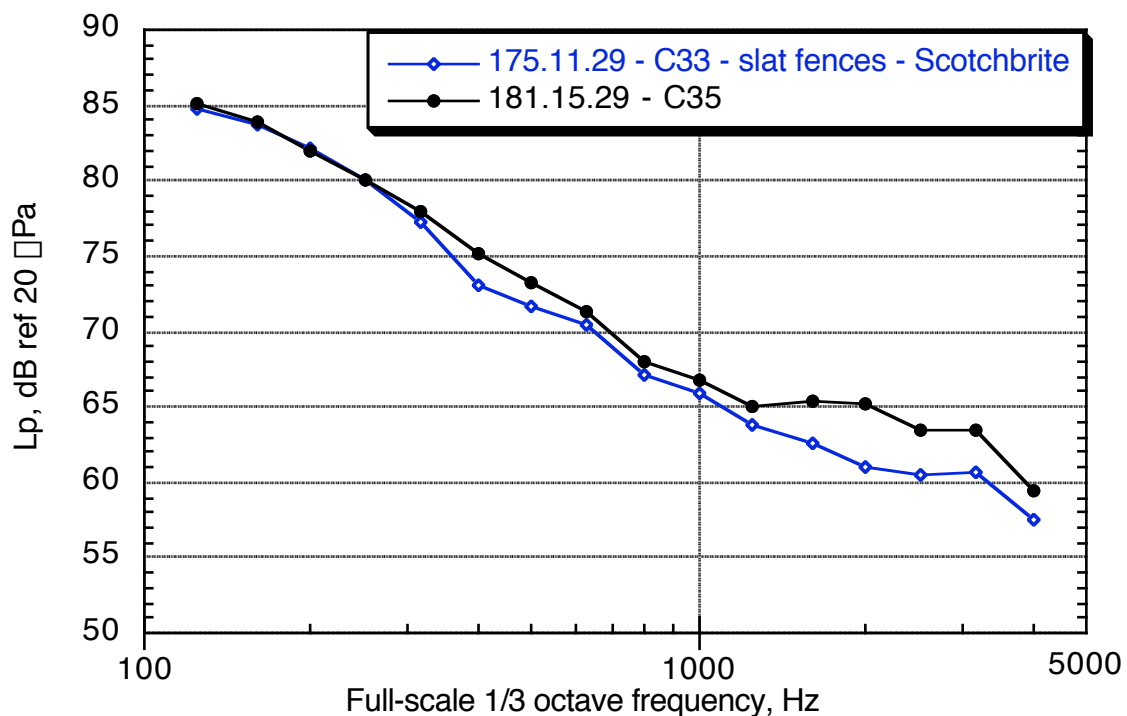


(a)  $\alpha = 4^\circ$ .

Figure 116. Effect of slat-tip fence on outboard edge of outboard slat: landing configuration,  $M = 0.21$ , traverse position = 150 in. downstream (Scotchbrite on the slat brackets).

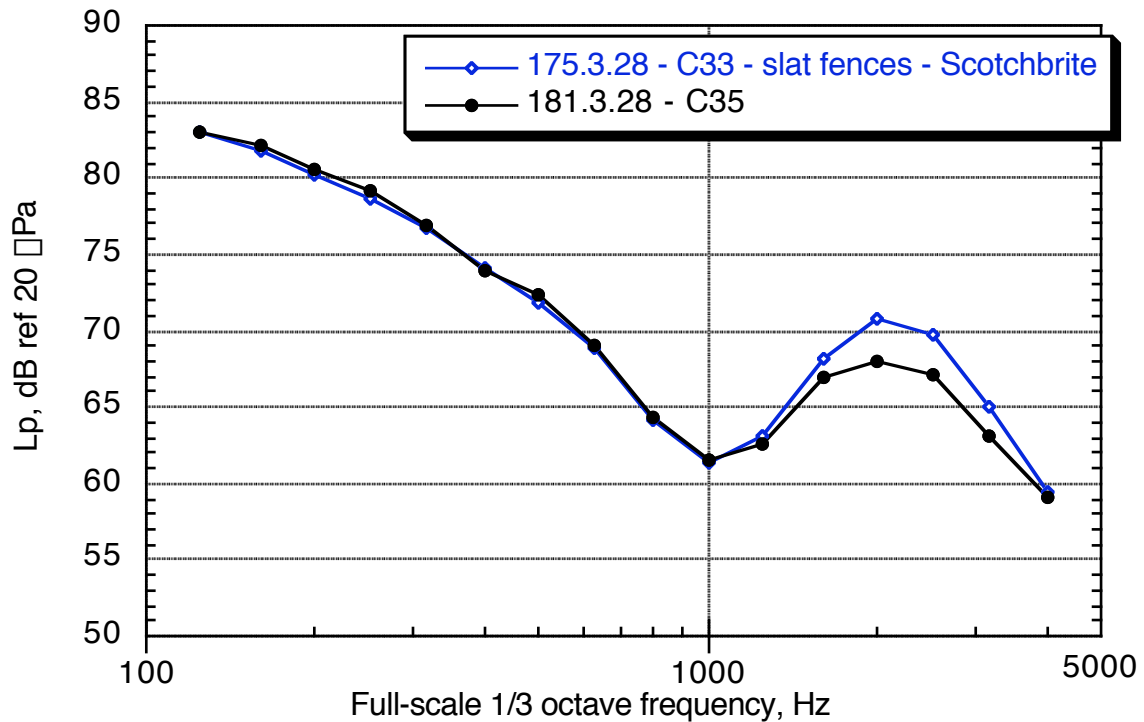


(b)  $\theta = 6^\circ$ .

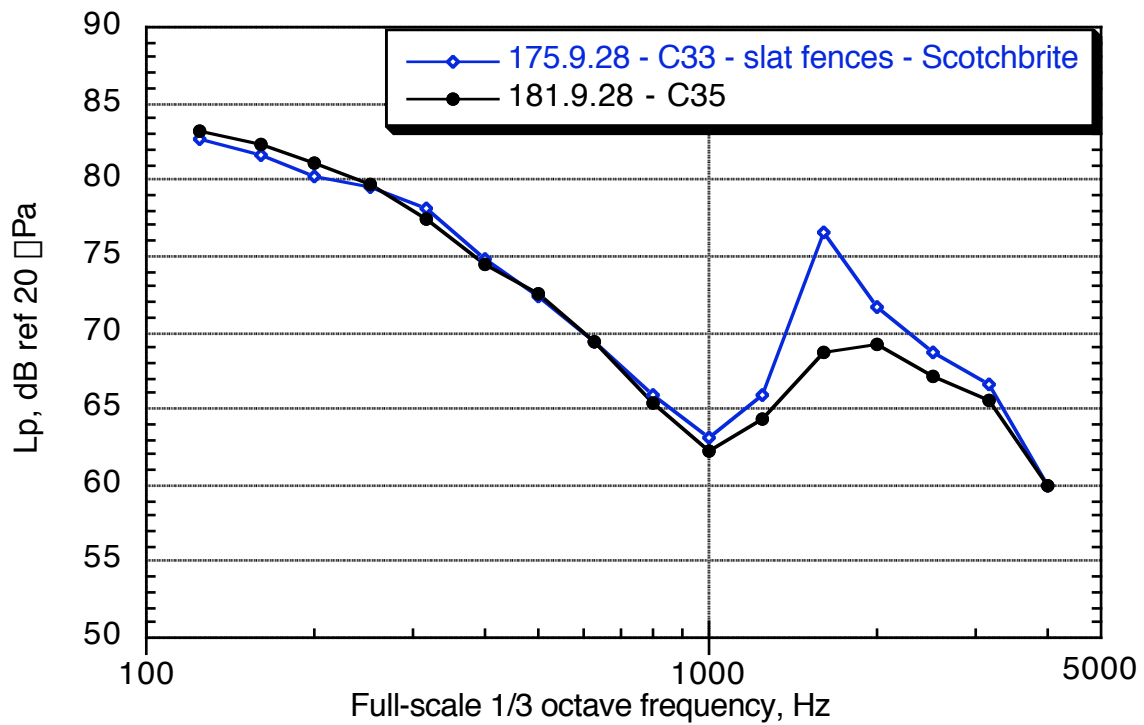


(c)  $\theta = 8^\circ$ .

Figure 116. Concluded.

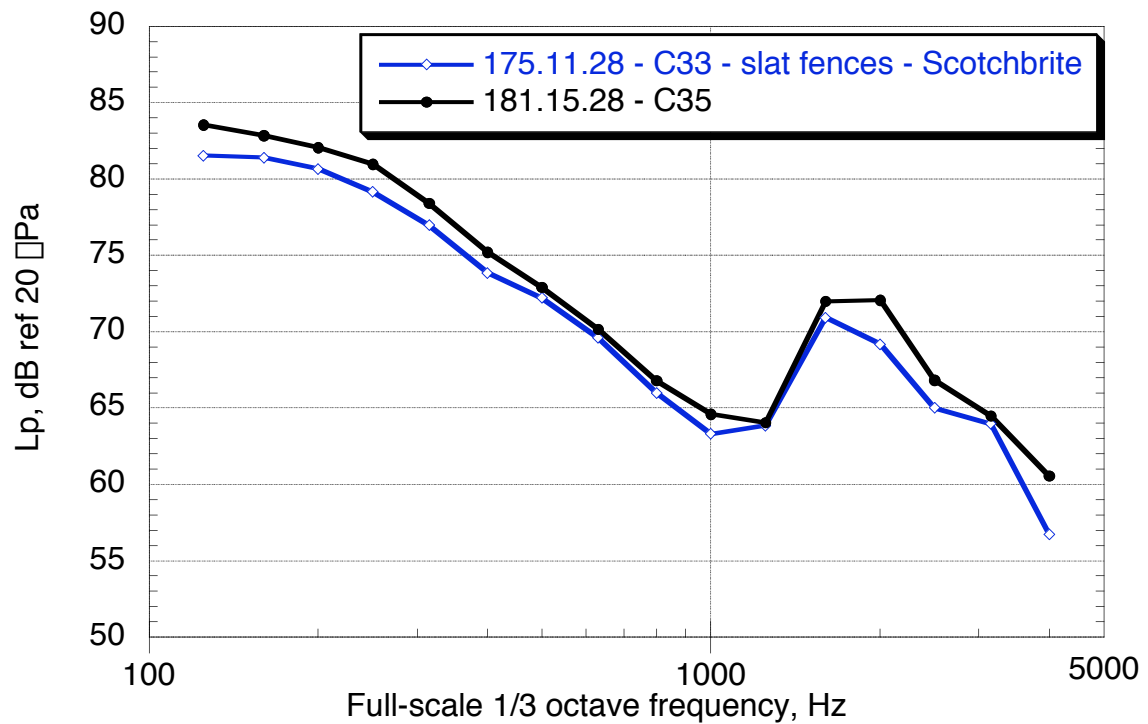


(a)  $\square = 4^\circ$ .



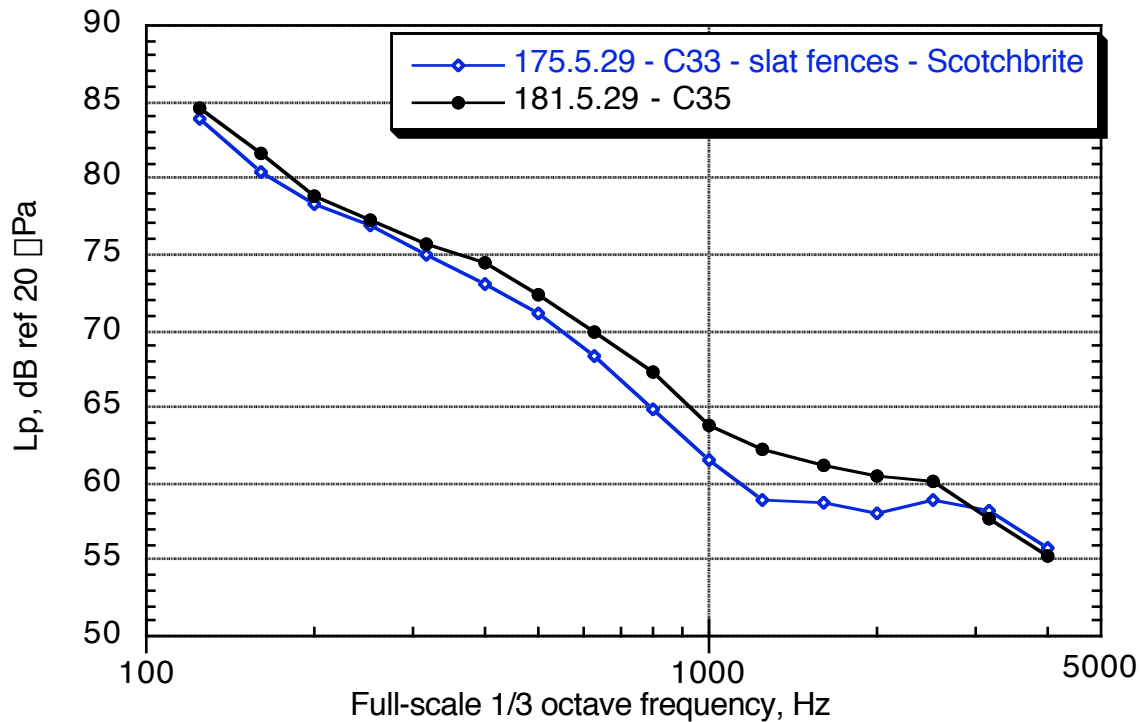
(b)  $\square = 6^\circ$ .

Figure 117. Effect of slat-tip fence on inboard-edge of outboard-slat: landing configuration,  $M = 0.21$ , traverse position = 150 in. downstream.

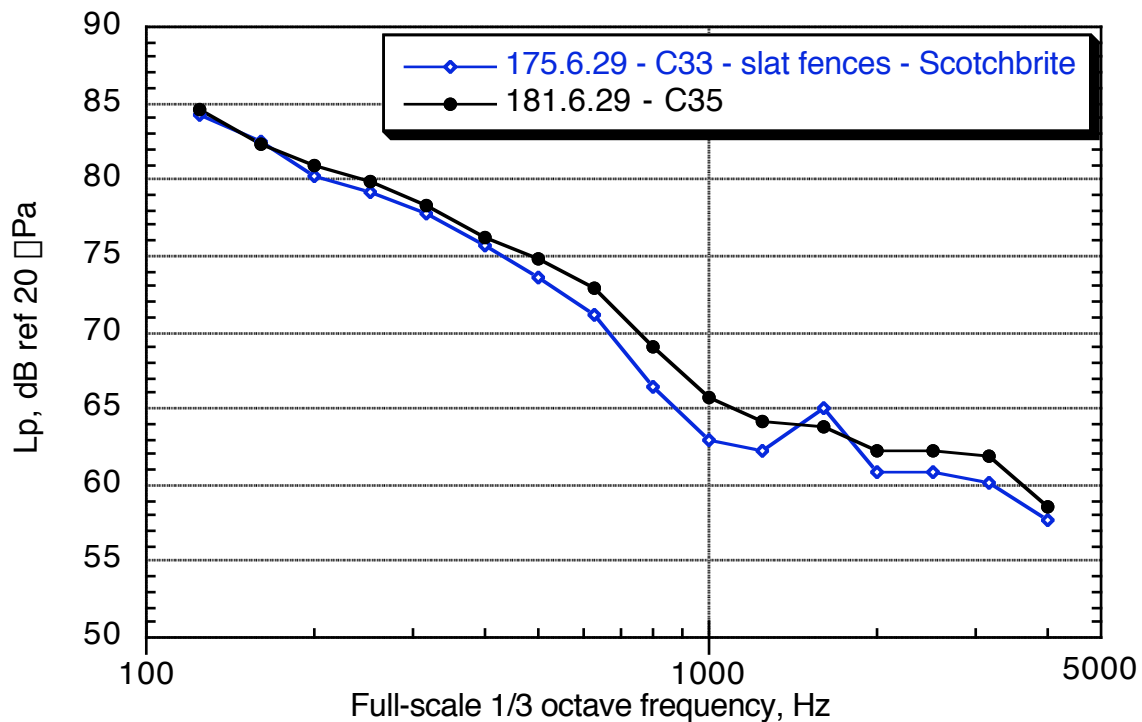


(c)  $\square = 8^\circ$ .

Figure 117. Concluded.

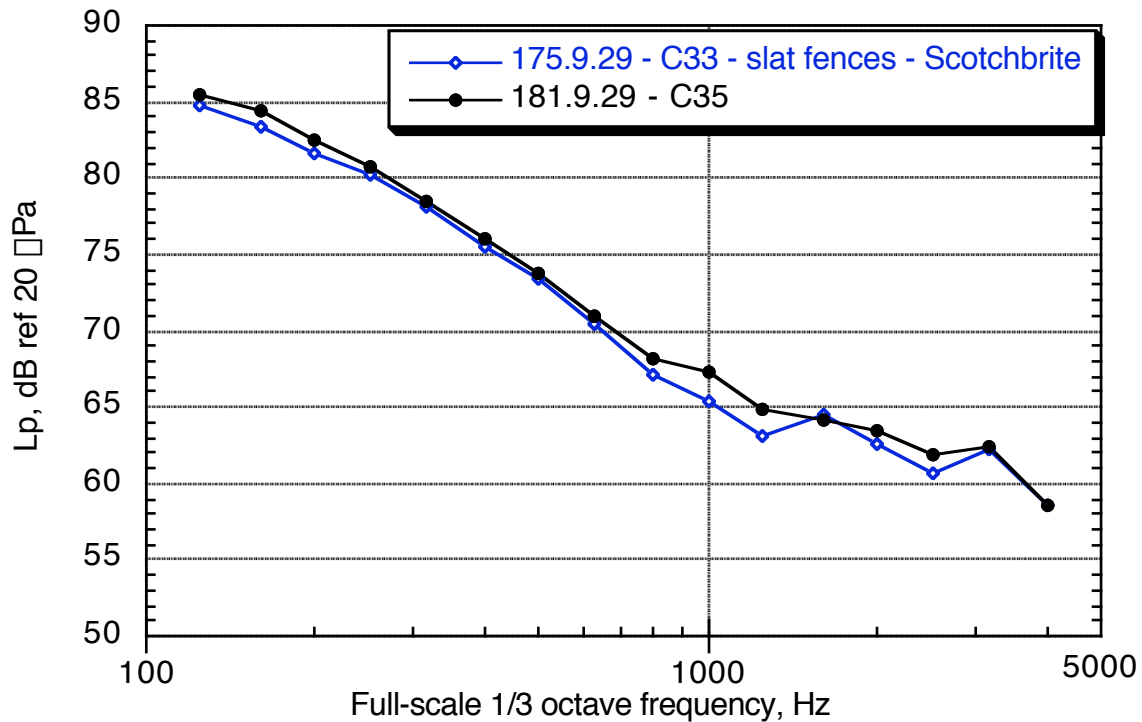


(a) Traverse = 100 in. upstream.

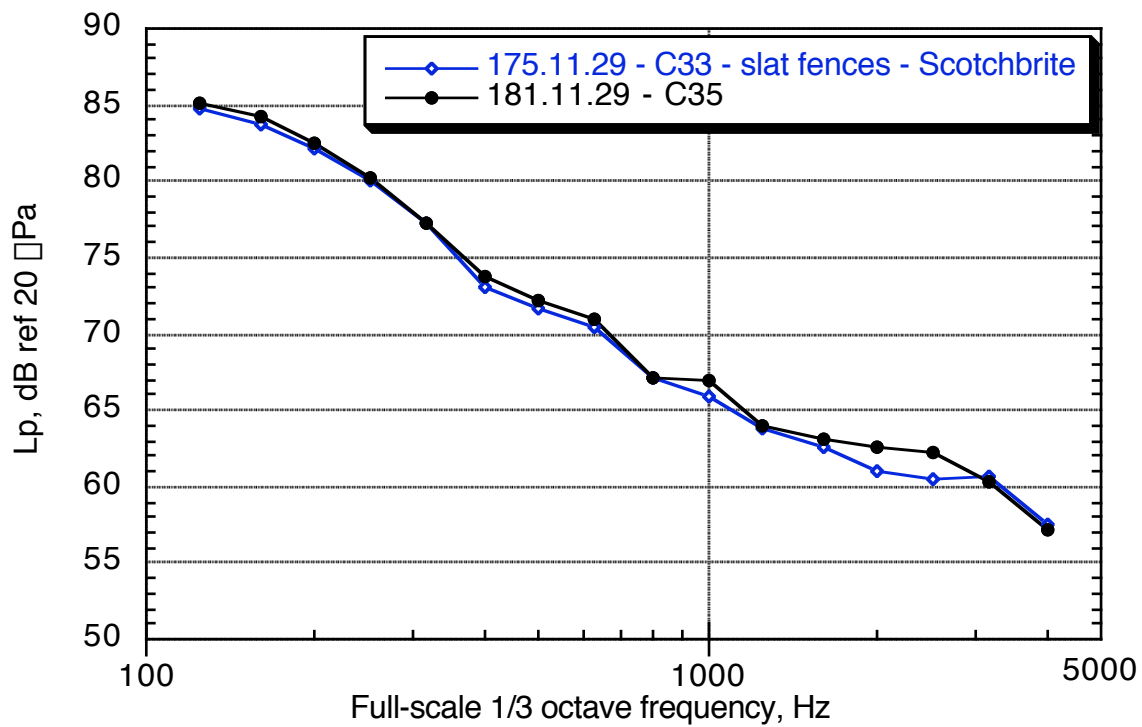


(b) Traverse = 0 in.

Figure 118. Effect of slat-tip fence on noise from outboard edge of outboard slat: landing configuration,  $M = 0.21$ ,  $\alpha = 6^\circ$ .

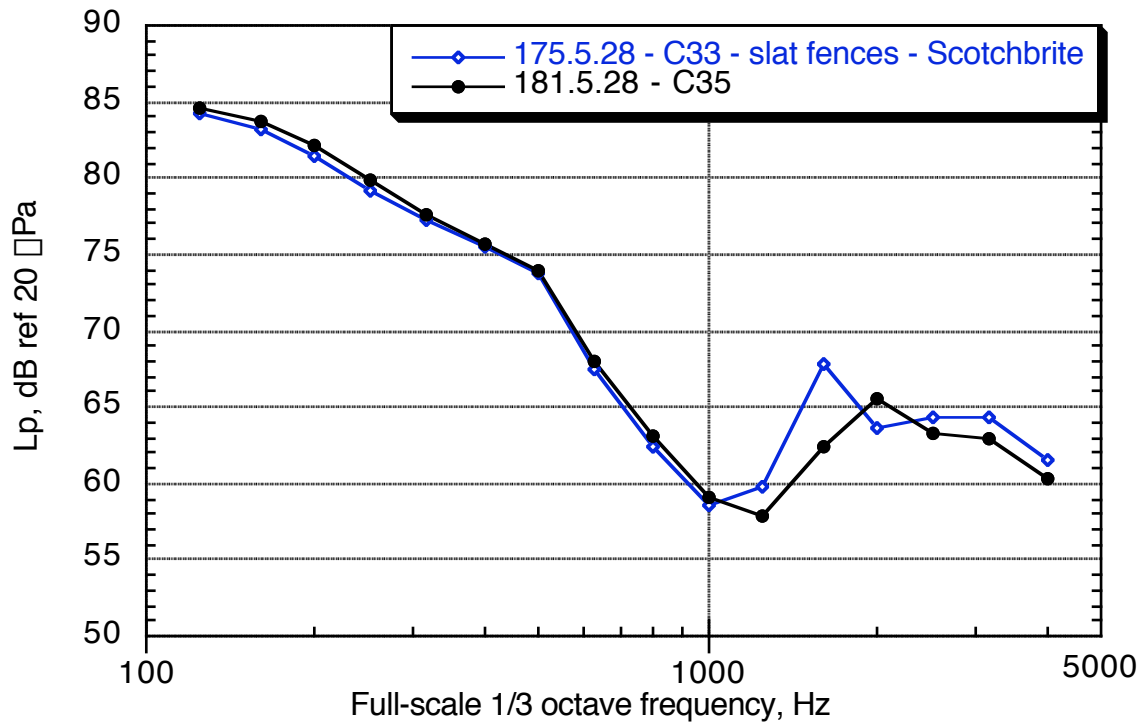


(c) Traverse = 150 in. downstream.

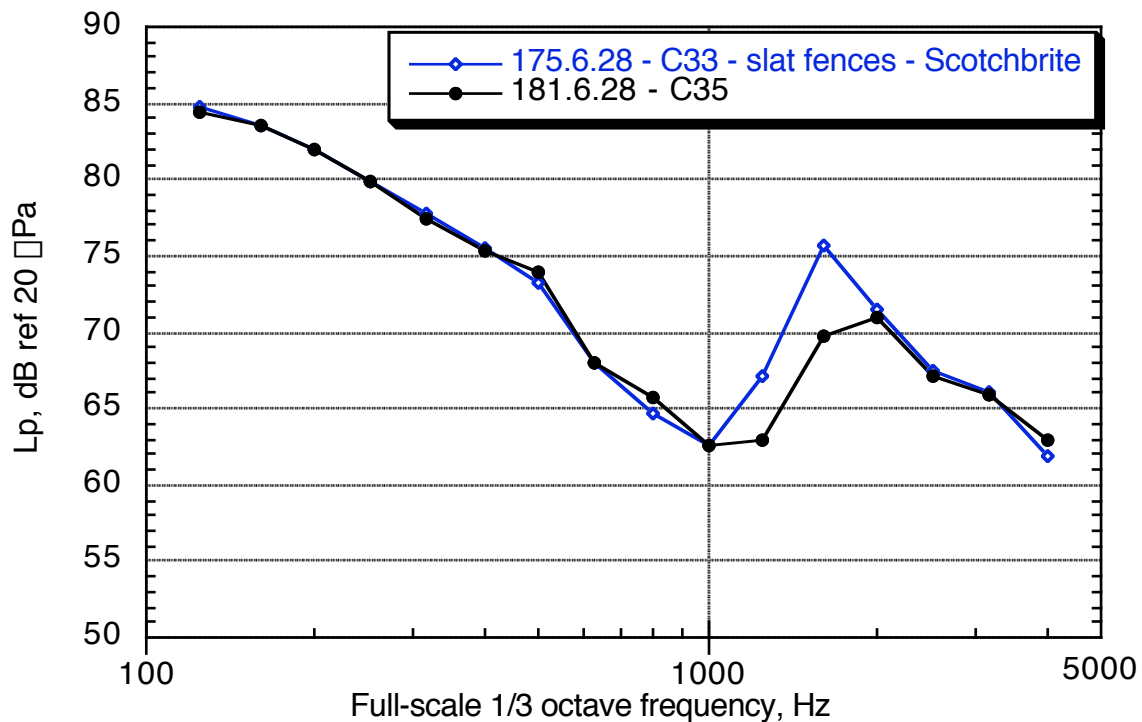


(d) Traverse = 250 in. downstream.

Figure 118. Concluded.

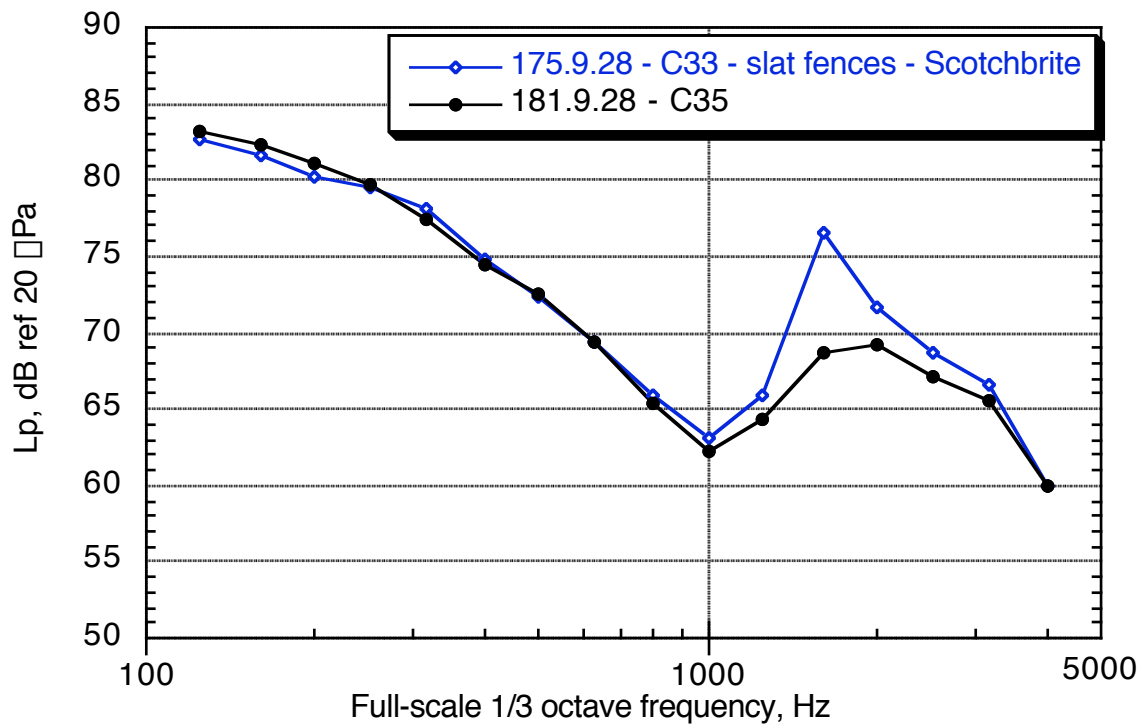


(a) Traverse = 100 in. upstream.

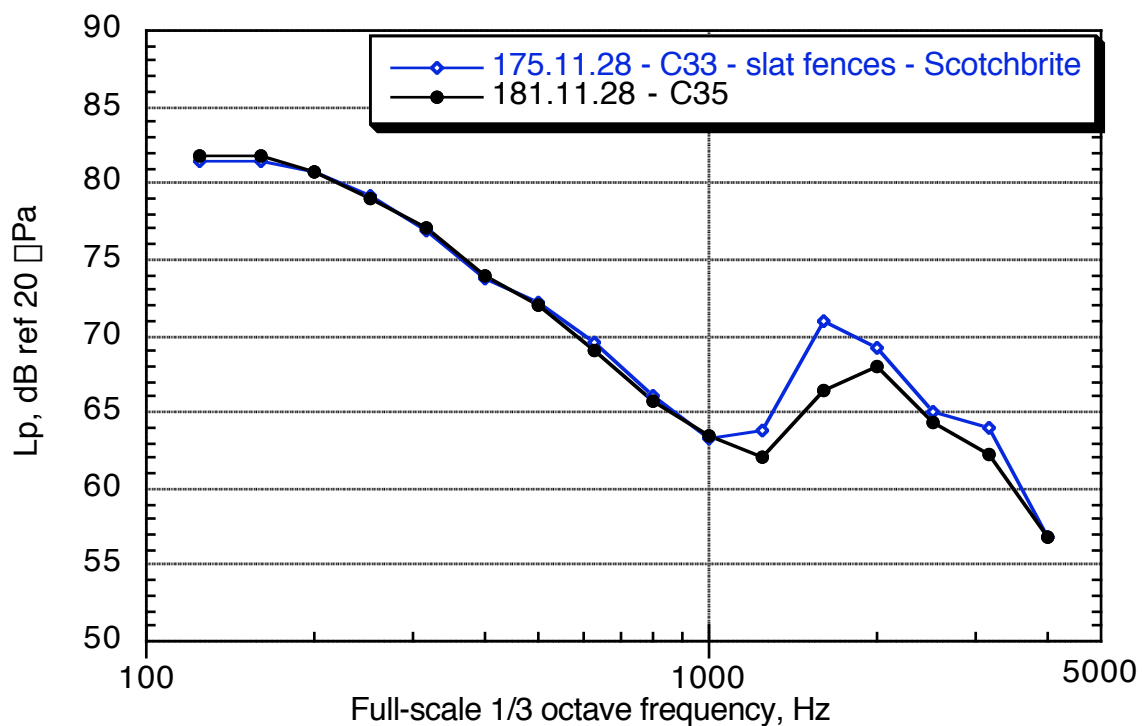


(b) Traverse = 0 in.

Figure 119. Effect of slat-tip fence on noise from inboard edge of outboard slat: landing configuration,  $M = 0.21$ ,  $\alpha = 6^\circ$ .

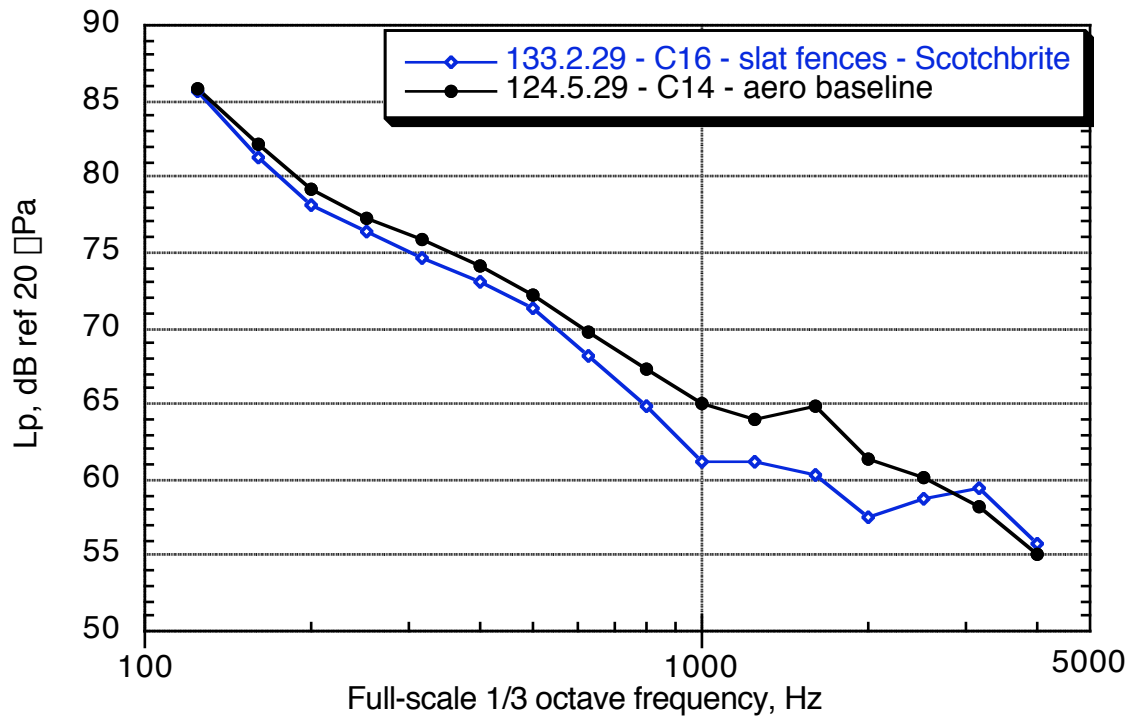


(c) Traverse = 150 in. downstream.

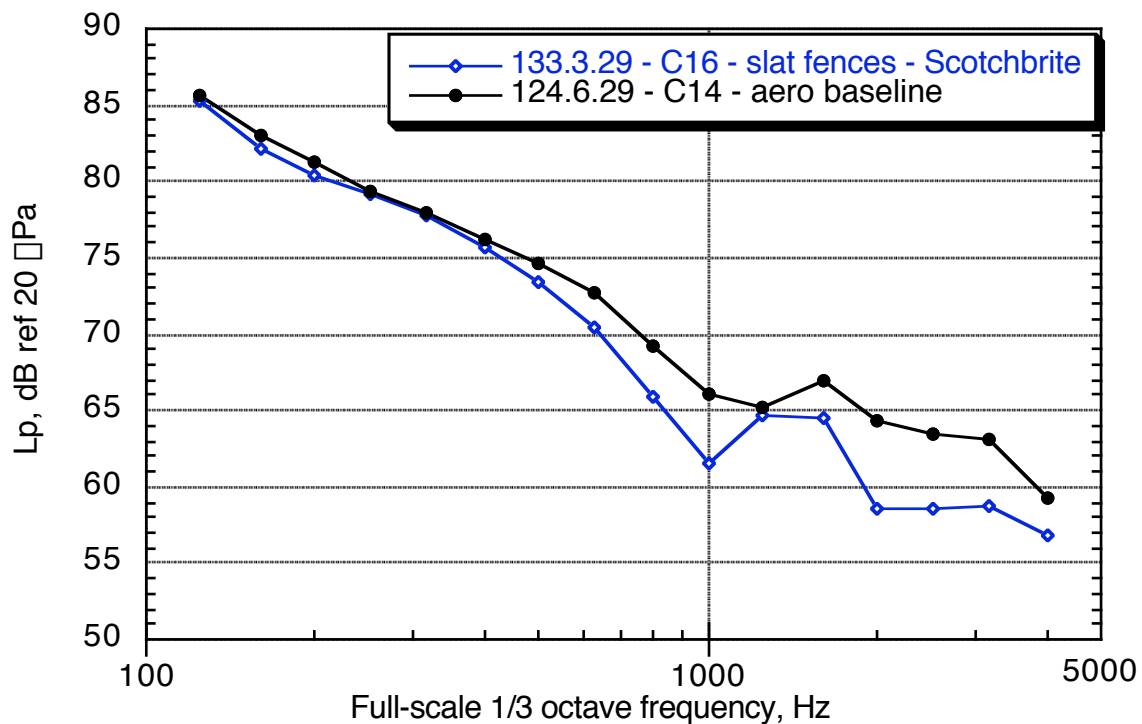


(d) Traverse = 250 in. downstream.

Figure 119. Concluded.

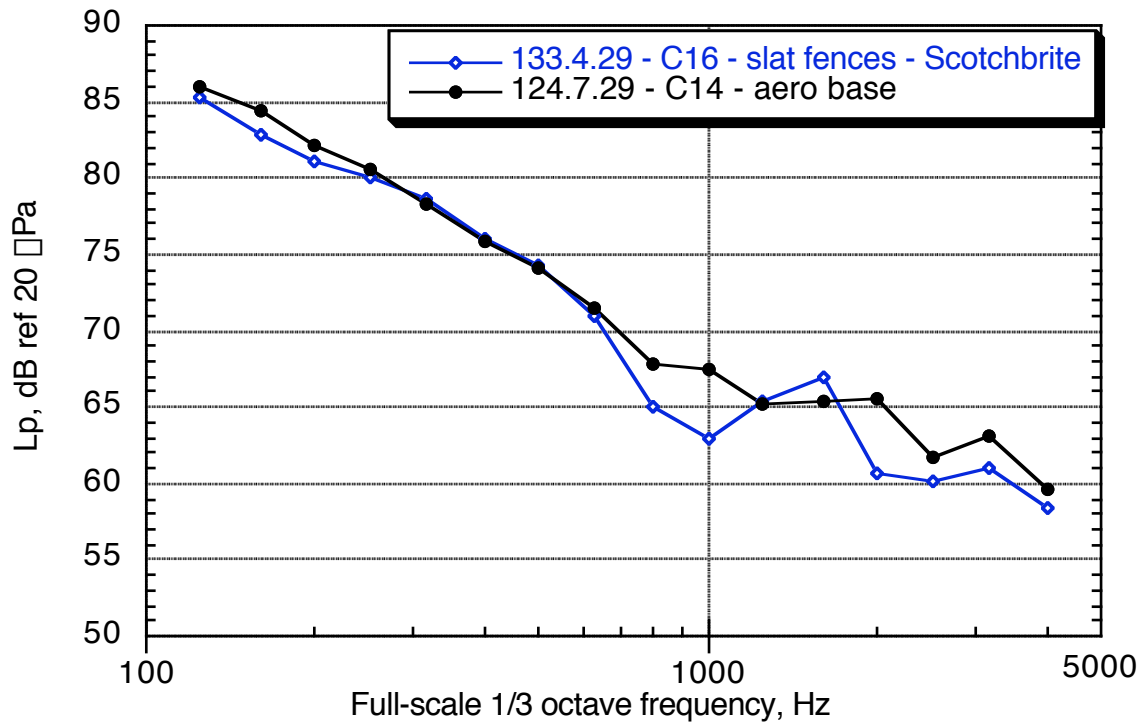


(a) Traverse = 100 in. upstream.

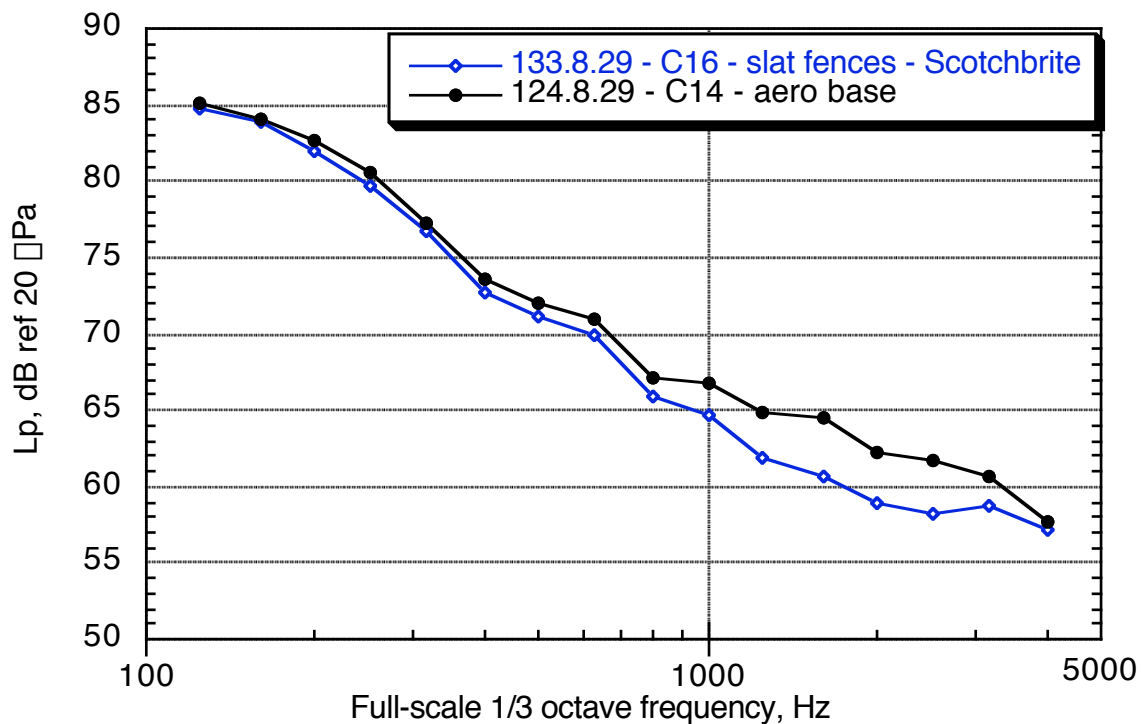


(b) Traverse = 0 in.

Figure 120. Effect of slat-tip fence on noise from outboard edge of outboard slat: approach configuration,  $M = 0.21$ ,  $\alpha = 6^\circ$ .



(c) Traverse = 150 in. downstream.



(d) Traverse = 250 in. downstream.

Figure 120. Concluded.



## APPENDIX A

### RUN SUMMARY

Table A.1 Run Matrix.

STAR 26% 777 40- by 80- Ft. Wind tunnel acoustic run synopsis									
Date	Run								
8/7	3								
8/8	4								
8/16	5-pt	1	2	3	4	5	6	7	8
	5-mic	F33	F70	F2	F29	F30	T37	T38	
8/9	10-pt	1	2	3	4				
	10-lev	0.0 v	0.152v	1.3v	5.45v				
8/9	11-pt	1	2						
	11-lev	90 dB	100 dB						
8/9	12-pt	1	2	3	4				
	12-lev	90 dB	100 dB	90dB off	100dB off				
	12-kev	on	on						
8/3	32-pt	3	4	5	6				
	32-M	0.18	0.21	0.26	0.33				
8/	33-pt	1	2						
	33-array	fixed	trav						
8/9	34-pt	5	6	7	8	9	10	11	12
	34-M	0.18	0.18	0.21	0.21	0.21	0.21	0.21	0.21
	34-array	fixed	T290u	fixed	T290u	T100u	T0	T150d	T350d
8/9	34-pt	15							
	34-M	0.26							
	34-array	T	T100u?						

Table A.1 Run Matrix (continued).

STAR 26% 777 40- by 80- Ft. Wind tunnel acoustic run synopsis											
Date	Run	51-pt	51-AOA	51-M	51-array	51-spkr	52-pt	52-M	52-array	52-spkr	53-pt
8/21	51-pt	3	4	5	6-X	7	8	9-X	10	11-X	R51: 'dirty' cruise, deer whistles X=pmat crash
	51-AOA	0°	4°	6°	0°	0°	0°	4°	8°	8°	
	51-M	0.181	0.181	0.181	0.21	0.21	0.21	0.21	0.21	0.21	
	51-array	fixed	fixed	fixed	T289u	fixed	fixed	T150d	T0	T200u	
	51-spkr						25W				
8/23	52-pt	3	4-X	5	6-X	7	8	9-X	10	11-X	R52: 'dirty' cruise, gear cavity speaker, AOA = 0
	52-M	0	0	0	0	0	0	0.179	0.179	0.179	
	52-array	fixed	T0.5d	T0.5d	T150d	fixed	fixed	fixed	fixed	fixed	
	52-spkr	25W	25W	25W	25W	25W	2.5W	2.5W	7.5W	7.5W	
	53-pt	1	2	3	4	5	6				R53: 'dirty' cruise, gear cavity speaker, AOA = 0,
	53-array	fixed	fixed	fixed	T150d	T150d	T150d				M = 0.21
	53-spkr	2.5W	7.5W	25W	2.5W	7.5W	25W				
8/23	54-pt	1	2-X	3	4-X	5	6-X	7	8	9	R54: 'dirty' cruise, gear cavity speaker
	54-AOA	0	0	0	0	0	8	10	12	14	fixed array
	54-M	0.2			0.21	0.21	0.21		0.209	0.208	0.257
	54-spkr	2.5W	7.5W	7.5W	25W	0	0	0	0	0	
	54-pt	11									R54: 'dirty' cruise, gear cavity speaker
	54-AOA	6									fixed array
	54-M	?									
	54-spkr	0									
8/23	55-pt	1	2								R55: 'dirty' cruise, gear cavity speaker
	55-spkr	7.5W	25W								fixed array, M = 0.33

Table A.1 Run Matrix (continued).

STAR 26% 777 40- by 80- Ft. Wind tunnel acoustic run synopsis											
Date	Run										
8/24	59-pt	3	4	5	6	8	9	10	12	14	16
	59-AOA	-4°	-2°	0°	2°	4°	5°	6°	8°	10°	12°
	59array	fixed									
	59-pt	18	21-X	22	23						
	59-AOA	14°	0°	4°	8°						
	59array	T150d	T150d	T150d	T150d						
8/24	60-pt	1	2	3-X	4-X	5	7-X	8	10-X	11	13
	60-AOA	-4°	-2°	0°	2°	2°		4°	6°	6°	8°
	60-pt	15-X	17	19							
	60-AOA	10°	12°	14°							
8/29	67-pt	3	4	5	6	7	8	9	10	11	R67 baseline landing, M = 0.18, fixed array
	67-AOA	-4°	-2°	0°	2°	4°	6°	8°	10°	12	Config 2
8/29	68-pt	1	2	3	4	5	6	7	8	9-X	R68 baseline landing, M = 0.18, trav. Array
	68-AOA	-4°	-2°	0°	2°	4°	4°	4°	4°	4°	Config 2
	68array	T150d	T150d	T150d	T150d	T100u	T0	T50d	T100d	T150d	
8/29	69-pt	1	2	3	4	5	6	7	8-X	9	R69 baseline landing, M = 0.21, fixed array
	69-AOA	-4°	-2°	0°	2°	4°	6°	8°	10°	12°	Config 2
8/29	70-pt	1	2	3	4	5	6	7	8-X	9	R70 baseline landing, M = 0.21, trav array
	70-AOA	-4°	-2°	0°	2.4°	4°	4°	4°	4°	4°	Config 2
	70array	T150d	T150d	T150d	T150d	T100u	T0	T50d	T100d	T150d	T200d
	70-pt	11	12	13	14	15-X	16	17	18		R70 baseline landing, M = 0.21, trav array
	70-AOA	4°	4°	6°	6°	6°	6°	6°	6°		Config 2
	70array	T250d	T350d	T100u	T0	T50d	T100d	T150d	T200d		

Table A.1 Run Matrix (continued).

STAR 26% 777 40- by 80- Ft. Wind tunnel acoustic run synopsis									
Date	Run	72-pt	5-X	7	9	7-X	6	7-X	
8/30	72-AOA	0°	4°	8°					R72: Landing baseline + fairing filled, $M = 0.21$
8/30	73-pt	1	2	3-X	4	5-X	6	7-X	
	73-AOA	6°	6°	6°	8°	10°	12°		R73: Landing baseline + fairing filled, $M = 0.21$
	73array	T150d	T200d	T250d	T350d	T150d	T150d		trav. Array, config 3
8/30	74-pt	1	2	3-X	4	5	6	7	R74: Landing baseline + fairing filled, $M = 0.18$
	74-AOA	4°	6°	6°	6°	6°	6°	6°	
	74array	T150d	T100d	T100d	T50d	T100d	T150d	T250d	trav array, config 3 (aero baseline)
8/30	74-pt	11-X	12						R74: Landing baseline + fairing filled, $M = 0.18$
	74-AOA	10°	12°						
	74array	T150d	T150d						trav array, config 3 (aero baseline)
8/30	75-pt	3	4	5	6-X	7	8	9	R75: Landing, no gear, $M = 0.21$
	75-AOA	6°	0°	2°	4°	6°	8°	10°	
	75array	fixed	fixed	fixed	fixed	fixed	fixed	12°	config 3 (aero baseline)
8/30	75-pt	14							R75: Landing, no gear, $M = 0.21$
	75-AOA	8°							config 3 (aero baseline)
	75array	150d							
8/31	77-pt	4	5	6	7	8	9-X	10	R77: Acoustic landing baseline, inboard flap filled
	77-AOA	-2°	0°	2°	4°	6°	8°	10°	
	77array	fixed	fixed	fixed	fixed	fixed	fixed	12°	no gear, outboard flap fairing removed, $M = 0.18$
								4°	config 4
8/31	77-pt	17							R77: Acoustic landing baseline, inboard flap filled
	77-AOA	8°							no gear, outboard flap removed, $M = 0.18$
	77array	T150d							config 4

Table A.1 Run Matrix (continued).

STAR 26% 777 40- by 80- Ft. Wind tunnel acoustic run synopsis									
Date	Run	78-pt	5.	6.	7.	8.	9.	10.	11.
8/31	78-AOA	4. -2. fixed	0. 2. fixed	4. 6. fixed	6. 8. fixed	10. 12. fixed	11. 12. fixed	15. 4. fixed	16. 6. fixed
	78array	T150d						T150d	T150d
	78-pt	17							
	78-AOA	8. T150d							
	78array								
8/31	79-pt	1	2	3-X	4	5	6	7	8
	79-AOA	-4. T150d	-2. T150d	0. T150d	2. T150d	4. T150d	4. T100u	4. T0	4. T50d
	79array							T100d	T150d
	79-pt	11	12	13	14	15	16	17-X	18
	79-AOA	4. T250d	4. T350d	6. T100u	6. T0	6. T50d	6. T100d	6. T200d	6. T250d
	79array							T200d	T350d
	79-pt	21	22	23-X	24	25	26	27	28
	79-AOA	8. T100u	8. T0	8. T50d	8. T100d	8. T150d	8. T200d	8. T250d	8. T350d
	79array							T150d	T150d
8/31	80-pt	1	2	3	4	5	6	7	8-X
	80-AOA	-4. T150d	-2. T150d	0. T150d	2. T100u	4. T0	4. T50d	4. T100d	4. T200d
	80array							T150d	T200d
	80-pt	11	12	13	14	15	16	17	18
	80-AOA	4. T250d	4. T350d	6. T100u	6. T0	6. T50d	6. T100d	6. T200d	6. T250d
	80array							T250d	T350d
	80-pt	21	22	23	24	25	26	27	28
	80-AOA	8. T100u	8. T0	8. T50d	8. T100d	8. T150d	8. T200d	8. T250d	8. T350d
	80array							T150d	T150d

Table A.1 Run Matrix (continued).

STAR 26% 777 40- by 80- Ft. Wind tunnel acoustic run synopsis										
Date	Run									
9/4	81-pt	4	5	6	7	8	9	10	11	R81: Landing, gear off, slat&flap tip fence, M = 0.18 boundary layer rakes, fixed array, config 5
	81-AOA	-2°	0°	2°	4°	6°	8°	10°	12°	
9/4	82_pt	2	3	4	5	6	7	8	9	R82: Landing, gear off, slat&flap tip fence, M = 0.21 boundary layer rakes, fixed array, config 5
	82-AOA	-2°	0°	2°	4°	6°	8°	10°	12°	
9/4	83-pt	1	2	3	4	5	6	7	8	R83: Landing, gear off, slat&flap tip fence, M = 0.21 boundary layer rakes, config 5
	83-AOA	4°	6°	6°	6°	6°	6°	8°	8°	
	83array	T150d	T100u	T0	T150d	T250d	T150u			
9/4	84-pt	2	3	4	5	6	7	8	9	R84: Landing, gear off, slat&flap tip fence, M = 0.18 config 5
	84-AOA	4°	6°	6°	6°	6°	6°	8°	8°	
	84array	T150d	T100u	T0	T150d	T250d	T150d			
9/5	87-pt	4	5	6	7	8	9	10	11	R87: Landing, gear off, slat&flap tip fence, M = 0.18 flap TE serrations, config = 6, fixed array
	87-AOA	-2°	0°	2°	4°	6°	8°	10°	12°	
9/5	88-pt	2	3	4	5	6	7	8	9	R88: Landing, gear off, slat&flap tip fence, M = 0.21 flap TE serrations, config = 6, fixed array
	88-AOA	-2°	0°	2°	4°	6°	8°	10°	12°	
9/5	89-pt	1	2	3	4	5	6	7	8	R89: Landing, gear off, slat&flap tip fence, M = 0.21 flap TE serrations, config = 6, fixed array
	89-AOA	4°	6°	6°	6°	6°	6°	8°	8°	
9/5	90-pt	1	2	3	4	5	6	7	8	R90: Landing, gear off, slat&flap tip fence, M = 0.18 flap TE serrations, config = 6
	90-AOA	4°	6°	6°	6°	6°	6°	8°	8°	
	90array	T150d	T100u	T0	T150d	T250d	T150d			
9/5	91-pt	1	2	3	4	5	6	7	8	R91: Landing, gear off, slat&flap tip fence, M = 0.21 flap TE serrations, config = 6
	91-AOA	4°	6°	6°	6°	6°	6°	8°	8°	
	91array	T150d	T100u	T0	T150d	T250d	T150d			

Table A.1 Run Matrix (continued).

STAR 26% 777 40- by 80- Ft. Wind tunnel acoustic run synopsis									
Date	Run								
9/5	92-pt	4	5	6	7	8	9	10	11
	92-AOA	-2°	0°	2°	4°	6°	8°	10°	12°
9/5	93-pt	2	3	4	5	6	7	8	9
	93-AOA	-2°	0°	2°	4°	6°	8°	10°	12°
9/5	94-pt	1	2	3	4	5	6		
	94-AOA	4°	6°	6°	6°	6°	8°		
	94array	T150d	T100u	T0	T150d	T250d	T150d		
9/5	95-pt	1	2	3	4	5	6		
	95-AOA	4°	6°	6°	6°	6°	8°		
9/6	96-pt	4	5	6					
	96-AOA	-2°	0°	2°					
9/6	97-pt	2	3	4	5	6	7	8	10
	97-AOA	-2°	0°	2°	4°	6°	8°	10°	12°
9/6	98-pt	1	2	3	4	5	6		
	98-AOA	4°	6°	6°	6°	6°	8°		
	98array	T150d	T100u	T0	T150d	T250d	T150d		
9/6	99-pt	2	3	4	5	6	7	8	9
	99-AOA	-2°	0°	2°	4°	6°	8°	10°	12°
9/6	100-pt	1	2	3	4	5	6	7	8
	100-AOA	4°	6°	4°	6°	6°	6°	6°	8°
	100array	fixed	fixed	T150d	T100u	T0	T150d	T250d	T150d

Table A.1 Run Matrix (continued).

STAR 26% 777 40- by 80- Ft. Wind tunnel acoustic run synopsis										
Date	Run									
9/7	101-pt	4	5	6	7	8	9	10	11	
	100AOA	-2°	0°	2°	4°	6°	8°	10°	12°	
9/7	102-pt	1	2	3	4	5	6			
	102AOA	4°	6°	6°	6°	6°	8°			
	102array	T151d	T100u	T0	T150d	T250d	T150d			
9/7	103-pt	2	3	4	5	6	7	8	9	
	103AOA	-2°	0°	2°	4°	6°	8°	10°	12°	
9/7	104-pt	1	2	3	4	5	6			
	104AOA	4°	6°	6°	6°	6°	8°			
	104array	T151d	T100u	T0	T151	T250d	T150d			
9/7	105-pt	4	5	6	7	8	9	10	11	
	105AOA	-2°	0°	2°	4°	6°	8°	10°	12°	
9/7	106-pt	1	2	3	4	5	6			
	106AOA	4°	6°	6°	6°	6°	8°			
	106array	T151d	T100u	T0	T151d	T250d	T150d			
9/7	107-pt	2	3	4	5	6	7	8	9	
	107AOA	-2°	0°	2°	4°	6°	8°	10°	12°	
9/7	108-pt	1	2	3	4	5	6			
	108AOA	4°	6°	6°	6°	6°	8°			
	106array	T151d	T100u	T0	T150d	T250d	T150d			

Table A.1 Run Matrix (continued).

STAR 26% 777 40- by 80- Ft. Wind tunnel acoustic run synopsis										
Date	Run									
9/10	109-pt	4	5	6	7	8	9	10	11	R109: Approach config 11, gear off, R750 flap tip, M = 0.21
	109AOA	-2°	0°	2°	4°	6°	8°	10°	12°	cove filler, (R750=R#33), fixed array
										#5 slat bracket fairing upstream of OFOE
9/10	110-pt	1	2	3	4	5	6			R110: Approach config 11, gear off, R750 flap tip, M=0.21
	110AOA	4°	6°	6°	6°	6°	8°			cove filler, (R750=R#33),
	110array	T151d	T100u	T0	T150d	T250d	T150			#5 slat bracket fairing upstream of OFOE
9/10	111-pt	2	3	4	5	6	7	8	9	R111: Approach config 11, gear off, R750 flap tip, M=0.18
	111AOA	-2°	0°	2°	4°	6°	8°	10°	12°	cove filler, (R750=R#33), fixed array
										#5 slat bracket fairing upstream of OFOE
9/10	112-pt	1-X	2	3	4	5	6			R112: Approach config 11, gear off, R770 flap tip, M=0.18
	112AOA	4°	6°	6°	6°	6°	8°			cove filler, (R750=R#33),
	112array	T151d	T100u	T0	T150d	T250d	T150d			#5 slat bracket fairing upstream of OFOE
9/11	114-pt	4	5	6	7	8	9	10	11	R114: Approach config 12, gear off, R500 flap tip, M=0.21
	114AOA	-2°	0°	2°	4°	6°	8°	10°	12°	cove filler, (R500=R#34), fixed array
										#4 slat bracket fairied, #1,#9 slat bracket scotch brite
9/11	115-pt	1	2	3	4	5	6			R115: Approach config 12, same as R114, M=0.21
	115AOA	4°	6°	6°	6°	6°	8°			
	115array	T150d	T100u	T0	T150d	T250d	T150d			
9/11	116-pt	2-X	3	4	5	6	7	8	9	R116: Approach config 12, same as R114, M = 0.18
	116AOA	-2°	0°	2°	4°	6°	8°	10°	12°	
9/11	117-pt	1	2	3	4	5	6			R117: Approach config 12, same as R114, M = 0.18
	117AOA	4°	6°	6°	6°	6°	8°			
	117array	T150d	T100u	T0	T150d	T250d	T150d			
9/13	119-pt	4	5	6						R119: Approach acoustic baseline, config 13, M=0.21
	119AOA	-2°	0°	2°						fixed array

Table A.1 Run Matrix (continued).

STAR 26% 777 40- by 80- Ft. Wind tunnel acoustic run synopsis									
9/13	120-pt	2	3	4					
	120AOA	-2°	0°	2°					
9/14	121-pt	4	5	6	7	8	9	10	11
	121AOA	-2°	0°	2°	4°	6°	8°	10°	12°
9/14	122-pt	1	2	3	4	5	6	7	8
	122AOA	4°	4°	4°	4°	6°	6°	6°	6°
	122array	T100u	T0	T150d	T250d	T100u	T0	T150d	T250d
9/14	122-pt	11	12	13	14				
	122AOA	8°	8°	10°	12°				
	122array	T150d	T250d	T150d					
9/14	123-pt	2	3	4	5	6	7	8	9
	123AOA	-2°	0°	2°	4°	6°	8°	10°	12°
9/14	124-pt	1	2	3	4	5	6	7	8
	124	4°	4°	4°	4°	6°	6°	6°	6°
	124array	T100u	T0	T150d	T250d	T100u	T0	T150d	T250d
9/14	124-pt	11	12	13	14				
	124AOA	8°	8°	10°	12°				
	124array	T150d	T250d	T150d					
9/14	126-pt	4	5	6	7	8	9	10	11
	126AOA	-2°	0°	2°	4°	6°	8°	10°	12°
9/14	127-pt	1	2-X	3	4	5	6	7	8
	127AOA	4°	4°	4°	4°	4°	6°	6°	6°
	127array	T100d	X	T0	T150d	T250d	T100u	T0	T150d
									T100u

Table A.1 Run Matrix (continued).

STAR 26% 777 40- by 80- Ft. Wind tunnel acoustic run synopsis									
	127-pt	11	12	13					
	127AOA	8.	8.	8.					
	127array	T0	T150d	T250d					
9/14	128-pt	3	4						
	128AOA	10.	12.						
	128array	T150d	T150d						
9/14	129-pt	2	3	4	5	6	7	8	9
	129AOA	-2.	0.	2.	4.	6.	8.	10.	12.
9/14	130-pt	1	2	3	4	5	6	7	8
	130AOA	4.	4.	4.	4.	6.	6.	6.	8.
	130array	T100u	T0	T150d	T250d	T100u	T0	T150d	T250d
9/14	130-pt	11	12	13	14				
	130AOA	8.	8.	10.	12.				
	130array	T150d	T250d	T150d	T150d				
9/14	131-pt	3	4	5					
	131AOA	4.	6.	10.					
	131array	T150d	T150d	T150d					
9/17	132-pt	4	5	6	7	8	9	10	12
	132AOA	-2.	0.	2.	4.	6.	8.	10.	12.
9/17	133-pt	1	2	3	4	5	6	7	8
	133AOA	4.	6.	6.	6.	6.	6.	6.	8.
	133array	T150d	T100u	T0	T50d	T100d	T150d	T200d	T250d
9/17	134-pt	3	4	5	6	7	8	9	10
	134AOA	-2.	0.	2.	4.	6.	8.	10.	12.

Table A.1 Run Matrix (continued).

STAR 26% 777 40- by 80- Ft. Wind tunnel acoustic run synopsis											
9/17	135-pt	1	2	3	4	5	6	7	8	9	10
	135AOA	4°	6°	6°	6°	6°	6°	6°	6°	6°	R135:approach, aero baseline, config 16 M=0.18
	135array	T150d	T100u	T0	T50d	T100d	T150d	T200d	T250d	T350d	scotchkbitre all slat brackets, slat Fences
9/17	136-pt	3	4	5	6	7	8	9	13	14	R136:approach, aero base + C17, M=0.18
	136AOA	-2°	0°	2°	4°	6°	8°	10°	4°	6°	scotchkbitre all slat brackets + flap edge microtabs 1
	136array	fix	T150d	T150d							
9/17	137-pt	1	2	3	4	5	6	7	11	12	R137:approach, aero base +config 17, M=0.18
	137AOA	-2°	0°	2°	4°	6°	8°	10°	4°	6°	scotchkbitre all slat brackets + flap edge microtabs 1
	137array	fix	T150d	T150d							
9/17	138-pt	3	4	5	6	7	8	9	13	15	R138:approach, aero base + C18, M=0.21
	138AOA	-2°	0°	2°	4°	6°	8°	10°	4°	6°	scotchkbitre all slat brackets + flap edge microtabs 2
	138array	fix	T150d	T150d	(microtab angle change)						
9/17	139-pt	3	4	5	6	7	8	9	13	15	R139:approach, aero base + C18, M=0.18
	139AOA	-2°	0°	2°	4°	6°	8°	10°	4°	6°	scotchkbitre all slat brackets + flap edge microtabs 2
	139array	fix	T150d	T150d							
9/18	140-pt	3	4	5	6	7	8	9	10	11	R140:approach, aero base/weasel,C19,M=0.21
	140AOA	4°	6°	8°	10°	12°	4°	6°	8°	10°	scotchkbitre all slat brackets, extra slat bracket, etc.
	140array	fix	fix	fix	fix	fix	fix	T100u	T100u	T100u	B.L. trips on B slat and OB slat 3rd from py on
											dummy bracket between brackets on 4th seg. From pyl.
											removable serrated trailing edge slat on 5th OB slat
											seg.
140-pt	13	14	15	16	17	18	19	20	21	22	
	140AOA	4°	6°	8°	10°	12°	4°	6°	8°	10°	deer whistle on lower cusp of 6th slat OB of pylon in-
	140array	T0	T0	T0	T0	T0	T150d	T150d	T150d	T150d	board of OB bracket, slat Fences
140-pt	23	24	25	26	27						
140AOA	4°	6°	8°	10°	12°						
140array	T250d	T250d	T250d	T250d	T250d						

Table A.1 Run Matrix (continued).

STAR 26% 777 40- by 80- Ft. Wind tunnel acoustic run synopsis												
9/18	141-pt	3	4	5	6	7	8	9	10	12	13	R141:approach,config 20,M=0.21
	141AOA	4°	6°	8°	10°	12°	4°	6°	8°	10°	12°	scotch brite all brackets, non serrated slat TE
	141array	fixed	fixed	fixed	fixed	fixed	fixe	T150d	T150d	T150d	T150d	between brackets on 5th slat seg. Rounded flap fence LE.
9/18	142-pt	3	4	5	6	7	8	9	10	11	12	R142: approach, config 21,M=0.21
	142AOA	4°	6°	8°	10°	12°	4°	6°	8°	10°	12°	non serrated slat TE slat #5, rounded flap fence LE
	142array	fixed	fixed	fixed	fixed	fixed	fixed	T150d	T150d	T150d	T150d	flap fence, scotch brite removed
9/18	143-pt	3	4	5	6	7	8	9	10	11	12	R143:approach, config 22, M=0.21
	143AOA	4°	6°	8°	10°	12°	4°	6°	8°	10°	12°	
	143array	fixed	fixed	fixed	fixed	fixed	fixed	T150d	T150d	T150d	T150d	
9/19	144-pt	4	5	6	7	8	9	9	10	11	12	R144: approach, config 23, R34 flap tip, M = 0.21
	144AOA	0°	4°	6°	8°	10°	12°					scotchbrite brackets, slat fences, fixed array
9/19	145-pt	1	2	3	4	5	6	7	8	9	10	R145: approach, config 23, M = 0.21
	145AOA	4°	4°	4°	4°	4°	6°	6°	6°	6°	8°	
	145array	T100u	T0	T150d	T251d	T100u	T0	T150d	T250d	T100u	T0	
	145-pt	11	12	13	14	15	16	17	18	19	20	
	145AOA	8°	10°	10°	10°	10°	10°	12°	12°	12°	12°	
	145array	T150d	T250d	T100u	T0	T150d	T250d	T100u	T0	T150d	T250d	
9/20	146-pt	4	5	6	7	8	9					R146:Approach, config 24, gen2 weasel, M = 0.21
	146AOA	0°	4°	6°	8°	10°	12					slat fences, scotchbrite brackets, fixed array
9/20	147-pt	1	2	3	4	5	6	7	8	9	10	R147: Approach, config 24
	147AOA	4°	4°	6°	6°	6°	6°	8°	8°	10°	10°	
	147array	T150d	T0	T100u	T0	T150d	T250d	T150d	T0	T100u	T0	
	147-pt	11	12	13	14							
	147AOA	10°	10°	12°	12°							
	147array	T150d	T250d	T150d	T0							

Table A.1 Run Matrix (continued).

STAR 26% 777 40- by 80- Ft. Wind tunnel acoustic run synopsis										
9/21 149-pt 4 5 6 7 8 9										R149: landing, config 3, hifi gear, M = 0.21
149AOA 0° 4° 6° 8° 10° 12°										
9/21 150-pt 1 2 3 4 5 6 7 8										R150: landing, config 3, hifi gear, M = 0.21
150AOA 4° 4° 4° 6° 6° 6° 6° 8°										
9/21 150array T100u T0 T150d T250d T100u T0 T150d T250d T100u T0										
150-pt 11 12 13 14 15 16 17 18 19 20										
150AOA 8° 8° 10° 10° 10° 10° 12° 12° 12° 12°										
9/21 150array T150d T250d T100u T0 T150d T250d T100u T0 T150d T250d										
9/21 151-pt 2 3 4 5 6 7										R151: landing, config 3, hifi gear, M = 0.18
151AOA 0° 4° 6° 8° 10° 12°										fixed array
9/21 152-pt 4 5 6 7 8 9										R152: landing, config 25 hifi gear, M = 0.21
152AOA 0° 4° 6° 8° 10° 12°										scotchkbitre brackets, slat fences, fixed array
9/21 153-pt 1 2 3 4 5 6 7 8 9 10										R153: landing, config 25, hifi gear M = 0.21
153AOA 4° 4° 4° 6° 6° 6° 6° 8° 8°										scotchkbitre brackets, slat fences
9/21 153array T100u T0 T150d T250d T100u T0 T150d T250d T100u T0										
153-pt 11 12 13 14 15 16 17 18 19 20										
153AOA 8° 8° 10° 10° 10° 12° 12° 12° 12° 12°										
9/21 154-pt 2 3 4 5 6 7 8 9 10 11										R154: landing, config 25, hifi gear, M = 0.18
154AOA 0° 4° 6° 8° 10° 12° 12° 12° 12° 12°										scotchkbitre brackets, slat fences, fixed array(pt 2-20)
9/21 154array fixed T150d T250d T100u T0 T150d T250d T100u T0 T150d T250d										

Table A.1 Run Matrix (continued).

STAR 26% 777 40- by 80- Ft. Wind tunnel acoustic run synopsis											
9/24	157-pt	1	2	3	4	5	6	7	8	9	10
	157AOA	4°	4°	4°	4°	6°	6°	6°	8°	8°	
	157array	T100u	T0	T150d	T250d	T100u	T0	T150d	T250d	T100u	T0
	157-pt	11	12	13	14	15	16	17	18	19	20
	157AOA	8°	8°	10°	10°	10°	10°	12°	12°	12°	12°
	157array	T150d	T250d	T100u	T0	T150d	T250d	T100u	T0	T150d	T250d
9/24	159-pt	4	5	6	7	8	9				
	159AOA	0°	4°	6°	8°	10°	12°				
	160-pt	1	2	3	4	5	6	7	8	9	10
	160AOA	4°	4°	4°	4°	6°	6°	6°	8°	8°	
	160array	T100u	T0	T150d	T250d	T100u	T0	T150d	T250d	T100u	T0
	160-pt	11	12	13	14	15	16	17	18	19	20
	160AOA	8°	8°	10°	10°	10°	10°	12°	12°	12°	12°
	160array	T150d	T250d	T100u	T0	T150d	T250d	T100u	T0	T150d	T250d
9/24	162-pt	4	5	6	7	8	9				
	162AOA	0°	4°	6°	8°	10°	12°				
	163-pt	1	2	3	4	5	6	7	8	9	10
	163AOA	4°	4°	4°	4°	6°	6°	6°	8°	8°	
	163array	T100u	T0	T150d	T250d	T100u	T0	T150d	T250d	T100u	T0
9/24	163-pt	11	12	13	14	15	16	17	18		
	163AOA	8°	8°	10°	10°	10°	10°	12°	12°		
	163array	T150d	T250d	T100u	T0	T150d	T250d	T100u	T0		

Table A.1 Run Matrix (continued).

STAR 26% 777 40- by 80- Ft. Wind tunnel acoustic run synopsis									
9/24	164-pt	3	4						R164, config 28, M = 0.21, continue R163
	164AOA	12'	12'						
	164array	T150d	T250d						
9/26	166-pt	4	5	6	7	8	9		R166, landing, config 29, simple gear, M=0.21
	166AOA	0'	4'	6'	8'	10'	12'		slats 2,3,4 serrated, scotch brackets, fairing #8
									fixed array
9/26	167-pt	1	2	3	4	5	6	7	R167, landing, config 29, M=0.21
	167AOA	4'	4'	4'	4'	6'	6'	6'	
	167array	T100u	T0	T150d	T250d	T100u	T0	T50d	T200d
	167-pt	11	12	13	14	15	16	17	
	167AOA	6'	6'	8'	8'	8'	8'	10'	
	167array	T250d	T350d	T100u	T0	T150d	T250d	T100u	T0
	167-pt	21	22	23	24				
	167AOA	12'	12'	12'	12'				
	167array	T100u	T0	T150d	T250d				
9/26	169-pt	4	5	6	7	8	9		R169, landing, config 30, simple gear no doors, M=0.21
	169AOA	0'	4'	6'	8'	10'	12'		fixed array
	170-pt	1	2	3	4	5	6	7	
	170AOA	4'	4'	4'	4'	6'	6'	6'	
	170array	T100u	T0	T150d	T250d	T100u	T0	T150d	T250d
	170-pt	11	12	13	14	15	16	17	
	170AOA	8'	8'	10'	10'	10'	10'	12'	
	160array	T150d	T250d	T100u	T0	T150d	T250d	T100u	T0
9/26	172-pt	3	4	5	6	7			R172, landing, config 31, simple gear no doors, M=0.21
	172AOA	6'	6'	6'	6'	6'	6'		unmodified tire tread exposed
	172array	fixed	T100u	T0	T150d	T250d			

Table A.1 Run Matrix (continued).

STAR 26% 777 40- by 80- Ft. Wind tunnel acoustic run synopsis									
									R173, landing, config 32, simple gear no doors, M=0.21
modified tire tread exposed									
									R174, landing, config 33, gear off, fixed array, M = 0.21
scotchbite brackets, slat fences, serrate slats 2,3,4									
									R175, landing, config 33, M = 0.21
9/27	173-pt	3	4	5	6	7			
	173AOA	6°	6°	6°	6°	6°			
	173array	fixed	T100u	T0	T150d	T250d			
9/27	174-pt	4	5	6	7	8	9		
	174AOA	0°	4°	6°	8°	10°	12°		
	175array	T100u	T0	T150d	T250d	T100u	T0	T50d	T100d
9/27	175-pt	1	2	3	4	5	6	7	8
	175AOA	4°	4°	4°	4°	6°	6°	6°	6°
	175array	T100u	T0	T150d	T250d	T100u	T0	T50d	T100d
9/27	175-pt	11	12	13	14	15	16	17	18
	175AOA	6°	6°	8°	8°	8°	10°	10°	10°
	175array	T250d	T350d	T100u	T0	T150d	T250d	T100u	T0
9/27	175-pt	21	22	23	24				R175
	175AOA	12°	12°	12°	12°				
	175array	T100u	T0	T150u	T250d	T100u	T0	T50d	T250d
9/27	177-pt	4	5	6	7	8	9		
	177AOA	0°	4°	6°	8°	10°	12°		
	177array	T100u	T0	T150d	T250d	T100u	T0	T50d	T100d
9/27	178-pt	1	2	3	4	5	6	7	8
	178AOA	4°	4°	4°	4°	6°	6°	6°	6°
	178array	T100u	T0	T150d	T250d	T100u	T0	T50d	T100d
9/27	178-pt	11	12	13	14	15	16	17	18
	178AOA	6°	6°	8°	8°	8°	10°	10°	10°
	178array	T250d	T350d	T100u	T0	T150d	T250d	T100u	T0
9/27	178-pt	21	22	23	24				R178
	178AOA	12°	12°	12°	12°				
	178array	T100u	T0	T150d	T250d	T100u	T0	T50d	T250d
9/27	178-pt	21	22	23	24				R178
	178AOA	12°	12°	12°	12°				
	178array	T100u	T0	T150d	T250d	T100u	T0	T50d	T100d

Table A.1 Run Matrix (continued).

STAR 26% 777 40- by 80- Ft. Wind tunnel acoustic run synopsis																							
9/27	180-pt	4	5	6	7	8	9												R180, landing, no gear, config35, M = 0.21, fixed array				
	180AOA	0°	4°	6°	8°	10°	12°												slat serrations only				
9/27	181-pt	1	2	3	4	5	6	7	8	9	10	R181, landing, no gear, config 35, M=0.21											
	180AOA	4°	4°	4°	4°	6°	6°	6°	6°	6°	6°	slat serrations only											
	180array	T100u	T0	T150d	T250d	T100u	T0	T50d	T100d	T150d	T200d												
	181-pt	11	12	13	14	15	16	17	18	19	20	R181											
	181AOA	6°	6°	8°	8°	8°	8°	10°	10°	10°	10°												
	181array	T250d	T350d	T100u	T0	T150d	T250d	T100u	T0	T150d	T250d												
	181-pt	21	22	23	24								R181										
	181AOA	12°	12°	12°	12°																		
	181array	T100u	T0	T150d	T250d																		
9/28	184-pt	4	5	6	7	8	9	10	R184, landing, no gear, config36,M=0.21											slats 2,3,4 gap sealed (1/2" PVC), fixed array			
	184AOA	0°	4°	6°	8°	10°	11.5°	12°												slats 2,3,4 gap sealed			
9/28	185-pt	1	2	3	4	5	6	7	8	9	10	R185, landing,no gear,config36,M=0.21											
	185AOA	4°	4°	4°	4°	6°	6°	6°	6°	6°	6°												
	185array	T100u	T0	T150d	T250d	T100u	T0	T50d	T100d	T150d	T200d												
	185-pt	11	12	13	14	15	16	17	18	19	20	R185											
	185AOA	6°	6°	8°	8°	8°	8°	10°	10°	10°	10°												
	185array	T250d	T350d	T100u	T0	T150d	T250d	T100u	T0	T150d	T250d												
	185-pt	21	22	23	24								R185										
	185AOA	12°	12°	12°	12°																		
	185array	T100u	T0	T150d	T250d																		
9/28	187-pt	3	5	6	6								R187,landing,no gear,config36,M=0.21										
	185AOA	6°	6°	6°	6°								slats 2,3,4 gap sealed, repeat points										
	185array	T0	T0	T0	T0																		

Table A.1 Run Matrix (continued).

STAR 26% 777 40- by 80- Ft. Wind tunnel acoustic run synopsis											
9/28	188-pt	1	2	3	4	5	6	7			
	188AOA	0°	2°	4°	6°	8°	10°	12°			
	188array	T0	T0	T0	T0	T0	T0	T0	R188, landing, no gear, config 36, M=0.21 slats 2,3,4 gap sealed, repeat points		
9/28	189-pt	3	4	5	6	7	8	9	10	11	12
	189Mach	0.238	0.238	0.238	0.238	0.238	0.22	0.22	0.22	0.20	0.20
	189array	T100u	T0	T150d	T250d	T100u	T0	T150d	T250d	T100u	T0
	189-pt	13	14								
	189Mach	0.20	0.20								
	189array	T150d	T250d								
9/28	190-pt	1	2	3	4	5	6		R190, landing, no gear, config 37, Mach sweep slat serrations only, AOA=6°, fixed array		
	190Mach	0.24	0.22	0.20	0.18	0.15	0.12				
9/28	191-pt	1	2	3	4	5	6	7	8	9	10
	191Mach	0.18	0.18	0.18	0.18	0.15	0.15	0.15	0.15	0.12	0.12
	191array	T100u	T0	T150d	T250d	T100u	T0	T150d	T250d	T100u	T0
	191-pt	11	12								
	191Mach	0.12	0.12								
	191array	T150d	T250d								



## APPENDIX B

### CONFIGURATION SUMMARY

Table B.1 Configuration Summary.

Config.	Description	Detent	#8	Gear	Slat treatment	Flap treatment	bracket treatment	Runs	Notes
1x	dirty cruise	cruise	on	-	-	-	-	51, 52, 53, 54, 55	dirty model
1	cruise	cruise	on	-	-	-	-	59, 60	claxed model
2	aero baseline	landing	on	on	-	-	-	67, 68, 69, 70	all tire treads taped for duration of test
3a	aero baseline + filled fairing	landing	on	on	-	-	-	72, 73, 74, 75, 149, 150, 151	inboard fairing filled with foam and tape. All configurations after this point have this mod
3	aero baseline + filled fairing	landing	on	off	-	-	-	75	
4	acoustic baseline	landing	off	off	-	-	-	77, 78, 79, 80	
5	fences + mylar	landing	off	off	tip fences	tip fence	-	81, 82, 83, 84	Dave Driver TF Mylar installed, boundary layer rakes installed forward and aft of model for remainder of test
6	serrated tip	landing	on	off	tip fences	serrated tip	-	87, 88, 90, 91	
7	microtabs + thin trailing edge	landing	off	off	thin trailing edge + fences	microtabs 1	-	92, 93, 94, 95	OFOE tabs $\alpha = 50^\circ$ , IFOE flap $\alpha = 70^\circ$
8	cove filler + porous tip R34	landing	off	off	cove filler	R34 porous tip (LE opening closed)	-	96, 97, 98, 99, 100	R34+Pulorator 387 Rayls porous tip
9	cove filler + porous tip R34 LE open	landing	off	off	cove filler	R34 porous tip (LE opening open)	-	101, 102, 103, 104	
10	cove filler + porous tip R33	landing	off	off	cove filler	R33 porous tip (LE opening closed)	-	105, 106, 107, 108	R33+Pulorator 483 Rayls porous tip
11	cove filler + porous tip R33 + mod bracket	approach	off	off	cove filler	R33 porous tip (LE opening closed)	5th bracket from tip faired	109, 110, 111, 112	5th bracket from tip is faired with a quasi streamwise fairing
12	cove filler + porous tip R34 + mod bracket + scotch	approach	off	off	cove filler	R34 porous tip (LE opening closed)	4th bracket from tip faired + brackets 1 + 9 scotch britten	114, 115, 116, 117, 119, 120, 126, 127, 128, 129, 130	
13	acoustic baseline	approach	off	off	-	-	-	121, 122, 123, 124	
14	aero baseline	approach	on	off	-	-	-		
15	scotch brite + slat fences	approach	off	off	tip fences	-	scotch brite	131	
16	scotch brite + slat fences	approach	on	off	tip fences	-	scotch brite	132, 133, 134, 135	OFOE tabs $\alpha = 50^\circ$ , IFOE flap $\alpha = 70^\circ$ , zip ties on bracket 4 scotch changed
17	microtabs + slat fences + scotch	approach	off	off	tip fences	microtabs 1	scotch brite	136, 137	
18	microtabs + slat fences + scotch	approach	off	off	tip fences	microtabs 2	scotch brite	138, 139	OFOE tabs $\alpha = 70^\circ$ , IFOE tabs $\alpha = 70^\circ$ , B.L. trip w/ 24 grit micro-beads, dummy bracket is large—more like a cove fence, trailing edge serrations are 60 notches centered on local free-stream, deer whistle placed on lower cusp of the most outboard slat, just IB of OB bracket
19	slat treatment special	approach	off	off	Boundary Layer trips on 1st slat IB and 3rd slat OB of pylon + dummy bracket between brackets of 4th slat OB of pylon + serrated trailing edge between brackets of 5th slat OB	serrated tip	scotch brite	140	

Table B.1 Configuration Summary (concluded).

Config.	Description	Detent	#8	Gear	Slat treatment	Flap treatment	bracket treatment	Runs	Notes
20	slat treatment special approach	off	off	Boundary Layer trips + dummy bracket + serrated trailing edge	modified tip fence	scotch brite	141	tip fence modified to reduce noise	
21	slat treatment special with filled trailing edge approach	off	off	Boundary Layer trips + dummy bracket + non-serrated trailing edge	modified tip fence	scotch brite	142	serrated trailing edges have been filled with a flat plate	
22	slat treatment special II approach	off	off	Boundary Layer trips + dummy bracket + serrated trailing edge between brackets of 5th slot of pylon	modified tip fence	-	143	serrated trailing edge moved to 5th slot outboard of pylon	
23	quiet scotch approach	off	off	tip fences	porous tip R34	scotch brite	144, 145		
24	modified serrated tip approach	off	off	slat fences	modified serrated tip	scotch brite	146, 147	serrated tip teeth have been reduced from 3in to 2in, mounted directly to trailing edge of outboard flap	
25	quiet slats landing	on	on	tip fences	-	scotch brite	152, 153, 154		
26	serrated slats landing	on	on	slats 3 & 4 (from tip) serrated trailing edge + tip fences	-	scotch brite	156, 157	slats 3 & 4 (from tip) have serrations, .25" deep, 60° included angle, 1" centers	
27	serrated slats - scotch landing	on	on	3 & 4 serrated + slat fences	-	scotch brite on B slot #7 only	159, 160		
28	2nd gen flap tip fence landing	off	on	simple + doors (simple struts & links)	modified tip fence	scotch brite	162, 163, 164		
29	simple gear landing	on	2, 3, 4, serrated + fences	-	scotch brite	166, 167			
30	simple gear no doors landing	on	2, 3, 4, serrated + fences	-	scotch brite	169, 170			
31	exposed tire treads landing	on	simple w/ forward IB tire tread exposed	2, 3, 4, serrated + fences	-	scotch brite	172		
32	modified tire treads landing	on	simple w/ forward IB modified tire tread exposed	2, 3, 4, serrated + fences	-	scotch brite	173	exposed tire treads have been rounded slightly with a round wood file.	
33	gear off landing	off	2, 3, 4, serrated + fences	-	scotch brite	174, 175			
34	no scotch landing	off	2, 3, 4, serrated + fences	-	-	177, 178	slat fence tape may have been broken		
35	just serrations landing	off	2, 3, & 4 serrated	-	-	180, 181			
36	sealed gap landing	off	2 & 3 sealed gap + 2, 3, & 4 serrated	-	-	184, 185, 187, 188	slats 2 & 3 (counting in) have the gap sealed with .5" pvc pipe		
37	mach sweep landing	on	2, 3, & 4 serrated	-	-	189, 190, 191			

## APPENDIX C

### MODEL AND ARRAY GEOMETRY

The STAR 26%-scale Boeing 777 wind tunnel model consisted of the left half of the airplane (empennage and nose gear omitted) secured to the semispan mount in the NASA Ames 40- by 80-Foot Wind Tunnel. The wing tip extended 26 ft towards the wind tunnel ceiling, and the two microphone arrays were located to the left of the model (looking upstream) to measure the acoustic field underneath the aircraft model.

#### C.1 Model Locations Relative to the Acoustic Arrays

Four coordinate systems are referenced in the STAR test as follows (fig. C.1):

1. Wind tunnel coordinate system: origin at tunnel floor, test section turntable center,  $X_w$ —downstream,  $Y_w$ —cross-stream right (pilot's view),  $Z_w$ —up
2. Model coordinate system: origin at semispan turntable pivot, with model at  $\alpha = 0^\circ$ ,  $X_m$ —upstream,  $Y_m$ —up toward left wingtip,  $Z_m$ —toward fuselage ceiling (wind tunnel right wall)
3. Large fixed array (96-in.-diam pattern) center: origin at center of array face,  $X_a$ —upstream,  $Y_a$ —toward top of array,  $Z_a$ —normal to array face
4. Traversing array (40-in.-diam pattern) center: same coordinate system as large array, but relative to center and face of traversing array

Figure C.1 shows the wind tunnel coordinates of the fixed and traversing array positions,  $X_a = 0$  in.

Wind tunnel acoustic arrays are typically placed in the geometric near-field of the test article, but in the far-field of individual compact sources distributed over the model surface. This is done not only because of the proximity of the wind tunnel walls, but also for the benefit of high spatial resolution and improved signal-to-noise ratio. Consequently, different model sources (e.g. landing gear, flap edge) are located at different angles and distances relative to the center of the array during the same measurement cycle. A complete characterization of the array sources must include the radiation angles and propagation distances, incorporating convection effects at each measurement location.

The following measurement geometry is defined in model coordinates at  $\alpha = 0^\circ$ , with the origin on the tunnel floor at the center of the model pivot (not the test section turntable center). A planar representation of the wing, with  $6.7^\circ$  dihedral is shown in figure C.2, with the center of the array represented as the solid dot located at  $X_m(a)$ ,  $Y_m(a)$ ,  $Z_m(a)$ . A typical source location,  $X_m(s)$ ,  $Y_m(s)$ ,  $Z_m(s)$  shown in the vicinity of the wing outboard trailing edge appears to be translated downstream to location  $X_m(sc)$ ,  $Y_m(sc)$ ,  $Z_m(sc)$  due to convection effects. The source locations tabulated in this section are approximations based on the wing geometry used in the array processing software. Figure C.3 shows the various components of the high-lift system.

For 11 wing source locations, the following parameters were computed for several array locations:  $R$ ,  $R_c$  – physical and convected distances from source to array-center

$\alpha$ ,  $\alpha_c$  – physical and emission angles relative to upstream direction (source to array-center).

$\alpha = \alpha_c = 0^\circ$  for upstream radiation

$\alpha$  – physical slant angle (source to array-center)  $\alpha = 0$  for radiation directly below aircraft.

Equations relating these quantities are as follows (Soderman and Allen 2002):

$$\alpha = \tan^{-1} \frac{Y_M(a) - Y_M(s)}{\sqrt{(X_M(a) - X_M(s))^2 + (Z_M(a) - Z_M(s))^2}} \quad (C.1)$$

$$\beta = 90^\circ + \tan^{-1} \frac{(X_M(s) - X_M(a))}{\sqrt{(Y_M(s) - Y_M(a))^2 + (Z_M(s) - Z_M(a))^2}} \quad (C.2)$$

$$R = \sqrt{(X_M(a) - X_M(s))^2 + (Y_M(a) - Y_M(s))^2 + (Z_M(a) - Z_M(s))^2} \quad (C.3)$$

$$\theta_c = \cos^{-1} \left[ M \sin^2(\beta) + \cos(\beta) \sqrt{1 - M^2 \sin^2(\beta)} \right] \quad (C.4)$$

$$R_c = \frac{R}{M \cos(\beta) + \sqrt{M^2 \cos^2(\beta) - M^2 + 1}} \quad (C.5)$$

The coordinates of 11 wing noise source points are defined for  $\beta = 0^\circ$  in table C.1 below:

Table C.1 Wing source locations in model coordinates (inches, model scale), dihedral = 6.7°.

Source	X <sub>m(s)</sub> , in.	Y <sub>m(s)</sub> , in.	Z <sub>m(s)</sub> , in.
Wing outboard trailing edge (WOTE)	-137.8	310.9	30.5
Aileron outboard edge (AOE)	-133.6	300.9	29.4
Aileron inboard edge (AIE)	-107.7	239.1	22.5
Outboard flap, outboard edge (OFOE)	-106.5	230.2	16.6
Outboard flap, inboard edge (OFIE)	-64.05	114.0	8.4
Flaperon, outboard edge (FOE)	-61.3	109.8	0.6
Flaperon, inboard edge (FIE)	-57.7	87.8	1.4
Aft flap, outboard edge (AFOE)	-59.0	91.2	23.1
Aft flap, inboard edge (AFIE)	-54.9	33.5	31.4
Inboard slat, inboard edge (ISIE)	67.9	34.7	9.8
Inboard slat, outboard edge (ISOE)	35.2	81.9	11.2
Outboard slat, inboard edge (OSIE)	23.7	99.5	13.1
Outboard slat, outboard edge (OSOE)	-117.2	303.3	19.05
Landing gear truck center (LGTC)	-30.2	54.9	44.0

Relative to the model origin, the center of the large array is located at  $X_M(a) = -116$ ,  $Y_M(a) = 78$ , and  $Z_M(a) = -316$  in. (model coordinates). Geometrical and emission angles and distances to the center of the large array are tabulated below in table C.2.

Table C.2 Geometrical and emission angles and distances from source to center of large, fixed array ( $M = 0.22$ ).

Source	$\alpha$	$\beta$	R	$\alpha_c$	R <sub>c</sub>
WOTE	-33.848	87.015	418.05	74.323	433.61
AOE	-32.798	87.548	411.44	74.851	425.86
AIE	-25.447	91.268	374.98	78.562	382.48
OFOE	-4.584	91.483	365.85	78.779	372.85
OFIE	-6.5766	99.521	314.06	86.990	310.16
FOE	-5.6530	99.755	322.83	87.233	318.53
FIE	-1.7452	100.49	320.14	87.996	314.98
AFOE	-2.5236	101.01	298.65	88.537	293.25
AFIE	8.7010	101.97	294.42	89.539	288.03
ISIE	6.6044	119.23	376.65	108.16	345.92
ISOE	-0.62625	114.80	360.48	103.28	336.23
OSIE	-3.4394	112.96	358.21	101.27	336.32
OSOE	-33.916	89.830	403.75	77.121	414.16
LGTC	4.6230	107.45	286.11	95.340	274.13

Relative to the model origin, the center of the small traversing array was located at  $X_M(a) = +100$ , 0, -150, +250 in.,  $Y_M(a) = 106$ , and  $Z_M(a) = -227$  in. (model coordinates). Data were often taken at other array positions and are available in electronic file format, but not presented in the report.

Physical and emission angles and distances to the center of the traversing array at the four principal locations are presented in tables C.3–C.6.

Table C.3 Geometrical and emission angles and distances from source to center of small traversing array,  $X_M(a) = +100$  in. (upstream location),  $M = 0.22$ ,  $\theta = 0^\circ$ .

Source	$\theta$	$\phi$	R	$\theta_c$	Rc
WOTE	-30.305	54.148	405.97	43.877	474.75
AOE	-29.328	54.045	397.85	43.786	465.41
AIE	-22.296	53.704	350.87	43.491	410.89
OFOE	-21.253	52.931	342.63	42.821	402.22
OFIE	-1.6701	53.137	273.46	42.999	320.81
FOE	-0.78050	54.675	278.96	44.335	325.68
FIE	3.7927	55.135	275.90	44.735	321.64
AFOE	3.2876	52.126	258.94	42.126	304.73
AFIE	16.211	53.392	259.84	43.220	304.58
ISIE	16.616	82.608	249.41	70.006	263.20
ISOE	5.5662	74.852	248.05	62.591	269.71
OSIE	1.4800	72.382	252.05	60.278	276.62
OSOE	-31.010	55.444	382.93	45.006	445.96
LGTC	12.811	55.576	230.28	45.120	268.07

Table C.4 Geometrical and emission angles and distances from source to center of small traversing array,  $X_M(a) = 0$  in. (array cross-stream from model center),  $M = 0.22$ ,  $\theta = 0^\circ$ .

Source	$\theta$	$\phi$	R	$\theta_c$	Rc
WOTE	-35.047	67.282	356.73	56.112	396.38
AOE	-33.980	67.469	348.66	56.285	387.17
AIE	-26.098	69.151	302.61	57.833	334.07
OFOE	-25.043	68.711	293.41	57.427	324.42
OFIE	-2.0035	73.682	227.97	62.055	247.66
FOE	-0.92373	74.926	235.71	63.227	254.93
FIE	4.4804	75.696	233.62	63.955	251.96
AFOE	4.0028	73.907	212.74	62.266	230.93
AFIE	19.652	75.241	215.70	63.524	233.02
ISIE	16.145	105.35	256.49	93.670	247.84
ISOE	5.7058	98.359	242.00	86.367	239.91
OSIE	1.5454	95.637	241.40	83.574	241.75
OSOE	-35.899	69.614	336.45	58.261	370.83
LGTC	15.395	80.972	192.33	69.002	203.46

Table C.5 Geometrical and emission angles and distances from source to center of small traversing array,  $X_M(a) = -150$  in. (downstream),  $M = 0.22$ ,  $\theta = 0^\circ$ .

Source	$\theta$	$\phi$	R	$\theta_c$	Rc
WOTE	-38.471	92.129	329.28	80.015	334.11
AOE	-37.179	92.915	322.47	80.809	326.24
AIE	-27.746	98.507	285.94	86.520	283.31
OFOE	-26.658	99.035	276.82	87.065	273.75
OFIE	-1.9430	111.45	235.06	100.18	222.28
FOE	-0.89134	111.29	244.27	100.01	231.12
FIE	4.2813	112.18	244.46	100.96	230.59
AFOE	3.8054	114.01	223.75	102.95	209.73
AFIE	18.450	114.50	229.22	103.48	214.49
ISIE	12.495	131.38	329.64	122.32	292.66
ISOE	4.5591	127.72	302.69	118.16	271.57
OSIE	1.2583	125.87	296.45	116.07	267.44
OSOE	-38.476	95.938	317.07	83.881	317.18
LGTC	13.141	122.24	224.58	112.01	204.89

Table C.6 Geometrical and emission angles and distances to center of small traversing array,  $X_M(a) = -250$  in. (downstream),  $M = 0.22$ ,  $\theta = 0^\circ$ .

Source	$\theta$	$\phi$	R	$\theta_c$	Rc
WOTE	-36.102	108.83	347.66	96.815	331.39
AOE	-34.685	109.87	342.44	97.931	325.16
AIE	-24.866	116.71	316.58	105.38	293.29
OFOE	-23.720	117.69	308.75	106.46	285.07
OFIE	-1.5906	130.36	287.13	120.71	254.48
FOE	-0.73644	129.66	295.65	119.91	262.58
FIE	3.5227	130.34	297.02	120.69	263.25
AFOE	3.0426	133.06	279.77	123.81	246.01
AFIE	14.715	133.08	285.57	123.83	251.10
ISIE	10.199	142.12	402.79	134.35	345.90
ISOE	3.7047	139.98	372.36	131.85	321.44
OSIE	1.0243	138.73	364.18	130.38	315.37
OSOE	-35.206	112.84	342.19	101.14	321.43
LGTC	10.123	139.17	290.52	130.90	251.30

## C.2 High-Lift System Characteristics

The STAR model high-lift system consisted of a multi-element inboard flap, a single-element outboard flap, and a single-slotted slat both inboard and outboard as illustrated in figure C.3. Most of the characteristic dimensions from the high-lift system are listed in table C.7. Figure C.4(a) shows a 3-dimensional CAD model of the wing with the high-lift system deployed in the landing configuration. Noise treatment devices were applied to the outboard slat edges and the outboard

edges of both the inboard and outboard flap. Profiles of the treated edges are shown in figure C.4. Each cut is parallel with the slat or flap edge and not necessarily perpendicular to the leading edge of the element or streamwise.

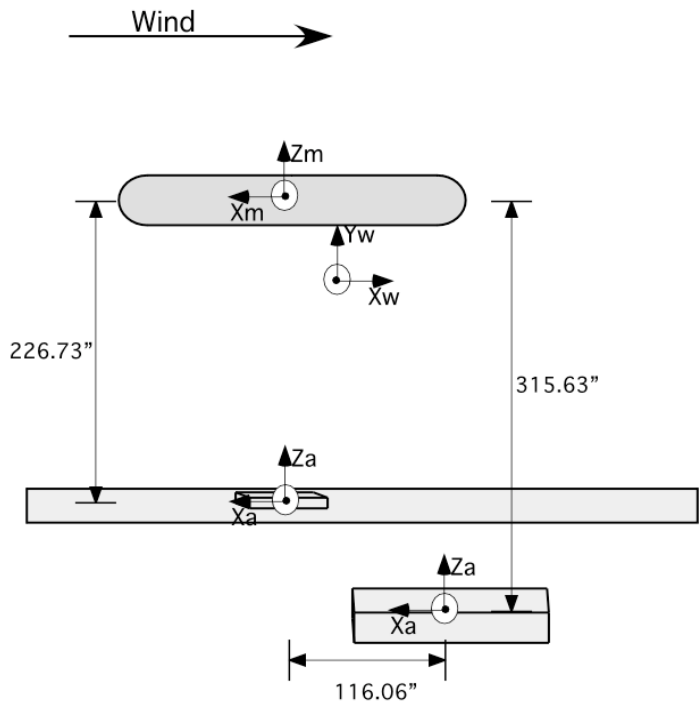
Table C.7 STAR model characteristics.

wing span*	52.0 ft
wing area†	311.3 sq ft
wing aspect ratio	8.7
mean aerodynamic chord	6.0 ft
wing sweep	31.5 deg
wing dihedral	6 deg
main flap span	57.6 in.
aft flap span	57.6 in.
inboard flap main element inboard edge chord	14.7 in.
inboard flap aft element inboard edge chord	12.0 in.
outboard flap span	129.3 in. along flap LE
outboard flap inboard edge chord	19.5 in. perp. to LE
outboard flap outboard edge chord	8.9 in. perp. to LE
aileron span	67.2 in.
aileron mean chord	5.7 in.
outboard slat span	242.8 in. along LE
outboard slat inboard edge chord	6.95 in.
outboard slat outboard edge chord	6.41 in.
outboard slat inboard end slat gap	0.70 in.
outboard slat outboard end slat gap	0.75 in.
inboard slat span	57.6 in. along LE
inboard slat inboard edge chord	9.75 in.
inboard slat outboard edge chord	6.7 in.
inboard slat inboard end slat gap	0.02 in.
inboard slat outboard end slat gap	0.12 in.

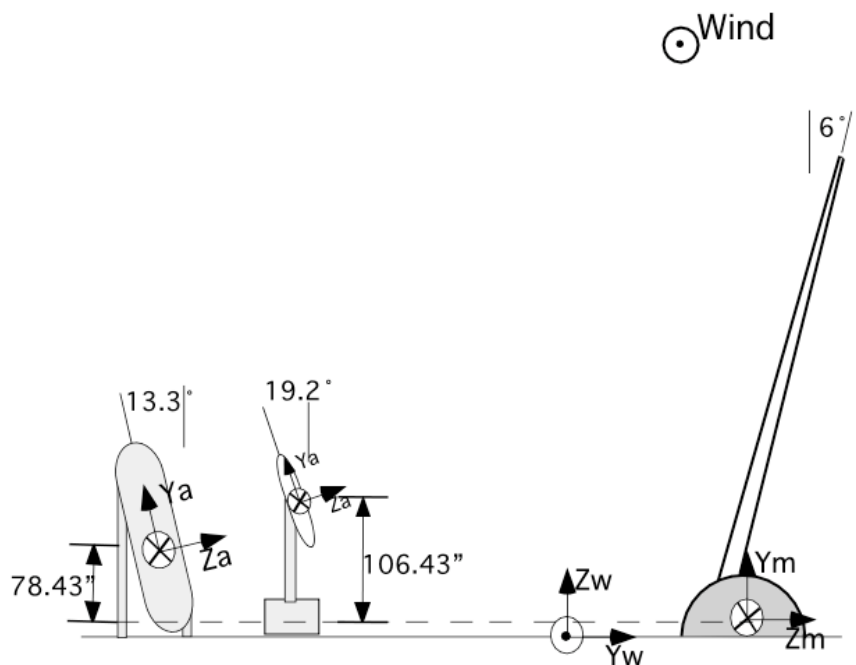
\* Model semispan = 26.0 ft.

† Model semispan wing area = 155.7 ft<sup>2</sup>.

## APPENDIX C FIGURES



(a) Top view.



(b) Side view.

Figure C.1. Wind tunnel layout.

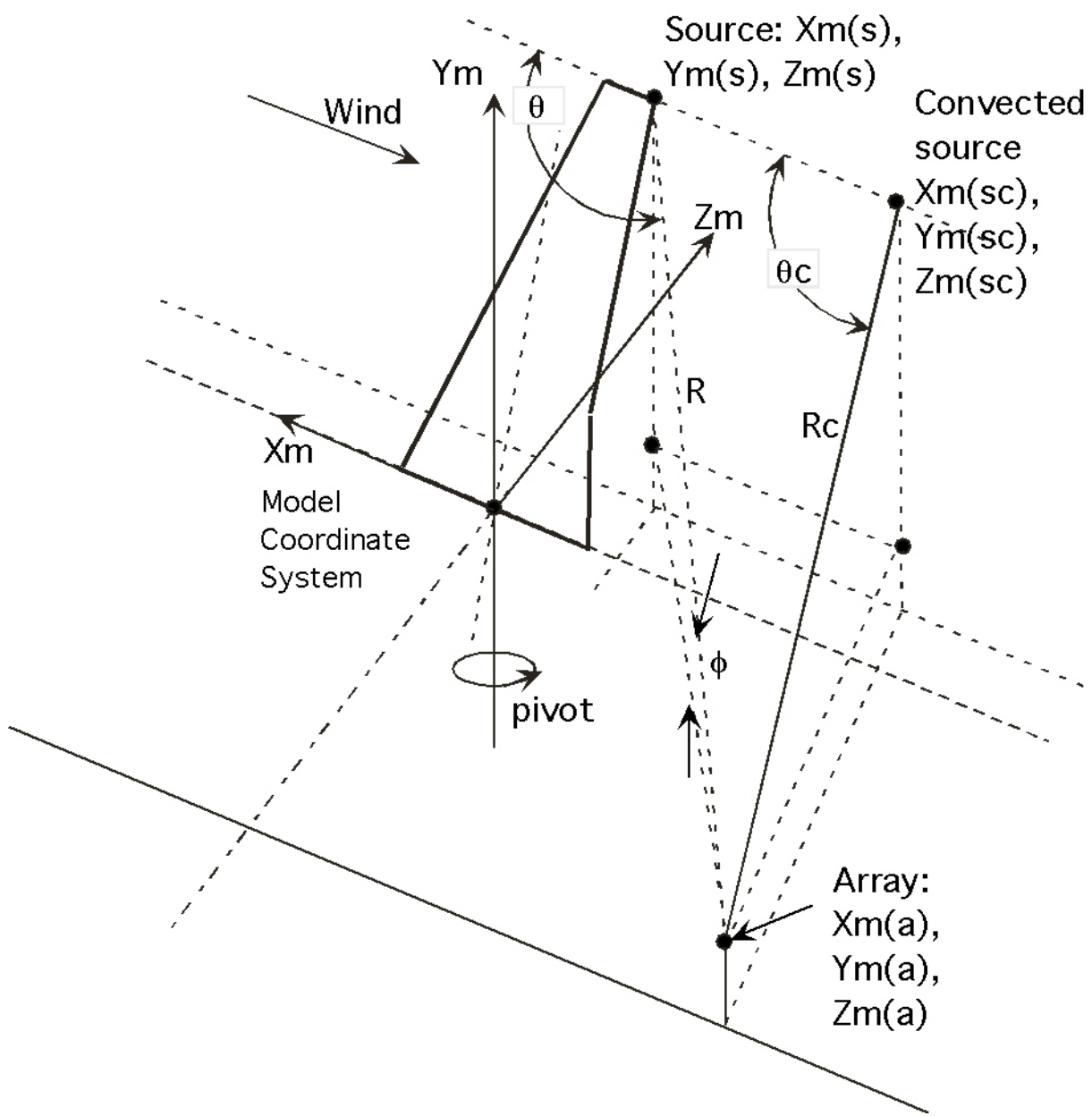
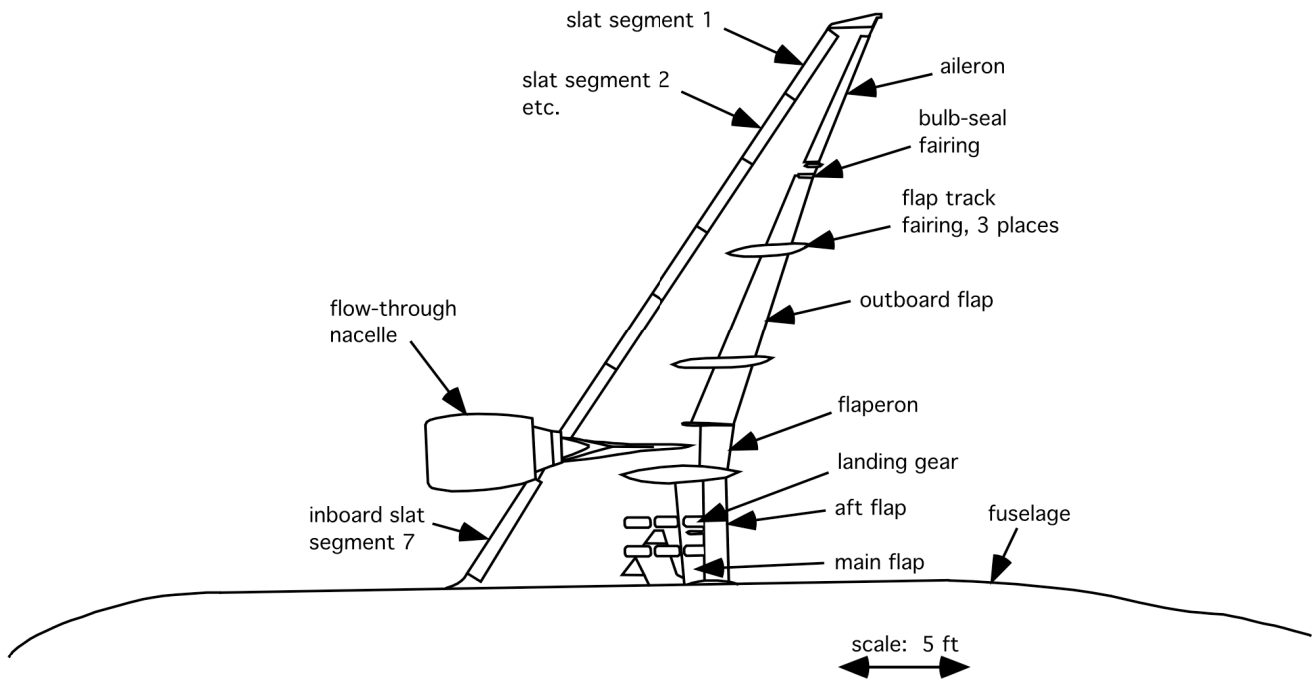
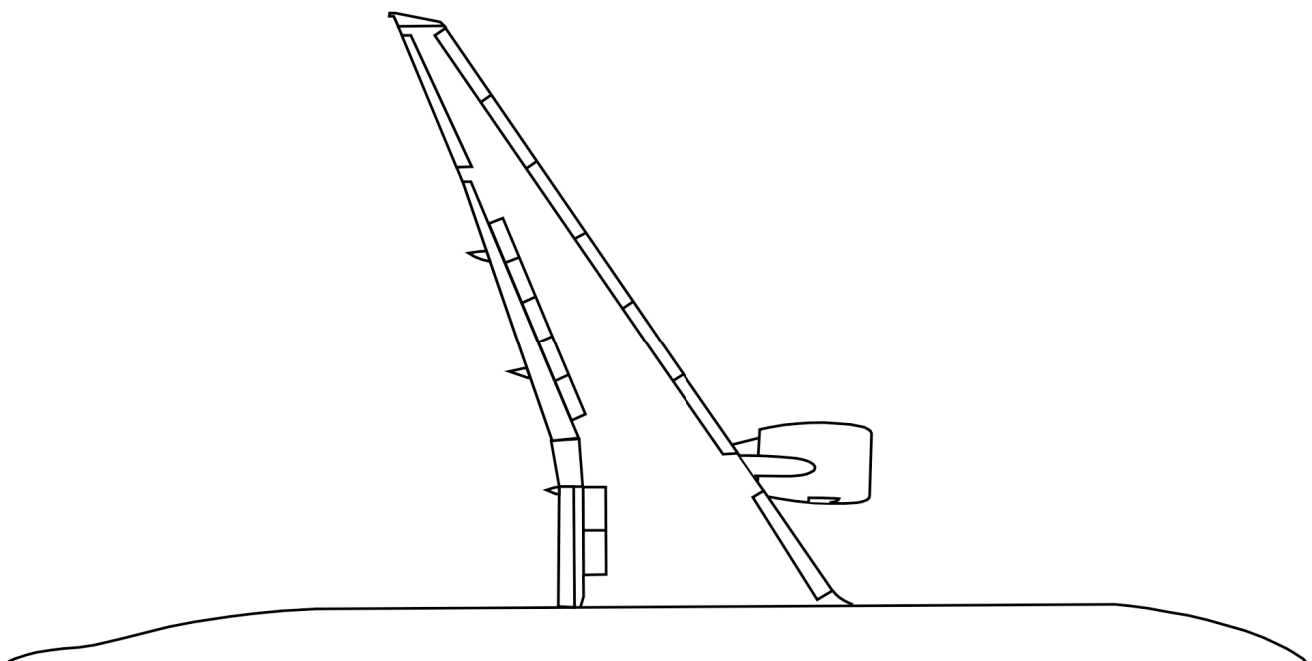


Figure C.2. Geometry of planar wing model at  $\theta = 0^\circ$  and array in model coordinates.

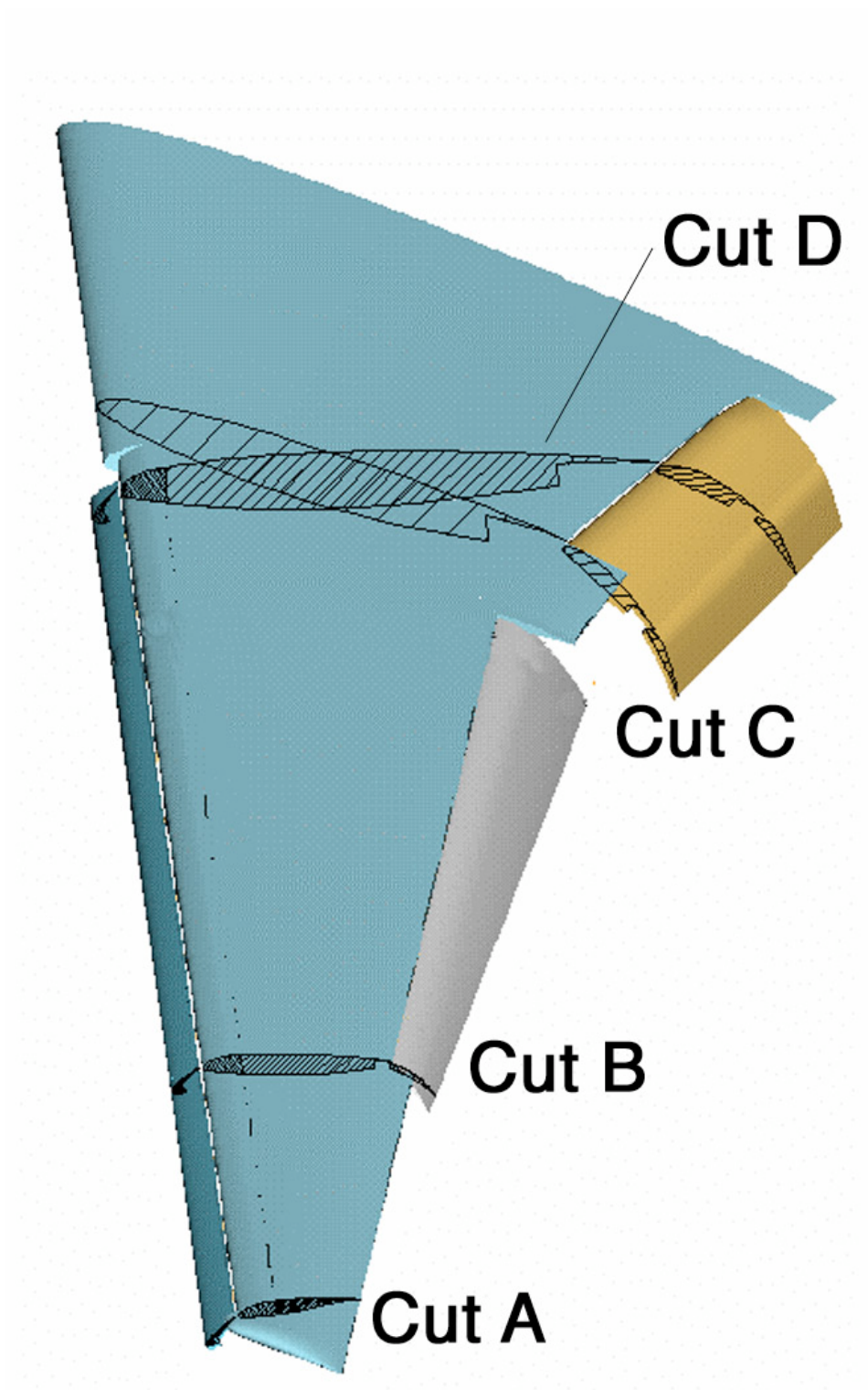


(a) Model fly-over view.



(b) Top view of the model.

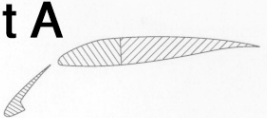
Figure C.3. Sketch of the upper and lower surface of the STAR model.



(a) Three-dimensional drawing showing the high-lift system profile cut locations.

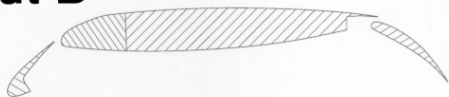
Figure C.4. Landing configuration high-lift system geometry.

### Cut A

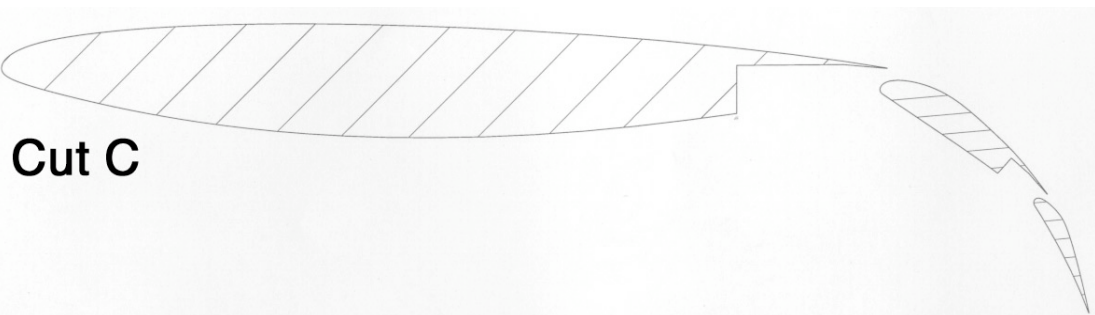


(b) Profile of the outboard edge of the outboard slat (OSOE) in landing configuration.

### Cut B

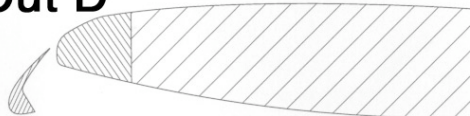


(c) Profile of the outboard edge of the outboard flap (OFOE).



(d) Profile of the outboard edge of aft flap (IFOE).

### Cut D



(e) Inboard-slat inboard-edge (OSIE) profile in landing configuration.

Figure C.4. Concluded.



## APPENDIX D

### INTEGRATED SOURCE SPECTRA METHOD

To aid the data analysis, we integrated the acoustic energy in the scan plane to arrive at the far-field sound level spectra radiated by the key noise source regions. Because a simple summation of acoustic energy recorded at all scan points would result in an exaggerated sound level, we used the integration method described here.

A calibrated phased-microphone array aimed directly at a point noise source in free space will record a peak level equal to that measured by an omnidirectional microphone. However, since we seldom have a point source or a definitive source location, we scan many points in a region that includes the source and create a noise map. Because the phased array has finite beamwidth, any scan point away from the source will generate a false sound level depending on beam shape and scan-point location. And if the sources are distributed, as they often are, the levels at each scan point including the peak will be amplified by leakage from neighboring sources into the main or side lobes of the array pattern. In some cases we can avoid false sources created by side lobes by observing that they move on the scan plane as frequency is varied. As yet, we have been unable to automate that observation skill.

#### D.1 Integration Method

To address the integration problem, Bob Dougherty, formerly with Boeing Co., proposed a scheme based on the idea that integration of a monopole in a region would also result in an amplified level because of finite beamwidth. And because a monopole is well behaved, the amplification can be computed for a given array response. Dougherty developed the following equation\* for correcting an array measurement using an estimate of the array response to a monopole—an equation that we apply to all sources.

$$p_t^2 = \frac{p_R^2 \cdot \iint p_i^2 dA}{\iint p_{R_i}^2 dA} \cdot \frac{p_R^2 \iint p_i^2}{\iint p_{R_i}^2} \quad (D1)$$

where

$p_t^2$  = estimate of the total squared acoustic pressure due to all sources in the integration region A

$p_R^2$  = computed array response to a monopole source set equal to the maximum measured source level and location in scan plane region A (see Mosher 1996) for array response to a monopole)

$p_i^2$  = measured array response at location i in region A

$p_{R_i}^2$  = estimated array response to the above monopole source computed at location i in the scan plane (Mosher 1996)

---

\*Format from memo by M. Mosher 1996.

As long as the sources in the integration region are compact enough to be represented by a monopole, the integrated level is reasonably accurate. This suggests that integrations should be performed on reasonably small regions in the scan plane. From experience, we know that each integration region must contain many scan points.

Ames personnel have developed two algorithms for defining the sources and integration regions used to generate integrated sound levels and spectra. The 'Hayes' algorithm searches the array images frequency by frequency, uses certain criteria such as "Is the noise spot on the model" and "Is the spot within 8 dB of the maximum found," and draws boxes around identifiable sources wherever they occur on the model. The boxed regions are then integrated by computing the array response to an equivalent monopole that would generate the peak level in the box. The Dougherty algorithm is simpler in that the user defines a reasonably compact integration box such as the slat tip region on a model illustrated in figure D.1 (Soderman et al. 2002), and the code computes integrated sound levels by computing the array response to an equivalent monopole for that box for all frequencies. The first method has the problem that the spectra contain many dropouts at frequencies where no significant noise source image was found by the array. The boxes can also get quite large at low frequency or for distributed sources. The second method has the problem that background noise at a given frequency will be integrated in a box if the airframe source is not active at that frequency. A comparison of the two methods is illustrated in figure D.2. Fortunately, the two methods appear to agree over much of the spectrum for slat-tip noise. Clearly, the fixed box or Dougherty method is more informative because the entire spectrum is generated. That is the method that was used for this data analysis.

## D.2 Scaling the Acoustic Spectra

The narrowband acoustic frequencies measured during this study were scaled to full scale:

$$f_{fs} = f_{ss} * SF = f_{ss} * 0.26 \quad (D2)$$

where  $f$  = frequency and subscripts  $fs$  and  $ss$  correspond to full scale and small scale, respectively. The scale factor  $SF = 0.26$ .

The full-scale third-octave spectra were computed from a summation of the full-scale narrowband data in each band and incorporation of standard filter shape corrections. It was assumed that the acoustic energy sums incoherently in each third-octave band. No other adjustments were made to the sound levels. The source-to-array distance,  $d_{ss}$ , in the wind tunnel is equivalent to a full-scale distance:

$$d_{fs} = \frac{d_{ss}}{SF} = 3.85 d_{ss} \quad (D3)$$

For example, consider one small-scale frequency band (150 Hz wide) centered at 1 kHz. Using equations (D2) and (D3), a small-scale sound level of 80 dB at 1 kHz measured in the wind tunnel 10 ft from the model would scale to 80 dB at 260 Hz full scale at an equivalent distance of 38.5 ft.

That sound level would contribute to the computed third-octave band level centered at 250 Hz. Several small-scale bands fall in each full-scale third-octave band.

### D.3 Array Cavity Simulations

As discussed in the section on array design, the condenser microphone diaphragms were flush mounted in an array plate, which was recessed 1.0 in. into the array fairing for the large array and 0.5 in. for the traversing array (Burnside et al. 2002). Each recess was then covered by a porous Kevlar cloth pulled taut. The separation of microphones from the flow minimizes boundary-layer noise and greatly reduces flow noise compared with flush mounted designs (Jaeger et al. 2000). The drawback is that the Kevlar attenuates sound somewhat and creates acoustic resonances that interfere with the acoustic signals from the model.

To address these problems, a study was done in our anechoic chamber to identify the nature and magnitude of the problem and to develop a correction scheme for the acoustic spectra.

#### Fixed Array

To simulate the fixed array with a 1-in.-deep recessed array plate, a 22-in.-diam, nominally 1-in.-deep circular cavity was installed in the anechoic chamber with a Kevlar cover over the recess. Two microphones were flush-mounted in the plate: microphone 1 at 4-in. radius and microphone 2 at 8-in. radius. The simulated array geometry was then radiated with broadband (white) acoustic energy from a loudspeaker 14.5 ft away. To vary acoustic incidence angle, the array was rotated about an axis perpendicular to the vector connecting loudspeaker and array center.

Figure D.3(a) is an example of the acoustic resonance modes measured in the cavity at microphone 1. Cavity depth modes are given by  $f = \frac{nc}{2d}$ . With a cavity depth,  $d$ , of 0.956 in. and a sound speed\* of 1,115 ft/sec, the following modes would be generated:

mode, n	f, Hz
1	6,997
2	14,000
3	20,993

These are reasonably close to the measured mean resonances. The cavity mean resonances near 7 kHz, 14 kHz, and 21 kHz correspond to depth modes of  $\frac{1}{2}$ ,  $\frac{1}{1}$ , and  $\frac{3}{2}$ . The “fuzz” or ripple on the spectra appears random and may indicate inadequate averaging of the white noise data. Similar results were found at microphone 2 (fig. D.3(b)); the average of the two microphones was used in the final correction.

Figure D.3 shows that the cavity resonances grow with frequency because Kevlar impedance goes up with frequency and more energy gets trapped. Kevlar is almost invisible to low-frequency sound. A cosine function was fitted to the data as shown. The mean levels decay exponentially with

---

\*  $c = 20.05 * \sqrt{273.2 + T_{cent}}$  m/sec ==> 1115 ft/sec.

frequency above 10 kHz, implying that the increasing resistance allows less and less energy to enter the cavity as frequency increases.

The cavity resonance frequencies increase as incidence angle is changed relative to normal incidence. This is consistent with Fahy's model for a waveguide (Fahy 2001). A component of the depth modes propagates in the cavity parallel to the Kevlar. The resulting waveguide modes propagate at a phase speed above the local sound speed and appear at a higher frequency than the source frequency. This frequency increase is locked to incidence angle. The result is that the spectra are dispersed; that is, the spectra tend to stretch out with increasing incidence angle.

Using the average of the two microphone signals, the fixed array total Kevlar effects are summarized as cosine curve fits to the data as shown in figure D.4. Corrections in decibels were generated for incidence angles of 0°, 10°, 15°, 20° and 30°.

$$\begin{aligned}
 \Delta dB_{0^\circ} &= 0.26 f \cos(f \Delta 0.00038f^2 \Delta 8) \Delta 0.0065f^2 \\
 \Delta dB_{10^\circ} &= 0.25 f \cos(f \Delta 0.00038f^2 \Delta 8) \Delta 0.005f^2 \\
 \Delta dB_{15^\circ} &= 0.24 f \cos(f \Delta 0.00038f^2 \Delta 8.25) \Delta 0.007f^2 \\
 \Delta dB_{20^\circ} &= 0.26 f \cos(f \Delta 0.00038f^2 \Delta 8.5) \Delta 0.007f^2 \\
 \Delta dB_{30^\circ} &= 0.22 f \cos(f \Delta 0.00038f^2 \Delta 9.3) \Delta 0.005f^2
 \end{aligned} \tag{D4}$$

where  $\Delta dB$  is the data correction to be subtracted from the data,  $f$  is frequency in kHz, and the cosine function is in radians. Corrections are not applied above 15.5 kHz, which is considered the upper limit of the fixed array. Above that limit, side-lobe interference rendered the source images and integrations uncertain.

Figure D.5 shows the effect of equation D4 on speaker-to-array calibration data in the 40 x 80 without wind. The corrections are cutoff at frequencies above the range of interest for the large array (15.5 kHz). Although the corrections are incorporated in the integrated spectra, no corrections to the array images have been used. Such corrections would make the images slightly brighter or dimmer at different frequencies, but would likely be inconsequential to the interpretation of the graphical results.

### Traversing Array

The traversing array cavity was simulated in the anechoic chamber with a 41-in.-diam, nominally 0.5-in.-deep circular cavity covered by Kevlar cloth. Two microphones were flush mounted in the back plate: microphone 1 at 2.51-in. radius and microphone 2 at 19.91-in. radius. Complex depth and radial acoustic modes were excited.

Figure D.6(a) shows the cavity mean resonances for microphone 1 at 2.5 kHz and 6 kHz, which correspond to radial modes with  $\Delta/4$  and  $\Delta/8$  equal to array radius. The radial modes and related circumferential modes are modeled as Bessel functions (see Fahy 2001, sec. 8.7.4). The worst case

was at 10° incidence. The peak at 17 kHz corresponds to the first depth mode if the cavity depth was approximately 0.1 in. less than the 0.5 in. assumed.

The strong ripple on the spectra occurs predominantly at 660 Hz, which is a radial mode at  $\square$  equal to array radius. Other ripples have been identified at 320 Hz, which is a radial mode at  $\square$  equal to array diameter. The ripples vary with microphone position as shown in figure D.6b for microphone 2, implying that the ripples would average out for an array of many microphones.

As with the 1-in.-deep cavity, resonances grow with frequency, because Kevlar impedance goes up with frequency and more energy gets trapped. The mean levels decay exponentially, with frequency implying that the increasing Kevlar resistance allows less and less energy to enter the cavity. Kevlar tautness has a minor effect on cavity resonance.

The best curve fits to the traversing array mean-resonance curves were multi-degree polynomials, as shown in figure D.7. The coefficients are listed in table D1 for incidence angles of 0°, 10°, 15°, 20°, and 30°. The decibel corrections in figure D.7 have been incorporated in the integrated spectra, but no correction has been made to the array images.

$$\square \text{dB} = a_0 + a_1 f + a_2 f^2 + \dots + a_9 f^9 \quad (\text{D5})$$

where  $f$  = frequency, kHz.

Table D.1 Polynomial coefficients for equation D5 and figure D.7.

	0° incidence	10° incidence	15° incidence	20° incidence	30° incidence
$a_0$	-0.6856900000000	-0.9180100000000	1.8737000000000	-2.1857000000000	6.8173000000000
$a_1$	-0.4824950000000	1.0697000000000	-4.3770500000000	2.7414450000000	-12.4611000000000
$a_2$	1.1338150000000	-0.0352550000000	3.5334000000000	-0.6836150000000	8.1967500000000
$a_3$	-0.4431600000000	-0.0625335000000	-1.1805400000000	0.0508520000000	-2.2684500000000
$a_4$	0.0769570000000	0.0087716050000	0.2050600000000	-0.0009857000000	0.3155300000000
$a_5$	-0.0078029000000	-0.0004134150000	-0.0211360000000	-0.0000182370000	-0.0243010000000
$a_6$	0.0005046235000	0.0000064504000	0.0013483500000	0.0000004866200	0.0010554550000
$a_7$	-0.0000203574800		-0.0000520945000		-0.0000242215000
$a_8$	0.0000004587165		0.0000011114200		0.0000002283750
$a_9$	-0.0000000043454		-0.0000000100073		

## APPENDIX D FIGURES

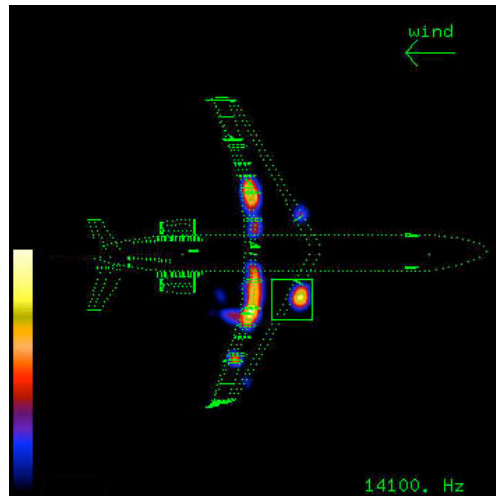


Figure D.1. An example of an integration box around a noise source found in an array scan of a wind tunnel model (Mosher 1996).

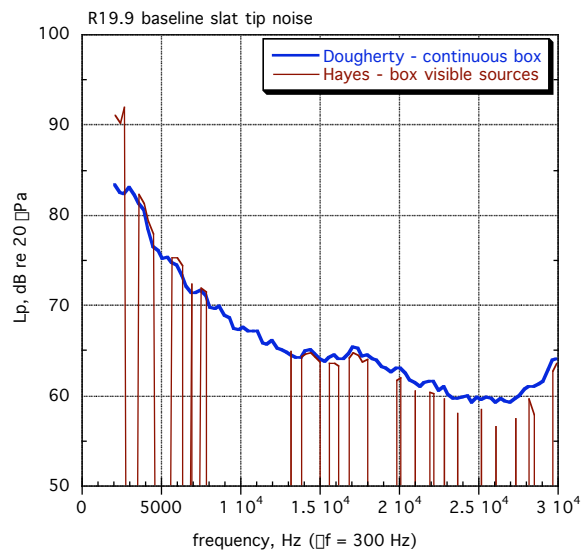
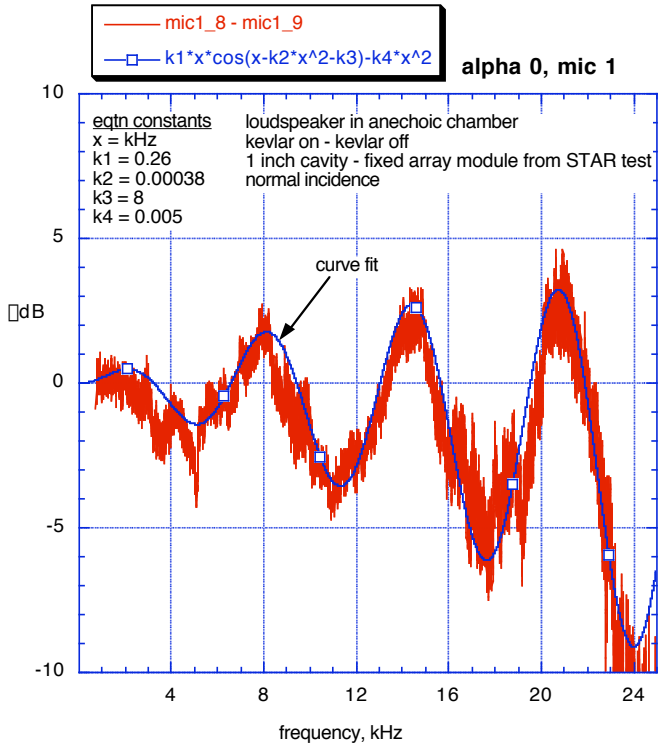
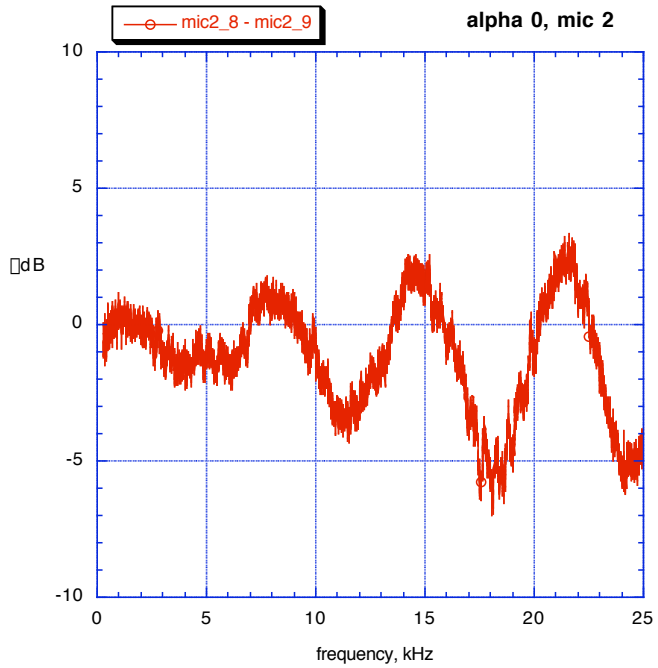


Figure D.2. Integrated spectra from the integration region in figure D.1 using a fixed or continuous boxing method and an automatic boxing method that only accepts visible sources.



(a) Resonance at microphone 1.



(b) Resonance at microphone 2.

Figure D.3. Cavity resonances in 1.0-in.-deep cavity at 0° incidence; LpKevlar On – LpKevlar Off. A typical curve fit is shown resonance.

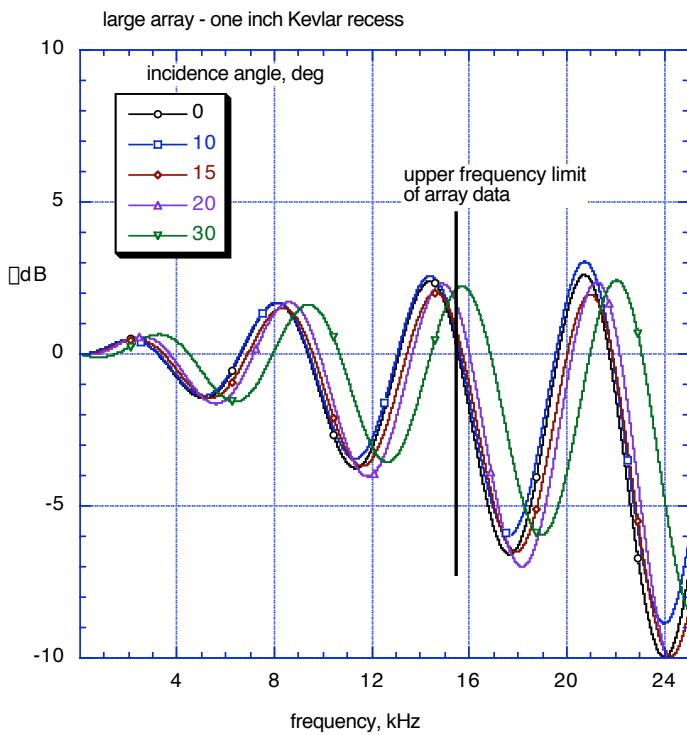


Figure D.4. Curve fit ensemble currently used in the integration software to correct narrow-band spectra, 1.0-in.-deep cavity. LpKevlar On – LpKevlar Off .

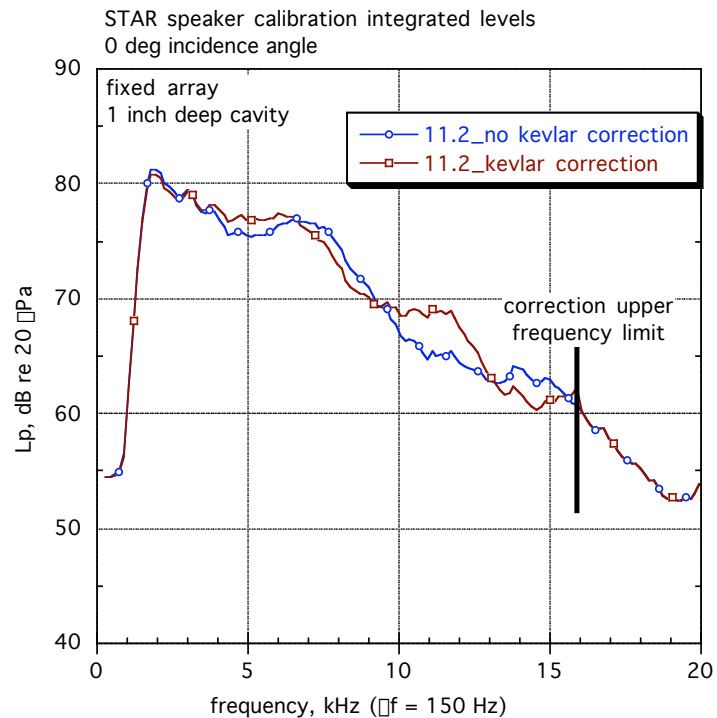
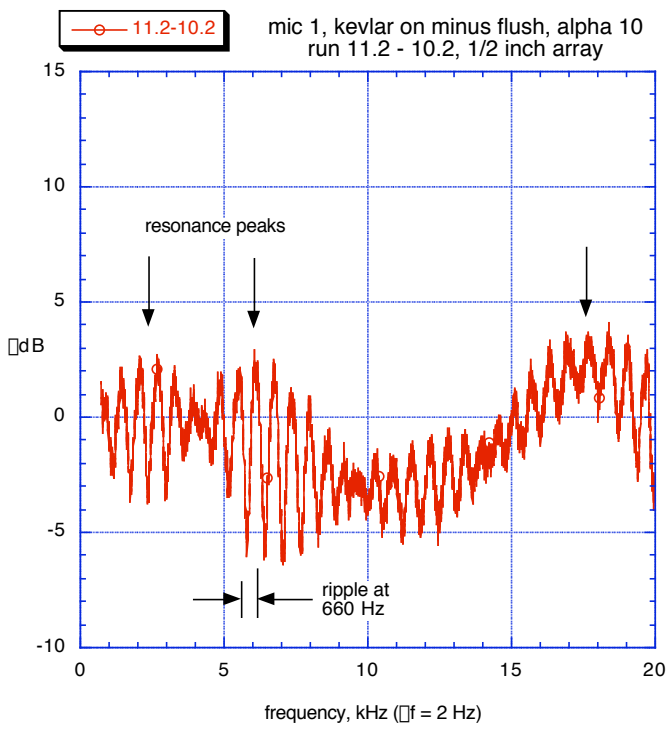
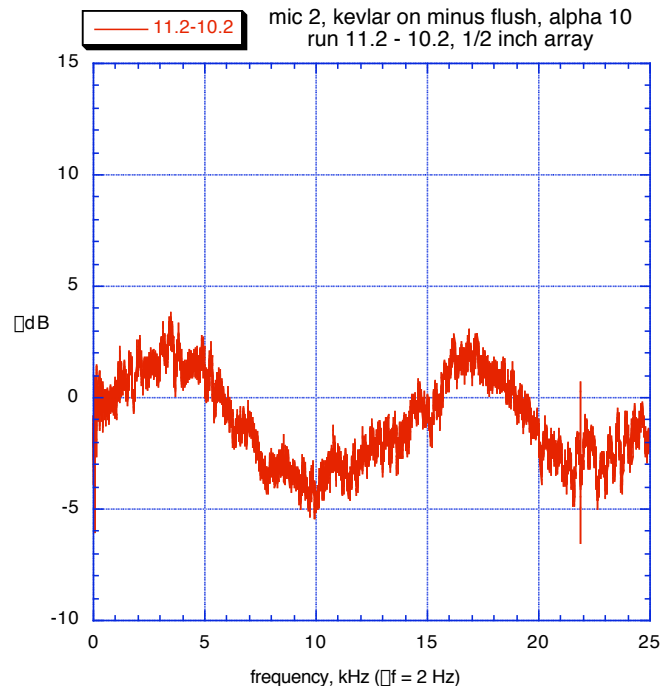


Figure D.5. STAR speaker calibration data with and without Kevlar cavity correction. Speaker in free space in the 40x80; wind off.



(a) Resonance at microphone 1.



(b) Resonance at microphone 2.

Figure D.6. Cavity resonance in 0.5-in.-deep cavity at  $10^\circ$  incidence; LpKevlar On – LpKevlar Off. Ripples are spaced approximately 660 Hz.

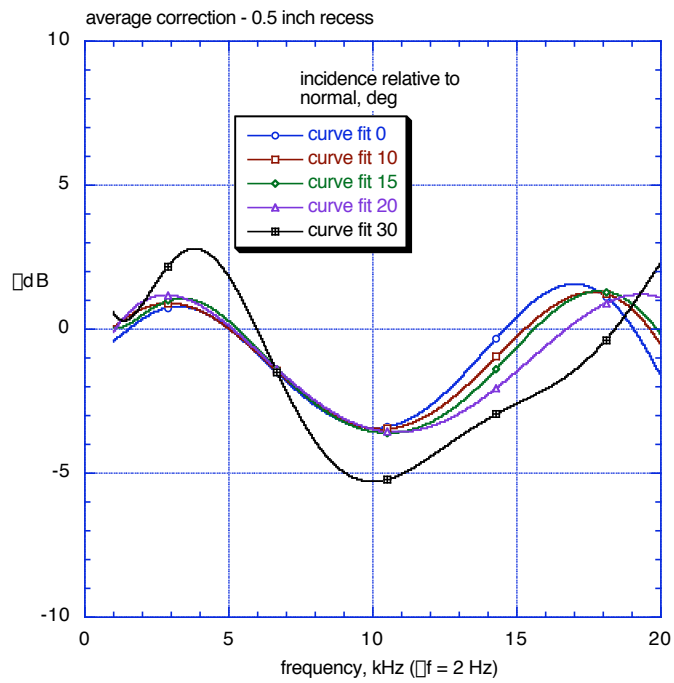


Figure D.7. Curve fit ensemble currently used in the integration software to correct narrow-band spectra, 0.5-in.-deep cavity. LpKevlar On – LpKevlar Off.

## APPENDIX E

### ARRAY MICROPHONE LOCATIONS

Table E.1 Traversing array microphone positions (relative to array center).

Microphone	x (inches)	y (inches)	Microphone	x (inches)	y (inches)
1	2.5761	2.4864	36	-4.7895	12.468
2	-1.5686	3.2184	37	-13.338	-0.70213
3	-3.5456	-0.49733	38	-3.4539	-12.902
4	-0.62267	-3.5258	39	11.203	-7.2719
5	3.1608	-1.6817	40	10.378	8.408
6	-1.6593	-1.8784	41	-2.3657	-14.565
7	1.2737	-2.1585	42	13.121	-6.7507
8	2.4465	0.54437	43	10.475	10.393
9	0.23827	2.495	44	-6.647	13.174
10	-2.2992	0.99759	45	-14.583	-2.2508
11	1.0162	-5.4758	46	18.273	2.7545
12	5.5218	-0.72564	47	3.027	18.23
13	2.3965	5.0273	48	-16.402	8.5122
14	-4.0407	3.8327	49	-13.164	-12.969
15	-4.8938	-2.6586	50	8.2664	-16.528
16	-8.9894	-0.3462	51	-17.224	-0.67318
17	-2.4486	-8.6564	52	-4.6824	-16.589
18	7.4761	-5.0038	53	14.331	-9.5796
19	7.0691	5.5639	54	13.539	10.669
20	-3.1071	8.4425	55	-5.9629	16.173
21	-3.8081	6.8019	56	13.498	-0.67774
22	-7.6458	-1.5198	57	4.8157	12.628
23	-0.91723	-7.7413	58	-10.522	8.4823
24	7.0789	-3.2645	59	-11.319	-7.3857
25	5.2923	5.7237	60	3.5266	-13.047
26	7.0973	3.4923	61	3.2316	19.416
27	-1.1282	7.8291	62	-17.468	9.0735
28	-7.7946	1.3463	63	-14.027	-13.809
29	-3.6891	-6.9971	64	8.7983	-17.608
30	5.5146	-5.6707	65	19.465	2.9266
31	9.7308	4.4593	66	-19.432	-4.3123
32	-1.2341	10.633	67	-1.9037	-19.814
33	-10.493	2.112	68	18.256	-7.9334
34	-5.2513	-9.3272	69	13.186	14.911
35	7.248	-7.8765	70	-10.106	17.149

Table E.2 Large array microphone positions (relative to array center).

Microphone	x (inches)	y (inches)	Microphone	x (inches)	y (inches)
1	36.911	-3.7874	36	-26.885	-18.172
2	45.826	14.884	37	-27.626	24.77
3	24.941	6.2648	38	-45.817	14.913
4	19.391	11.914	39	-23.857	9.6008
5	31.208	9.6641	40	-22.69	1.7681
6	37.667	23.221	41	-30.924	10.537
7	40.025	22.416	42	-44.121	3.3707
8	28.274	20.025	43	-45.555	5.4086
9	34.966	13.283	44	-34.644	0.4316
10	33.724	9.2957	45	-36.092	9.8197
11	21.739	21.346	46	-32.743	12.314
12	32.431	-1.0928	47	-30.135	-4.4804
13	7.7995	-36.276	48	-25.587	19.956
14	28.311	-38.988	49	15.025	33.926
15	13.663	-21.786	50	0.0305	48.183
16	17.321	-14.763	51	1.7621	25.656
17	18.831	-26.696	52	-5.3271	22.126
18	33.721	-28.652	53	0.4692	32.667
19	33.683	-31.144	54	-10.423	43.004
20	27.779	-20.705	55	-8.9277	44.998
21	23.435	-29.153	56	-10.291	33.083
22	19.258	-29.203	57	-1.8093	37.361
23	27.017	-14.082	58	1.5983	34.945
24	8.9785	-31.183	59	-13.57	27.278
25	-32.092	-18.624	60	11.077	30.501
26	-28.336	-38.97	61	4.3001	-7.0258
27	-16.5	-19.724	62	-5.3531	-6.2607
28	-8.6904	-21.034	63	-7.6085	3.1565
29	-19.574	-26.157	64	0.6508	8.2115
30	-16.835	-40.922	65	8.0107	1.9185
31	-19.216	-41.656	66	4.159	0.8721
32	-11.112	-32.817	67	2.1146	-3.686
33	-20.488	-31.294	68	-2.8521	-3.1502
34	-21.826	-27.337	69	-3.8773	1.7391
35	-5.0475	-30.046	70	0.4558	4.225

## APPENDIX F

### LIST AND DESCRIPTION OF DATA FILES

- \*rawth01.bin – binary file containing microphone voltages, e.g., 123000PMA00141004rawth01.bin
- \*rawth01.nc – Netcdf<sup>a</sup> file containing the data acquisition parameters and test conditions, e.g., 123000PMA00141004rawth01.nc
- \*rawth99.nc – Netcdf file containing all the information from the above files, e.g., 123000PMA00141004rawth99.nc
- \*procd\*.nc – Netcdf file containing array processed data, e.g., 123000PMA00141004procd38.nc
- \*procd\*.\* – ASCII file containing the integration region geometry for each frequency, e.g., 150008procd29.cove
- \*procd\*.\*.out – ASCII file containing the results of the narrowband integration, e.g., 150008procd29.cove.out
- \*procd\*.\*.outto – ASCII file containing the 1/3-octave integrated data, e.g., 150008procd29.cove.outto

---

<sup>a</sup> Netcdf is platform independent data storage format. Information about Netcdf and libraries to read and write data in netcdf format can be found at the following url:  
<http://www.unidata.ucar.edu/packages/netcdf/>

# REPORT DOCUMENTATION PAGE

Form Approved  
OMB No. 0704-0188

Public reporting burden for this collection of information is estimated to average 1 hour per response, including the time for reviewing instructions, searching existing data sources, gathering and maintaining the data needed, and completing and reviewing the collection of information. Send comments regarding this burden estimate or any other aspect of this collection of information, including suggestions for reducing this burden, to Washington Headquarters Services, Directorate for Information Operations and Reports, 1215 Jefferson Davis Highway, Suite 1204, Arlington, VA 22202-4302, and to the Office of Management and Budget, Paperwork Reduction Project (0704-0188), Washington, DC 20503.

1. AGENCY USE ONLY (Leave blank)	2. REPORT DATE October 2004	3. REPORT TYPE AND DATES COVERED Technical Memorandum	
4. TITLE AND SUBTITLE Aeroacoustic Study of a 26%-Scale Semispan Model of a Boeing 777 Wing in the NASA Ames 40- by 80-Foot Wind Tunnel		5. FUNDING NUMBERS UPN 781	
6. AUTHOR(S) W. Clifton Horne <sup>1</sup> , Nathan J. Burnside <sup>2</sup> , Paul T. Soderman <sup>1</sup> , Stephen M. Jaeger <sup>3</sup> , Bryan R. Reinero <sup>2</sup> , Kevin D. James <sup>1</sup> , and Thomas K. Arledge <sup>1</sup>		8. PERFORMING ORGANIZATION REPORT NUMBER A-0410923	
7. PERFORMING ORGANIZATION NAME(S) AND ADDRESS(ES) <sup>1</sup> Ames Research Center, Moffett Field, CA 94035-1000 <sup>2</sup> AerospaceComputing Inc., Ames Research Center, Moffett Field, CA 94035-1000 <sup>3</sup> Colin Gordan and Associates, San Bruno, CA		10. SPONSORING/MONITORING AGENCY REPORT NUMBER NASA/TP-2003-212802	
9. SPONSORING/MONITORING AGENCY NAME(S) AND ADDRESS(ES) National Aeronautics and Space Administration Washington, DC 20546-0001			
11. SUPPLEMENTARY NOTES Point of Contact: W. Clifton Horne, Ames Research Center, MS 247-A, Moffett Field, CA 94035-1000 (650) 604-4571		12a. DISTRIBUTION/AVAILABILITY STATEMENT Unclassified — Unlimited Subject Category 01      Distribution: Standard Availability: NASA CASI (301) 621-0390	
12b. DISTRIBUTION CODE			
13. ABSTRACT (Maximum 200 words) An acoustic and aerodynamic study was made of a 26%-scale unpowered Boeing 777 aircraft semispan model in the NASA Ames 40- by 80-Foot Wind Tunnel for the purpose of identifying and attenuating airframe noise sources. Simulated approach and landing configurations were evaluated at Mach numbers between 0.12 and 0.24. Cruise configurations were evaluated at Mach numbers between 0.24 and 0.33. The research team used two Ames phased-microphone arrays—a large fixed array and a small traversing array—mounted under the wing to locate and compare various noise sources in the wing high-lift system and landing gear. Numerous model modifications and noise alleviation devices were evaluated. Simultaneous with acoustic measurements, aerodynamic forces were recorded to document aircraft conditions and any performance changes caused by the geometric modifications. Numerous airframe noise sources were identified that might be important factors in the approach and landing noise of the full-scale aircraft. Several noise-control devices were applied to each noise source. The devices were chosen to manipulate and control, if possible, the flow around the various tips and through the various gaps of the high-lift system so as to minimize the noise generation. Fences, fairings, tip extensions, cove fillers, vortex generators, hole coverings, and boundary-layer trips were tested. In many cases, the noise-control devices eliminated noise from some sources at specific frequencies. When scaled to full-scale third-octave bands, typical noise reductions ranged from 1 to 10 dB without significant aerodynamic performance loss.			
14. SUBJECT TERMS Airframe noise, Phased-microphone array, Traversing array, Large array, Cove filler, Slat fence, Flap-edge fence, Serrated trailing edge, Flap-edge microtabs, Subsonic Transport Aeroacoustic Research (STAR), Advanced Subsonic Technology (AST), NASA Ames 40- by 80-Foot Wind Tunnel		15. NUMBER OF PAGES 214	
16. PRICE CODE			
17. SECURITY CLASSIFICATION OF REPORT Unclassified	18. SECURITY CLASSIFICATION OF THIS PAGE Unclassified	19. SECURITY CLASSIFICATION OF ABSTRACT Unclassified	20. LIMITATION OF ABSTRACT